UNIVERSITY OF LEEDS

Self-Mixing in Terahertz Quantum Cascade Lasers

James Thomas Keeley

Submitted in accordance with the requirements for the degree of Doctor of Philosophy

University of Leeds
Institute for Microwaves & Photonics
School of Electronic & Electrical Engineering

April 2016

The candidate confirms that the work submitted is his/her own, except where work which has formed part of jointly authored publications has been included. The contribution of the candidate and the other authors to this work has been explicitly indicated below. The candidate confirms that appropriate credit has been given within the thesis where reference has been made to the work of others.

A number of publications have arisen from the work presented in this thesis:

Chapters 3.2.2 & 4.2:

P. Dean, A. Valavanis, J. T. Keeley, K. Bertling, Y. L. Lim, R. H. S. Alhathlool, A. D. Burnett, L. H. Li, S. P. Khanna, D. Indjin, T. Taimre, A. D. Rakić, E. H. Linfield, and A. G. Davies, "Terahertz imaging using quantum cascade lasers-a review of systems and applications," *J. Phys. D. Appl. Phys.*, vol. 47, p. 374008, sep 2014

Work, including experimental set-up, hardware control and data gathering and analysis, in Chapters 6.2 and 6.3 was performed by myself under supervision of Dr. Paul Dean. Figures 15 (c), 16 (b) and 17 (a) come from data processing/analysis completed by myself.

Chapter 3.3:

P. Dean, O. Mitrofanov, J. T. Keeley, I. Kundu, L. H. Li, E. H. Linfield, and A. Giles Davies, "Apertureless near-field terahertz imaging using the self-mixing effect in a quantum cascade laser," *Appl. Phys. Lett.*, vol. 108, p. 091113, feb 2016

Work, including experimental set-up, hardware control and data gathering and analysis was performed by myself with supervision from Dr. Paul Dean and Dr. Oleg Mitrofanov. Figures 2, 3 and 4 were generated from data processing/analysis completed by myself.

Chapter 4.2:

P. Dean, A. Valavanis, J. T. Keeley, K. Bertling, Y. L. Lim, R. H. S. Alhathlool, S. Chowdhury, T. Taimre, L. H. Li, D. Indjin, S. J. Wilson, A. D. Rakić, E. H. Linfield, and A. Giles Davies, "Coherent three-dimensional terahertz imaging through self-mixing in a quantum cascade laser," *Appl. Phys. Lett.*, vol. 103, no. 18, p. 181112, 2013

I was responsible for the experimental system and data gathering for the sample with 10µm-tall steps. Data processing/analysis was completed in collaboration with Dr. Alex Valavanis under supervision of Dr. Paul Dean.

Chapter 5.2:

J. T. Keeley, P. Dean, A. Valavanis, K. Bertling, Y. L. Lim, R. H. S. Alhathlool, T. Taimre, L. H. Li, D. Indjin, A. D. Rakić, E. H. Linfield, and A. G. Davies, "Three dimensional terahertz imaging using swept-frequency feedback interferometry with a quantum cascade laser," *Opt. Lett.*, vol. 40, p. 994, mar 2015

In addition to writing the publication, I was responsible for the experimental set-up, and hardware control and data gathering software. I also performed the data processing/analysis for the paper.

Chapter 5.3:

S. Han, K. Bertling, P. Dean, J. T. Keeley, A. D. Burnett, Y. L. Lim, S. P. Khanna, A. Valavanis, E. H. Linfield, A. G. Davies, D. Indjin, T. Taimre, and A. D. Rakić, "Laser Feedback Interferometry as a Tool for Analysis of Granular Materials at Terahertz Frequencies: Towards Imaging and Identification of Plastic Explosives," *Sensors*, vol. 16, p. 352, mar 2016

In this work, I helped Dr. Karl Bertling and Dr. Andrew Burnett with sample preparation. Data gathering and initial analysis were also performed by myself under supervision of Dr. Paul Dean and Dr. Bertling.

Chapter 5.4:

P. Dean, J. T. Keeley, A. Valavanis, K. Bertling, Y. L. Lim, T. Taimre, R. H. S. Alhathlool, L. H. Li, D. Indjin, A. D. Rakić, E. H. Linfield, and A. G. Davies, "Active phase-nulling of the self-mixing phase in a terahertz frequency quantum cascade laser," *Opt. Lett.*, vol. 40, p. 950, mar 2015

I was responsible for experimental set-up, and hardware control and data gathering software. I also performed initial data processing/analysis for the paper, which was finalised for publication by Dr. Paul Dean.

This thesis is dedicated to my Grandparents; Tommy & Veronica Ratcliffe. I couldn't ask for better and I've never known anyone so proud of everything I achieve.

Acknowledgements

First and foremost, I have to give my sincere gratitude to my supervisor Paul Dean for his invaluable ideas, support and direction throughout not only my PhD, but also the preceding Masters that made me realise what a stimulating endeavour this project would be. Whether we were working together in the lab or I needed help grasping a difficult concept you always made the time to make sure I had a complete understanding of the subject. I have no doubt that without your guiding hand I wouldn't have achieved half of what I have in the past few years. For that Paul, I thank you. It has been a pleasure to be your student.

I will be forever grateful to Edmund Linfield and Giles Davies, for not only helping guide me through this process, but for piquing my interest in terahertz when I was just starting out as a fresher (all those years ago). Without your fun and interesting lectures I would never have considered studying this area of research. Thanks are due also to the Engineering and Physical Sciences Research Council (EPSRC) for funding this project and making it possible.

A special mention must also go to Alex Valavanis. Not only did you always seem to have the answer to any question I could think to ask, which was invaluable when I couldn't get my head around a topic, but you always took the time to make sure I understood the knowledge you were imparting. During my studies your encouragement made me believe that this PhD was always within my reach and your constant jokes around the lab kept the work fun. You were a pleasure to work with mate.

Speaking of people who were great to work with, I must also give a huge thanks to the staff & students who I've shared a lab and office with during the tenure of my studies, especially Burnie, Josh, Reshma, Dave, Siddhant, Dong, Iman, Helen and Chris R. You guys kept the long lab hours interesting and enjoyable, so thank you for that.

I can't even imagine what my PhD life would have been without the friends I had outside of the lab. Thierry, Lawrence, Adam[1] and Ciára, not a single day went by where you guys didn't make me laugh and you have no idea how grateful I am for all of you! You

were always the first to hear about my work, whether I was moaning or bragging about it, and I also love you guys for always acting that you were interested when I was excitedly rambling on about my research, even if I'd lost you 5 minutes before.

Outside of work, most of my time over the past 4 years has been spent with my ever evolving Freestyle family. You guys all made the time so enjoyable its crazy; whether we were sat on a 30 hour coach ride to tour, feeling the nerves set in as we were about to hit a stage or just acting like idiots on a night out, I wouldn't change a second of it. Freestyle was the perfect distraction from work when I needed it and my time as PR Sec and winning awards with you all particularly will stay with me for the rest of my life.

Finally, I'd be remiss not to mention my own personal cheering squad; my family. Mum, Nick, Hannah, Anaya, Granddad and Nan, you have been there for me every single step of the way with nothing but proud and encouraging words and support (I'm not sure there is a single person Granddad knows who doesn't know every detail of my research!). I love you guys and couldn't have completed this journey without you. You're the best!

Abstract

Terahertz (THz) quantum cascade lasers (QCL) have stimulated significant interest in THz laser imaging systems due to their compact size, broad spectral coverage ($\sim 1.2 - 5.2$ THz) and high output power (>1 W).

Due to their continuous wave (CW) narrowband emission and quantum noise limited linewidths, THz QCLs are particularly suited to coherent detection, but the majority of previously reported imaging systems have employed incoherent detection. Furthermore THz detectors typically fall into one of two categories (thermal or electrical), both of which have downsides (slow response rate or limited frequency range respectively).

Self-mixing (SM) can be seen as a solution to these problems while also gaining the advantages of a reduced experimental set-up and cost, and increased sensitivity. SM occurs when radiation emitted from a laser is re-injected into the laser cavity by reflection from a remote target. The re-injected field interferes with the intracavity field, resulting in perturbations to both the measured output power and laser terminal voltage that depend on both the amplitude and phase of the reflected field.

In this work, new SM imaging and modulation techniques were developed for both two- (2D) and three-dimensional (3D) imaging systems, including improvements leading to improved acquisition speed and depth resolution.

Other techniques were developed to identify parameters of the QCL spectral emission and tunability, and SM was also exploited for extraction of optical parameters of explosive materials; a precursor to identification of such materials, something that is very important to national security and public safety.

Further work was also developed in the areas of phase-nulling for the purpose of vibromacy measurements and extraction of laser parameters, and near-field (NF) spectroscopy, which has led to a massively improved lateral imaging resolution ($\sim 1\,\mu$m).

List of publications

Journal papers

The following journal and conference papers were published by the author during the course of the presented work.

- P. Dean, A. Valavanis, J. T. Keeley, K. Bertling, Y. L. Lim, R. H. S. Alhathlool, S. Chowdhury, T. Taimre, L. H. Li, D. Indjin, S. J. Wilson, A. D. Rakić, E. H. Linfield, and A. Giles Davies, "Coherent three-dimensional terahertz imaging through self-mixing in a quantum cascade laser," *Appl. Phys. Lett.*, vol. 103, no. 18, p. 181112, 2013
- P. Dean, A. Valavanis, J. T. Keeley, K. Bertling, Y. L. Lim, R. H. S. Alhathlool, A. D. Burnett, L. H. Li, S. P. Khanna, D. Indjin, T. Taimre, A. D. Rakić, E. H. Linfield, and A. G. Davies, "Terahertz imaging using quantum cascade lasers-a review of systems and applications," *J. Phys. D. Appl. Phys.*, vol. 47, p. 374008, sep 2014
- J. T. Keeley, P. Dean, A. Valavanis, K. Bertling, Y. L. Lim, R. H. S. Alhathlool, T. Taimre, L. H. Li, D. Indjin, A. D. Rakić, E. H. Linfield, and A. G. Davies, "Three dimensional terahertz imaging using swept-frequency feedback interferometry with a quantum cascade laser," *Opt. Lett.*, vol. 40, p. 994, mar 2015
- P. Dean, J. T. Keeley, A. Valavanis, K. Bertling, Y. L. Lim, T. Taimre, R. H. S. Alhathlool, L. H. Li, D. Indjin, A. D. Rakić, E. H. Linfield, and A. G. Davies, "Active phase-nulling of the self-mixing phase in a terahertz frequency quantum cascade laser," *Opt. Lett.*, vol. 40, p. 950, mar 2015
- P. Dean, O. Mitrofanov, J. T. Keeley, I. Kundu, L. H. Li, E. H. Linfield, and A. Giles Davies, "Apertureless near-field terahertz imaging using the self-mixing effect in a quantum cascade laser," *Appl. Phys. Lett.*, vol. 108, p. 091113, feb 2016
- S. Han, K. Bertling, P. Dean, J. T. Keeley, A. D. Burnett, Y. L. Lim, S. P. Khanna, A. Valavanis, E. H. Linfield, A. G. Davies, D. Indjin, T. Taimre, and A. D. Rakić, "Laser

Feedback Interferometry as a Tool for Analysis of Granular Materials at Terahertz Frequencies: Towards Imaging and Identification of Plastic Explosives," *Sensors*, vol. 16, p. 352, mar 2016

Conference papers

- J. T. Keeley, P. Dean, R. H. S. Alhathlool, A. Valavanis, Y. L. Lim, R. Kliese, M. Nikolić, L. H. Li, D. Indjin, A. D. Rakić, E. H. Linfield, and A. G. Davies, "Terahertz interferometry and imaging using self-mixing in a quantum cascade laser," in *UK Semicond. Inst. phys.*, 2013
- P. Dean, T. Taimre, K. Bertling, Y. L. Lim, J. T. Keeley, A. Valavanis, R. H. S. Alhathlool, S. P. Khanna, M. Lachab, D. Indjin, E. H. Linfield, A. G. Davies, and A. D. Rakić, "Coherent imaging and sensing using the self-mixing effect in THz quantum cascade lasers," in *12th Int. Conf. Intersubband Transitions Quantum Wells*, 2013
- A. D. Rakić, T. Taimre, K. Bertling, Y. L. Lim, P. Dean, J. T. Keeley, A. Valavanis, R. H. S. Alhathlool, S. P. Khanna, M. Lachab, D. Indjin, Z. Ikonić, P. Harrison, E. H. Linfield, and A. G. Davies, "Self-mixing effect in THz quantum cascade lasers: Applications in sensing and imaging," in *2013 IEEE 4th Int. Conf. Photonics*, pp. 18–20, IEEE, oct 2013
- A. Valavanis, P. Dean, L. H. Li, A. D. Burnett, J. T. Keeley, S. Chowdhury, R. H. S. Alhathlool, L. Chen, J. Zhu, Y. Han, J. R. Freeman, S. P. Khanna, D. Indjin, A. G. Davies, E. H. Linfield, and T. Taimre, "High-power (> 1 Watt) terahertz frequency quantum cascade lasers for stand-off imaging," in *Sensors Electron. Panel Spec. Meet. NATO*, 2014
- P. Dean, T. Taimre, H. S. Lui, K. Bertling, Y. L. Lim, A. Valavanis, J. T. Keeley, R. H. S. Alhathlool, S. Chowdhury, L. H. Li, S. P. Khanna, M. Lachab, D. Indjin, A. D. Rakić, E. H. Linfield, and A. G. Davies, "Coherent THz imaging using the self-mixing effect in quantum cascade lasers," in *Opt. Sensors*, (Barcelona), 2014

- J. T. Keeley, P. Dean, K. Bertling, A. Valavanis, T. Taimre, Y. L. Lim, R. H. S. Alhathlool, S. Chowdhury, L. H. Li, D. Indjin, E. H. Linfield, and A. G. Davies, "Electrical Modulation Schemes for Imaging by Self-Mixing in Terahertz Quantum Cascade Lasers," in *Int. Quantum Cascade Laser Sch. Work.*, 2014
- P. Dean, J. T. Keeley, K. Bertling, A. Valavanis, T. Taimre, Y. L. Lim, R. H. S. Alhathlool, S. Chowdhury, L. H. Li, D. Indjin, A. D. Rakić, E. H. Linfield, and A. G. Davies, "Electrical feedback control of a THz QCL under optical feedback," in *Int. Quantum Cascade Laser Sch. Work.*, 2014
- J. T. Keeley, P. Dean, A. Valavanis, K. Bertling, Y. L. Lim, R. H. S. Alhathlool, T. Taimre, D. Indjin, A. D. Rakić, E. H. Linfield, and A. G. Davies, "Three-dimensional terahertz imaging using swept frequency feedback interferometry with a quantum cascade laser," in *UK Semicond. Inst. phys.*, 2015
- P. Dean, J. T. Keeley, A. Valavanis, K. Bertling, Y. L. Lim, T. Taimre, R. H. S. Alhathlool, L. H. Li, D. Indjin, A. D. Rakić, E. H. Linfield, and A. G. Davies, "Active phase-nulling of the self-mixing phase in a terahertz frequency quantum cascade laser," in *13th Int. Conf. Intersubband Transitions Quantum Wells*, 2015

Contents

List of Figures

List of abbreviations

2D – Two-dimensional

3D – Three-dimensional

AC – Alternating current

AlGaAs – Aluminium-Gallium-Arsenide

ANSOM – Apertureless near-field scanning optical microscopy

BTC – Bound-to-continuum

CRI – Complex refractive index

CSL – Chirped superlattice

CW – Continuous wave

DAQ – Data acquisition (board)

DFB – Distributed feedback

DC – Direct current

DR – Dynamic range

DRI – Diffuse reflectance imaging

ERF – Edge response function

FFT – Fast Fourier transform

FOM – Figure of merit

FTIR – Fourier transform infrared (spectroscopy)

FWHM – Full-width half-maximum

GaAs – Gallium-Arsenide

ISAR – Inverse-synthetic aperture radar

IV – Current-voltage

LI – Lasing power-current

LIA – Lock-in amplifier

LO – Longitudinal-optical (phonon)

LPF – Low pass filter

MBE – Molecular beam epitaxy

Mid-IR – Mid-infrared

NDR – Negative differential resistance

NF – Near-field (spectroscopy)

NPSD – Noise power spectral density

OF – Optical feedback

PID – Proportional-integral-derivative

QCL – Quantum cascade laser

RMS – Root mean square

RP – Resonant phonon

SD – Standard deviation

SISP – Semi-insulating surface plasmon

SM – Self-mixing

SNR – Signal-to-noise ratio

TC – Time constant

TDS – Time domain spectroscopy

THz – Terahertz

TPI – Terahertz pulsed imaging

1 Introduction

The terahertz (THz) frequency range of the electromagnetic spectrum[2,3] (roughly defined as the frequencies between 300 GHz to 10 THz) sits in the region between areas covered by electronic techniques (radio and microwave) and photonic techniques (infrared and visible). Due to sitting at this crossing point, it has been a region rarely utilised with few high power sources available. It remains today one of the least developed regions of the electromagnetic spectrum, mostly due to the lack of compact, efficient sources, but recent interest in the range has led to a rise in development of the region.

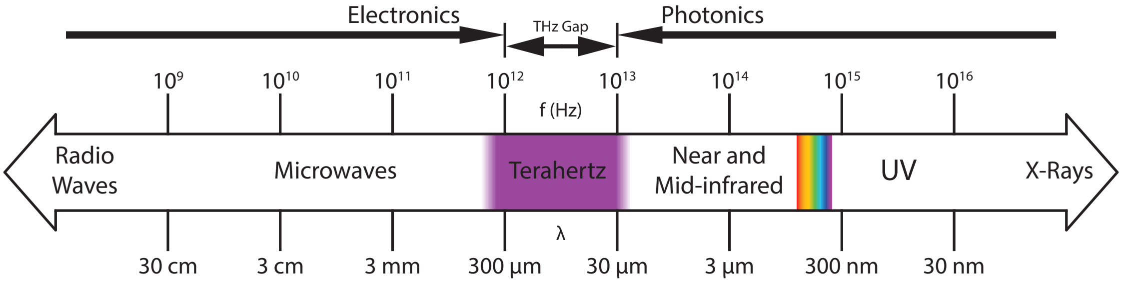

Figure 1.1: The electromagnetic spectrum. Adapted from Williams.[4]

1.1 Terahertz radiation

These frequencies are of great interest to both the scientific and industrial communities due to unique properties of the THz region and the abundance of proposed applications including imaging,[5] astronomy[6] and spectroscopy[7]. The ability to penetrate clothing and packaging materials make it ideal for security purposes[8] such as airport and postal scanning where it can be used to detect concealed weapons.[9] The non-ionising,[10] non-destructive properties of THz radiation make it an attractive alternative to X-rays in regard to airport imaging in particular, as a way of reducing exposure to damaging radiation. Another area of application of THz where this is a highly inviting feature is medical imaging[11] where THz imaging systems have been demonstrated for such uses as the detection of cancerous tissue[8,12] and imaging of an extracted human tooth.[13] Due to many chemical species presenting strong rotational and vibrational absorption lines in the

THz range, spectroscopy and astronomical applications have also been areas of significant interest. Such applications have included identification of drugs[14] and explosive materials[15] for pharmaceutical and security requirements, and probing the spectra of thermal emissions from stellar dust clouds for the purposes of searching for extrasolar planets.[16]

Even with research into THz applications spanning over 60 years, industrial impact has been minimal, mainly due to the lack of high-power sources, the generally complicated nature of THz systems and the requirement of cryogenic cooling. The lack of such sources has been described as the "Terahertz Gap".[3] As such, there has been an increased need for high-power compact THz systems that can operate at room temperature. Generation of coherent terahertz radiation has traditionally involved either extending electronic techniques to higher frequencies or extending photonic techniques to longer wavelengths. Electric devices, such as Gunn oscillators and Schottky diode multipliers, have trouble operating beyond 100 GHz due to capacitance and transit-time limitations causing high frequency roll-off.[17,18] Photonic traditional semiconductor lasers, however, are restricted to high frequency emission by the material bandgap that dictates the emission frequency. Further to this, the small energy level separations (1-10 THz → 4-40 meV) are similar in energy to phonon resonances, which tend to depopulate excited states making population inversion difficult.

Early methods of producing THz radiation involved producing broadband THz through the use of photoconductive antennas.[19] Electron-hole pairs are excited through subpicosecond laser pulses, producing transient currents that result in broadband radiation emission in the THz range. An optical approach to a similar end of broadband THz emission involved using optical rectifiers but results in low output powers.[20] Other applications such as spectroscopy require high-powered, tunable narrowband sources.[21] Schottky diode multipliers are an electronic source of this through frequency upconversion from the microwave region.[6] Hydrogen-cyanide and methanol lasers are high-powered coherent narrowband photonic sources, but are very large and require kilowatt power supplies[21] making them of limited application.

In 2002 however, a compact, solid-state THz source was demonstrated in the THz quantum cascade laser (QCL).[22,23] Since these early developments continuous-wave (CW) output powers from THz QCLs have pushed beyond 100 mW,[24] with peak powers of 1 Watt[25] and operational temperatures reaching ∼200 K[26], although sadly not from the same device. THz QCLs have also been developed spanning 1.2-5 THz range (without the use of magnetic fields).

1.2 Laser design and Quantum cascade lasers

In general, lasers work when electrons transition between different energy levels, emitting photons as a loss of energy. This transition of energy can occur in two directions; if an electron is populating the upper lasing state when it is stimulated by a photon with energy $h\nu$ (where h is the Planck constant) equal to the energy difference of the lasing states $E_{21} = E_2 - E_1$, the electron transitions to the lower state, E_1, emitting a photon of the same wavelength and phase as the stimulating photon. This is demonstrated by Fig. 1.2(a). On the other hand, if the electron populates the lower state, when it is stimulated by an approaching photon, it absorbs the photon and raises its own energy to join the upper energy state; shown in Fig. 1.2(b). In order to emit light, a population inversion must exist where more electrons populate the upper lasing level than the lower level. Various designs of lasers have been proposed during the history of laser photonics and this property has been exploited in various ways.

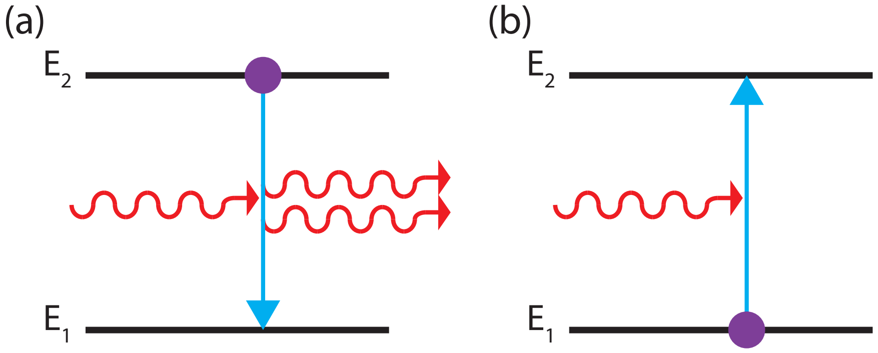

Figure 1.2: Electron transitions in a semiconductor device for photon (a) emission and (b) absorption.

For generic interband lasers, the conduction and valence bands of the semiconductor material that the laser consists of dictate the upper and lower lasing states, E_{C} and E_{V} respectively. In these devices, shown in Fig. 1.3(a), the energy of the emitted photons is equal to the bandgap of the material. This design requires different laser materials in order to produce lasers that emit different wavelengths. A different laser design involves quantum wells in order to produce multiple energy levels (known as subbands[27]) within both the conduction and valence bands (Fig. 1.3(b)). This allows the emission energy to be tailored to energies other than the bandgap where the width of the quantum wells controls the energy levels,[28] but one limitation is that because the created energy levels are within the conduction and valence bands, the emission energy is always greater than the bandgap energy. All known semiconductor bandgap energies equate to higher frequency emission than the THz region. In order to create optical transitions at THz energies, these subbands can be exploited in what is known as an intersubband device. In contrast to the previous device where electrons transition between subbands across the bandgap, in an intersubband device different states within the conduction band are employed (Fig. 1.3(c)). This results in an optical transition smaller than the bandgap of the device, allowing THz frequencies to be reached.

A QCL is formed through engineering of quantum wells to form a *superlattice*, where energy states from multiple quantum wells are designed to overlap to form *minibands* to allow fast scattering of electrons through the device. As shown in Fig. 1.4(a), these minibands can be utilised to form *injector* and *extractor* stages of the QCL in order to conduct electrons quickly between transitional energy levels. The injector stage allows electrons to efficiently tunnel into the upper lasing state when an electric field is applied to the device. The electron then transitions between two energy levels with a separation energy that equates to THz frequency, $E = h\nu$, emitting a THz photon. Through coupling of the lower energy state to the extractor miniband the electron quickly tunnels out of the transitional well. Careful engineering of the device allows this extraction miniband to form the injector miniband of the following quantum well system, permitting a single electron to cascade through multiple quantum well systems emitting multiple photons which results

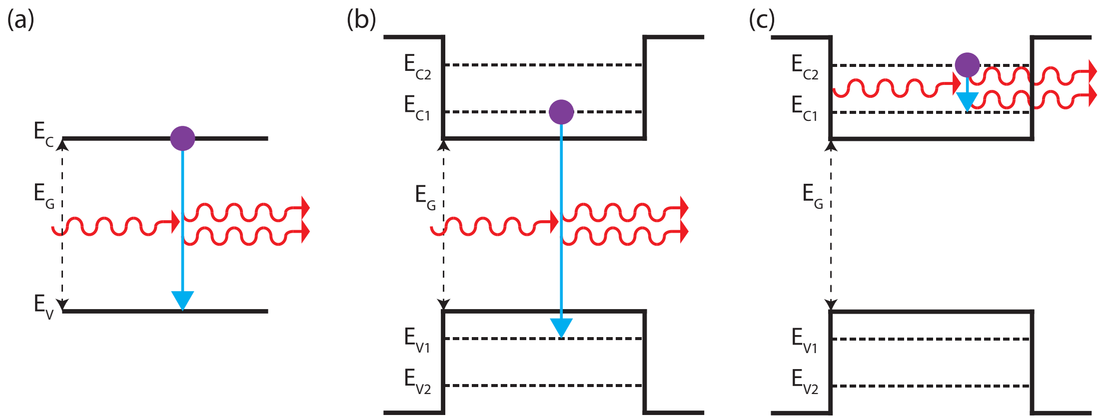

Figure 1.3: Schematic diagram of laser designs. (a) In an interband laser emission optical transitions occur between the conduction and the valence band edge, energies E_{C} and E_{V} respectively, and the emission energy is approximately equal to the bandgap, E_{G}. (b) In a quantum well laser, conduction and valence subbands control the optical transition and therefore emission energy, where this is larger than E_{G}. (c) Intersubband lasers contain optical transitions between subbands within the conduction band. Emission energies below E_{G} are possible.

in high emission power. A schematic depicting this cascade is shown in Fig. 1.4(b).

The first mid-infrared quantum cascade laser was developed in 1994 using a GaInAs/AlInAs heterostructure on an InP substrate.[23] LO- (longitudinal optical) phonon (latice vibrations) scattering was used as method of moving electrons from each lower lasing level. CW emission was demonstrated within a year by the same group at Bell Labs[30] and soon after, room temperature operation was achieved.[31] Due to the added complexities of the small relaxation energy required for THz emission, it took nearly 10 years following the development of the first QCL until a THz QCL was realised in 2002 emitting a few milliwatts of power at 4.4 THz.[22] This device employed a GaAs/AlGaAs *chirped superlattice* (CSL) design that utilised its miniband to form a population inversion by rapidly transferring electrons away from the lower lasing state (Fig. 1.5(a)). Other QCL design schemes have since been developed including *bound-to-continuum* (BTC) and *resonant phonon* (RP), shown in Fig. 1.5(b) and (c) respectively. The BTC design improves upon the initial CSL design by incorporating a diagonal-optical-transition in order to reduce non-radiative scattering of electrons from the upper lasing level. This resulted in better

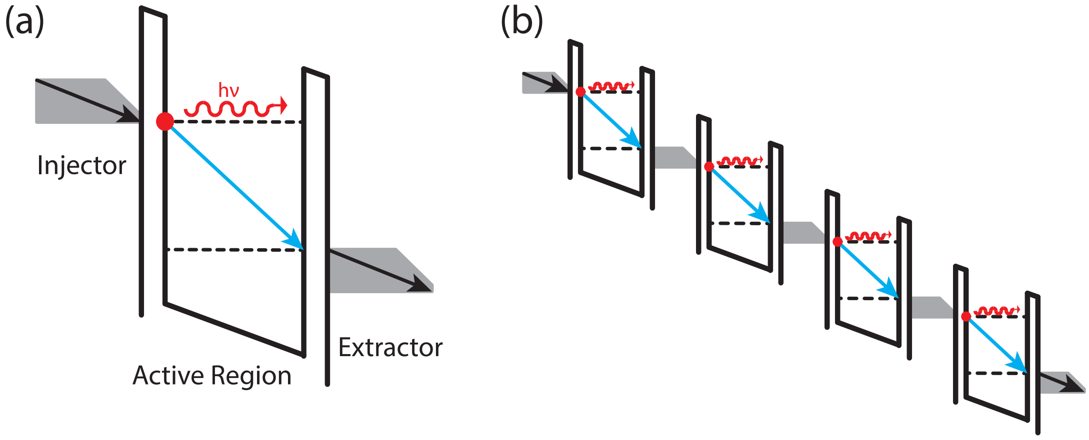

Figure 1.4: Schematic diagram of a quantum cascade laser. (a) All energy levels lie within the conduction band. Electrons enter from the injector, tunnel through the well barrier and optically transition to a lower energy stage. From here an extractor is used to quickly remove electrons. (b) Multiple well structures are fabricated together to create a cascade where a single electron causes emission of multiple photons. Adapted from Paiella.[29]

thermal performance when compared to the CSL design. A miniband of states is still used as the method of extracting electrons from the lower lasing state in the BTC design. The RP design[32] on the other hand utilises an LO-phonon similar to the first QCL, as a fast method of transporting electrons between consecutive active regions. Due to the high energies (36 meV in GaAs) required for the use of the LO-phonon as a method of depopulation, thermal backfilling is greatly reduced improving thermal performance.[33] However, this also increases the electric field required for alignment of wave functions in the device. A further advantage of the lack of a miniband is that an RP device requires less quantum wells for each active module, reducing molecular beam epitaxy (MBE) growth complexity. A third design[34] that melds the two transport methods of a miniband and LO-phonon scattering has shown promise more recently. This hybrid, or *interlaced*, design combines the diagonal transition of the BTC with a phonon-depopulation scheme of the RP design in order to gain benefits from both of the previous designs. The THz QCL with the highest reported power output (> 1 W) was constructed using a hybrid design.[25]

In order to direct the THz radiation in the growth direction a waveguide is required.

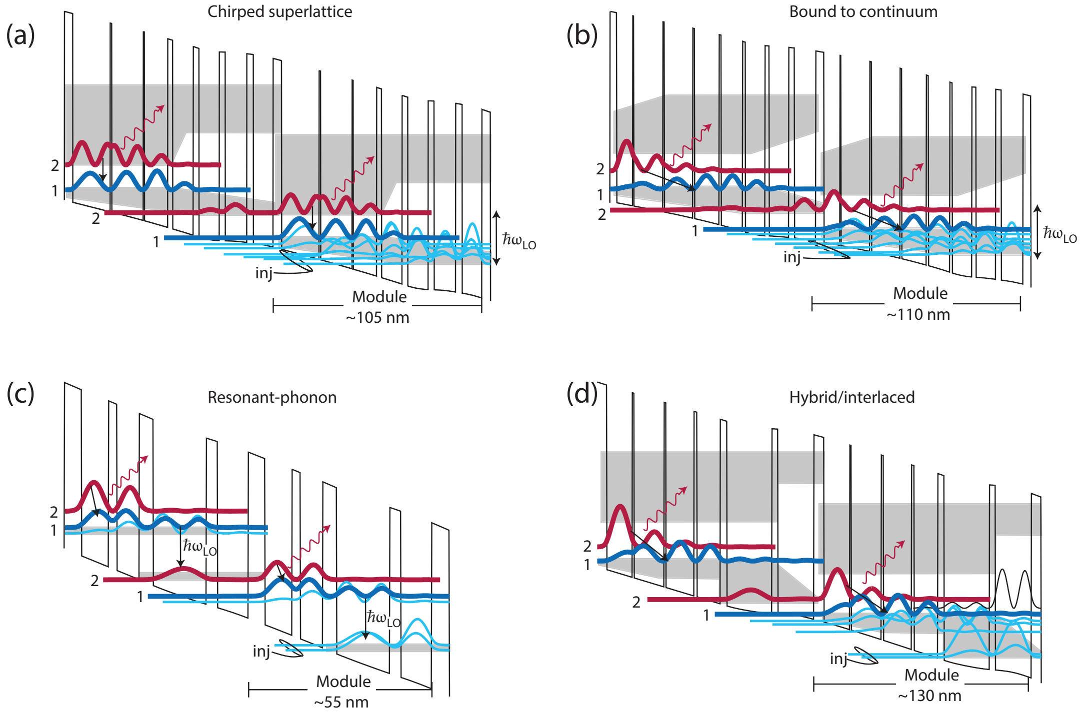

Figure 1.5: THz QCL design schemes. Major designs include (a) chirped superlattice, (b) bound-to-continuum, (c) resonant phonon and (d) hybrid/interlaced designs. Two identical modules of each are shown here, although typically $100 - 200$ cascaded modules are grown. The upper- and lower-radiative states are shown in red and blue respectively and the grey shaded regions correspond to minibands of states. Adapted from Williams[35]

Early THz QCL devices[22] used a semi-insulating surface plasmon (SISP) waveguide that utilised a single, upper metal contact in order to confine the generated THz radiation to the active region. Due to the lack of a material with a high confinement on the bottom of the active region however, ∼50% of the optical mode *leaks* into the substrate, as shown in Fig. 1.6(a). This design is also known as a single-metal design in other literature.[35] In order to improve thermal performance of THz QCLs a variation of the SISP design was developed where a metal contact layer was utilised below the active region, as well as above.[36] This *double-metal* design provided nearly perfect mode confinement. The current record for high-temperature operation of a THz QCL was obtained using a double-metal design.[26]

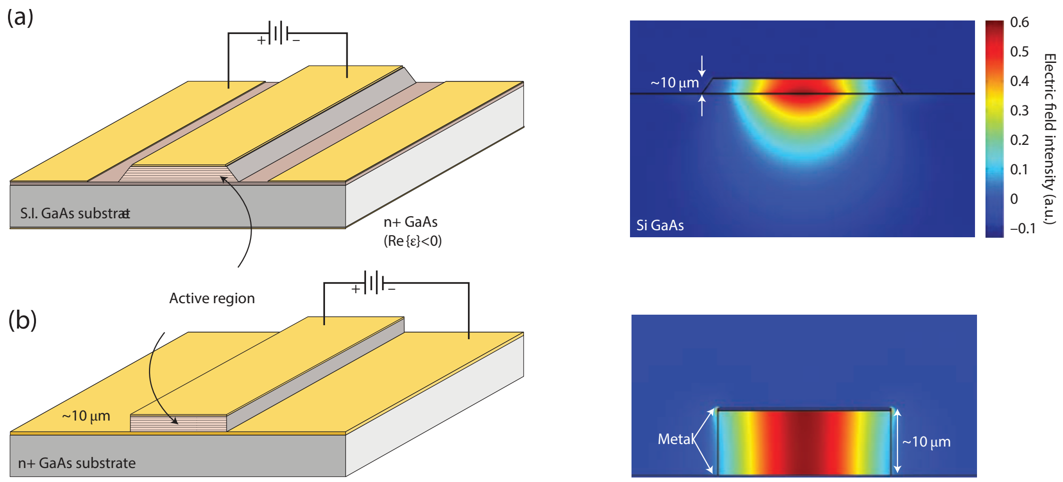

Figure 1.6: Terahertz QCL waveguides. Schematic diagram (left) and typical two-dimensional mode intensity pattern (right) for (a) semi-insulating surface plasmon and (b) metal-metal waveguides. Adapted from Williams[35]

QCL emission frequencies are characterised by Fabry-Pérot modes where multiple frequency emission is possible. Many applications of THz QCLs, such as the three-dimensional imaging techniques described in Chapters 4 and 5.2, require devices that emit at only a single frequency in order to simplify (or even make possible) analysis and understanding of obtained data. More complicated waveguide designs including distributed feedback (DFB) gratings[37] can be utilised in order to limit the availability of lasing to single-mode emission.

With the development of the THz QCL a solid-state, compact, high-power THz source was finally realised. These attributes marked its position as one of the most promising THz sources to date and it was quickly employed for many applications. One of the most fruitful applications areas for QCLs has been THz imaging.

1.3 Terahertz imaging

THz imaging has shown immense growth in the last few years as one of the most promising applications of THz radiation. THz imaging technologies have been developed for such purposes as biomedical imaging, pharmaceutical inspection, non-destructive analysis and spectroscopic identification of materials for security purposes.[8,38,39]

THz imaging as an application was proposed over 30 years ago[40] with early demonstrations appearing a few years later.[41,42] THz radiation promotes a unique array of properties that make it particularly attractive. THz, for one, is able to penetrate many dry, non-metallic materials that are opaque at visible and infrared frequencies, including plastics, paper, ceramics and wood. Transmission has also been shown through fabric, but only at low THz frequencies (<1 THz).[43] The diffraction-limited imaging resolution for THz imaging also has the advantage of being sub-millimetre, making it ideal for non-destructive inspection, quality control (for example to characterise quality of coating of pharmaceutical tablets) and for security scanning purposes.[39,44–46] Another property of THz radiation that has prompted imaging work is the ability to excite vibrational modes of materials that suffer no excitation from other frequency regimes. This property allows samples to be identified through their chemical compositions.[7,46–50] THz is also highly absorbed by water, and as such has shown promise in biomedical imaging as a use of distinguishing between different tissue types, and even for identifying cancerous tissues due to their higher than normal water content.[51,52]

Many THz imaging systems have previously employed THz time domain spectroscopy (TDS)[7], allowing spatial mapping of both the THz field amplitude and phase across the sample using high bandwidths (up to 100 THz)[53] but typically at low powers($\sim \mu$W) and low resolutions (>∼5 GHz). They also generally require bulky, expensive ultrafast laser sources for generation of the THz field and utilise mechanical scanning of their optical delay at each pixel, causing long imaging acquisition times. A number of narrowband CW sources have also been developed, including CW photomixers[54,55] and multiplied Gunn emitters,[56] but these typically also suffer from low power or are limited to sub-THz frequency emission.

THz QCLs, on the other hand, don't suffer from any of these downsides. THz QCL imaging systems are generally experimentally compact and require no ultrafast laser sources thereby also reducing cost,[57,58] have high acquisition rates and emit high THz powers. Systems have also been developed offering the potential for tunability,[59] and QCLs have a high spectral purity that is required for coherent, narrowband imaging.[60,61] QCL imaging can be broken down into two distinct groups; incoherent, where imaging systems are based purely on the measured THz power, and coherent imaging, where phase information of the THz beam is also recovered.

1.3.1 Incoherent imaging

In contrast to THz pulsed imaging (TPI) systems like TDS imaging set-ups, the majority of early THz QCL imaging systems discarded the advantages that coherent detection brought for the sake of experimental simplicity, using incoherent thermal detection. These sensors, such as cryogenically cooled bolometers[12,62,63] or pyroelectric sensors,[64] afforded high sensitivity and high dynamic range (up to 64 dB[62] has been demonstrated) allowing sensing of highly attenuating biological samples, for example.[12,63] THz QCL imaging systems have also demonstrated high spatial resolution when compared to TPI and lower-frequency based systems due to a reduction of the diffraction-limited beam resolution, through the use of higher operating frequencies of THz QCLs. Imaging resolutions of less than 250 µm[12,65–67] are common in THz QCL imaging, but this is still far above the wavelength dependant limit (∼64 µm at 3 THz[68] for example), mainly due to the irregular beam shape attributed to THz QCLs. The small aperture of the device waveguide (∼10 µm thick) causes high diffraction of the emitted beam, especially with double-metal waveguides due to their high confinement. SISP waveguides provide more ideal beam profiles, but even these suffer from an interference pattern due to duel-emission from the substrate and the waveguide itself.[57,58] Other approaches have been used to more efficiently couple the QCL emission to the end of a better beam profile, including hollow dielectric waveguides[69,70] or spatial filtering of the THz field with an aperture that is larger than the emission wavelength,[66] permitting transverse imaging resolutions of better than 70 µm, and axial resolution of ∼400 µm.

Most THz QCL imaging systems build images through raster-scanning the sample through the focused beam and recording on a pixel-by-pixel basis, but this can be not only slow (on the order of several minutes to hours for larger or high-resolution images) but also not applicable to real-world application. Image acquisition rate is generally dictated by pixel size, integration time per pixel (for averaging purposes) and speed of the detector. Thermal detectors are particularly poor in the final case, with response times on the order of ∼1-100 ms. This can translate to an imaging rate of longer than several seconds per pixel. A newer system[71] has demonstrated fast acquisition by deflecting a collimated THz beam onto a high density polyethylene (HDPE) mirror using a flat scanning mirror, the angle of which could be controlled to a resolution of 2 µrad, which translated to a transverse displacement across the sample surface controllable within 1 µm. After transmission through the sample, the beam was focused onto the detector and the fast scanning method resulted in an imaging time of 1.1 s for a 2D image of 4550 pixels (∼4140 pixels-per-second (pps)) over an area of 36 mm × 40 mm. This technique was utilised to produce high-speed three-dimensional (3D) imaging by computer tomography by rotating the sample on a rotational stage and taking successive 2D images; resulting in a 3D imaging rate of 3100 pps (60 different angles at 4550 pixels-per-image). Traditional computer tomography systems using raster-scanning report imaging rates of ∼6 pps at much lower resolutions (18 angles at 289 pixels-per-image).[72,73]

QCLs also open up the potential possibility of real-time (∼25 frames per second (fps)) THz imaging. One of the requirements of such a system would be the ability to illuminate a 2D sensor array with sufficient power density to achieve a reasonable noise figure, which the high power of the QCL would be more applicable to than other THz sources. Real-time THz imaging has previously been shown using a vanadium oxide microbolometer focal plane arrays[74–76] at 20 fps (limited by sampling techniques).

Stand-off imaging at long distances has also been demonstrated using THz QCLs, even though THz has many spectral absorption features in the atmosphere through water-vapour absorption. By carefully selecting frequencies away from these features, real-time incoherent THz QCL imaging with optical path lengths of $>25\,\mathrm{m}$[74] have been demonstrated at $\sim$4.9 THz. Using this system a real-time frame rate of 20 fps was achieved with an SNR of $\sim$2.5. It's worth noting that while this system is a huge achievement in the development of long-range THz imaging, it does not constitute true stand-off imaging as the microbolometer sensing array was at most 3.25 m away from the sample.

THz QCL imaging systems achieve high spectral power densities at high THz frequencies (>3 THz) that are ideal for spectral mapping of materials where traditional TPI systems struggle due to power roll-off at high frequencies. Their tunability, either through bias or temperature control, is very limited however which limits their spectroscopic application. In recent years a number of tuning schemes have been reported that look to improve this. These systems include external cavity[77,78], and coupled microcavity[79]devices, coupled-cavity devices based on vernier tuning[80], electrically switchable QCLs formed by bi-directional active regions[81] and stacks of electrically switchable lasing units in the same device.[82] Another approach[83] was achieved by tuning the growth parameters during the growth of one device leading to a "heterogeneous cascade" active region in which the GaAs well width was reduced by $\sim$10% through the structure. By applying varying electric fields to such a device, different energy levels align resulting in different areas of the active region emitting different wavelengths based on their well width. Such a design has been employed for multiple-frequency imaging[62] with 5 distinct emission frequencies ranging from 3.06 to 3.35 THz. This work demonstrated tunable QCLs as a real potential alternative for spectral identification of samples.

One final major THz imaging technique is diffuse imaging. Samples that are highly absorbing, either due to their thickness or a high attenuation coefficient at THz frequencies, cannot be used in generic transmission imaging systems as radiation will not pass entirely though the sample in large enough quantities to be detected. For these samples, a slightly more complicated system is required where diffuse or specularly reflected radiation is collected off the surface of the sample. Diffuse reflectance imaging (DRI) systems are more applicable to real-world stand-off imaging systems where the alignment required for specular imaging cannot be guaranteed. DRI is also more suited to imaging of powdered samples where subsurface scattering makes transmission measurements difficult and where the complex refractive index of the sample effects the diffuse scatter of radiation, allowing another method of material identification. Such a system[64] was utilised for the spatial mapping of powdered materials using exemplar powdered admixtures of polymethyl methacrylate (PMMA) and polystyrene due to the contrasting absorptions at THz frequencies (PMMA is highly absorbing, polystyrene is weakly absorbing). Equally spaced ratio mixtures ranging from 0:1 to 1:0 were placed in a polystyrene sample holder consisting of 10 mm-deep compartments and a polystyrene lid was fitted, as shown in Fig. 1.7(a). Figure 1.7(b) shows the specular reflectance image which consists of reflections off the lid of the sample holder, with no absorption measured from the powders. Figure 1.7(c), on the other hand, shows the image acquired through DRI where the variation in absorption of the various samples can be clearly identified due to the reduction in the specular component of reflection. The variation in measured signals from the various samples can be attributed to their relative absorption at 2.8 THz only, as the PMMA and polystyrene samples have similar particle sizes (∼5-6 μm) and refractive indicies (∼1.38-1.42), so similar scattering strengths would be expected. In order to quantify accurate values of sample reflectivity and remove variations due to inhomogeneity of samples, for example, averaging over the acquired pixels for a single sample can be utilised. To this end, DRI is more useful than sampling an individual position on the sample.

Throughout all of the mentioned incoherent imaging techniques, only the magnitude of the THz field is measured. As such, any phase information, which could be used for 3D measurement or measurement of the complex refractive index of a sample for example, is lost. In order to measure this component of the transmitted signal a coherent measurement

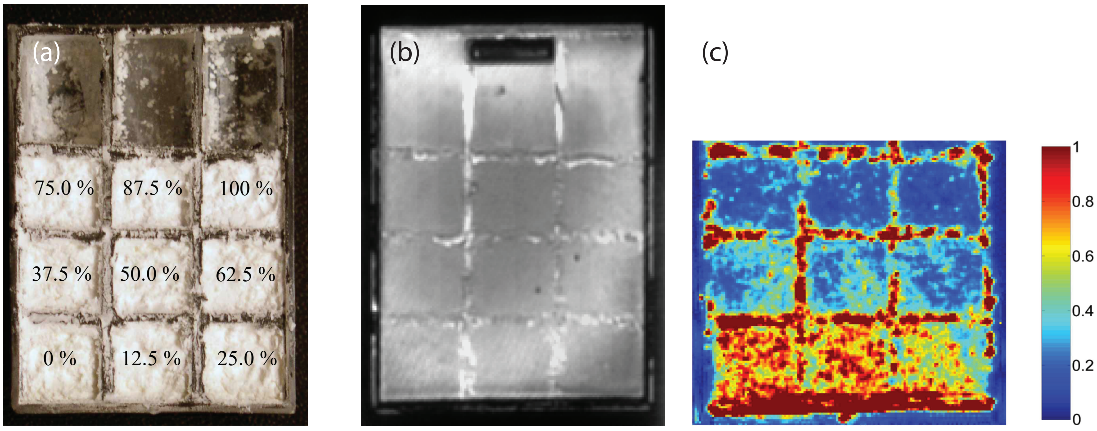

Figure 1.7: (a) Photograph, (b) specular and (c) diffuse reflection images of a polystyrene sample holder containing mixtures of PMMA and polystyrene powders. The % mass of PMMA is labelled on (a) for each powder and (b) and (c) were obtained at 2.8 THz using a pixel size of 250 µm. Adapted from Dean[64]

scheme is required.

1.3.2 Coherent imaging

One advantage that TPI has over most THz QCL imaging systems is that it is a coherent detection method, meaning that the system is sensitive to not only the magnitude of the THz field but also its relative phase as a function of frequency. One method of employing coherent detection of the THz field in a QCL imaging system is by mixing the THz field with a reference signal from a local oscillator to generate an intermediate frequency (IF) that can be measured using electronic detection. However, this requires a very stable THz frequency, and THz QCLs suffer from $\sim 1/f^2$ electrical and thermal noise components causing frequency broadening and drift on the order of up to several MHz over periods of seconds.[84–86] This drift facilitates the need for a feedback loop for real-time control of the emission frequency through the laser driver current and/or device temperature.[87,88]

A recent approach at coherent THz QCL inverse-synthetic aperture radar (ISAR) imaging[70] employed frequency stabilisation to a free-running CO_2 optically-pumped molecule laser operating at 2.41 THz. An IF frequency of 1.048 GHz was generated by mixing the two laser sources on a Schottky diode mixer (Ref. SD in Fig. 1.8(a)). Once the QCL emission frequency was stabilised, coherent detection was possible through the use of the molecule laser as a local oscillator for the reflected THz field, collected at a second Schottky mixer, Ref. SD in Fig. 1.8(a). A beam size of ∼2.5 inches at the sample allowed scanning in both azimuth and elevation angles, with both phase and amplitude data recorded at each orientation. Fourier transform analysis of this complex data allows the reproduction of a 2D azimuth-range image of the sample to be generated, as shown in Fig. 1.8(c) (Fig. 1.8(b) shows a photograph of the sample, an aluminium-coated plastic tank model). Using the scanning ranges listed, the resultant resolutions were 0.4 and 0.6 mm in azimuth and elevation respectively, and the scan time was 40 minutes with a per pixel dynamic range of ∼105 dB. Also, the resolution of the ISAR imaging system is dependant on the angular extent of the scan, meaning sub-mm resolution is possible for a fully illuminated target. As such, this system achieves high dynamic range, with the potential for high-resolution, stand-off imaging.

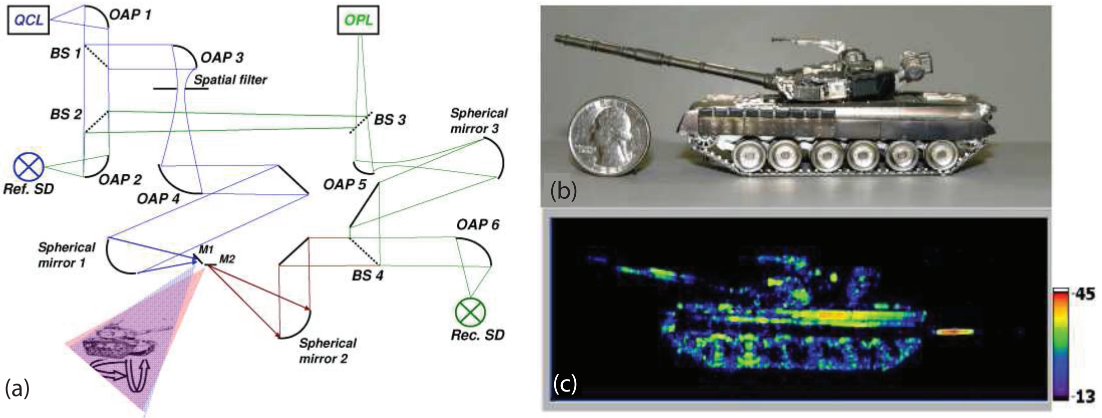

Figure 1.8: Coherent THz QCL ISAR imaging. (a) Schematic diagram of ISAR imaging system. (b) Photograph and (c) azimuth/elevation THz ISAR image of a aluminium-covered plastic tank model. Amplitude values in dB are indicated by the colour scale. Adapted from Danylov[70]

Another alternative approach to coherent QCL imaging employed stabilisation to a near-infrared fs-laser comb.[60] In this system, the QCL is stabilised using an electro-optic (EO) crystal to lock the QCL frequency to a high harmonic ($\sim 10^4$) of the fs-laser repetition frequency of ∼250 MHz. Through the use of a beam-splitter, a proportion of the fs-laser comb is also used for coherent sampling of the reflected THz field using a second EO detection system, as shown in the schematic diagram of this experiment in Fig. 1.9(a) as EO2. RF synthesisers, RF1 and RF2, supply mixing signals for the beat-notes generated by the EO crystals at 10 and 10.07 MHz respectively, down-converting the beat-frequency to allow measurement of the THz field at 70 kHz using a lock-in amplifier. The phase uncertainty of this system was reported as $\leq$3 deg/h, corresponding with a depth uncertainty of $<$1 μm in the profile height of samples such as the unwrapped depth profile of a 10 cent Euro coin displayed in Fig. 1.9(c). The corresponding power image for the same sample is shown in Fig. 1.9(b) demonstrating the schemes detection of sample reflectivity. Due to the conversion of the THz field to near-infrared frequencies used in this scheme, near-infrared detectors could be utilised for detection of the THz field, such as arrayed systems for full-field, real-time image capture.[89]

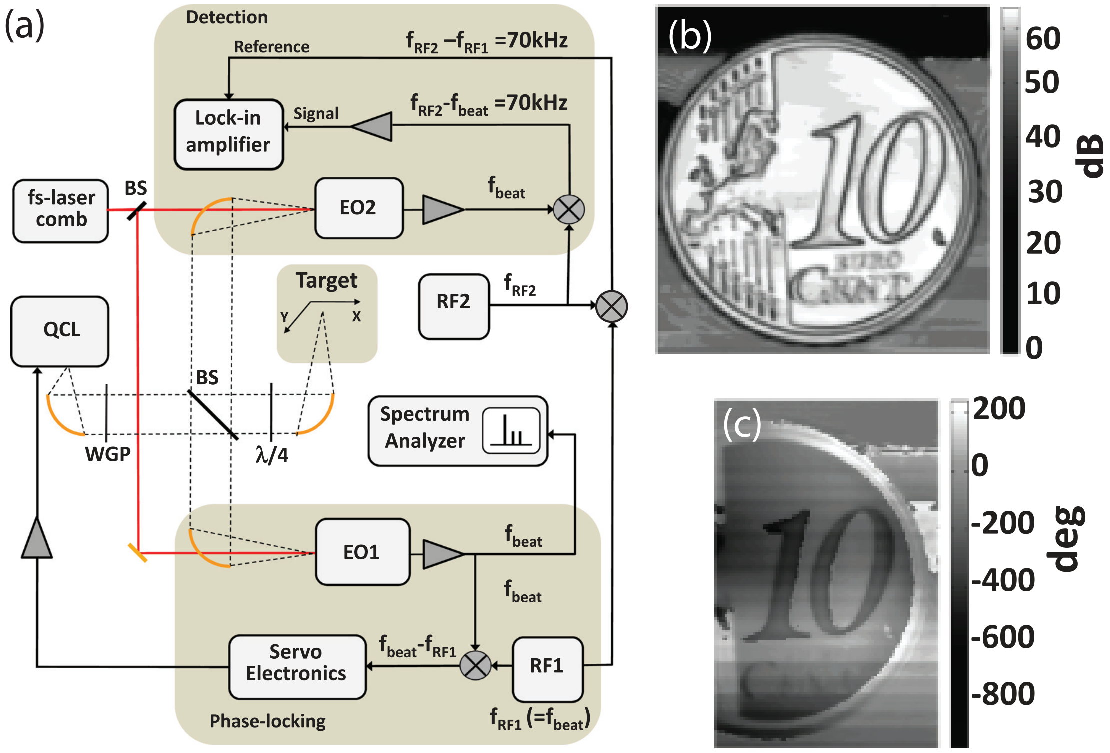

Figure 1.9: Coherent THz QCL imaging using electro-optic sampling. (a) Schematic diagram of EO imaging system. THz images of a 10 cent Euro coin demonstrating measurement of (b) THz power and (c) unwrapped phase values. Adapted from Ravaro[60]

While these systems gain the benefit of phase-detection over incoherent schemes, they require much more complicated experimental set-ups consisting of multiple laser and detector arrays for stabilisation and detection. More recently, another coherent THz QCL detection scheme has shown promise based on the self-mixing phenomenon that removes these limitations.

1.4 Self-Mixing

The self-mixing (SM) effect involves the feedback of the emitted laser radiation off an external reflector, back into the internal laser cavity through an emission facet of the device. The reflected radiation interferes with the inter-cavity field, causing perturbations to many of the lasing parameters such as the emission frequency, threshold gain, emitted power and terminal voltage. These parameters are sensitive to both the power and phase of the reflected field and this means that the laser cannot only be used as a source but also a coherent detector, which makes very compact optical imaging systems possible. One of the earliest uses of SM was the suppression of multiple emission modes of a Helium-Neon (He-Ne) laser[90,91] through the use of reflection off an external mirror in 1962. Further observations were made in 1963 that the output power of a He-Ne would vary when the external cavity length was changed. The external cavity periodicity of this variation was a half-wavelength of the emission frequency.[92] Early SM systems were measured by detecting such changes to the emission power of the device using a photodetector and emission from the rear laser facet.[93] Measurement of SM was later made more experimentally compact in 1972 by a discovery that changes could be measured on the voltage across the laser discharge tube[94] demonstrating that measurements of changes to the external cavity could be performed using only the laser and without the photodetector.

Even though these early experiments and findings were produced using large, bulky He-Ne lasers, similar experiments were performed with more compact semiconductor lasers that had recently been developed, in 1962.[95–98] These experiments found similar mode suppression effects that had been found in He-Ne lasers.[99,100] Work in 1968 demonstrated that the threshold carrier density of these semiconductor devices could be changed under feedback also, and that this work was dependant on the phase of the returning radiation.[101,102] Further studies in 1969 and 1970 also found a relationship between the laser behaviour and the amount of light coupled back into the device.[103,104]

Even with all of these observations no theoretical model for the operation of a laser under feedback had been proposed. In 1980 Lang and Kobayashi changed this when they published their equations describing how the relationship between changes to the carrier density due to feedback caused changes to the lasers refractive index, in turn altering its emission frequency.[105] This work allowed further understanding and modelling of self-mixing in a way that had not previously been possible. The nature of SM is covered in detail in Chapter 2. Soon after the development of the Lang/Kobayashi model, SM began to be exploited for sensing purposes, including measurement of laser parameters, and external objects such as for 3D imaging of exemplar samples.

Some of the earlier sensing demonstrations using optical feedback involved measuring the velocity of a diffuse target[106,107] using a CO_2 laser. This soon led to semiconductor velocity systems demonstrated in 1986,[108] and it was in this work that term "self-mixing" was first coined. Further experiments have been demonstrated showing the experimental use of self-mixing for a multitude of purposes in many fields including measuring velocity,[109–114] liquid flow rate,[110,115–120] displacement,[121–135] distance[122,136–138] and laser parameters such as the linewidth[139,140] and linewidth enhancement factor.[141–148]

More recently, SM has been exploited for imaging systems due to its sensitivity to both sample reflectivity and surface morphology as changes to the amplitude and phase of the reflected wave, respectively. Such imaging systems include surface profiling[149–151] and three-dimensional imaging.[137,152–157] In recent years, THz QCLs have been demonstrated as ideal candidates for feedback interferometry due to their compact size, large response bandwidths and stability under feedback.

1.4.1 THz QCL SM applications

One of the earlier THz QCL SM applications demonstrated was high-resolution imaging of exemplar samples[65]. The SM imaging system, shown in Fig. 1.10(a), was established with a 10 µm-thick BTC THz QCL emitting at ∼2.60 THz. By focusing the emitted radiation onto the sample, an external cavity was established between the target and the laser facet. By using a mechanical chopper to modulate the THz field, lock-in amplification was used to measure the small (∼mV) SM perturbation to the laser terminal voltage. As the sample was raster-scanned at the focus of the beam, the QCL terminal voltage is sampled at each pixel (250 µm for Fig. 1.10(b) and 100 µm for Fig. 1.10(c)) in order to acquire a 2D surface image. The SM amplitude is proportional to the sample surface reflectivity, but changes in the cavity length due to surface morphology and sample tilt also effect the terminal voltage through a phase perturbation to the returning field. This phase change shows as ringing on the surface of the scalpel blade in Fig. 1.10(b).

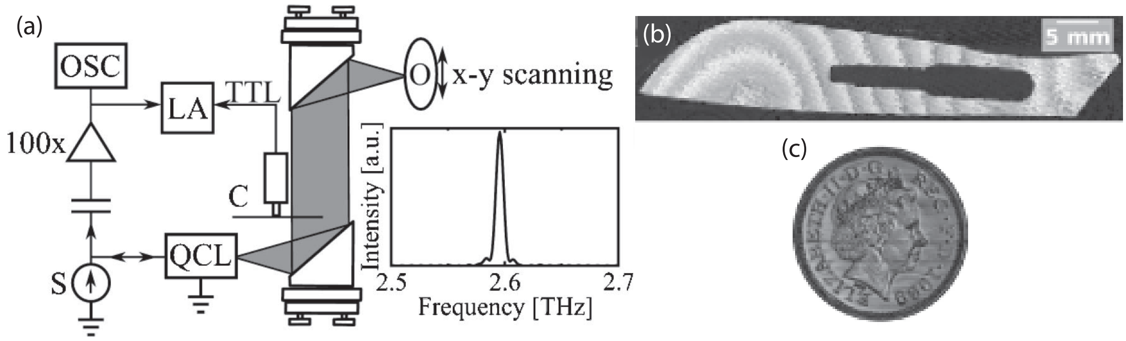

Figure 1.10: Schematic diagram of the experimental system used for THz imaging with a QCL. *S*, current source; *OSC*, oscilloscope; *LA*, lock-in amplifier; *C*, mechanical chopper. Inset: emission spectrum of the THz QCL, as measured using a Fourier-transform spectrometer. (b) Exemplar image of a scalpel blade obscured behind a high-density polyethylene FedEx envelope. (c) A high-resolution image of a British two-pence coin (diameter = 25.9 mm). Adapted from Dean[65]

By attenuating the cavity between the source and target, this system was shown to be highly sensitive, with measurement of the SM signal still possible with ∼48 dB of attenuation, corresponding to a detectable reflected power of 4 nW. Due to this, this technique was refined for long-range 2D SM imaging with a THz QCL.[158] By extending the collimated path of the THz beam to form a round-trip path length of 21 m, by folding the beam with planar mirrors, this experiment established the techniques applicability for long-range sensing. The sensitivity of the technique was also further tested by performing the experiment in an unpurged environment, where THz is known to be highly absorbed. For images acquired at 1 and 21 m, FOM (see Eq. (3.1)) values of $K = 61.5$ and $K = 43.5$ respectively were extracted, establishing that the technique could potentially even image at much longer distances. Based on the instantaneous free-running linewidth $\Delta f \sim 20 - 30\,\mathrm{kHz}$, the coherence length for a THz QCL (which dictates the maximum path length for coherent detection) can be estimated to be $L_\mathrm{c} = c/\Delta f \approx 10\,\mathrm{km}$ in a vacuum.[158]

Where-as in the above examples, the phase information measured from reflection off the sample relates to the sample depth, another exploitation is extraction of the complex permittivity of the sample; as used in THz time-domain reflection spectroscopy.[159] The phase-information measured previously isn't a true extraction of the phase difference between the emitted and returning waveform, rather the impact of this phase difference to the measured power. In order to extract a true phase component of the SM waveform, interferometric fringes are required, and can be generated through changing the external cavity length or chirping the frequency of the QCL. Using this swept-frequency technique, SM imaging has been performed[160] on a sample holder containing 3 different plastics, where the phase measured by the SM interferometric fringes is a combination of the complex permittivity of the sample and the sample depth. By imaging a flat structure, any tilt in the sample was removed by studying the interferometric fringes across the sample holder surface, meaning any measured phase changes were attributed to the samples refractive index.

The various phase offsets measured by the system can be viewed in Fig. 1.11(c) between the waveforms from each sample. By fitting an SM model based on the Lang-Kobayashi equations to the waveforms, the refractive index and extinction coefficient of each pixel, and therefore each sample, were obtained, by using references of known complex refractive index for calibration.

One of the previous coherent imaging techniques discussed above[70] where THz QCL SM imaging can be shown to give a much more compact set-up to a similar end is ISAR imaging.[161] Using a similar swept-frequency technique described for the purposes of re-

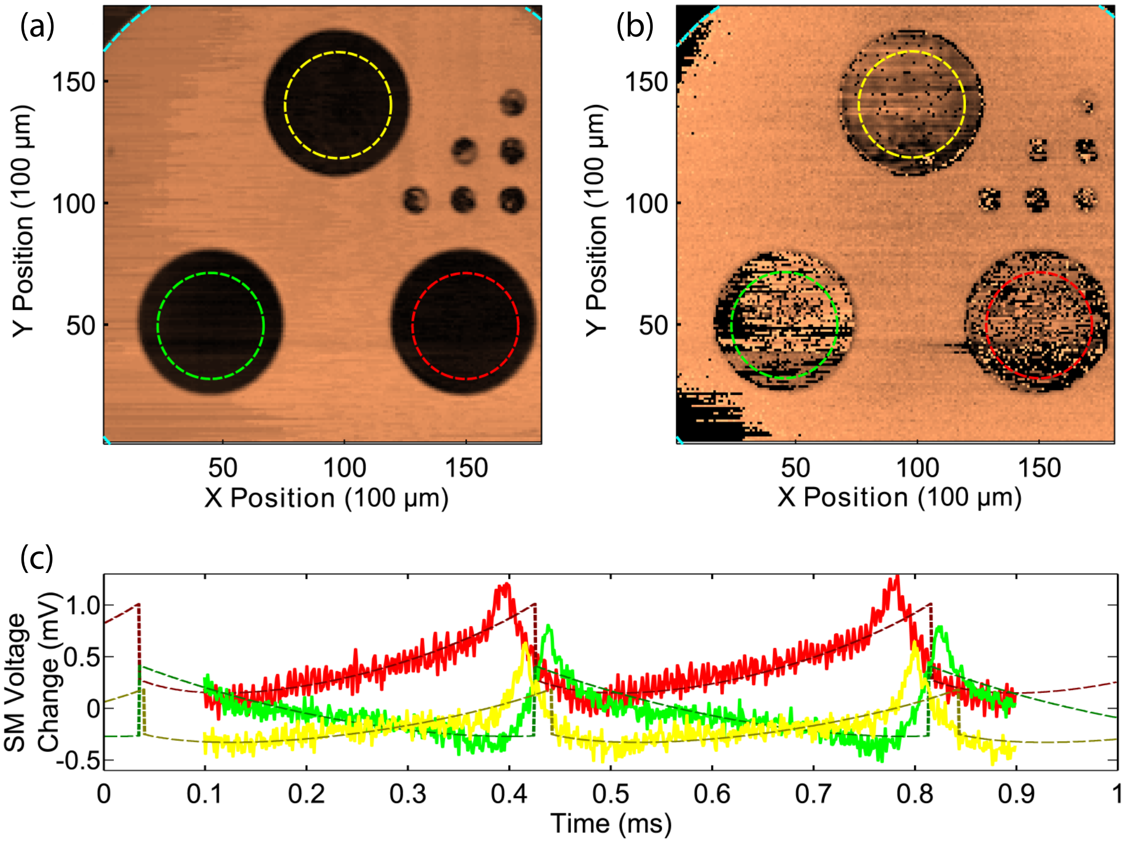

Figure 1.11: (a) Amplitude and (b) phase images of a sample holder filled with three plastics, extracted using SM interference imaging. The plastics under investigation are polycaprolactam (yellow), polyvinyl chloride (green) and polyoxymethylene (red). (c) Exemplar SM waveforms extracted from individual pixels of each of the materials (solid lines) and corresponding fits to an SM model (broken lines). Adapted from Taimre[160]

fractive index extraction above, various overlapping sections of a resolution target were imaged through an aperture. From each waveform, the aggregate complex reflection coefficient of the target at that position was extracted in order to calculate the relative magnitude and phase of the backscattered electric field. Using an ISAR matched-filter algorithm, these complex fields were analysed to recover high-resolution spatial dependencies of the complex reflectivity across the target. From a normal one-dimensional SM image of the resolution target the smallest line-pairs could be recovered at a signal variation of $\sim$2 dB. The processed ISAR image on the other hand could recover the same lines at a much sharper resolution with $\sim$50 dB signal variation; a significant improvement over the generic SM image in both contrast and spatial resolution.

Other than imaging, THz QCL SM has been used to study other areas of research, such as velocimetry of multiple external targets[162] simultaneously. While velocity of a single external target has shown to be measured using SM previously[109–114], the transparency of many materials at THz frequencies and the high stability of QCLs allows sensing of multiple targets to occur at the same time by creating a two-stage external cavity as shown in Fig. 1.12(a). The targets in this system were two identical polypropylene sheets (17% reflectance), T_1 and T_2, colinearly aligned along the optical axis at distances of 300 mm and 550 mm from the QCL facet mounted on linear translation stages. A variable aperture was introduced between the targets to allow control of the level of feedback from the further target. The two targets were moved at constant velocities of 0.5 mm/s and -5 mm/s respectively, where the sign indicates direction (negative is towards the laser facet).

Figure 1.12(b) shows the terminal laser voltage obtained while moving just T_1 (top), just T_2 (middle) and both targets simultaneously (bottom). The bottom waveform consists of a superposition of the two upper waveforms due to the perturbation from the two targets at the same time. The differential voltage waveforms in Fig. 1.12(c) shows the frequency of the SM fringe period as a series of voltage spikes, where the polarity of these indicate the direction of travel (negative polarity is a positive extension of the external cavity). Due to the different velocities, the interferometric fringes obtained occur at different

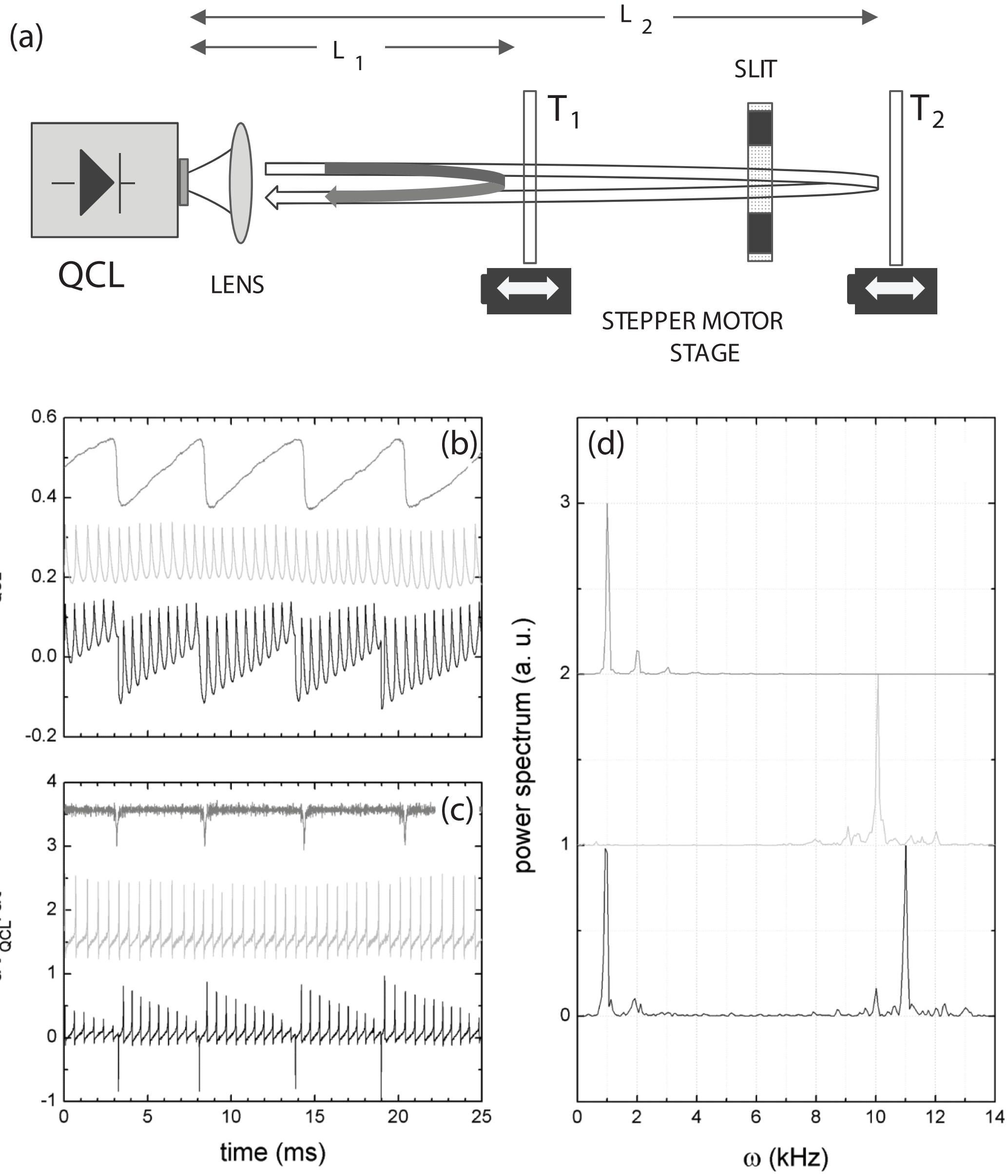

Figure 1.12: (a) Schematic diagram allowing for simultaneous velocimetric measurement of multiple external targets. (b) Oscilloscope traces of the interferometric measurements of movement of the targets independently (top and middle) and together (bottom). (c) Corresponding analogue derivatives and (d) normalised power spectra of the SM signals detected from the terminal voltage of the QCL. In all of (b)-(d) (top trace) T_1 moving at $v_1 = 0.5\,\mathrm{mm/s}$ extending the external cavity, (middle trace) T_2 moving at $v_1 =$ -5 mm/s shortening the external cavity. (bottom trace) T_1 and T_2 moving in opposite directions at their previously listed velocities. Adapted from Mezzapesa[162]

frequencies, and Fig. 1.12(d) shows the normalised power spectrum for the corresponding waveforms from (c). Here T_1 contains a low frequency peak at $\omega_1 = 4\pi v_1 \lambda \approx 1\,\mathrm{kHz}$, with harmonics at 2 and 3 kHz (top) and T_2 gives a peak at $\omega_2 = 4\pi v_2 \lambda \approx 10\,\mathrm{kHz}$ (higher order harmonics are not shown). The lower trace consists of a superposition of the above traces with major peaks at the frequencies of the targets, ω_1 and ω_2, and the sum frequency $\omega_1 + \omega_2$, where the amplitude corresponds to the proportion of feedback from the targets. Due to this, the component at ω_2 is much smaller than ω_1 but can be recovered from the sum frequency. This shows the high-sensitivity of SM and particular application of the THz regime to velocimetric measurement at stand-off distances.

As proven by this previous work, THz QCL SM shows great promise in making compact, sensitive, high-power imaging and sensing systems for a variety of purposes. This thesis will demonstrate some of the ways this area has been expanded on.

1.5 Structure of this thesis

Chapter 2 presents a study of the understanding of SM theory and how this relates to the various properties of the QCL, including simulations of the effect of various parameters on acquired waveforms. This theory will be related to the expected electrical and optical measurements performed with the QCL. Measurements will also be shown of a relationship between the differential-resistance of the QCL and the amplitude of the measured SM signal.

Chapter 3 will look at a number of methods of two-dimensional (2D) THz imaging using SM, with particular attention being paid to a number of different modulation schemes. Various studies of the quality of the acquired images will be presented including signal-to-noise ratio (SNR) and dynamic range. A new method of THz SM near-field (NF) reflectance imaging will also be presented that improves on previously reported lateral imaging resolution by orders of magnitude.

Three-dimensional THz SM imaging utilising a mechanical pullback technique will be demonstrated in Chapter 4, where exemplar structures are scanned to produce both sub-wavelength morphology and reflectance maps of the sample surface. A SM model is fitted to the acquired interferometric waveforms at each pixel to extract parameters of the acquired SM waveform in this method. This will be demonstrated for various modulation methods.

A swept-frequency technique will be utilised to various ends in Chapter 5. These measurements will include 3D imaging with an increased imaging speed and accuracy through a higher degree of averaging, extraction of the optical constants of explosive inhomogeneous materials such as complex refractive index, and phase-nulling of the external phase for the purposes of vibrometric sensing and real-time measurement of the laser tuning coefficient.

The final experimental chapter, Chapter 6, will demonstrate a study of the measurement of the laser emission spectra of a THz QCL using SM. This system employs a much reduced experimental complexity when compared to FTIR measurement and will also show a direct comparison to FTIR measurements that were taken simultaneously. Due to the sensitivity of SM, the frequency-pulling phenomenon of the QCL under feedback was also measured using this technique and will be shown as a method of extracting the feedback coefficient of the system.

Chapter 7 summarises the key result of the work and suggests topics of future work.

2 Self-mixing Theory

A basis for most theoretical modelling of the self-mixing effect is based on the Lang-Kobayashi[105] model which employs coupled rate equations for electric field and carrier density to describe the device under feedback. A three-mirror model consisting of a laser and external reflector[163] can also be used to describe a laser under feedback. To understand this model, we must initially consider the operation of a laser with no optical feedback present. The two- and three-mirror models described in this chapter are based on that derived by Tucker.[164]

2.1 Two-mirror model

A laser can be considered as a Fabry-Pérot cavity consisting of two mirrors, M_1 and M_2,[165] whose amplitude reflection coefficients are given as r_1 and r_2, and a gain medium with refractive index n_e. The length of the cavity is given the designation L. By injecting an electromagnetic wave from an external source away from M_1 and assuming a uniform plane wave travelling from M_1 to M_2 to simplify analysis, the behaviour of the laser can be determined. A schematic of such a device is shown in Fig. 2.1.

The electric field in the cavity is defined as

$$E(z,t) = E_0 \cos(\omega t - \beta z), \tag{2.1}$$

where z is the longitudinal distance along the cavity from M_1 to M_2, t is the time, E_0 is the amplitude of the electric field, $\omega = 2\pi\nu_0$ is the angular frequency of the wave, where the frequency of the wave is given by ν_0 and $\beta = 2\pi n_\mathrm{e}/\lambda$ is the wavenumber in the cavity determined by the wavelength of the wave λ.

The electric field can be split into real and imaginary components using $e^{(i\theta)} = \cos\theta + i\sin\theta$ to give

$$E(z,t) = Re[E_0 e^{(i(\omega t - \beta z))}] = Re[\widetilde{E} e^{(i\omega t)}], \tag{2.2}$$

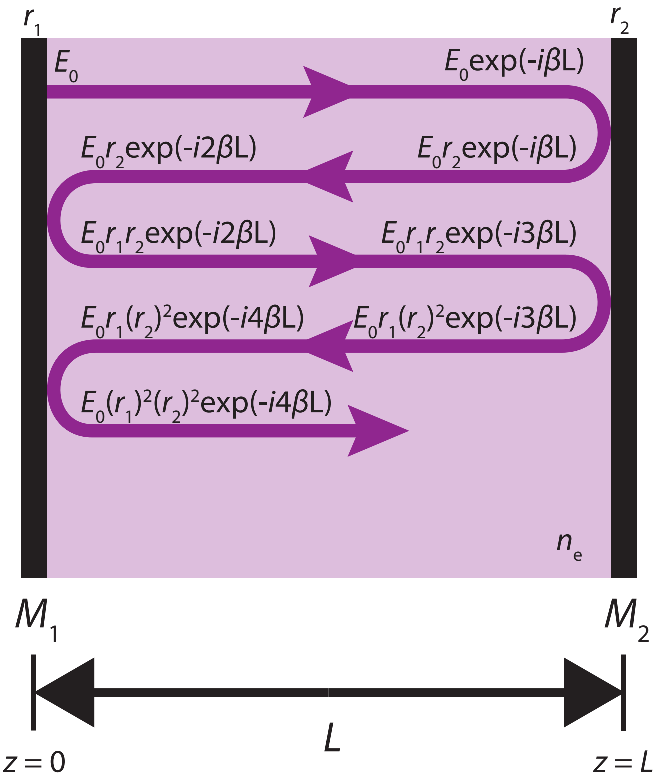

Figure 2.1: Two-mirror model of a laser cavity

where

$$\widetilde{E} = E_0 e^{(-i\beta z)}. \tag{2.3}$$

This notation of $\widetilde{E}$ allows expression of the total field (including both amplitude and phase) with no sinusoidal functions, simplifying further arithmetic of the optical cavity.

Fig. 2.1 shows the propagation of the electromagnetic wave E_0 from M_1 to M_2 undergoing a phase shift of βL. A component of this wave is then internally reflected, where the amplitude change is dictated by the reflection coefficient r_2, while the rest of the wave is emitted through the facet of the laser. The reflected field returns to M_1, undergoing another phase change of βL, and the reflection at M_1 results in another amplitude change, this time of r_1. After one full round trip of the laser cavity, the field is therefore $E_0 r_1 r_2 e^{-i2\beta L}$. This wave can continue to undergo multiple round-trip journeys through the gain medium. As lasers are continuous excitation sources, a second field E_0 will propagate with the initial field on the next round-trip journey through the cavity.

The full cavity field is equal to the superposition of each field in the cavity. When these fields have the same complex amplitude, and therefore the same phase, the laser output will be at its maximum. For this to occur, the round-trip phase shift of the initial wave must equal $m2\pi$, where m is an integer. By re-writing the phase constant in terms of wavelength, the maximum laser output power occurs when

$$\frac{m\lambda}{2} = n_{\mathrm{e}}L. \tag{2.4}$$

This is only satisfied for discrete wavelengths in a laser cavity due to its fixed length, known as *resonant* wavelengths. The range of these discrete wavelengths is limited by other laser parameters, including the laser gain spectrum and cavity losses. The laser cavity has a power gain per unit length, g, and power loss per unit length, α_{s}, both of which are functions of wavelength. The laser will only resonate for wavelengths where the power gain is greater than the power loss and since the internal laser power is proportional to the electric field squared, Eq. (2.3) can be re-written as

$$\widetilde{E} = E_0 e^{[(-i\beta+\frac{1}{2}(g(h\nu_0)-\alpha_{\mathrm{s}}(h\nu_0)))z]}, \tag{2.5}$$

which in turn makes a round-trip electric field of

$$E_0 r_1 r_2 e^{[(-i\beta+\frac{1}{2}(g(h\nu_0)-\alpha_{\mathrm{s}}(h\nu_0)))2L]}. \tag{2.6}$$

Assuming the wavelength in the cavity is a resonant wavelength, by splitting Eq. (2.6) into components of round-trip field $E_0e^{-j2\beta L}$ and a round-trip lasing condition $r_1r_2e^{(g(h\nu_0)-\alpha(h\nu_0))L}$, power gain exceeds power loss when

$$r_1 r_2 e^{(g(h\nu_0)-\alpha_{\mathrm{s}}(h\nu_0))L} = 1. \tag{2.7}$$

This is known as the amplitude condition for lasing, which can be rearranged to give the threshold gain condition

$$g_{\mathrm{th}} = \alpha_{\mathrm{s}} + \frac{1}{L} \ln\left(\frac{1}{r_1 r_2}\right). \tag{2.8}$$

By careful design of the laser cavity, *single mode* lasers that emit at only one wavelength can be engineered.

2.2 Three-mirror model

The two-mirror model can be expanded to account for external feedback reflecting off an external target and being re-injected back into the laser cavity by introducing a third mirror, M_{Ext}, with reflection coefficient $r_{2\mathrm{Ext}}$ at distance L_{Ext} from the laser facet M_2. The effective refractive index of the medium between M_2 and M_{Ext} is n_0. The wavenumber in the external cavity is defined as $\beta_0 = 2\pi n_0/\lambda$ where λ is the emission wavelength. In this model, there will be separate components for the internal round-trip of the laser cavity and the round-trip incurred by light reflected off the external reflector and back into the laser cavity. By analysing the electric field inside the device, shown in Fig. 2.2,[113,166,167] the behaviour of the device under feedback can be understood.

It's possible to combine the reflected fields from both M_2 and M_{Ext} into a single term, such that the three-mirror model can be simplified to a two-mirror model with a single, combined mirror having an effective complex reflection coefficient r_{Eff} given by[166,167]

$$r_{\mathrm{Eff}}(\nu) = r_2 + \left(1 - |r_2|^2\right) r_{2\mathrm{Ext}} e^{-i2\pi\nu\tau_{\mathrm{Ext}}}, \tag{2.9}$$

where ν is the emission frequency of the laser under feedback, $\tau_{\mathrm{Ext}} = 2L_{\mathrm{Ext}}n_0/c$ is the external cavity round-trip propagation time (assuming constant refractive index in the external cavity) and c is the speed of light in a vacuum. The two terms in Eq. (2.9) represent the reflection from the laser facet M_2 and the portion of light that is re-injected after reflection from the external mirror M_{Ext} and transmission through M_2, respectively. This equation is only true for a single round-trip of the external cavity, such as when the

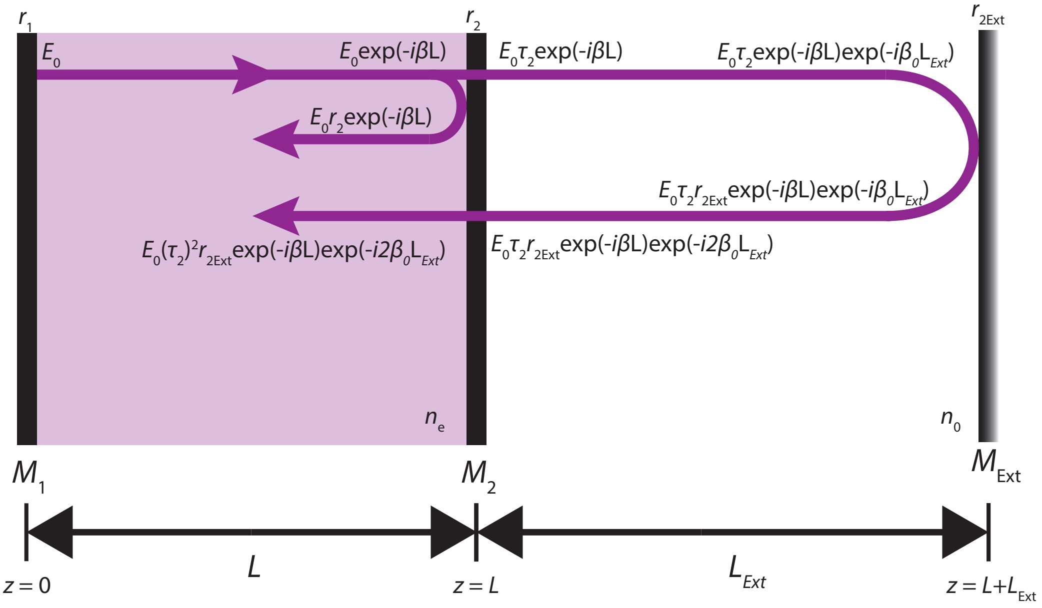

Figure 2.2: Three mirror model consisting of a laser and external cavity. This simplified model depicts the electric field behaviour of the laser under feedback.

laser is under weak feedback where $r_2 \gg r_{2\text{Ext}}$. For stronger feedback, a summation of the multiple reflected electric fields[168–170] that are injected into the internal cavity replaces the second term in Eq. (2.9). To simplify further analysis, and since it is the most common regime to observe self-mixing in quantum cascade lasers, any further theoretical work will assume operation of the laser under weak feedback.

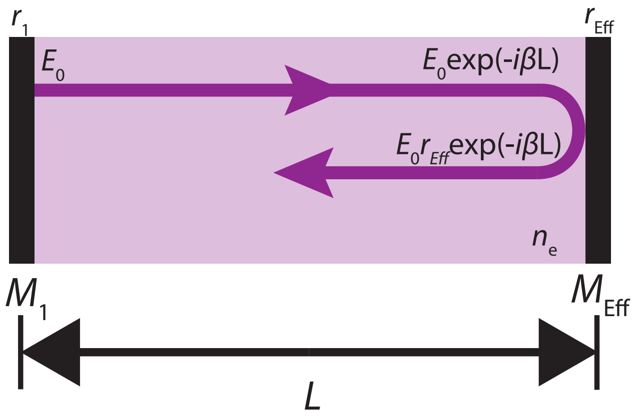

Figure 2.3: Equivalent two-mirror model of a laser cavity under optical feedback.

The effective reflectivity, r_{Eff}, can be rewritten as a single complex term

$$r_{\mathrm{Eff}}(\nu) = |r_{\mathrm{Eff}}(\nu)| e^{-i\phi_{\mathrm{r}}}, \tag{2.10}$$

where $|r_{\mathrm{Eff}}(\nu)|$ and ϕ_{r} are the amplitude and phase of the effective reflection coefficient. Under weak optical feedback, where $Re[r_{\mathrm{Eff}}(\nu)] \gg Im[r_{\mathrm{Eff}}(\nu)]$[110] due to $r_2 \gg r_{2\mathrm{Ext}}$, the amplitude and phase shifts of the reflection coefficient are given by

$$|r_{\mathrm{Eff}}(\nu)| \approx Re[r_{\mathrm{Eff}}(\nu)] \approx r_2[1 + \kappa_{\mathrm{Ext}} \cos(2\pi\nu\tau_{\mathrm{Ext}})], \tag{2.11}$$

$$\phi_{\mathrm{r}} \approx \frac{Im[r_{\mathrm{Eff}}(\nu)]}{r_2} \approx \kappa_{\mathrm{Ext}} \sin(2\pi\nu\tau_{\mathrm{Ext}}), \tag{2.12}$$

where

$$\kappa_{\mathrm{Ext}} = \frac{r_{2\mathrm{Ext}}}{r_2}\left(1 - |r_2|^2\right). \tag{2.13}$$

κ_{Ext} is a representation of the amount of light coupled back into the laser facet known as the feedback coupling coefficient. From an experimental viewpoint, κ_{Ext} is commonly represented by[166]

$$\kappa_{\mathrm{Ext}} = \epsilon\sqrt{\frac{R_{2\mathrm{Ext}}}{R_2}}(1 - R_2), \tag{2.14}$$

where ϵ is the coupling-efficiency factor to account for losses in the external cavity, system misalignment and mismatch between the reflected radiation and the cavity mode, and R_2 and $R_{2\mathrm{Ext}}$ are the power reflection coefficients of the facet M_2 and external mirror M_{Ext}, respectively.

The effect of optical feedback into the cavity is to change the properties of the laser emission, including the output frequency, linewidth, threshold gain and therefore output power. Assuming single-mode emission and frequency independent gain and loss values, the lasing condition given in Eq. (2.7) can be rewritten to account for the effective mirror as round-trip amplitude and phase conditions

$$r_1|r_{\mathrm{Eff}}|e^{(g(h\nu)-\alpha_{\mathrm{s}}(h\nu))L} = 1, \tag{2.15}$$

$$\frac{4\pi n_{\mathrm{e}}\nu L}{c} + \phi_{\mathrm{r}} = m2\pi, \tag{2.16}$$

where the effective reflectivity of the coupled-mirror is accounted for, $\beta = 2\pi n_{\mathrm{e}}\nu/c$[166] and $2\beta L + \phi_{\mathrm{r}} = m2\pi$.

The threshold gain for a laser under weak optical feedback, g_{c}, can by found by accounting for effective reflectivity in Eq. (2.8) and making use of Eq. (2.11)

$$g_{\mathrm{c}} = \alpha_{\mathrm{s}} + \frac{1}{L}\ln\left(\frac{1}{r_1 r_2[1+\kappa_{\mathrm{Ext}}\cos(2\pi\nu\tau_{\mathrm{Ext}})]}\right). \tag{2.17}$$

It follows that the change in threshold gain due to feedback can be calculated as

$$\Delta g = (g_{\mathrm{c}} - g_{\mathrm{th}}) = \frac{1}{L}\ln\left(\frac{1}{[1+\kappa_{\mathrm{Ext}}\cos(2\pi\nu\tau_{\mathrm{Ext}})]}\right) = \frac{-\ln[1+\kappa_{\mathrm{Ext}}\cos(2\pi\nu\tau_{\mathrm{Ext}})]}{L}. \tag{2.18}$$

Through expansion of the natural log into a power series[171], and since $\kappa_{\mathrm{Ext}} \ll 1$ for weak feedback, the change in threshold gain becomes

$$\Delta g = -\frac{\kappa_{\mathrm{Ext}}}{L}\cos(2\pi\nu\tau_{\mathrm{Ext}}). \tag{2.19}$$

The cosine term of this equation contains the round-trip phase shift of the external cavity, $\phi_{\mathrm{Ext}} = 2\pi\nu\tau_{\mathrm{Ext}}$, meaning the change in threshold gain is periodic along L_{Ext}. Also, $|\Delta g|$ will minimise, i.e. $\Delta g = 0$, when $\phi_{\mathrm{Ext}} = (1+2m)\pi/2$ where m is an integer.

Experimentally, the terminal voltage of the laser is monitored as a form of measuring self-mixing amplitude, due to a proportional change in terminal voltage with threshold gain[61,128]. An expression of ΔV_{SM} can be derived from Boltzmann's law of carrier density produced by a voltage V_{SM}[172]

$$N = N_0 e^{qV_{\mathrm{SM}}/2kT}, \tag{2.20}$$

where N and N_0 are the carrier densities with and without feedback respectively, q is the electron charge, k is the Boltzmann constant and T is the device temperature. By differentiating this with respect to voltage, the change in carrier density, ΔN_0 for change in voltage, ΔV_{SM}, can be calculated and rearranged to give

$$\Delta V_{\mathrm{SM}} = \left(\frac{2kT}{q}\right)\frac{\Delta N}{N_0}. \tag{2.21}$$

The change of refractive index, n_{e}, with carrier density, N, is related to the variation in gain by the linewidth enhancement factor, α, which can be expressed as[166]

$$\frac{\delta n_{\mathrm{e}}}{\delta N}(N - N_0) = -\frac{\alpha c}{4\pi\nu_0}(g_{\mathrm{c}} - g_{\mathrm{th}}), \tag{2.22}$$

where $g_{\mathrm{c}} - g_{\mathrm{th}} = \Delta g$. By combining Eqs. (2.21) and (2.22) the change in voltage under feedback can be related to the change in gain

$$\Delta V_{\mathrm{SM}} = -\left(\frac{2kT}{q}\right)\frac{\alpha c}{4\pi\nu_0}\Delta g\left(\frac{\delta N}{\delta n_{\mathrm{e}}}\right). \tag{2.23}$$

From Eqs. (2.14) and (2.19), this can be reduced to relate the change in voltage ΔV_{SM} to a change in the external cavity length L_{Ext} and the laser emission frequency under feedback ν

$$\Delta V_{\mathrm{SM}} \propto \epsilon\sqrt{R_{2\mathrm{Ext}}}\cos\left(\frac{2\pi L_{\mathrm{Ext}}\nu}{c}\right). \tag{2.24}$$

This relationship is fundamental to much of the work presented in this thesis where the reflectivity of the sample, or a change to the external cavity length or emission frequency causes a perturbation to the terminal voltage. This method is utilised in Chapters 3, 4, 5 and 6.

2.2.1 Excess phase equation

In order to determine the perturbation to the terminal voltage from Eq. (2.24), the lasing frequency under feedback first has to be obtained. Equation (2.16), the phase condition for lasing under feedback, suggests a change in frequency, and therefore refractive index of the laser, when feedback is present. Derivation of the excess phase equation will follow that presented by Petermann[166]. Whilst this theory was originally developed to describe interband lasers under feedback, it has also been widely adopted[128,173,174] to describe intersubband devices such as QCLs.

The total change in $n_{\mathrm{e}}\nu$ under feedback can be given by

$$\Delta(n_{\mathrm{e}}\nu) = \nu_0 \Delta n_{\mathrm{e}} + (\nu - \nu_0) n_{\mathrm{e}}. \tag{2.25}$$

By accounting for the carrier density in the device, the change in effective refractive index can be expressed as

$$\Delta n_{\mathrm{e}} = \frac{\delta n_{\mathrm{e}}}{\delta N}(N - N_0) + \frac{\delta n_{\mathrm{e}}}{\delta \nu}(\nu - \nu_0). \tag{2.26}$$

By combining Eqs. (2.16), (2.22), (2.25) and (2.26), the change in round-trip phase due to feedback, $\Delta\phi_{\mathrm{L}}$, known as the excess phase, can be expressed as

$$\Delta\phi_{\mathrm{L}} = \frac{4\pi L}{c}\left[-\frac{\alpha c}{4\pi}(g - g_{\mathrm{th}}) + \nu_0 \frac{\delta n_{\mathrm{e}}}{\delta \nu}(\nu - \nu_0) + n_{\mathrm{e}}(\nu - \nu_0)\right] + \phi_{\mathrm{r}}. \tag{2.27}$$

Of the 3 terms in the square brackets in Eq. (2.27), the final two can be simplified using the expression for the effective group refractive index, n_{g}, which accounts for dispersion of the refractive index. The spacing between adjacent frequencies in the laser emission can be calculated using[166]

$$n_{\mathrm{g}} = n_{\mathrm{e}} + \nu \frac{\delta n_{\mathrm{e}}}{\delta \nu}. \tag{2.28}$$

By substituting this into Eq. (2.27) the excess phase can be given as

$$\Delta\phi_{\mathrm{L}} = \frac{4\pi n_{\mathrm{g}} L}{c}(\nu - \nu_0) - \alpha(g_{\mathrm{c}} - g_{\mathrm{th}})L + \phi_{\mathrm{r}}, \tag{2.29}$$

which can be further reduced using the change in gain from Eq. (2.19) and the phase shift from Eq. (2.12)

$$\Delta\phi_{\mathrm{L}} = \frac{4\pi n_{\mathrm{g}} L}{c}(\nu - \nu_0) + \kappa_{\mathrm{Ext}}[\sin(2\pi\nu\tau_{\mathrm{Ext}}) + \alpha\cos(2\pi\nu\tau_{\mathrm{Ext}})]. \tag{2.30}$$

The round-trip delay of the laser cavity can be given by[166]

$$\tau_{\mathrm{L}} = 2n_{\mathrm{g}}L/c, \tag{2.31}$$

which can be substituted into Eq. (2.30) to simplify the first term, and the second term can also be rearranged to give

$$\Delta\phi_{\mathrm{L}} = 2\pi\tau_{\mathrm{Ext}}(\nu - \nu_0) + C\sin(2\pi\nu\tau_{\mathrm{Ext}} + \arctan\alpha), \tag{2.32}$$

where

$$C = \frac{\tau_{\mathrm{Ext}}}{\tau_{\mathrm{L}}}\kappa_{\mathrm{Ext}}\sqrt{1+\alpha^2}. \tag{2.33}$$

C is the feedback parameter, which quantifies how the optical feedback effects the behaviour of the laser. The value of C indicates which of the four feedback regimes the laser is operating in:[175]

- $C \ll 1$, the *very weak feedback regime.* $\Delta\phi_{\mathrm{L}}$ has a sinusoidal function.
- $0.1 < C < 1$, the *weak feedback regime.* The function of $\Delta\phi_{\mathrm{L}}$ begins to distort, becoming non-sinusoidal (see Fig. 2.4(a)).
- $1 < C < 4.6$, the *moderate feedback regime.* In this regime, the function becomes triple valued for certain values of ϕ_{L} (see Fig. 2.4(b)) and jumps in phase can occur due to this hysteresis. The interferometric signal becomes sawtooth in nature.
- $C > 4.6$, the *strong feedback regime.* The function may now become five-valued (see Fig. 2.4(c)) and become very unstable, potentially leaving the self-mixing regime completely.

The distortion observed in the periodicity of the function is due to larger feedback causing a larger change in the refractive index of the device, resulting in a further change in the external phase, $\Delta\phi_{\mathrm{L}}$. Due to the inherently stable nature of THz QCLs under feedback,[173] QCLs under feedback will not become unstable.

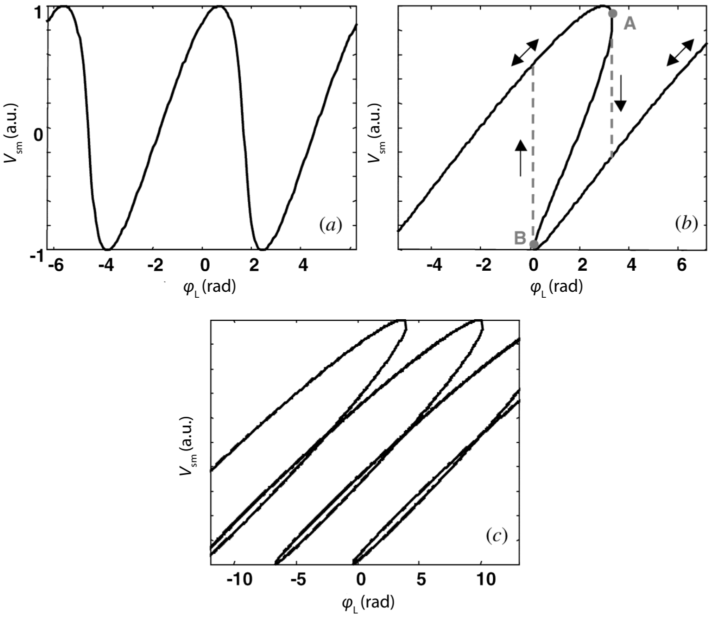

Figure 2.4: Calculated waveforms of V_{SM} for different values of the feedback parameter C. (a) $C = 0.7$, (b) $C = 3$ and (c) $C = 10$. In (b), the segment AB is unstable. When the system is in A and ϕ_{L} (or the external cavity length) is further increased, it jumps down along the broken line. When the system is in B and ϕ_{L} is further decreased, it jumps up. Adapted from Giuliani.[175]

In order to solve the excess phase equation, $\Delta\phi_{\mathrm{L}}$ can be equated to 0. Of the presented SM theory, the fundamental equations that form the basis of analysis in the work in this thesis are Eqs. (2.24) and (2.32). These equations describe the change in the terminal voltage of the QCL under feedback and it's relationship with certain experimental parameters, notably the targets reflectivity, the external cavity length, level of feedback and laser emission frequency.

2.2.2 Simulation of SM theory

By simulating the response of the excess phase equation for exemplar QCL parameters under the effect of a changing external cavity length it is possible to demonstrate the range of excess phase that would be expected in an experiment. This can in turn be used to simulate the SM effect on the terminal voltage of the laser and the emission frequency. The simulations were performed in MATLAB utilising code provided by Kliese[176] using the following QCL parameters

Table 1: Typical THz QCL parameters used in the following simulations.

Parameter	Value
ν_0	2.2415 THz
α[128,145]	0
L	0.3 m

2.2.2.1 Simulation of V_{SM}

The work presented in Chapters 4 and 6 will utilise an extension to the external cavity in order to produce interferometric fringes due to feedback. By simulating ΔL_{Ext} on the order of a few times the unperturbed emission wavelength ($\Delta L_{\mathrm{Ext}} = 300\,\mu\mathrm{m}$) the oscillation of V_{SM} can be demonstrated. Using a feedback parameter of $C = 0.5$ and Eq. (2.24), SM fringes can be simulated, as shown in Fig. 2.5.

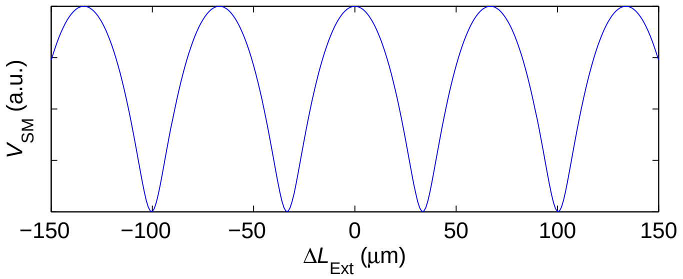

Figure 2.5: Simulation of SM fringes using Eq. (2.24) and $C = 0.5$ for a changing cavity length.

By simulating the same equation for various levels of feedback, the effect of C can be demonstrated, as shown in Fig. 2.6. While the periodicity of the waveform doesn't change,

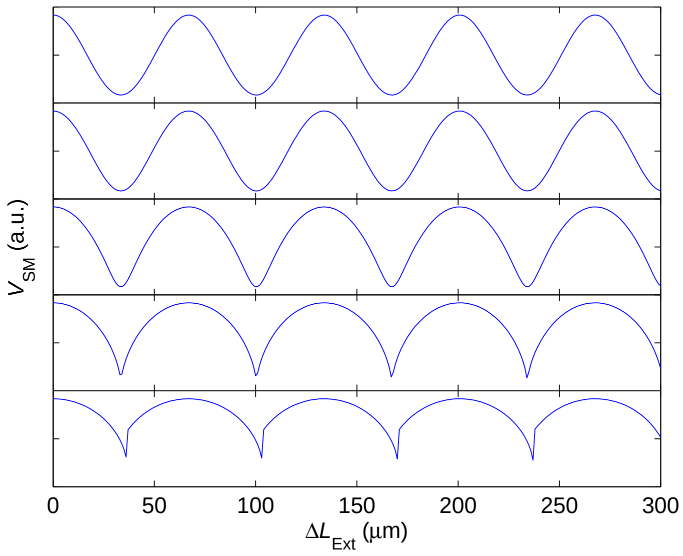

Figure 2.6: Simulation of SM fringes using Eq. (2.24) for a changing cavity length and various levels of feedback. Feedback levels of (a) $C = 0$, (b) $C = 0.1$, (c) $C = 0.5$,(d) $C = 1$ and (e) $C = 1.5$ are shown.

the shape does. Higher levels of feedback ($C > 1$) causes the waveform to fold back onto itself, which in reality translates to a voltage offset due to hopping. This is shown in Fig. 2.6(e).

Equation (2.24) dictates that the amplitude of the SM fringes is controlled by the reflectivity of the external target and coupling through the external cavity. By simulating various magnitudes, s, of this factor $R = s\epsilon\sqrt{R_{2\mathrm{Ext}}}$ the relationship is shown to be true. This simulation is shown in Fig. 2.7. This demonstrates a linear relationship between sample reflectivity and the amplitude of V_{SM}. Also, if the coupling into the facet is improved, the amplitude of V_{SM} will also increase. This effect will be used in Chapters 3 and 4. These parameters have no effect on the shape of the fringes.

2.2.2.2 Simulation of the excess phase equation

By substituting values from Table. 1 into the excess phase equation Eq. (2.32) oscillations of the excess phase due to the perturbed emission frequency under feedback (in this case over the range of $\nu_0 \pm 1000\,\mathrm{MHz}$) can be simulated for a range of feedback levels. From

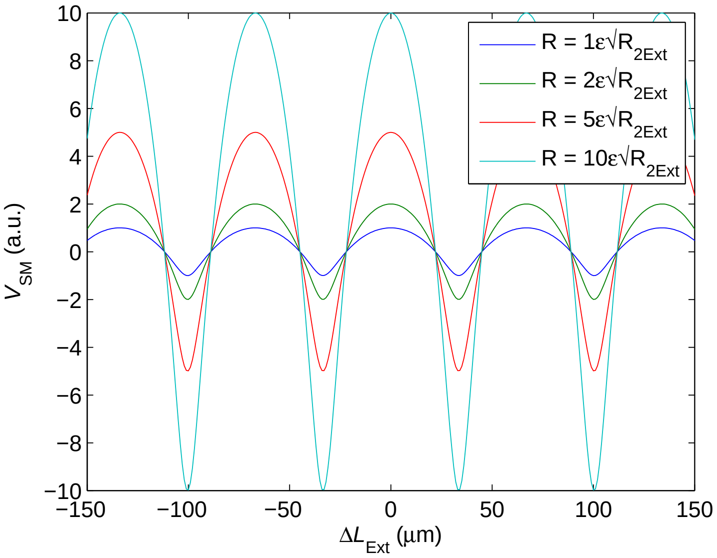

Figure 2.7: Simulation of SM fringes under different levels of external cavity attenuation and sample reflectivity $\epsilon\sqrt{R_{2\mathrm{Ext}}}$.

Fig. 2.8, it can be seen that for values of $C < 1$, only a single emission frequency exists for each value of excess phase. Under levels of stronger feedback ($C > 1$), there are multiple possible values of emission frequency for some values of excess phase, as shown in Fig. 2.9 for a feedback level of $C = 5$. Where multiple emission frequencies are possible, the laser can oscillate between them and become bistable.

This analysis also allows simulation of the frequency pulling effect, from changing the external cavity length, on the laser emission. This effect will be demonstrated experimentally in Chapter 6.5. For the same simulated cavity change ΔL_{Ext} as in previous simulations Fig. 2.10 can be produced. For moderate and strong feedback, the waveforms become so asymmetric that they fold over themselves, which causes a jump, as shown in Fig. 2.10 for a feedback level of $C = 1.5$. By performing the simulation for both an increasing and decreasing ΔL, the extent of the hysteresis becomes more prominent, as shown in Fig. 2.11. As feedback increases, the variation of emission frequency with external cavity length becomes more asymmetric, but retains a periodicity of $\lambda_0/2$ where $\lambda_0 = c/\nu_0$ is the unperturbed emission wavelength.

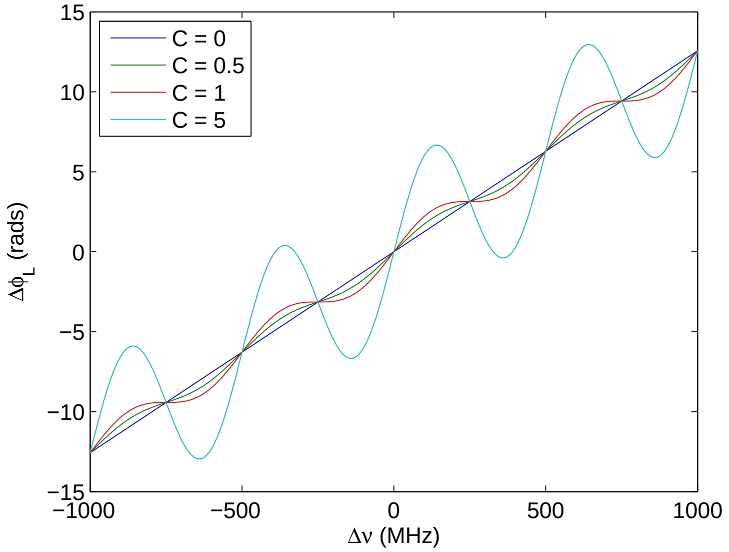

Figure 2.8: Simulation of the excess phase for various laser emission frequencies under different levels of feedback.

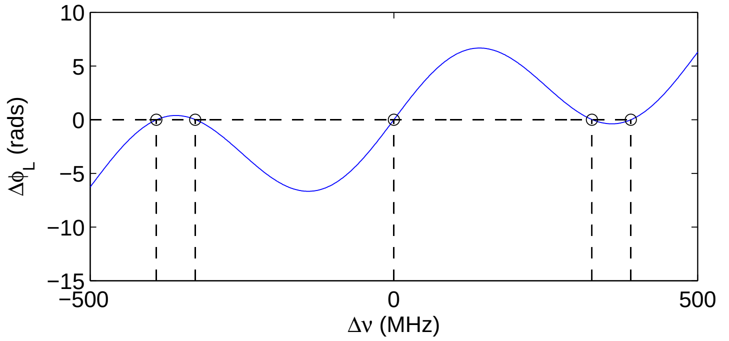

Figure 2.9: For strong feedback ($C = 5$), multiple emission frequencies may exist for one solution of excess phase.

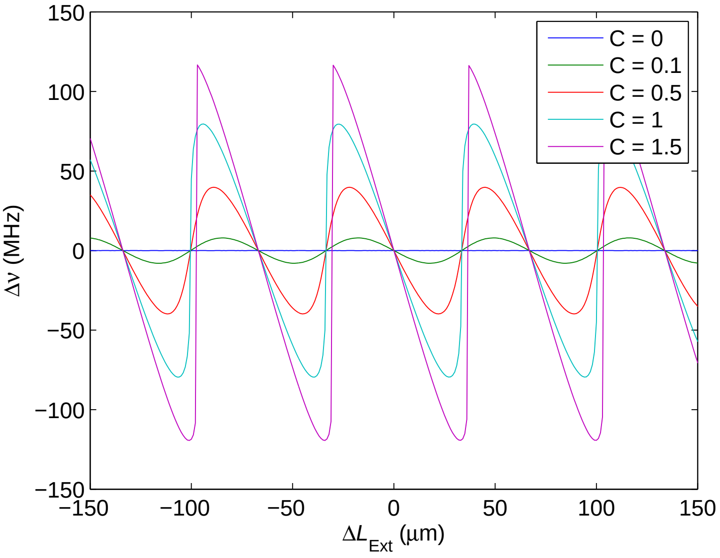

Figure 2.10: Simulation of the effect of an external cavity modulation on emission frequency for various feedback levels.

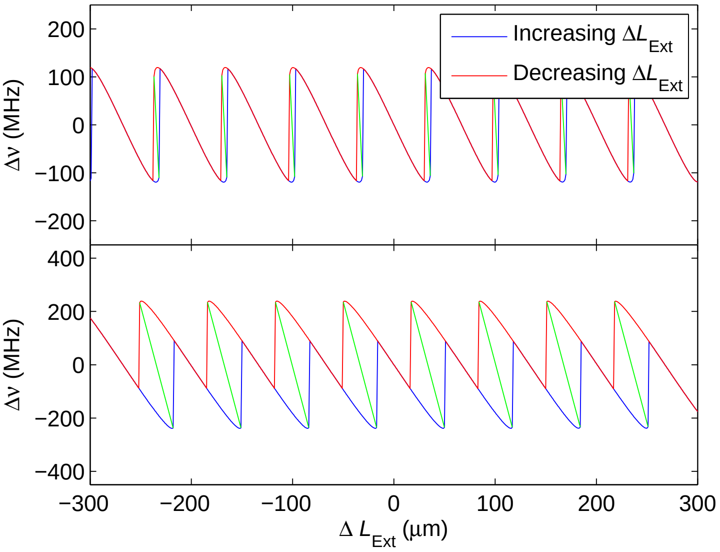

Figure 2.11: Simulation of the hysteresis in $\Delta\nu$ caused by strong feedback. Feedback levels of (a) $C = 1.5$ and (b) $C = 3$ are shown, where the green line has been added to show the approximate real waveform shape.

2.2.3 Mode-hopping due to optical feedback

As noted by Eq. (2.4), the laser will only emit at a number of resonant wavelengths dictated by the laser cavity length due to the distribution of Fabry-Pérot modes. The external cavity will also have a number of cavity modes related to its length, L_{Ext}. As the external cavity length changes, a technique used to create interferometric fringes in a number of measurements presented in this thesis, the emission frequency of the QCL will change. This can lead to changes dictated by both the internal and external cavity modes. The distribution of both of these sets of modes is illustrated in Fig. 2.12.[105]

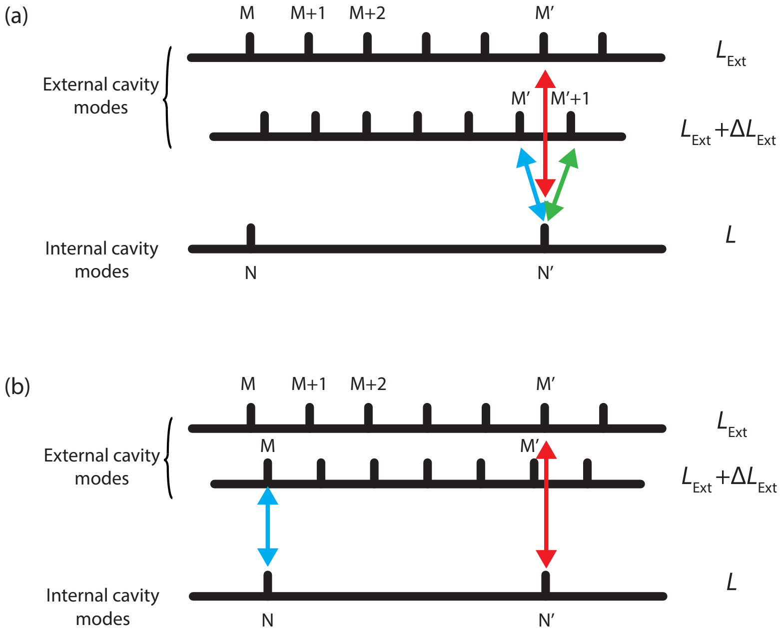

Figure 2.12: Relationship between external and internal cavity modes under the conditions (a) $L_{\mathrm{Ext}} = mL$ and (b) $L_{\mathrm{Ext}} \neq mL$.[105]

In the case where L_{Ext} equals an integer (m) multiple of L, the laser cavity length, the laser cavity separation is equal to an integer of the external cavity separation, as shown in Fig. 2.12(a). If one of the laser cavity modes (mode N') matches an external cavity mode (mode M') in frequency, there will also be matches in neighbouring modes (modes N and M for example). The laser will emit at the mode pair closest to the peak of the gain curve (modes N' and M' in Fig. 2.12(a), demonstrated by the red arrow). When the cavity length is increased slightly the spacing of the external cavity modes changes inversely. This, in turn, causes frequency mismatching and a less constructive interference between the emitted and reflected waves. If the mismatch is small enough, the laser will continue lasing on the same matched pair (blue arrow), but the laser may also begin emission on a neighbouring external mode, $M+1$ (green arrow). As the external cavity length continues to increase, the neighbouring mode $M+1$ will become the primary lasing mode. This effect has been demonstrated experimentally in Chapter 6, specifically in Fig. 6.6.

If in fact, L_{Ext} isn't close to an integer multiple of L, the resonant modes will be distributed as shown in Fig. 2.12(b). Assuming, at a particular external cavity length, there is a perfect mode match between modes M' and N' near the peak of the gain curve (red arrow); the laser will emit at this frequency. As the cavity length is changed, and mismatching of this pair occurs, matching of the neighbouring modes, M and N, improves and the laser emission frequency will change, jumping by an amount equal to the laser cavity mode separation. As the cavity length increases further, this will repeat with further jumps of the same separation due to the laser cavity mode separation until the oscillation frequency moves so far from the gain peak that it jumps back to a lower frequency match on the lower side of the gain peak. A similar effect can be achieved by changing the driving current of the laser which in turn changes the internal cavity spacing through a change to the emission frequency.

2.3 The effect of device resistance on V_{SM}

Previous SM theoretical models such as the Lang-Kobayashi model[105] and 3-mirror model[128,174] have been applied to describe the behaviour of SM in QCLs. These have shown good agreement with general SM behaviour; notably an increase in SM amplitude near the lasing threshold that then decays throughout the rest of the lasing range,[172] and variation of V_{SM} with laser frequency.[174] Nevertheless, there are effects that have been observed experimentally that aren't accounted for in these models.

One example of these existing models failing to reproduce experimentally-observed phenomena in THz QCLs under optical feedback, which has not been previously discussed, was observed during the work presented in this thesis. In particular, a dramatic increase in V_{SM} was observed at driving currents far beyond the laser threshold; specifically at driving currents where the device underwent a large change in differential resistance.

To experimentally measure the amplitude of V_{SM} across the operating range of a laser, the laser current can be stepped and a measurement of V_{SM} performed at each point. Here, this as accomplished by locking into a mechanical modulation of the laser light (as explained in Chapter 3.2.1) and maximising V_{SM} by matching the phase of the reflected and emitted waves by manually changing L_{Ext}.

The specific device used for this study was based on a 10 µm-thick BTC active region emitting at 2.53 THz ($\lambda \approx 119\,\mu\mathrm{m}$), which was processed into a SISP ridge waveguide with dimensions 2.4 mm × 150 µm. The device was cooled using a continuous-flow helium cryostat and maintained at a heat-sink temperature of 25 K. It was observed that for this device, when driven close to ∼935 mA, the subband re-alignment in the QCL caused a large change in voltage (∼500 mV) for a small current change (∼5 mA), resulting in a large change in differential resistance. At this operating point, it was also observed that V_{SM} dramatically increased by up to a factor of ×20. Figure 2.13 shows the mechanically modulated V_{SM} signal recorded with the device driven at the peak differential resistance (corresponding to a driving current of 934.4 mA), showing a V_{SM} of 139 mV RMS before any amplification. It is common to observe V_{SM} values on the order of a few mV with good alignment, but the phenomenon observed here significantly increased the signal beyond these typically observed values. The variation of V_{SM} across the full operating range of the device, as well as the I-V characteristic of the laser, are shown in Fig. 2.14. It can be seen that the peak in V_{SM} occurs at the same current as the abrupt change in device voltage.

By converting the I-V characteristic of the laser into a I-DR characteristic this correlation is even more apparent, as shown in Fig. 2.15. Here, at the point that the differential resistance increases (931 mA), V_{SM} starts to increase, peaking at the same current as the peak in differential resistance (935 mA). The second peak in V_{SM} at 943 mA also correlates to a peak in differential resistance, albeit a smaller peak.

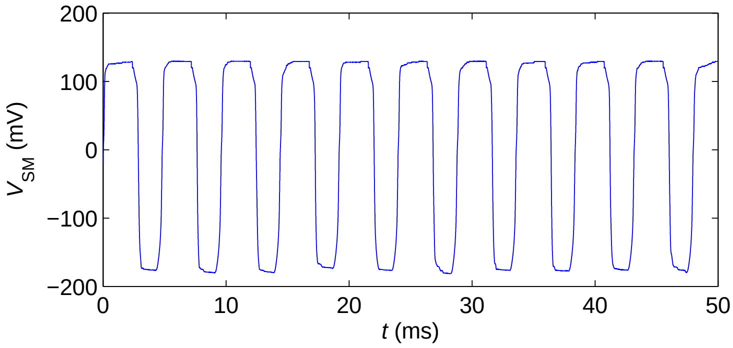

Figure 2.13: $V_{\mathrm{SM}_{\max}}$ RMS for the device (139 mV) was achieved at 934.4 mA where it was operating in a negative differential resistance (NDR) regime. This was measured using mechanical modulation as described in Chapter 3.2.1.

Previously reported SM models fail to account for this phenomenon. Typically[61,158] a linear relationship between the variation in V_{SM} and the variation in emitted power, P, is assumed

$$\Delta V_{\mathrm{SM}} \propto \Delta P, \tag{2.34}$$

where the emitted power is dependant on the SM phase such that

$$P(\tau_{\mathrm{Ext}}) = P_0[1 + m\cos(\tau_{\mathrm{Ext}})], \tag{2.35}$$

where m is an amplitude factor proportional to $\epsilon\sqrt{R_{2\mathrm{Ext}}}$. This assumption contradicts the enhancement of V_{SM} close to the threshold and what has been experimentally observed here.

Instead of using the traditional models (Lang-Kobayashi and the 3-mirror model) a density matrix model (DMM) can be used to simulate the device under feedback by accounting for subband alignment and photon-driven transport to describe the current transport in the device. Although the laser geometry is not considered in this model, the sensitivity to photon-driven transport is shown to be higher at the NDR region. Further description of this model can be found in Grier,[177] and is beyond the scope of this thesis; it is only reported to show comparison with experimental measurements here. In this way ΔV_{SM} is found to be non-proportional to ΔP. The SM voltage V_{SM} generated from

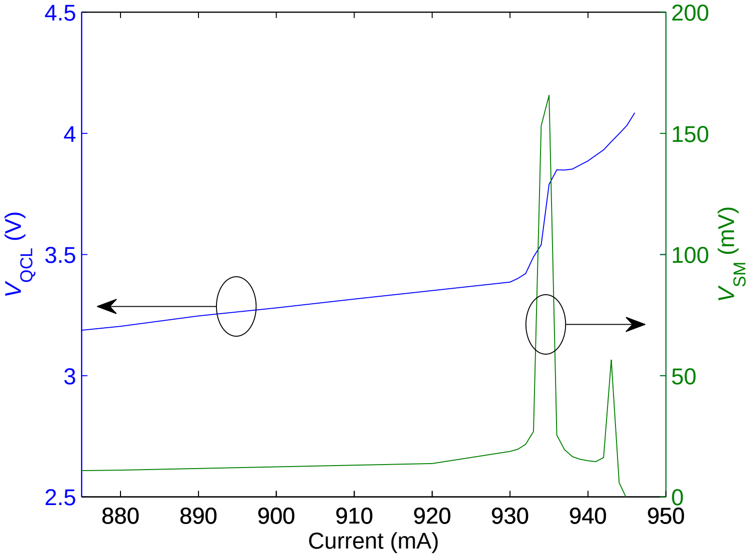

Figure 2.14: I-V and I-V_{SM} for a THz QCL. V_{SM} increases dramatically when the QCL reaches a region of large differential resistance at 935 mA bias.

the DMM is compared to the experimental measurement in Fig. 2.16 and shows good agreement.

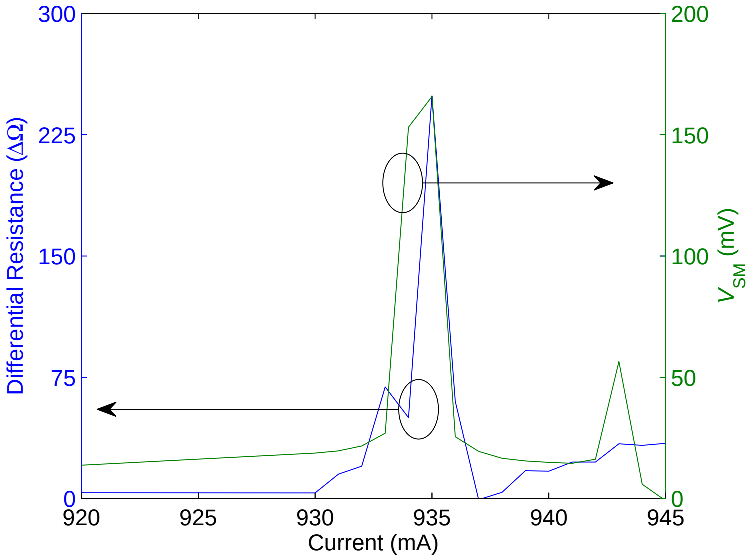

Figure 2.15: I-DR and I-V_{SM} for a THz QCL with a large NDR region.

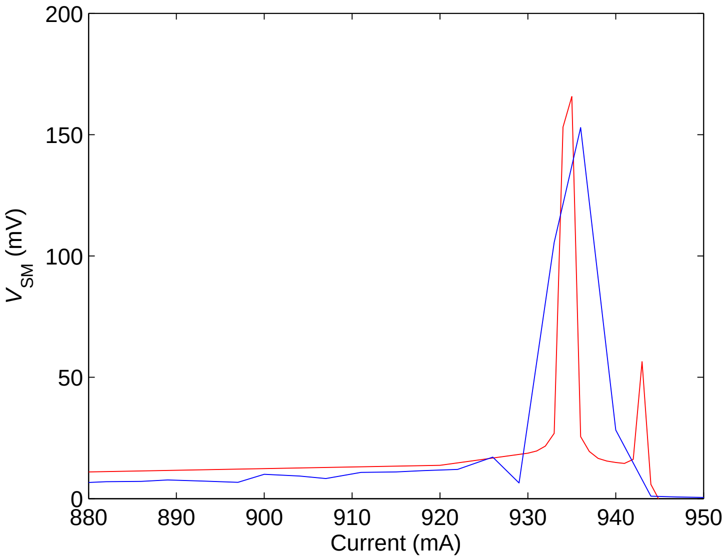

Figure 2.16: I-V_{SM} for a THz QCL. Both measured (red) and simulated (blue) waveforms show good agreement.

3 Two dimensional imaging

THz imaging systems have numerous potential applications including non-contact, non-destructive imaging of illicit materials,[10,49,178] biomedical imaging[12,54,119,179] and spectroscopic identification of optically identical or obscured substances.[7,38,46,64,180]. As such, one of the most basic functions required by most THz imaging system is the ability to perform two-dimensional (2D) imaging of targets. Generally this involves focusing the laser beam emitted from a THz source onto a point on a sample and collecting the radiation reflected-off or transmitted-through the sample. The sample can then be scanned orthogonal to the beam axis, creating a two-dimensional image. Image contrast arises due to spatial variation in the absorption, reflection and/or scattering properties of the sample. THz imaging has previously been demonstrated for both coherent and incoherent detection systems at a range of stand-off distances, imaging rates and resolutions and for many different types of samples;[46,68,181] see Chapter 1.3 for a more thorough history of THz imaging.

In this chapter, the characterisation of THz QCLs will be explained, and various methods of two-dimensional THz SM imaging will be demonstrated. 2D SM reflection imaging using both mechanical and electrical modulation schemes for the purposes of lock-in detection will be shown, as well as 2D imaging based on an apertureless near-field imaging scheme.

3.1 QCL characterisation and operation

In any laser imaging system, certain parameters of the laser source have to be known. In particular the relationship between the driving parameters of the source, the emission frequency and emitted power has to be characterised. General QCL characterisation can be summarised into three areas:

- Measuring the current-voltage relationship of the device.
- Measuring the relationship between driving conditions and emitted THz power.

- Measuring the relationship between driving conditions and emission frequency.

Measurements can be performed in two distinct modalities, firstly by biasing the QCL in a pulsed fashion where the device is only powered for a short period of time at a high repetition rate and secondly by powering the QCL in a continuous-wave fashion.

When the QCL is turned on, joule heating heats the device internally, which in turn degrades the power emitted from the device. By temporarily turning the QCL off the device has time to dissipate any heat generated during its 'on' period. This can be repeated at a high repetition rate ($> 100\,\text{kHz}$) to simulate quasi-continuous THz emission. In order to allow the device to cool sufficiently, the power is typically only supplied for a very small percentage of the time ($\sim 2\%$ duty cycle). This is shown in Fig. 3.1(a).

One disadvantage of operating a device in this manner is that the detectors used in THz measurements are generally thermal in nature and therefore operate too slowly to allow lock-in detection at such a high repetition rate. In order to allow lock-in detection, thereby improving the signal-to-noise ratio (SNR) of the measurement, the pulse-train powering the device is gated at a much lower frequency (typically ~ 167 Hz, the optimum response rate of the bolometer used in these measurements). This method is demonstrated in Fig. 3.1(b).

3.1.1 LIV measurement of a THz QCL

Due to their requirement for cryogenic cooling for operation, the QCL is mounted into a continuous flow, liquid helium (LHe) cryostat. In order to perform measurements at any temperature above the LHe base temperature ($\sim 4\,\text{K}$), a heater attached to the cryostat heat sink can be controlled using a proportional-integral-derivative (PID) temperature controller. Due to the potential loss of THz power through the atmosphere due to water absorption, in order to get an accurate measure of the emitted power from the device, the cryostat is mounted in a dry-nitrogen purged box and emission is coupled to a cryogenically-cooled bolometer using a pair of parabolic mirrors. A lock-in amplifier (LIA) measures the voltage signal produced by the bolometer in response to the amount

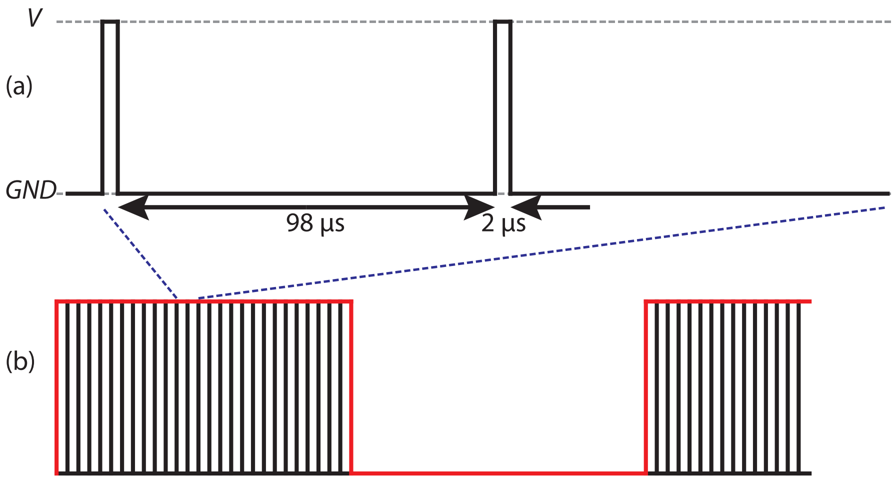

Figure 3.1: Driving a QCL in pulsed mode. (a) In pulsed mode, the QCL is driven for only a short percentage (2% here) of the time at a high frequency (10 kHz here) to reduce device heating. (b) This modulation can then be gated at a lower frequency to allow use with slow devices like bolometers.

of absorbed radiation. The gate-frequency of the driving pulses is used to synchronise the LIA. Using the set-up shown in Fig. 3.2, a LabVIEW program is run to measure the power-current-voltage (LIV) relationship of the QCL, through measurement of the bolometer voltage readout, driving current and terminal voltage of the device, respectively. This program allows the user to set the start, stop and step QCL driving currents for the measurement and controls the measuring process. The general process to gather the LIV data is shown in Fig. 3.3.

The measurement of power from the bolometer is qualitative, and therefore not an absolute value. In order to get an accurate measurement of the emitted QCL power the bolometer is replaced with a TK power meter once the full LIV measurement is complete. This sensor has a very slow response (many seconds) to get a power measurement, so a single measurement of power is taken at a single bias point. The voltage measurement from the bolometer is then scaled to give a real measurement of power over the entire operating range. A complete LIV for a 14µm-thick-BTC device of dimension 2.2 mm × 200 µm operating at ∼2.24 THz obtained using a combination of both of these techniques is shown in Fig. 3.4.

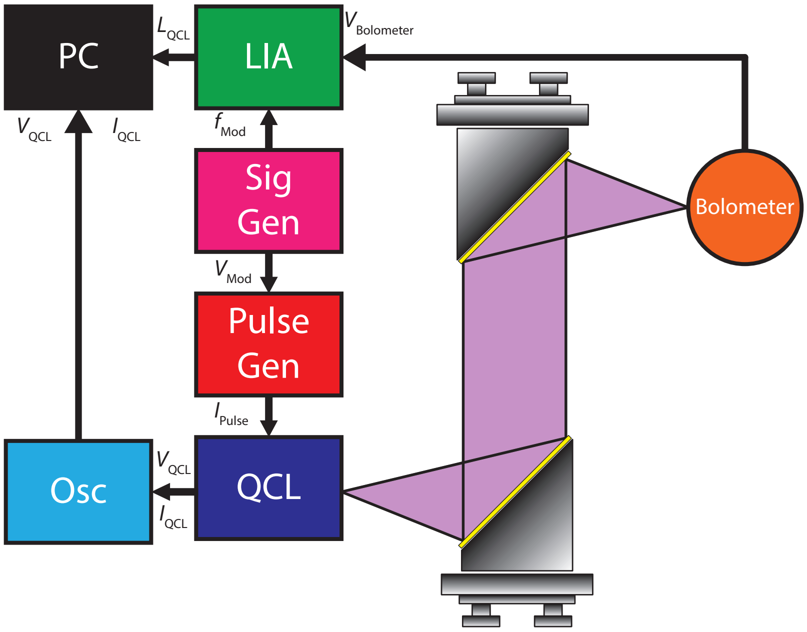

Figure 3.2: Schematic diagram of a QCL LIV characterisation under pulsed bias conditions. Control hardware includes a lock-in amplifier (LIA) to measure voltage output from the bolometer in response to the measured THz power, a signal generator (Sig Gen) and a pulse-generator (Pulse Gen) to drive the QCL in pulsed-mode, and an oscilloscope (Osc) to measure QCL drive current and terminal voltage.

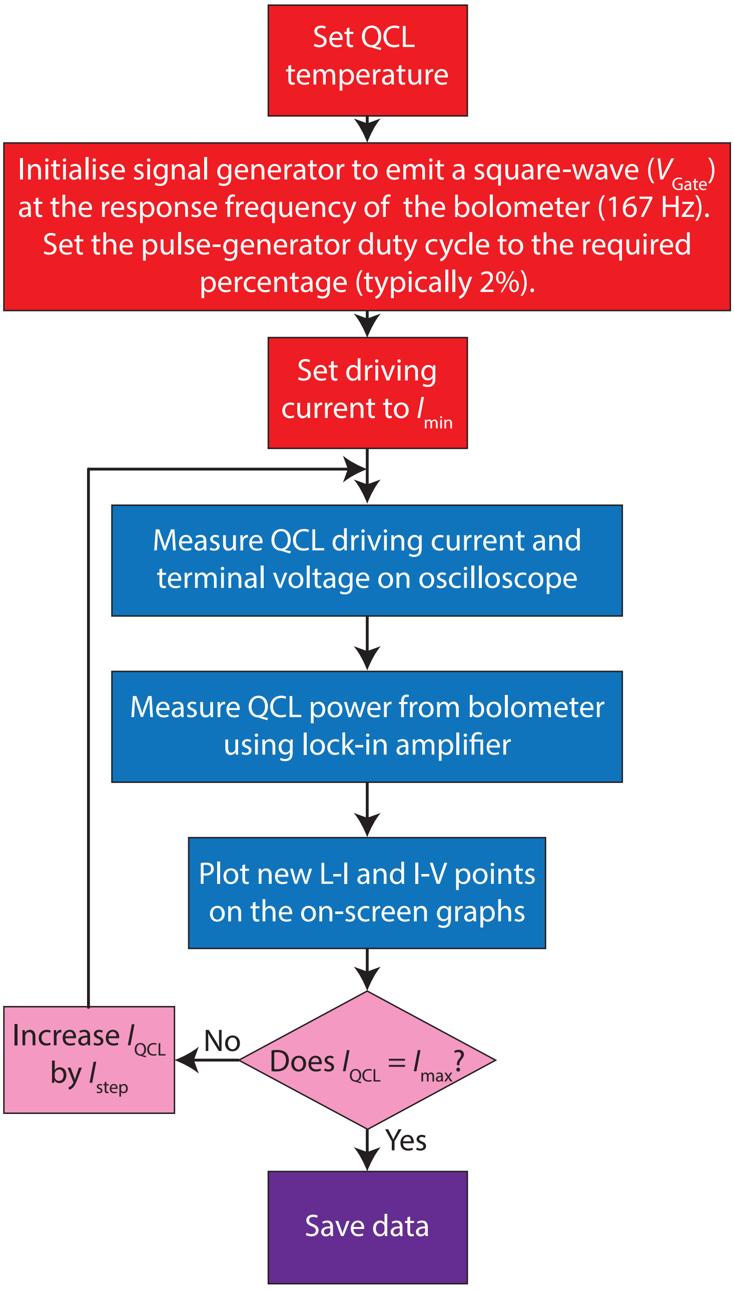

Figure 3.3: Schematic flow diagram of QCL pulsed characterisation.

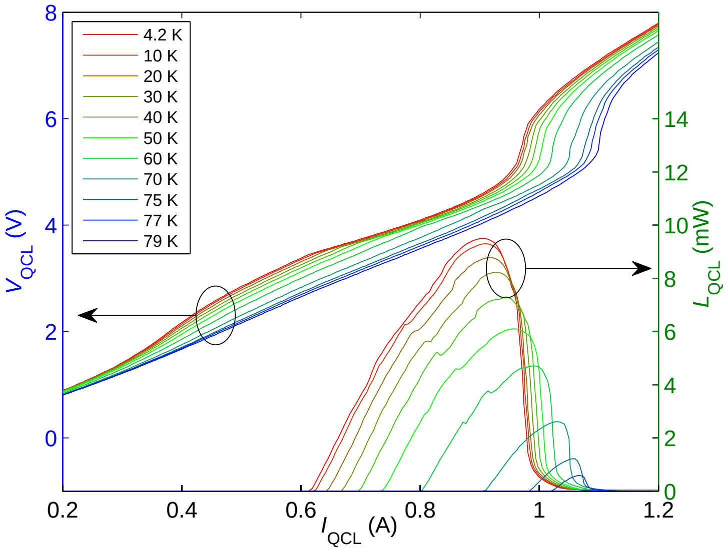

Figure 3.4: Measured LIV of a 14µm-thick-BTC device of dimensions 2.2 mm × 200 µm operating at ∼2.24 THz for various heat sink temperatures. The measurement was performed under pulsed operation using 2% duty cycle at a repetition rate of 10 kHz, gated at 167 Hz. Data gathered by Reshma A. Mohandas.

The duty cycle of the driving-pulses is then incrementally increased up to 95% (the maximum of the pulse generator) to see if the QCL can handle operation with minimal time to cool. If the QCL is still emitting under these driving conditions, continuous-wave (CW) measurements can be attempted which involve a slightly different electrical set-up and controlling LabVIEW program. In order to characterise a QCL under CW operation, a DC power supply must be used instead of the pulse-generator, and electrical gating cannot be used as this would negate the CW nature of the measurement. For CW measurements the THz beam is optically modulated with a mechanical chopper to provide a synchronisation frequency for the LIA. The experimental set-up is shown in Fig. 3.5 and the measurement procedure is very similar to that of the pulsed-measurement, as shown in Fig. 3.6. The CW LIV for the same laser as above is shown in Fig. 3.7.

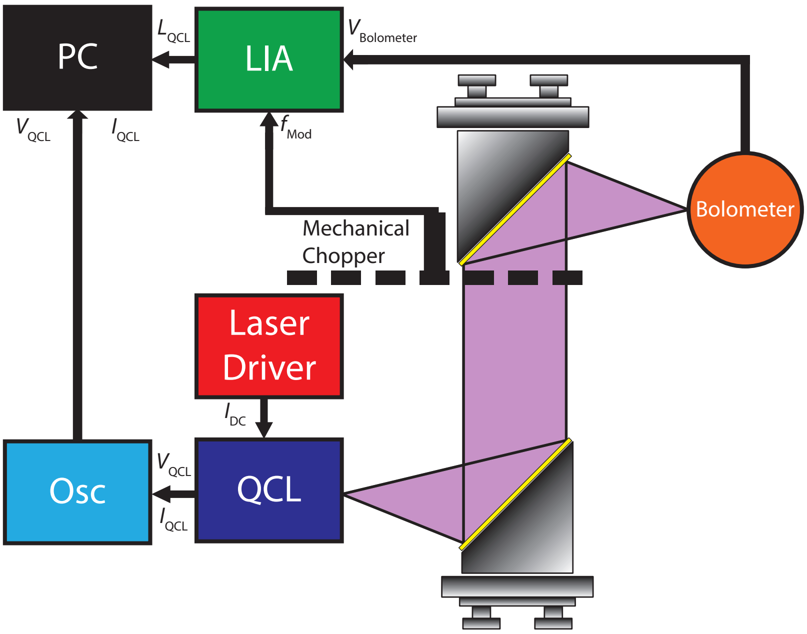

Figure 3.5: Schematic diagram of a QCL LIV characterisation under continuous-wave driving conditions. Control hardware includes a lock-in amplifier (LIA) to measure voltage output from the bolometer in response to the measured THz power, a DC laser driver to drive the QCL and an oscilloscope (Osc) to measure QCL drive current and terminal voltage. A mechanical chopper provides a modulation frequency to synchronise the LIA.

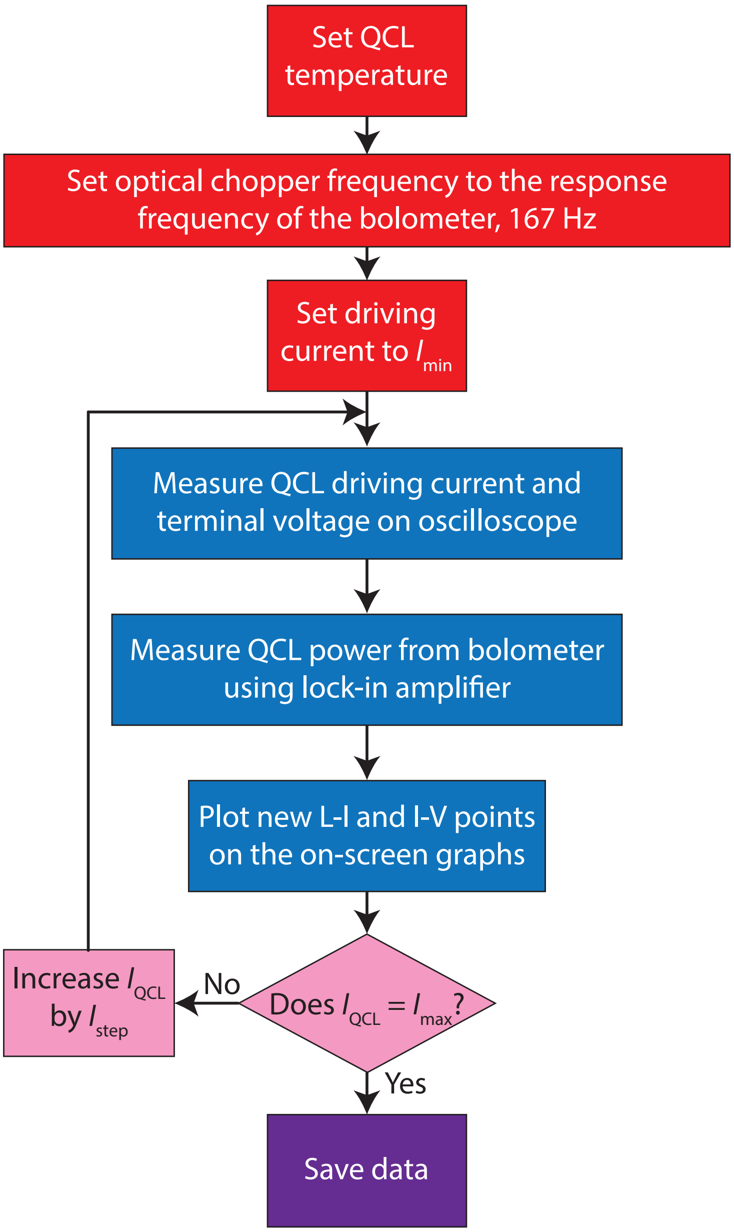

Figure 3.6: Schematic flow diagram of QCL CW characterisation.

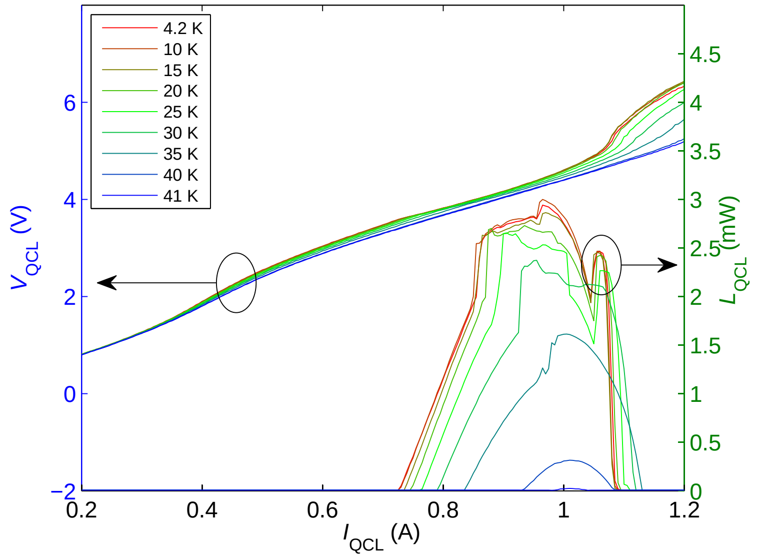

Figure 3.7: Measured LIV of a 14 µm-thick-BTC device of dimensions 2.2 mm × 200 µm operating at ∼2.24 THz at various heat sink temperatures under continuous-wave operation. Data gathered by Reshma A. Mohandas.

3.1.2 Spectral measurement of a THz QCL

Once the electrical and optical properties of the QCL are known, the spectral properties can be examined. The emitted THz power for a particular driving current was measured during the LIV measurement, but this doesn't tell us anything about what frequency the QCL is emitting at or if the device is emitting at single or multiple frequencies.

To measure the spectral emission from the THz QCL, a Fourier-Transform Infrared (FTIR) Interferometer can be utilised. An FTIR is based on a Michelson Interferometer,[182] in which the emission from the laser is split along two paths, a stationary reference path and a path with variable length. These two beams are recombined at the detector where they interfere, resulting in interferometric fringes as the variable path length is changed. This system is shown in Fig. 3.8.

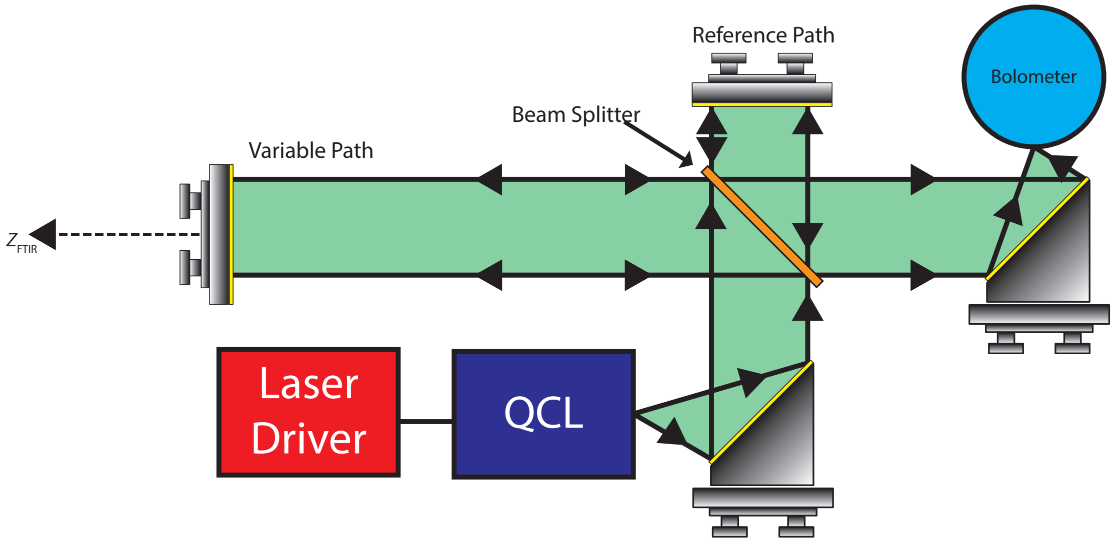

Figure 3.8: Schematic experimental set-up to measure the emission spectra of a QCL.

By performing a Fast Fourier Transform (FFT) on the extracted interferometric fringes it is possible to recover the emission spectra based on the spatial frequency and amplitude of the fringes, as shown in Fig. 3.9.

This can be performed under both pulsed and continuous-wave operation of the device. A Bruker FTIR (Model number: IFS-66) is used to measure the spectral response over

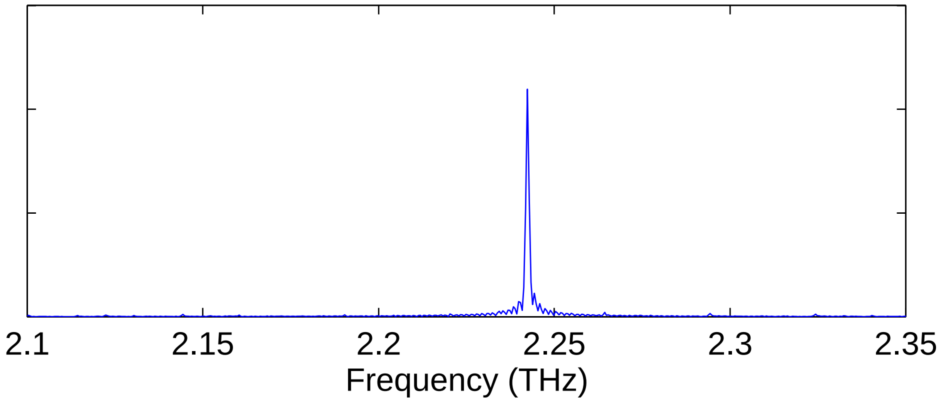

Figure 3.9: Spectrum of a 14µm-thick-BTC device of dimensions 2.2 mm × 200 µm operating at ∼2.24 THz driven under CW conditions at 800 mA obtained using an FTIR.

the operating range of the QCL. The procedure for measuring the spectra of a device involves aligning the QCL through the FTIR in order to give the maximum signal at the bolometer, signifying optimum alignment. Once a driving current and temperature is set, an FTIR scan is performed by extending the variable path length and recording the bolometer output throughout the range of movement. On the interferometric fringes obtained in this way, an FFT is performed to convert the data recorded in the time domain into the frequency domain, resulting in a plot of the emission spectra of the QCL at that particular driving condition. This can be repeated for a range of driving currents and heat sink temperatures in order to quantify the spectral response of the device throughout its range of operation.

The spectral properties of the QCL are of particular importance to SM measurements, and it is often desirable to operate the QCL under conditions that produce single-mode emission. This measurement procedure allows suitable operating conditions (driving current, heat sink temperature) to be identified.

3.2 Two-dimensional THz imaging based on self-mixing

Once the electrical and optical properties of the THz QCL are known, the device can be used for experiments such as imaging, as explained at the beginning of this chapter. A typical THz reflection imaging set-up is shown in Fig. 3.10 where the THz radiation emitted from a QCL is collected and focused by a pair of parabolic mirrors onto the sample surface (a scalpel blade here). Upon contact with the sample, the THz radiation is reflected or scattered and is collected by another pair of mirrors and coupled into a detector such as a bolometer.Depending on the sample under investigation, the reflected/scattered power can be small (∼nW). To enable lock-in detection the THz signal must be modulated at a known frequency. Mechanical modulation, as shown in Fig. 3.5, is an example of this.

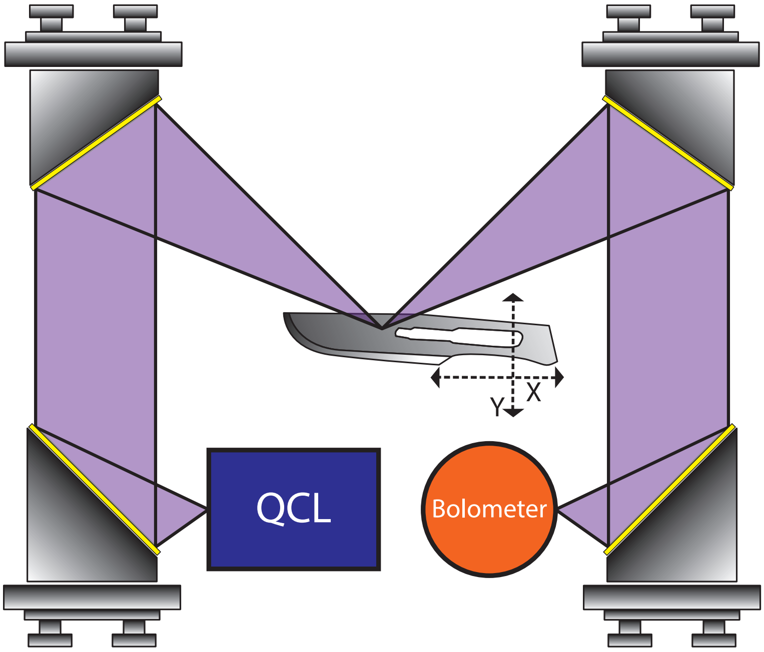

Figure 3.10: Generic THz reflection imaging set-up.

The focal point of the THz beam on the sample can be thought of as one pixel, and the sample is mounted on an electronically controlled mechanical translation stage in order to raster-scan the sample in two dimensions to build up an entire matrix of pixels to form an image.

Two-dimensional (2D) imaging based on the SM technique takes this experimental arrangement and greatly simplifies it. By removing the external detector, the collecting parabolic mirrors can also be removed. In this case the sample can simply be reorientated to reflect the THz field back into the QCL facet, as shown in Fig. 3.11. Reflected radiation is measured as a perturbation to the QCL terminal voltage using a LIA in order to increase SNR.

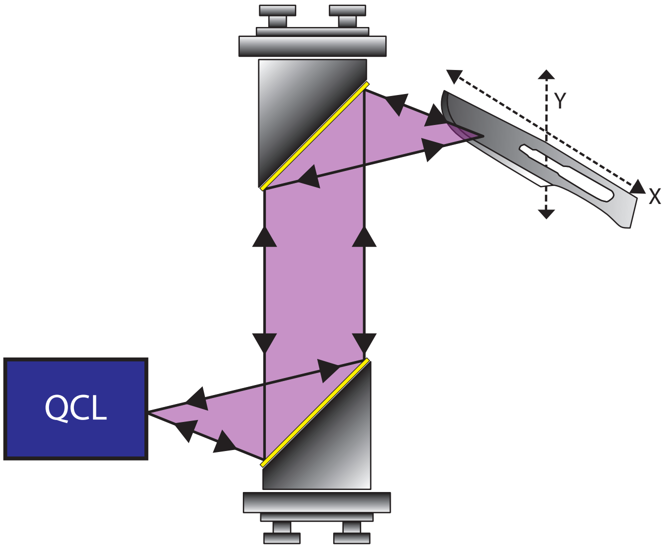

Figure 3.11: Schematic of a 2D reflection imaging system based on self-mixing.

This set-up has the advantages of being more experimentally compact and having a reduced cost when compared to the previous set-up. Also, this system is sensitive to the surface morphology of the sample due to the coherent nature of self-mixing. By removing the slow, thermal detection methods commonly used in 2D reflectance imaging, an SM approach has the potential to image at a higher acquisition rate as the sensing time of the phenomenon is only limited by the relaxation time of the QCL, which is on the order of ~ps.

A crucial aspect of these imaging experiments is the form of modulation applied to allow LIA detection of the SM voltage signal. Two methods will be discussed in the following sections.

3.2.1 Self-mixing imaging based on mechanical modulation

As with bolometric detection, 2D imaging systems based on SM can utilise lock-in detection to maximise its sensitivity to small signals. A modulation technique is any method that can be used to periodically vary the THz power reaching the detector (the emitting and detecting QCL in the case of SM) at a known frequency. A reference signal at this frequency can then be used as a reference for a LIA in order to distinguish the THz radiation emitted from the QCL from other background radiation that could otherwise also be measured by the detector. In this way, measurement noise can be reduced. Two methods of modulation for the purpose of lock-in amplification will be discussed in the following chapters; mechanical and electrical modulation (see Chapter 3.2.2).

3.2.1.1 Experimental set-up & measurement technique

The THz QCL used for the following measurements consisted of a $10\,\mu$m-thick bound-to-continuum active region[183] emitting at $\sim$2.65 THz ($\lambda \approx 113\mu$m), which was processed into a semi-insulating surface-plasmon (SISP) ridge waveguide with dimensions of $3\,\mathrm{mm} \times 140\,\mu$m. The device was cooled using a continuous-flow helium cryostat and maintained at a heat-sink temperature of 25 K. The threshold current at this temperature was 1000 mA. For this experiment a current source was used to drive the QCL just above its lasing threshold, I_{TH}, at 1050 mA where it is most sensitive to the SM phenomenon.[65] A pair of 2-inch-diameter $f/2$ parabolic mirrors focused the THz beam onto a point on the sample surface. The spot size of the focussed beam in this system is typically $\sim$250 μm in diameter.[65] The external cavity length was 0.41 m through an unpurged environment. A mechanical chopper was used to modulate the THz beam at a frequency f_{Mod}. The sample (a scalpel blade) was raster-scanned using computer-controlled mechanical translation stages perpendicular to the beam in both X- and Y-directions at the focus and the terminal voltage of the QCL was measured by a LIA synchronised to f_{Mod}. Due to the small V_{SM} signal, a $6\times$ differential amplifier was used to amplify the signal into the LIA. A schematic set-up of this experiment is shown in Fig. 3.12.

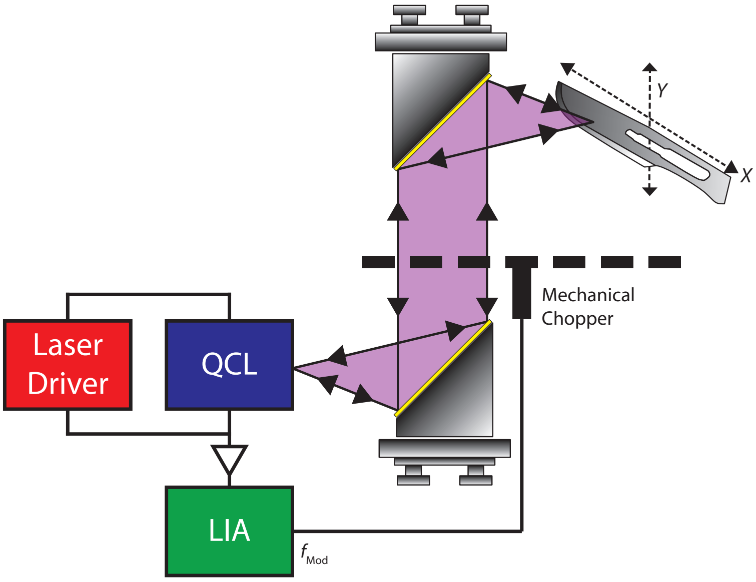

Figure 3.12: Schematic diagram of the experimental apparatus used for mechanical modulation 2D imaging measurements.

3.2.1.2 Mechanical modulation

Mechanical modulation describes the action of using a physical source to block and unblock the THz radiation at a known frequency. To this end, a mechanical chopper is placed with it's blades in the THz beam.

When the chopper is in the open position, as shown in Fig. 3.13(a), the THz beam is able to travel past the blades to the external reflector. Upon reflecting the beam travels back through the open chopper to the laser facet and causes a change V_{SM} to the terminal voltage. When the chopper rotates into the closed position, as shown in Fig. 3.13(b), the THz beam hits the chopper blade and reflects away from the QCL facet due to the angle of the blade. This stops the radiation reaching the facet and prevents any SM effect. The terminal voltage of the QCL returns to the unperturbed QCL voltage, V_{QCL}. In order to minimise transient time where the blade is only partially obscuring the field, the chopper is typically placed close to the focus of the beam.

As the QCL terminal voltage oscillates between V_{QCL} and $V_{\mathrm{QCL}}+V_{\mathrm{SM}}$ at the frequency of the mechanical modulation, a LIA can amplify the signal at this frequency

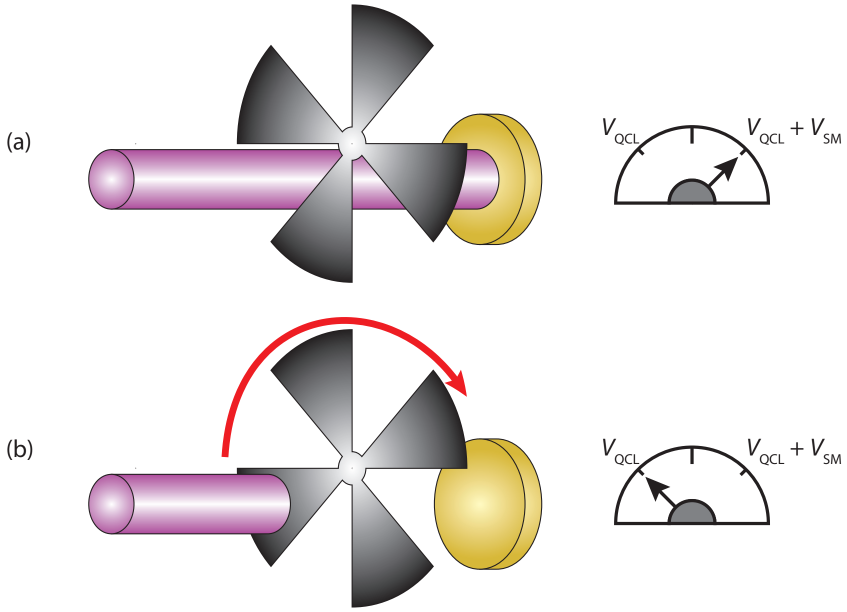

Figure 3.13: Mechanical modulation of a SM THz system.

allowing detection of small voltage changes on the QCL terminal voltage even when the change (V_{SM}) is orders of magnitude smaller (normally $\sim$ µV, but can be $\sim$mV depending on device differential resistance) than the unchanging unperturbed terminal voltage ($\sim$5 V). Exemplar data recovered using mechanical modulation of shown in Fig. 3.14.

As the LIA measures differential change, the actual terminal voltage isn't measured here; only the small change in voltage due to the modulated feedback V_{SM}. This allows the sensitivity of the LIA to be adjusted to give much more accurate measurement of the voltage changes caused by self-mixing.

3.2.1.3 Experimental procedure

Self-mixing arrangements need an external target to reflect radiation back into the laser facet. The target is first roughly positioned at the beam focus and aligned roughly perpendicular to the beam axis giving a self-mixing signal that is detectable on the LIA. This signal will be related to both the sample reflectivity and distance from the laser, as given by Eq. (2.24). A fast, broad-area scan with large ($\sim$1 mm) pixels is then used to determine the optimum scan area of the X and Y translation stages. By producing low

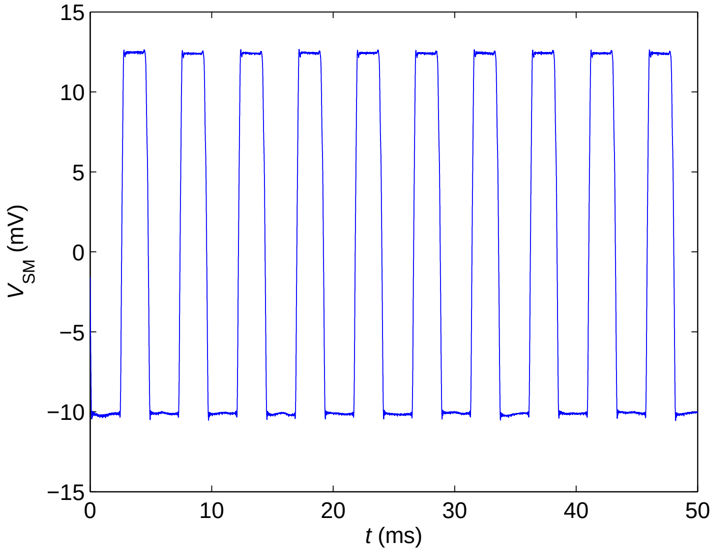

Figure 3.14: Exemplar data gathered using mechanical modulation.

resolution images in this way, the acquisition time is dramatically reduced when compared to high resolution (e.g. $0.25 \times 0.25\,\mathrm{mm}$ pixel) images. As long as the time constant (TC) of the LIA is kept above the modulation time of the modulation technique, it can also be reduced to further speed up image acquisition. Doing so will increase noise in the image, but for alignment purposes this isn't a problem. An example of an initial low-resolution image acquired for alignment purposes is shown in Fig. 3.15. All images in the experimental procedure section here were acquired with mechanical modulation. When the sample is positioned outside of the beam spot, the THz radiation isn't reflected back into the laser facet and SM doesn't occur. Here the terminal voltage will equal V_{QCL}, and the self-mixing voltage measured by the LIA will equal $\sim 0\,\mathrm{mV}$, which will be represented as the background (dark blue) shown in the image.

As self-mixing systems are coherent by nature, the distance between the laser facet and sample surface affects V_{SM}, as described in Eq. (2.24). This means that if translation of the sample in the X-Y plane causes a change in external cavity of $\lambda/2$ or greater, the self-mixing signal will change through minima and maxima along the sample surface. With a flat sample, orientated perfectly perpendicular to the THz beam the entire image will exhibit the same measured SM voltage, assuming the sample reflectivity remains constant

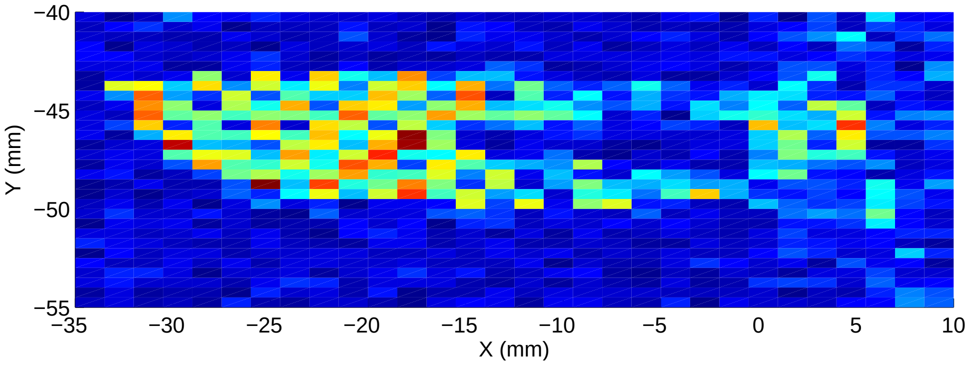

Figure 3.15: 2D THz SM image gathered at low resolution ($1.5 \times 0.5\,\mathrm{mm}$) for the purpose of alignment.

across the surface. However if the sample is orientated such that the external cavity changes by $> \lambda/2$ through translation of the sample in the imaging plane, an interference pattern will appear across the image. This pattern can be seen on the tilted sample shown in Fig. 3.16. As the sample becomes more perpendicular to the THz beam the fringes separate and become broader along the surface. These fringes can occur in both vertical- and horizontal-directions where vertical fringes indicate a tilt across the sample horizontally, and horizontal fringes indicate the sample having a vertical tilt.

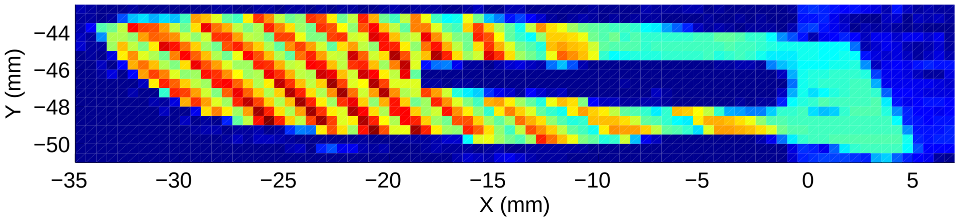

Figure 3.16: 2D THz SM image. Interferometric fringes along flat portions of the sample indicate a tilt in the sample away from the laser.

This phenomenon also means that for samples that aren't perfectly flat, the surface morphology of the sample can be resolved, where even surface depth changes $< \lambda/2$ can be resolved as a change in V_{SM}. This can be exploited to perform three-dimensional imaging of samples, as described in Chapter 4. The depth angle of the sample can be slightly altered by means of the sample holder jog-dials, such that the sample can be brought to a more perpendicular orientation to the imaging plane. As the sample gets brought closer to the optimum imaging plane in each dimension, the fringes relating to the cavity length in that dimension will broaden. A scalpel blade that has had tilt minimised along both directions is shown in Fig. 3.17.

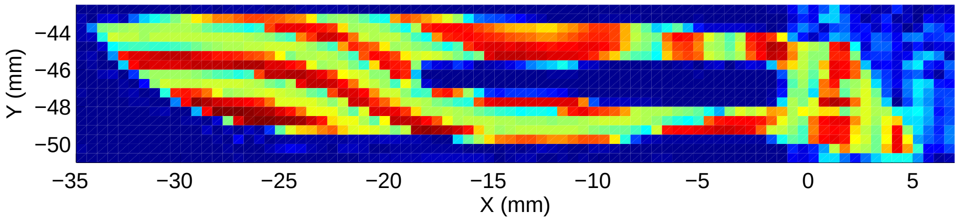

Figure 3.17: 2D THz SM image after sample tilt has been optimised showing broader fringes arising from the surface morphology of the blade.

From this image an estimation of the change in cavity length across the surface of the scalpel blade can be taken as approximately $3\times\lambda/2$ which is $\sim$ 150 µm. Once this low resolution scan shows a good representation of the sample and any tilt has been suitably reduced, a high resolution (0.25 × 0.25 mm) scan can be taken, as shown in Fig. 3.18.

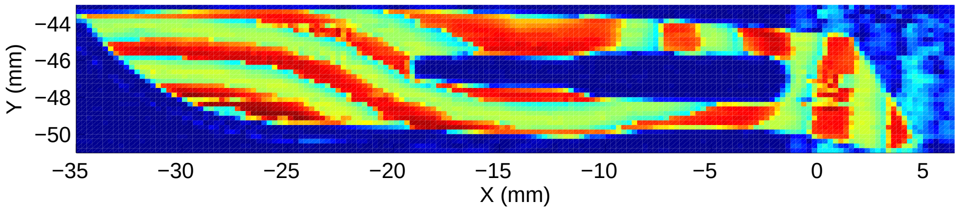

Figure 3.18: 2D THz SM image gathered at high resolution (0.25 × 0.25 mm).

Once a high resolution scan has been obtained, the sample may still not be perfectly aligned at the focus of the THz beam, at which position the best resolution will be achieved. Repeated scans can be taken with the external cavity length varied slightly to obtain as sharp an image as possible. As the cavity length, L_{Ext}, changes, the positions of the observed fringes will also change as given by Eq. (2.24). This is demonstrated in Fig. 3.19.

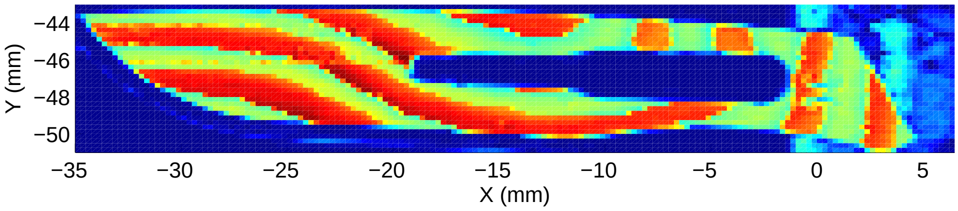

Figure 3.19: 2D THz SM image gathered at high resolution (0.25 × 0.25 mm). The distance between the sample and laser has been changed by $\Delta L_{\mathrm{Ext}} \approx \lambda/2$ from Fig. 3.18.

3.2.1.4 Discussion & limitations of mechanical modulation for 2D imaging

Figure 3.20 shows an exemplar two-dimensional image of a scalpel blade taken using the above set-up using a modulation frequency of 200 Hz and a time constant of 50 ms.

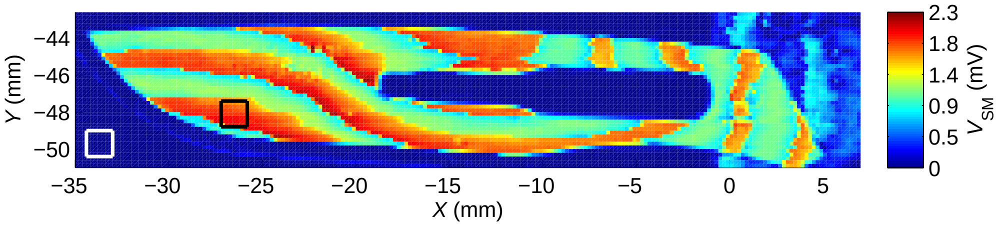

Figure 3.20: 2D SM image taken with mechanical modulation. White and black areas used for analysis of the figure of merit.

Due to the nature of mechanical modulation only the small change in voltage due to the modulated feedback is measured by the LIA. This means that the sensitivity (and hence dynamic range) of the LIA can be adjusted to provide the most accurate analogue-to-digital (ADC) conversion of the signal. The LIA used in these measurements had a 15-bit ADC, so with a sensitivity setting of 5 mV (giving a maximum measurable signal of 15 mV) changes of 458 nV were distinguishable in principle, but other noise sources degrade this value. Other sources of noise within the system will include voltage noise from the laser driver and noise developed through thermal fluctuations in the laser. These voltage noise components will also translate to frequency drift within the device, leading to further voltage noise at the laser terminals. The LIA will also have a degree of electrical noise from the mains. A study of the signal-to-noise ratio (SNR) of this measurement is presented below.

As a measure of the quality of the images this method produces, a figure of merit (FOM) for the images can be calculated. To do this, the average signal sampled from areas of both the peak of the SM fringes on the foreground, and the background of the image are calculated, as well as the standard deviation of the signal within those areas. The figure of merit of the image can then be defined as[158]

$$FOM = \frac{\overline{V_{\mathrm{SM}}} - \overline{V_{\mathrm{QCL}}}}{\sigma_{V_{\mathrm{QCL}}}}, \tag{3.1}$$

where V_{SM} is the area with the maximum average SM voltage (black square), V_{QCL} is an exemplar background area (white square) and $\sigma_{\mathrm{V_{QCL}}}$ is the standard deviation of the chosen background area. In order to ensure the foreground region corresponds to the maximum measured signal, the image is raster scanned in post-processing to determine the square of 7×7 pixels giving the largest mean value.

Using the above equation and image, the foreground has a mean value of 1.79 mV, the background has a mean value of 19.3 µV and standard deviation of 3.7 µV. This results in a FOM of 477. This value will be compared with values obtained using electrical modulation techniques in Chapter 3.2.2.

Another method to quantify the modulation scheme is to perform a study of the signal-to-noise ratio (SNR) and dynamic range (DR) of measurements obtained with mechanical modulation as a function of modulation frequency. In order to measure the SNR, V_{SM} was first measured at a particular modulation frequency, then the THz beam was blocked and V_{SM} was measured again to provide a background measurement, V_0. The laser terminal voltage was measured for a period of 10 seconds with a LIA TC of 5 ms, storing every second sample, resulting in 1000 samples for each modulation frequency. This was repeated for various modulation frequencies between 15 and 225 Hz. The SNR and DR of the technique can be established using the equations

$$SNR = \frac{\overline{V_{\mathrm{SM}}} - \overline{V_0}}{\sigma_{V_{\mathrm{SM}}}}, \tag{3.2}$$

$$DR = \frac{\overline{V_{\mathrm{SM}}} - \overline{V_0}}{\sigma_{V_0}}, \tag{3.3}$$

where $\overline{V_{\mathrm{SM}}}$ is the mean SM signal, $\overline{V_0}$ is the mean differential terminal voltage without feedback and $\sigma_{V_{\mathrm{SM}}}$ and σ_{V_0} are their respective standard deviations over the full sample range. The results of this are shown in Fig. 3.21(a) and 3.21(b).

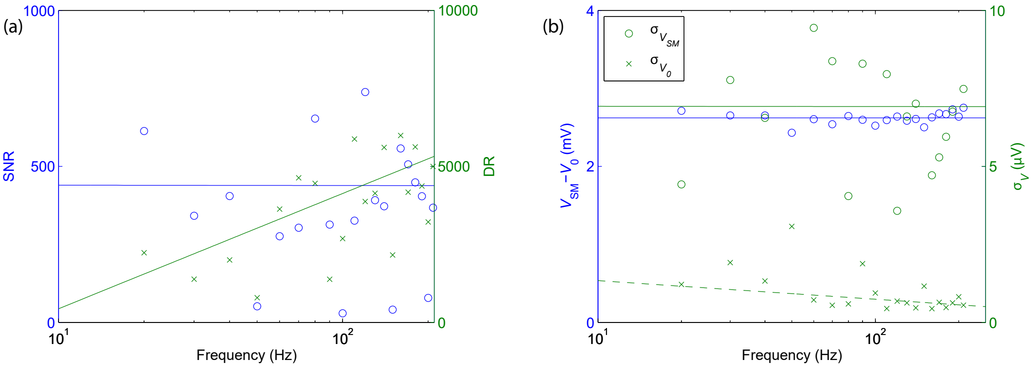

Figure 3.21: SNR and DR measurements for mechanical modulation. (a) Signal-to-noise ratio and dynamic range measurements for mechanical modulation. DR increases with frequency due to a loss of $1/f$ noise, but due to a larger thermal noise component under feedback SNR remains ∼450. (b) V_{SM} remains constant throughout the measurement range. The standard deviation of the background noise, σ_{V_0}, is shown to reduce with frequency as a reduction of 1/f noise. $\sigma_{V_{\mathrm{SM}}}$ does not decrease with frequency. Fitted lines added to guide the eye.

In Fig. 3.21(b) the SM voltage can be seen to remain constant throughout the measurement range as expected, as the high frequency limit of the laser driver is not reached at the modulation frequencies possible from the chopper. At lower modulation frequencies, more mechanical noise would be expected from the chopper resulting in a larger standard deviation which in turn degrades the SNR and DR. As the TC of the LIA is kept constant the measurement bandwidth stays fixed, but through increasing the modulation frequency, the centre frequency of the measurement band is moved away from the noise sources mentioned above that are more prevalent at lower frequencies. This can be seen in Fig. 3.21(b) as a reduction in the standard deviation of V_0 as the modulation frequency increases. During the measurement of the standard deviation of the voltage with feedback, $\sigma_{V_{\mathrm{SM}}}$, thermal fluctuations appear to have resulted in a higher degree of noise. Due to this higher magnitude, any improvement in SNR due to a higher modulation frequency is not visible. As neither the SNR nor DR have reached a peak at the maximum modulation frequency of 225 Hz, one would expect further improvement if higher mechanical modulation frequencies were possible.

In an effort to quantify the noise equivalent power (NEP) under mechanical modulation, measurements were performed where V_{SM} was recorded under feedback as the external cavity was changed in order to create interferometric fringes which were sampled using the LIA. This was repeated for varying levels of attenuation in the external cavity and the attenuation was increased until no THz was fed back into the device and self-mixing no longer occurred. As more attenuation was added, the LIA sensitivity could be increased as the overall measured signal reduced. SM fringes for two different double-pass levels of attenuation, 0 and 74.5 dB, are shown in Fig. 3.22.

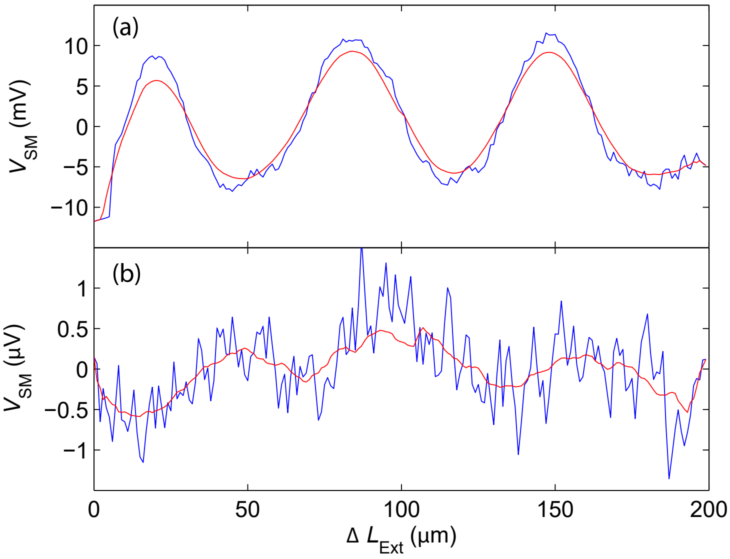

Figure 3.22: SM fringes measured under mechanical modulation for (a) 0 and (b) 75 dB double-pass attenuation with LIA sensitivities and TCs of (a) 10 mV and 500 ms and (b) 2 μV and 2 s. The recorded data (blue) has been smoothed (red) for clarity.

In order to quantify the attenuation of the attenuators used, the QCL power was measured with zero attenuation and with each attenuator between it and a TK power meter. The double-pass level of attenuation at the point where SM was observed but attenuation was at its maximum was calculated to be 74.5 dB, meaning that changes as small as 561 fW of power are measurable using this technique. This value was calculated from the known emission power of 15.7 µW during the measurement with 74.5 dB of attenuation when interferometric fringes were still observable.

3.2.2 Self-mixing imaging based on electrical modulation

As discussed in the previous chapter, one of the major limiting factors of using mechanical modulation is the inherently low modulation frequency which limits the image acquisition speed, SNR and DR. In an attempt to improve image acquisition speed from that of mechanical modulation, the physically moving components can be removed. By instead modulating the device electrically the mechanical chopper can be taken out of the system, and the THz power can still be modulated to allow lock-in amplification.

In the previous mechanical modulation technique, the device output is kept stable and the THz power is blocked from returning to prevent feedback at a known frequency. In contrast to this, in order to electrically modulate the THz QCL, the device lasing is actively modulated at a known frequency. The device is driven below threshold and a square-wave is employed to periodically drive the current above threshold. In this way, the electrical modulation switches the SM effect in a way analogous to the mechanical chopper. The TTL signal of the modulating waveform is used as the LIA trigger. This method allows the device to be modulated at a much higher frequency (> 100 kHz), as is shown in Fig. 3.23 where the device only lases when the drive current, I_{QCL}, is greater than the threshold current, I_{TH}.

3.2.2.1 Experimental set-up & measurement technique

Similar to the mechanical modulation method of two-dimensional imaging, a LIA was used to recover the QCL voltage at the modulation frequency. Unlike in the previous method however, as the LIA measures the change in V_{QCL} at the reference frequency, the LIA measures the combined voltage change due to the square-wave current modulation and also that caused by feedback. The sensitivity of the LIA is limited to the amplitude of

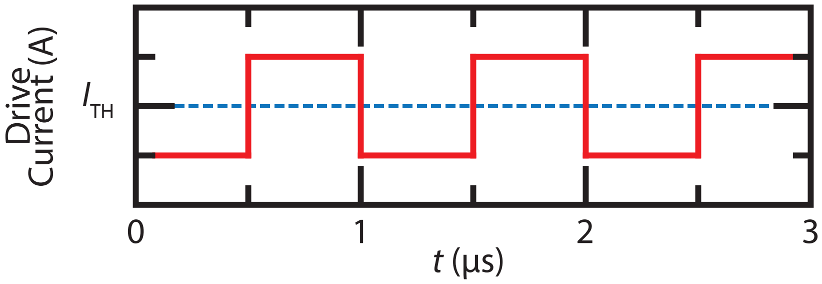

Figure 3.23: Electrical modulation technique. The QCL is biased below its threshold current, I_{TH}, and a modulation is then applied to drive the QCL into the lasing regime.

the change being measured, so in order to optimise sensitivity of the LIA, the change in voltage due to the current modulation must be minimised relative to the change due to feedback. To this end, the device was DC biased just below threshold at 975 mA, with a small (75 mA) square-wave modulation applied onto this to drive the device into a lasing regime where it is most sensitive to the self-mixing effect. In order to modulate the QCL by 75 mA, a 375 mV modulation signal is supplied to the laser driver that has a current/voltage gain of 0.2 A/V. The previous experimental set-up was therefore slightly adapted to include a signal generator to create the square-wave used for modulation and the LIA trigger. The modified set-up is shown in Fig. 3.24.

Using this scheme, the measured differential voltage is the sum of both V_{SM} and V_{Mod} and is on the order of ~75 mV. In order to extract the value of V_{SM} from this, V_{Mod} must be removed. To measure V_{Mod} the THz beam is blocked to prevent the self-mixing effect, and multiple pixels are measured to allow averaging of V_{Mod}. With no feedback, the measured voltage will only have a contribution from V_{Mod} and can be removed from V_{QCL} during the analysis stage to leave the small V_{SM} signal.

3.2.2.2 Discussion & limitations of electrical modulation for 2D imaging

Figure 3.25 shows a 2D image acquired using electrical modulation at the same conditions as Fig. 3.20 (where possible); 200 Hz modulation and 50 ms TC. Due to the nature of electrical modulation with lock-in amplification, where the LIA also measures the change in

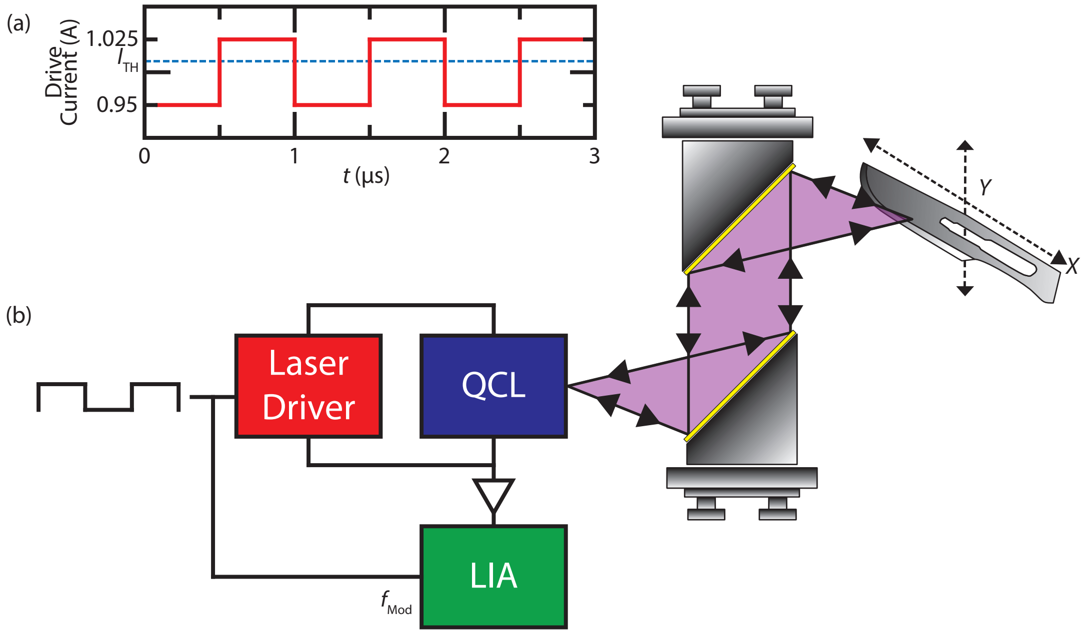

Figure 3.24: Schematic diagram of the experimental apparatus used for electrical modulation 2D measurements. (a) A square-wave modulation is applied to the sub-threshold driver current to drive the QCL just above I_{TH} and into the lasing regime. (b) The frequency of the electrical modulation (f_{Elec}) is used to synchronise a lock-in amplifier to measure the QCL voltage. A pair of parabolic mirrors focus the QCL beam to a point, at which the sample is raster scanned using computer controlled mechanical translation stages.

voltage due to the modulation scheme itself, the LIA sensitivity was dramatically increased (50 mV) from that used for mechanical modulation (5 mV). The figure shows that a similar value for V_{SM} was obtained; 1.46 mV, compared to 1.77 mV for mechanical modulation. However a much higher standard deviation on the background voltage is observed in this case 40.3 μV compared to 3.7μV. Indeed, significant noise can be observed in the background region of Fig. 3.25. The reason for this is unclear, but could be due to electrical noise associated with the current driver. An alternative explanation is noise arising from the feedback of radiation due to reflection from the cryostat window. The effect of such feedback would not be recovered by the LIA in the case of mechanical modulation, since the chopper is positioned externally to the cryostat in that case. Also, the oscillation of the driving current of the QCL may also translate to thermal fluctuations within the device. Both these current and thermal changes would cause frequency drift leading to voltage fluctuations. Due to the impact of the larger noise value, the FOM for this image is only 36, compared to 477 in the previous modulation scheme.

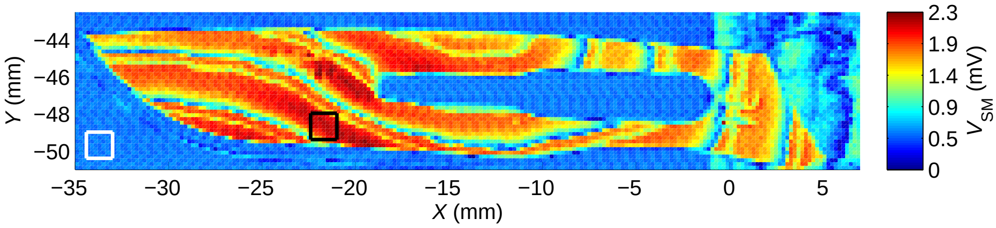

Figure 3.25: 2D SM image taken with electrical modulation under the same conditions as Fig. 3.20, 200 Hz modulation and 50 ms TC. White and black areas used for analysis of the figure of merit.

A major advantage of electrical modulation is that by removing the mechanical components of the modulation scheme, the modulation frequency could rise dramatically. In the previous technique the mechanical chopper maximum rotation speed limited the frequency that the THz beam could be modulated to ∼200 Hz, but by implementing this new scheme the laser can be modulated at much higher frequencies, beyond 100 kHz. In principle the QCL can be modulated up to GHz frequencies, dictated by the relaxation time of the device, but the laser driver used in this system has a 3 dB roll-off on it's modulation capability at 100 kHz, limiting this scheme. Higher modulation frequencies allow not only faster image acquisition, but also higher averaging to reduce noise in the measurement.

The following images, Figs. 3.26(a) and 3.26(b), show images acquired at the same acquisition speed, using a TC of 50 ms but with higher modulation rates. Due to the faster modulation, a reduction of 1/f noise occurs, while the measurement bandwidth is held constant by keeping the same TC. This combination leads to an improved SNR of the acquired images.

Whilst similar values of V_{SM} are obtained using 20 kHz and 60 kHz modulation (0.97 mV and 0.84 mV respectively), the slight reduction is due to the roll-off of the high-frequency response of the current driver modulation. As the modulation frequency increases, the background noise is dramatically reduced through a reduction of 1/f noise, dropping to

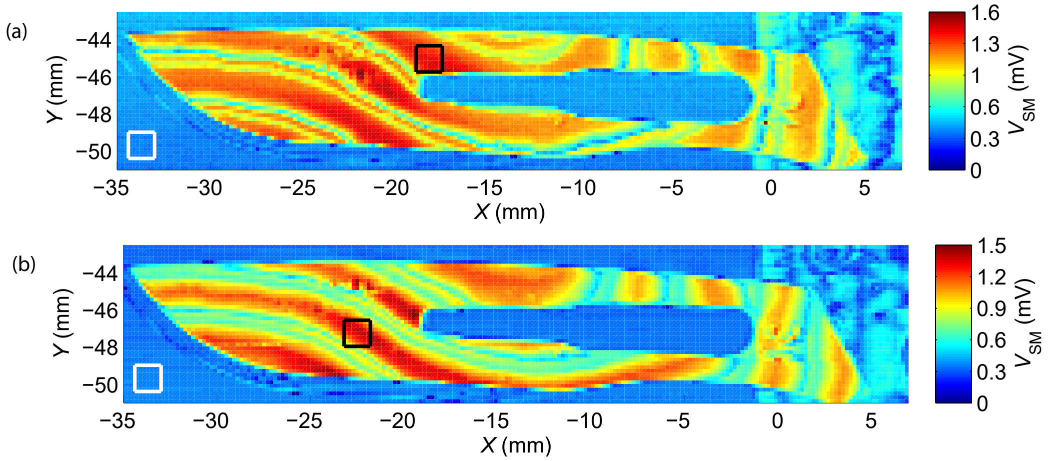

Figure 3.26: 2D SM image taken with electrical modulation with (a) 20 kHz modulation and 50 ms TC and (b) 60 kHz modulation and 50 ms TC. White and black areas used for analysis of the figure of merit.

14.1 µV with 20 kHz modulation and 7.6 µV with 60 kHz. This brings it in line with that of mechanical modulation even with the reduced LIA sensitivity. These values mean that the FOM for these images are 69 and 111 respectively.

The above images show that those produced using mechanical and electrical modulation for the same acquisition speed have similar quality. This is achieved by countering the increased low-frequency noise associated with the electrical modulation technique by exploiting the ability to modulate at higher frequencies where noise is lower.

This higher modulation frequency can also be employed to a different end; to increase acquisition speed and produce images faster than would be possible with mechanical modulation. The limiting factor on image acquisition so far has been the modulation frequency and the associated TC of the LIA. Electrical modulation increases the modulation frequency beyond that possible with mechanical modulation, so the TC of the LIA can now be reduced to allow faster image acquisition as given by

$$t_{\mathrm{acquisition}} = t_{\mathrm{samp}} n_{\mathrm{pixels}}, \tag{3.4}$$

where $t_{\mathrm{samp}} = 2 * t_{\mathrm{TC}}$ is the sampling time per pixel, t_{TC} is the time constant of the LIA which is limited by the modulation frequency, and n_{pixels} is the number of pixels acquired throughout the acquisition. The following figure, Fig. 3.27, was acquired with 60 kHz modulation and 5 ms TC making image acquisition 10 times faster than the previous image.

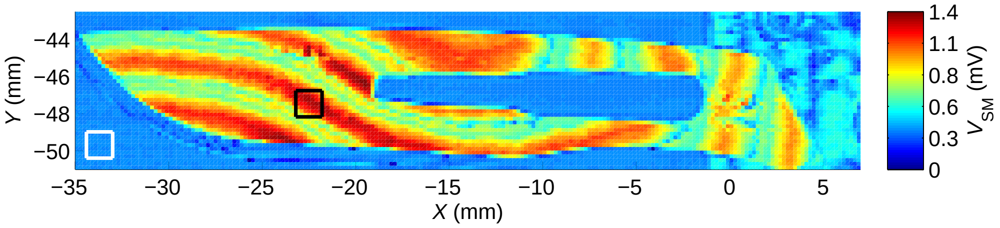

Figure 3.27: 2D SM image taken with electrical modulation with 60 kHz modulation and 5 ms TC. White and black areas used for analysis of the figure of merit.

Even though this image was acquired in approximately a tenth of the time of the previous images, the V_{SM} and noise values (0.82 mV and 5 µV) are very similar to those acquired in Fig. 3.26(b), suggesting that this previous image was over-averaged. Through reduction of the imaging time, thermal drift in the laser is reduced, resulting in the lower noise value. The FOM of Fig. 3.27 is 165, which is comparable to that obtained using the mechanical modulation scheme, even with the 10× decrease in imaging time.

The final quantifiers for this modulation technique are its signal-to-noise ratio and the dynamic range. Using the same analysis method discussed in previous Chapter 3.2.1.4, the differential voltage without feedback, V_0 is removed from the perturbed differential voltage under feedback V_{SM} and divided by the foreground and background noise to obtain SNR and DR responses. This is shown as a function of modulation frequency in Figs. 3.28(a) and 3.28(b).

Unlike in the mechanical modulation technique, both responses here rise and fall over the measured modulation range. The rise observed up to ∼6-10 kHz arises from the stable value of V_{SM} and a reduction of σ_{V_0} and $\sigma_{V_{\text{SM}}}$ over this range due to a reduction in 1/f noise. This is similar to the rise in DR observed in Fig. 3.21(a). After the SNR peaks at a value of ∼250 it decreases back towards 0 beyond 100 kHz. This decrease is caused by the high-frequency modulation limit on the laser driver. This could be prevented with the

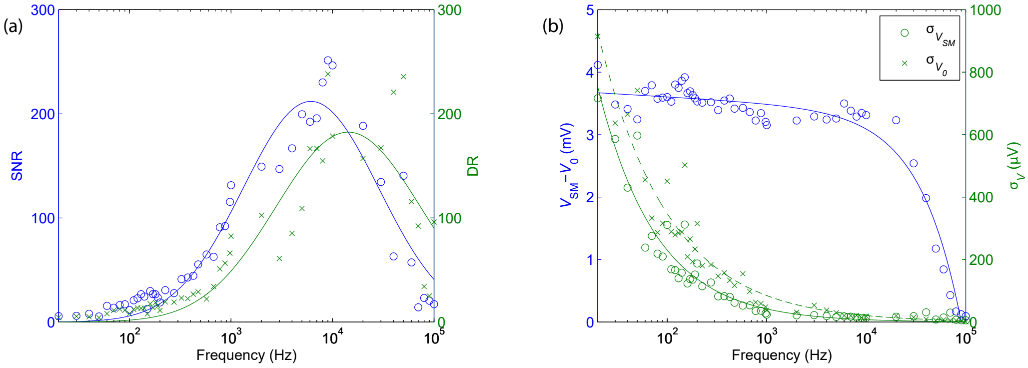

Figure 3.28: SNR and DR measurements for electrical modulation. (a) Signal-to-noise ratio and dynamic range measurements for electrical modulation. Both SNR and DR increase with frequency due to a loss of 1/f noise until a peak is reached. At modulation frequencies above this, SNR and DR decreases due to the high frequency response of the modulation threshold of the laser driver. (b) $\overline{V_{\mathrm{SM}}} - \overline{V_0}$ demonstrates the high-frequency roll-off of the laser driver, and standard deviation of the foreground and background noise, σ_{V_0} and $\sigma_{V_{\mathrm{SM}}}$ respectively, shows the 1/f response. Fitted lines added to guide the eye.

use of a different laser driver to allow higher frequency modulation which could result in an even higher SNR.

3.2.3 Comparison of modulation schemes for 2D imaging based on self-mixing

As mechanical modulation is limited to low modulation frequencies (<∼ 200 Hz), the SNR and DR of the system are similarly limited. If the mechanical modulation frequency could be improved, 1/f noise and mechanical, acoustic noise would decrease further resulting in an improvement in the SNR and DR.

Another major limitation of using mechanical modulation is due to the fact that the chopper has to physically rotate making it operationally slow. The chopper used in 2D imaging measurements discussed above is limited to a modulation frequency of ∼200 Hz which limits the overall acquisition speed of the measurement. To allow stabilisation of the system from pixel-to-pixel, two time constants per sample are allowed, as described in Eq. (3.4). As such, for a LIA TC of 5 ms, 10 ms sampling time is required per pixel. For acquisition of an image such as Fig. 3.20 which measures 211×43 pixels with a mechanical modulation of 200 Hz and TC of 50 ms, a total acquisition time would take

907 seconds. A similar image acquired with 60 kHz electrical modulation and a TC of 5 ms (10 ms sampling time per pixel) would take 91 seconds. The TC of the LIA is limited by the buffer input frequency of 200 Hz. If the TC could be reduced further, in line with the electrical modulation frequency (10 µs which relates to a modulation frequency of 100 kHz), an imaging time of 0.18 seconds would be possible, not accounting for translation motion time.

The addition of a chopper means more optical components are involved in the mechanical modulation system making the experiment less compact that a system employing electrical modulation. However the lack of electrical modulation that is inherently measured by the LIA means that it avoids the larger LIA sensitivity required by such a system. The FOM of images gathered using a mechanically modulated system are better than the electrical alternative as such, even with the higher modulation frequencies of such a system leading to a reduction of 1/f noise.

3.3 Near-field spectroscopy

In the two-dimensional measurements presented so far, the pixel size of the images has been limited to the spot size of the THz QCL which is on the order of ∼250 µm. In an attempt to increase the lateral resolution of the images obtainable using self-mixing a different technique can be employed.

Near-field (NF) THz imaging[184] has previously shown great potential for measuring sub-wavelength features on samples. Applications demonstrated to date include mapping of charge-carriers in semiconductors and nanostructures,[185,186] characterisation of THz waveguides[187,188] and THz microscopy of biological samples.[189] In order to bypass the diffraction limit imposed during traditional far-field imaging, several techniques have been used. One such example is placing a sub-wavelength aperture to limit the beam laterally at its focus or limit the detection area in the near-field,[190–192] but this technique has been shown to be limited by the strong beam attenuation caused by the aperture. Another method is to place the THz source or detector in close proximity to the sample,[193–195] but this can lead to very difficult experimental set-ups.

A method that has shown more promise in the THz range is a technique adapted from apertureless (scattering-type) near-field scanning optical microscopy (ANSOM).[184,186,196–200]

3.3.1 Apertureless near-field imaging

Apertureless near-field imaging implements a scattering probe that is placed in close proximity to the sample and the reflected or scattered field is detected in the far-field. The near-field interaction between the sample surface and the probe tip causes a modification to the scattered field allowing properties of the sample surface at the point of interaction to be measured with a spatial resolution determined by the dimensions of the probe tip, independent of radiation wavelength. A schematic of how reflection apertureless NF imaging occurs is shown in Fig. 3.29.

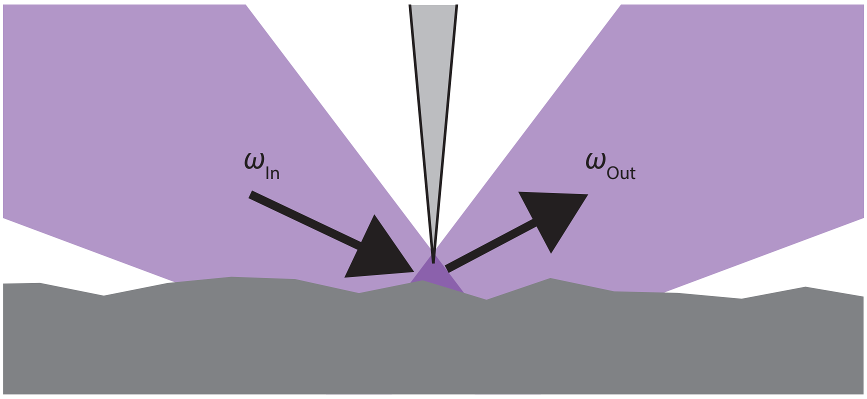

Figure 3.29: A probe tip is brought close to the sample surface in order to confine the field energy of the incident radiation in the near-field.

In order to improve SM imaging lateral resolution using this technique, the THz beam is focused onto the tip of the probe and the field that is scattered back to the laser facet is measured.[201] In order to measure the voltage perturbation caused by the scattered field, the probe tip is modulated perpendicularly to the sample surface to allow lock-in amplification at the frequency of the probe dither.

3.3.2 Experimental set-up

The THz QCL consisted of a 10 µm-thick BTC active region emitting at 2.53 THz ($\lambda \approx 119$ µm), which was processed into a SISP ridge waveguide with dimensions 2.4 mm × 150 µm. The device was cooled using a continuous-flow helium cryostat and maintained at a heat-sink temperature of 25 K. A current source was used to drive the laser at a constant current of 945 mA.

The usual 2D imaging system based on SM shown in Fig. 3.11 was adapted with the second parabolic mirror focused down onto the sample surface at a $\theta \approx 50^\circ$ angle, as shown in Fig 3.30(a) and 3.30(b). The length of the external cavity formed between the tip of the needle probe and the QCL facet was $L_0 = 0.40$ m. Without the needle probe in place, the THz field reflects off the sample surface away from the laser facet so self-mixing only occurs from radiation scattered from the sample surface. When the needle is brought into the focus of the field at a separation distance d from the surface, scattering occurs off the tip which feeds back into the laser facet, as shown in Fig. 3.30(c) by the green arrow. The simplified ray model shown in red and blue also shows how radiation can scatter from the surface from a reflection from the tip, and vice-versa, respectively. Radiation travelling along these unwanted reflection paths will still be measured by the system. In order to facilitate lock-in amplification the needle probe is dithered sinusoidally in the Z-direction using a piezoelectric translation stage. The modulation to the THz near-field and the scattered reflection caused by the movement of the probe tip are measured as changes to V_{SM} on the terminal of the laser. As only the THz field scattered from the tip is measured, only a very small amount of THz radiation is reflected back into the facet. Therefore lock-in amplification is required to measure the changes in voltage on the order of ~10 µV. By employing this technique with SM, sensitivity to the phase of the reflected field is also obtained. The sample is mounted on a three-dimensional translation stage to allow it to be positioned at the focus of the THz beam and raster-scanned to produce the two-dimensional images.

In order to find the optimal bias condition for the QCL, the laser bias was stepped

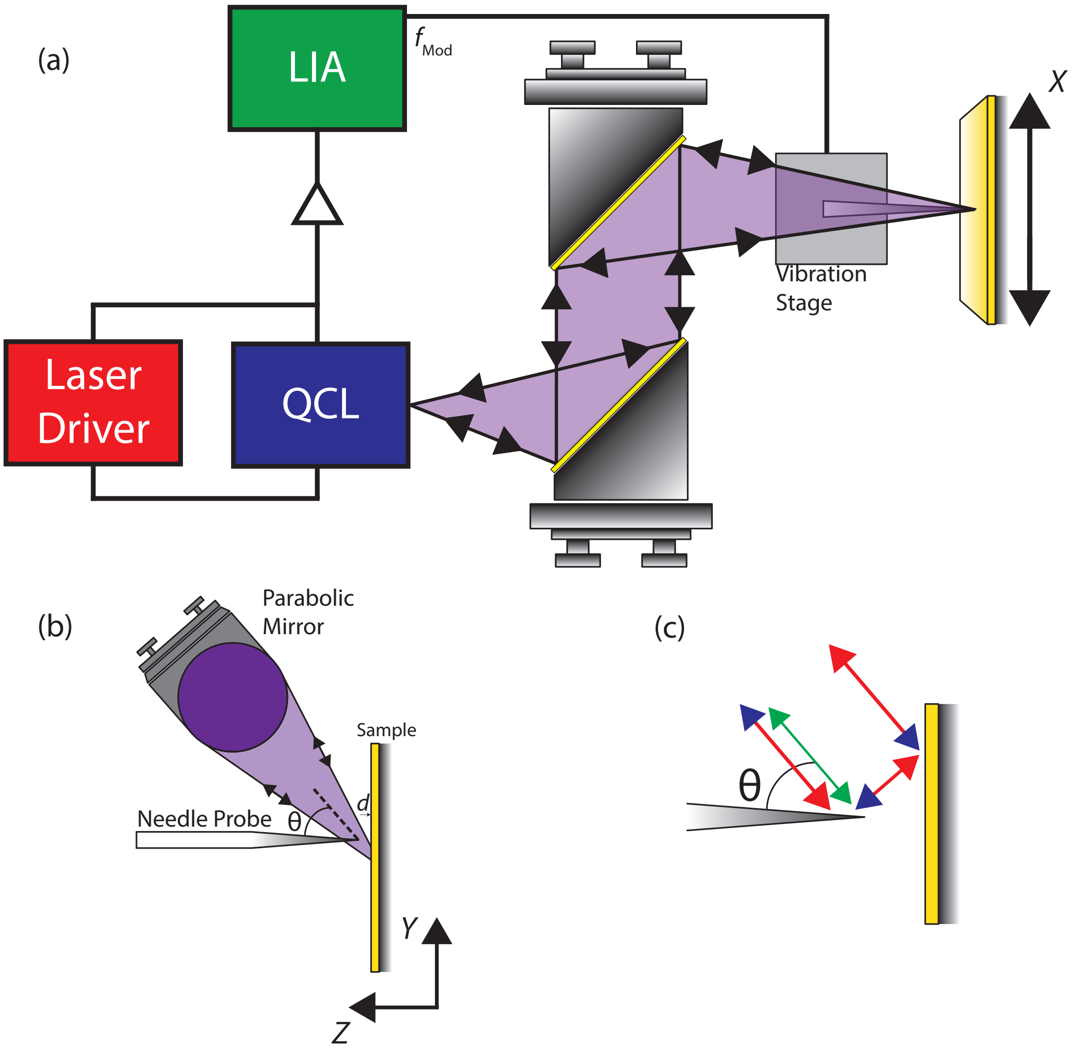

Figure 3.30: Schematic diagram of the experimental set-up used in near-field spectroscopic 2D reflectance imaging. (a) Self-mixing experimental set-up employing lock-in detection of the scattered THz field, synchronised with the modulation frequency, f_{Mod}, of the probe needle. (b) The final parabolic mirror is angled such that V_{SM} is $0\,\mu\text{V}$ when the needle isn't present and is angled at an elevation angle of $\theta \approx 50°$ relative to the needle axis. The needle is dithered sinusoidally in the Z-direction using a piezoelectric stage. (c) Simple ray model describing how radiation scatters from the tip (green), from the surface after a reflection from the tip (red) and from the tip after a reflection from the surface (blue).

while the probe needle tip was modulated in the focus of the beam. Fig. 3.31 shows that the optimal bias was just above threshold, at 910 mA. The behaviour of sensitivity to feedback just beyond the lasing threshold is common to SM systems.[65] Due to correction of a grounding problem of the system after this measurement, the threshold moved to 930 mA with the optimal driving current at 945 mA.

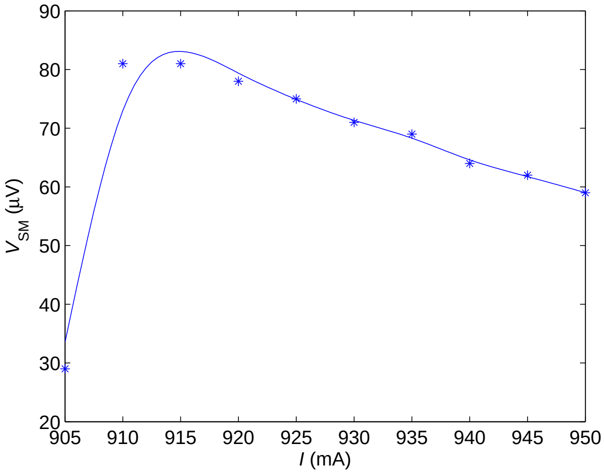

Figure 3.31: Experimental data showing V_{SM} caused by scattering from the probe tip in free space, for various bias conditions. The fitted curve is added to guide the eye.

To further optimise the experimental set-up, the position of the probe needs to be optimised in order to maximise V_{SM}. The probe tip was placed within the focus of the THz field, with no surface to cause a NF effect, so any change to the laser terminal voltage is purely due to scattering from the probe tip.

Fig. 3.32 shows the optimal needle position at ∼0 mm along the direction of the Z-stage controlling the sample position.

3.3.3 Surface approach technique

The near-field effect only occurs when the probe tip is in close proximity (∼1 μm) to the sample surface. In order to measure and quantify this effect a technique was utilised where the needle was dithered in the focus of the THz beam, and the sample was brought towards the probe tip in the direction of modulation, Z, while V_{SM} was measured. The sample

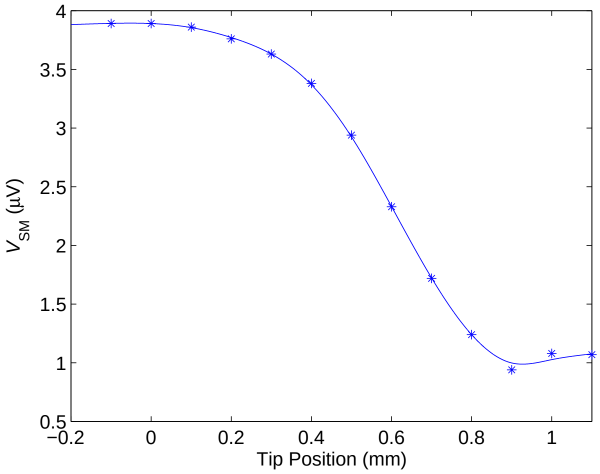

Figure 3.32: Experimental data showing V_{SM} caused by scattering from the probe tip in free space, for various probe positions in the Z-direction as shown in Fig. 3.30(b). The fitted curve is added to guide the eye.

consisted of an aluminium-coated mirror mounted on a mechanical translation stage.

With the needle in the focus of the THz beam, and the mirror positioned outside of the focus at the start of its scan range (d>300 μm), the background scattered field from the tip causes a non-zero SM signal of ∼20 μV as shown in Fig. 3.34. As the surface of the sample is brought in close proximity to the tip, the THz field is reflected off the surface onto the probe tip, and vice-versa, before scattering into the laser facet as shown in Fig. 3.30(c). As the round trip distance between the laser facet, sample surface and needle changes, the phase of the scattered field changes resulting in oscillations in V_{SM}. These oscillations are system and alignment dependant and are of the order $\lambda/2\cos(\theta) \approx 95$ μm. This relationship arises from the angle that the THz beam approaches the sample surface, as shown in Fig. 3.30(c), and is caused by the round-trip phase of the field at the location of the probe tip. At the point of near-field interaction (d<30 μm) the magnitude of V_{SM} is amplified dramatically, as shown in Fig. 3.34.

The entire scattered field E_{Tot} consists of various components such that

$$E_{\mathrm{Tot}} = E_{\mathrm{s}} + E_{\mathrm{b}} + E_{\mathrm{NF}}, \tag{3.5}$$

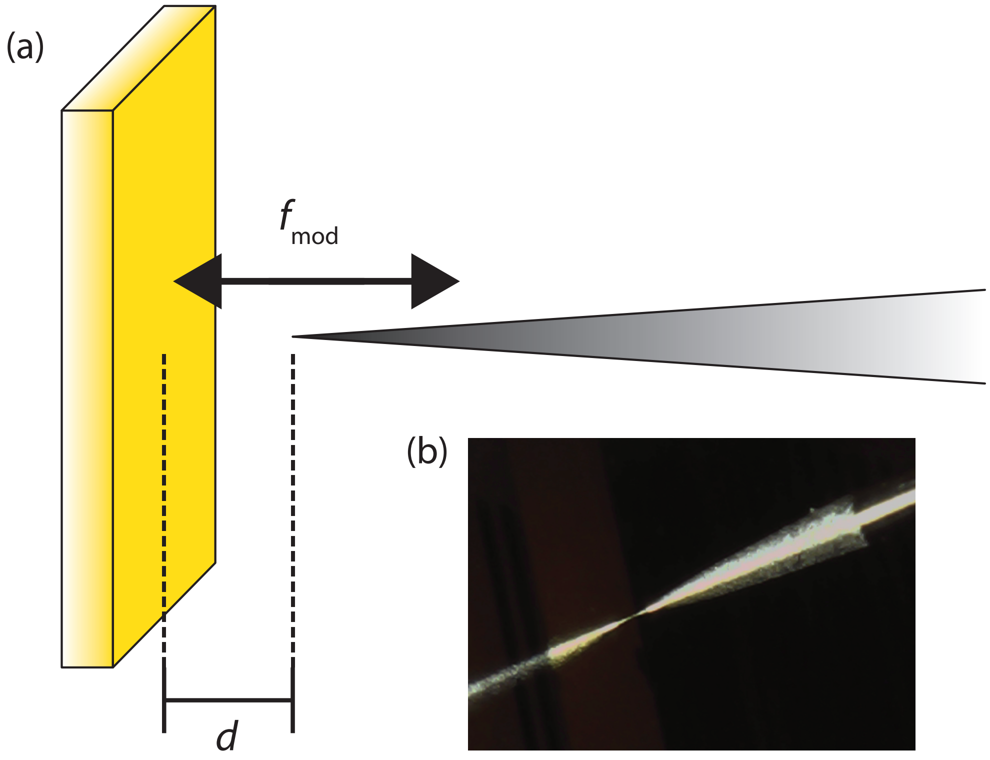

Figure 3.33: (a) The needle is modulated perpendicular to the surface with frequency f_{mod}. (b) Photograph of the probe tip in close proximity to the mirror, taken with a remote camera with 25× objective lens.

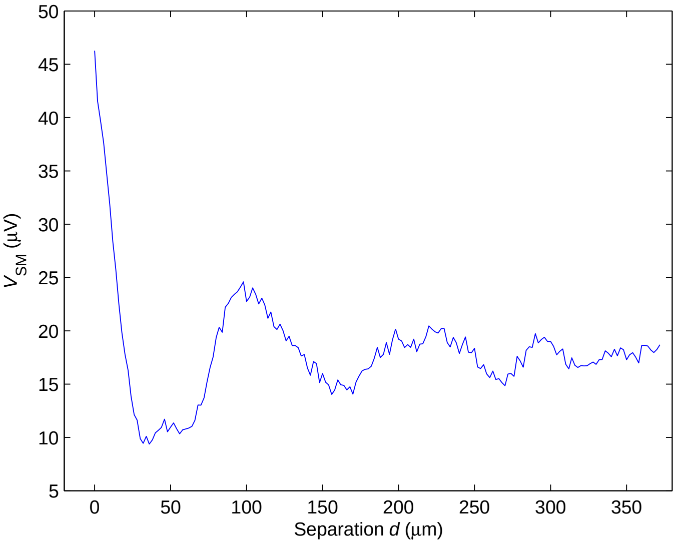

Figure 3.34: The sample was brought close to the needle, showing the phase sensitivity of the measurement and also the NF effect that causes the signal to increase sharply when the distance between the probe tip and the sample approaches 0 µm.

where E_s is the background field directly scattered from the sample surface and E_b is the field scattered from the probe tip and shaft, as well as the reflections from one to the other and into the laser facet, with no NF effect present.[202–204] E_NF is the amplification arising due to the NF enhancement when the sample and needle separation distance approaches 0 µm. The needle modulation and LIA remove the unwanted E_s component. E_NF can be further discriminated from the tip-scattered background signal, E_b, through demodulation at the second and higher harmonics of the modulation frequency.[205 204]

The near-field enhancement has been previously described using a coupled dipole model[196,203] where the probe tip is regarded as a sphere with radius R and polarizability α that is polarised by the incident field E_0. An image dipole is induced in the dielectric sample, with permittivity ϵ_s, by this dipole; shown in Fig. 3.35.

This image dipole couples with the probe tip dipole to produce an effective polarizability of the probe-sample system given by

$$\alpha_\mathrm{eff} = \frac{\alpha[1 + (\epsilon_\mathrm{s} - 1)/(\epsilon_\mathrm{s} + 1)]}{1 - \frac{\alpha(\epsilon_\mathrm{s}-1)/(\epsilon_\mathrm{s}+1)}{16\pi(R+d)^3}}, \tag{3.6}$$

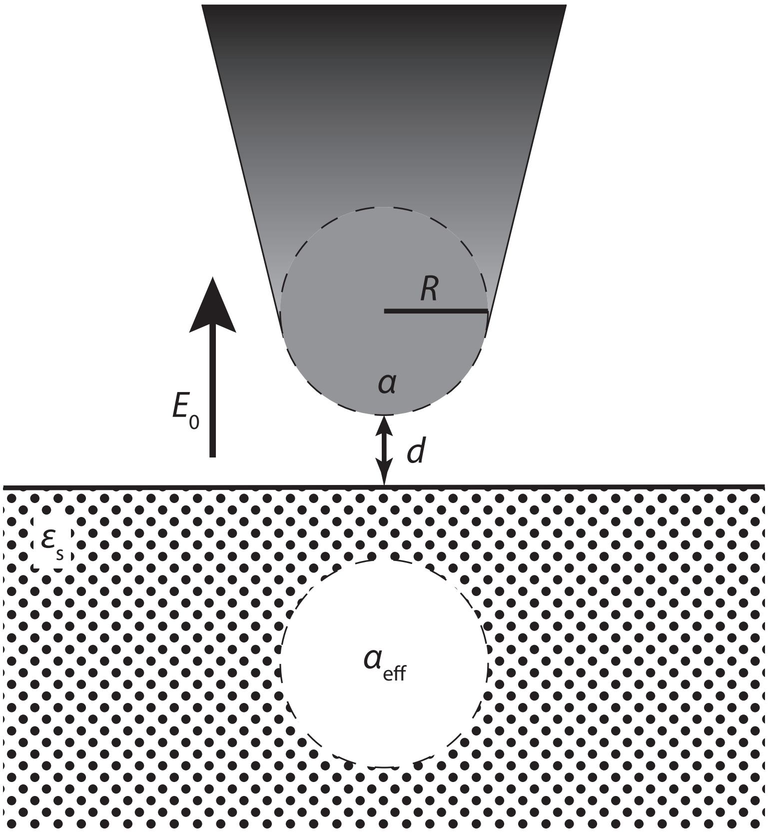

Figure 3.35: Coupling of a probe dipole and image dipole at small distances d. The field E is assumed perpendicular to the sample surface due to the orientation of the beam path.

where d is the separation between the probe tip and the sample surface. Considering only the intended radiation path (green arrow in Fig. 3.30c), as d approaches 0, the near-field term of the field, E_{NF}, gains a large enhancement, with the entire scattered field varying $\propto \alpha_{\mathrm{eff}} E_0$. It is not so simple to relate the measured signal to α by $V_{\mathrm{SM}} \propto \alpha_{\mathrm{eff}} E_0$ due to the alternate feedback paths described in Fig. 3.30(c).

As this technique is phase sensitive it is possible to map the phase of THz field along the modulation axis Z when moving through the focus of the beam at angle θ. To investigate how the external cavity length affects the measured signal the position of the needle and sample were stepped through the beam focus by ΔZ. For each measurement the separation between the sample and needle is swept from 150 µm to 0 µm. For an increment step of ΔZ, the round-trip path length in the external cavity formed between the tip and the QCL facet decreases from the nominal value $2L_0$ by an amount $2\Delta Z\cos(\theta)$. Figure 3.36 shows the recovered signal with respect to the separation between the needle and sample d. Consecutive vertical plots correspond to needle positions varying by 2 µm along the Z-axis.

The background signal observed for large sample-tip separations, E_{b}, which can be seen for values of $d > \lambda$, represents scattering from the needle tip with no surface present. It can be seen to decrease with increasing ΔZ. For values of Z when $L_0 = [(m \pm 1/4)\lambda/2]$, where m is an integer value, this background signal would minimise. Experimentally, this component was observed to oscillate between negative and positive peaks for round-trip external cavity lengths equivalent to $m\lambda/2$ and $(m + 1/2)\lambda/2$ respectively.

Through these scans, the amplitude of the enhanced NF signal recorded at d=0 varies with the round-trip phase, with both positive and negative values observed. For a cavity change of $\Delta z \approx 6$µm a minima is observed, which represents a phase contrast between the background and NF signals. The equivalent maxima is observed at $\Delta z \approx 18$µm. Near-field phase sensitivity has been shown with previous ANSOM implementations, dependant on sample composition.[205] Equation (3.5) also suggests that the phase and amplitude of the scattered field demonstrates optical properties of the sample's surface at the probe tip. This interaction can be further utilised for high-resolution imaging.

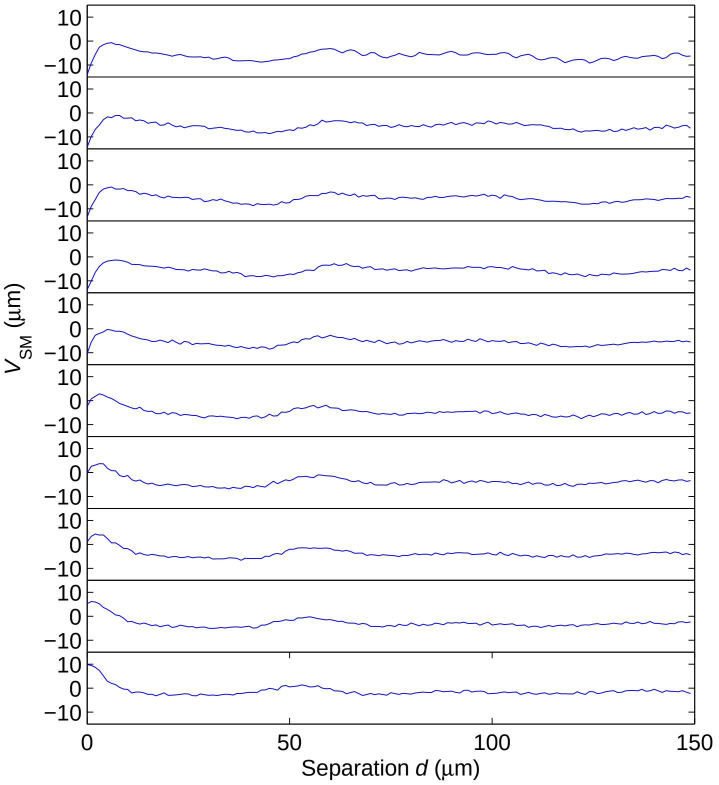

Figure 3.36: Self-mixing voltage V_{SM} recorded as a function of tip-sample separation d, for different positions of the needle tip in the beam focus. The approach curves correspond to the needle tip being stepped in the Z-direction by an amount varying (top to bottom) from $\Delta Z = 0\,\mu\mathrm{m}$ to $\Delta Z = 18\,\mu\mathrm{m}$ in steps of $2\,\mu\mathrm{m}$.

3.3.4 Two-dimensional reflectance imaging using the near-field effect

This technique made it possible to create 2D reflection images of a sample using NF self-mixing imaging. The sample was a quartz substrate patterned with a $2\,\mathrm{mm} \times 5\,\mathrm{mm}$ rectangular region of 115-nm-thick gold defined using photolithography. It was positioned close to the probe tip ($d \approx 0\,\mu\mathrm{m}$) and the external cavity was adjusted to give the largest possible NF signal. The corner of the gold region was raster scanned in the X-Y plane perpendicular to the probe shaft and V_{SM} was measured for each pixel.

Limited by the resolution of the motion controller, the sample was stepped using 1 µm pixels resulting in the 2D image shown in Fig. 3.37. The contrast in the image comes from the change in permittivity of the surface at the probe tip.

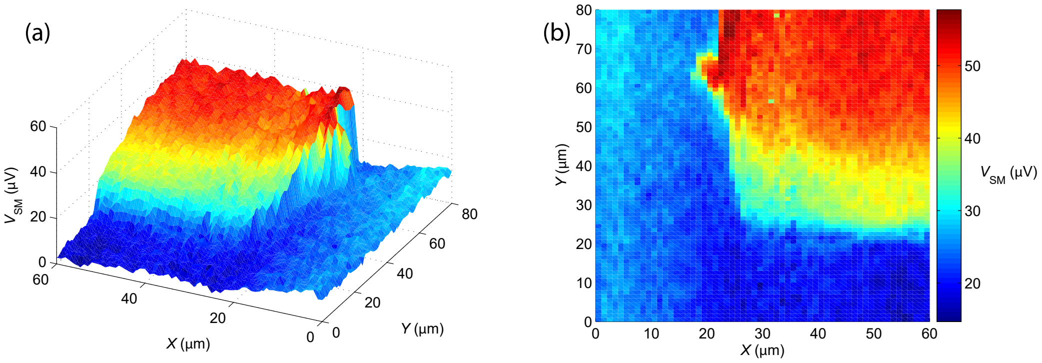

Figure 3.37: The corner of a resolution target consisting of 115-nm-thick gold deposited onto a quartz substrate was scanned perpendicular to the needle tip and V_{SM} was recorded at each pixel to map the sample reflectivity. The large signal occurs on the gold region of the resolution target and the colour scale corresponds to the magnitude of V_{SM}.

In order to determine the resolution of the acquired image, edge response functions (ERFs) along each scan dimension were extracted by averaging 10 consecutive rows covering the edges of the gold-covered regions of the sample. These are shown for the X- and Y-dimensions respectively in Fig. 3.38.

To quantify these ERFs in terms of resolution, the full-width half-maximum (FWHM) of the normalised first-order spatial derivatives can be calculated. These spatial derivatives are shown in Fig. 3.39. The spatial resolutions obtained from these are calculated as $\sigma_{\mathrm{x}} \approx 1\mu\mathrm{m}$ and $\sigma_{\mathrm{y}} \approx 4\mu\mathrm{m}$.

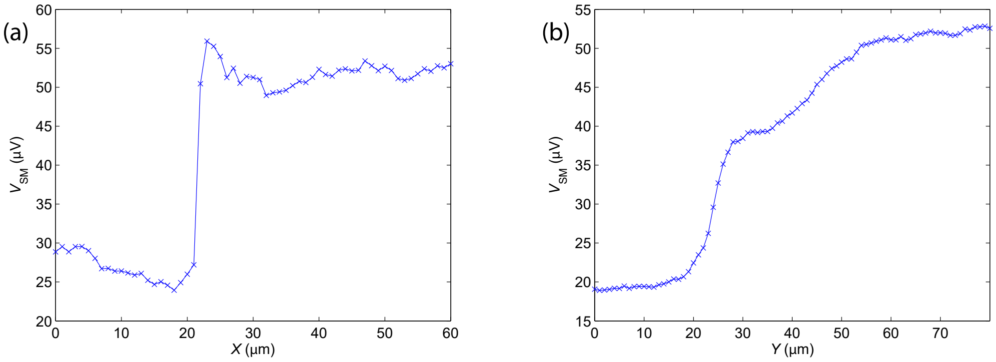

Figure 3.38: The ERFs extracted from averaging 10 consecutive rows of pixels of the gold coated regions in the X- and Y-dimensions, respectively.

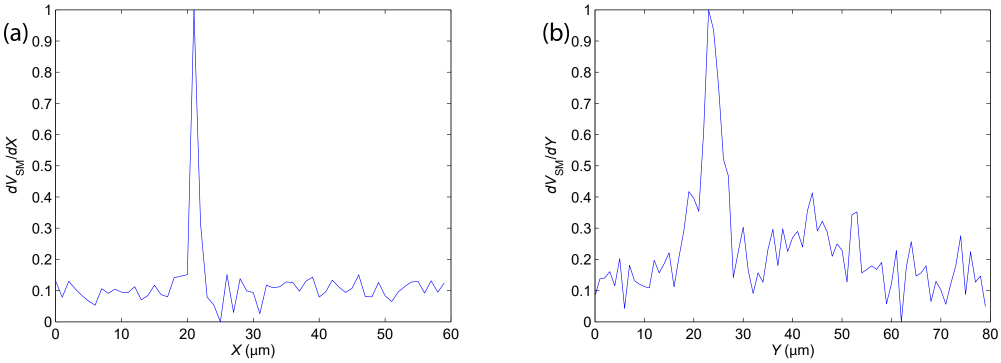

Figure 3.39: Normalised first-order spatial derivatives of the edge response functions of the acquired image in both the X- and Y-dimensions respectively.

The obtained value for σ_{x} is consistent with the dimensions of the probe tip and represents a resolution of $\sim \lambda/100$. These measurements show the highest image resolution achieved with a THz QCL obtained to date of 1µm. The lower spatial resolution obtained in the Y-dimension can be attributed to the experimental illumination orientation due to the set-up geometry. In this geometry, reflections from the sample surface outside of the NF of the tip could contribute to the scattered field, broadening the resolution of the system in the Y-dimension.

4 Three dimensional imaging with mechanical pullback

In the previous chapter, Chapter 3, techniques for two-dimensional THz imaging were demonstrated that utilised self-mixing as a detection method. Figures 3.16 through 3.19, amongst others, demonstrate that not only can this technique measure sample reflectivity, but also sub-wavelength surface morphology. In these images the curvature of the scalpel blade caused a change in the external cavity length leading to a change in the phase of the returning field. This change can be measured as a perturbation of the terminal voltage.

In order to perform three-dimensional (3D) THz self-mixing measurements of samples, the phase and amplitude of the SM signal must be resolved. Equation (2.24) demonstrates that the terminal voltage perturbations caused by the SM effect have a sinusoidal dependency on the external cavity length and this can be exploited to perform 3D measurements of samples. By extending the external cavity over more than one fringe ($\lambda/2$), this sinusoidal change to the terminal voltage can be measured for which the amplitude is proportional to the reflectivity of the sample surface and the phase is proportional to the external cavity length. Due to this, changes in sample surface reflectivity and depth result in different waveform amplitudes and phases, respectively.

4.1 Experimental set-up & measurement technique

The THz QCL used in the following measurements consisted of a 10-µm-thick bound-to-continuum active region[183] emitting at ∼2.65 THz ($\lambda \approx$113 µm), which was processed into a SISP ridge waveguide with dimensions of 3 mm × 140 µm. The device was cooled using a continuous-flow helium cryostat and maintained at a heat-sink temperature of 25 K. The threshold current at this temperature was 1000 mA.

This technique utilised a similar set-up to that shown in Chapter 3 (Fig. 3.11) and is based on previously published SM systems,[65] but a third translation stage was added to facilitate the required external cavity extension in the Z-dimension needed to build up the interferometric fringes for 3D imaging. The sample was raster-scanned in the X- and Y-dimensions using step sizes of 0.1 and 1.5 mm respectively and at each (X, Y)

location the sample was swept through the beam focus by 0.5 mm in the Z-direction to record the required interferometric waveform. A scan depth of 0.5 mm corresponded to 9 interferometric fringes, and a high sampling resolution of 0.5 µm (corresponding to 1/100th of a fringe) allowed accurate recording of the waveform shape. The output from the LIA was fed into the XPS ADC input to allow accurate recording of both the sample position and QCL terminal voltage. Using an LIA time constant of 10 ms resulted in a scan time of 20 seconds per (X, Y) pixel.

Radiation from the laser was focused onto the sample using a pair of 2-inch-diameter $f/2$ off-axis parabolic reflectors, where the mean distance between the laser facet and the target was 0.41 m through an unpurged atmosphere. The beam spot size on the sample is estimated to be ∼250 µm. The laser radiation reflected from the sample was coupled back to the QCL facet along the same optical path as the emitted beam.

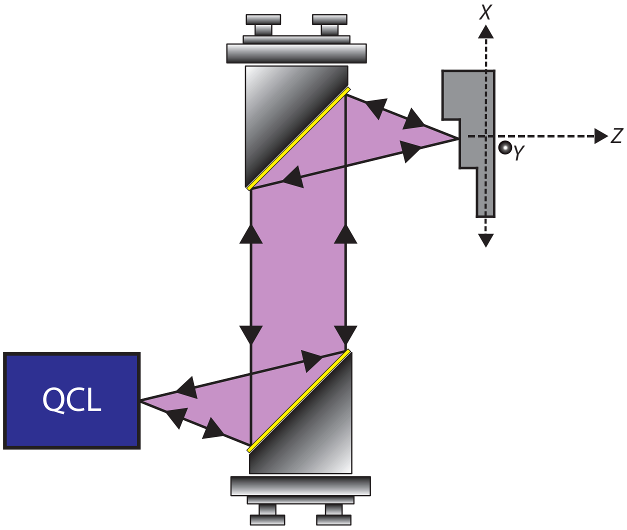

Figure 4.1: Schematic diagram of the experimental apparatus used for 3D coherence imaging measurements. The experimental set-up is similar to that of the 2D coherent imaging set-up described in Chapter 3.2.1, but to create the interferometric waveforms, from which the surface depth and reflectivity profile are extracted, the sample has to be mechanically scanned through the beam focus in the Z-direction at each (X, Y) location.

To demonstrate measurement of both reflectivity and depth, a sample consisting of bulk GaAs semiconductor wet-etched to 3 different steps (in the X-dimension) of height 10 µm was fabricated by Dr. Siddhant Chowdhury. Half of this sample was then coated with 125-nm-thick layer of gold resulting in areas of differing height and reflectivity. A 3D optical profile of the sample was obtained using a non-contact Bruker NPFlex 3D optical profilometer and is shown in Fig. 4.2.

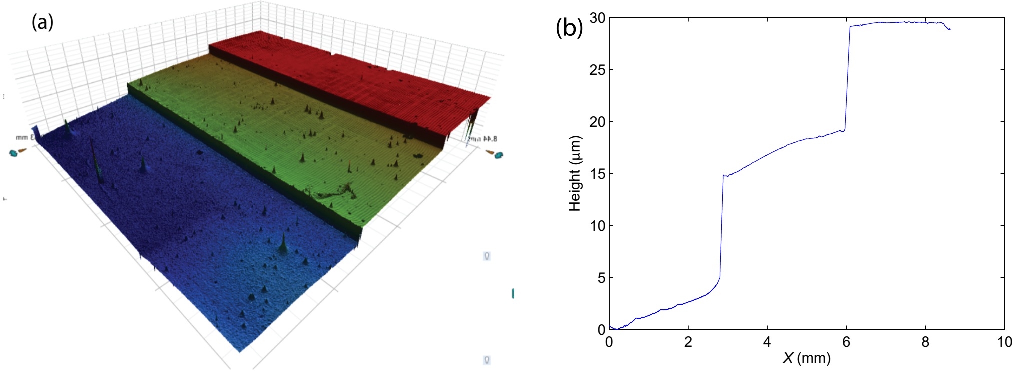

Figure 4.2: (a) 3D and (b) 2D optical profile of the sample obtained using a non-contact Bruker NPFlex 3D optical profilometer.

Exemplar waveforms shown in Fig. 4.3 demonstrate the change in V_{SM} over the pull-back range of the sample for two locations on the surface. The sinusoidal oscillation of the waveform has a repetition length of $\lambda/2$ due to the round-trip nature of the experiment. The variations in amplitude and phase equate to measurable differences in sample reflectivity and surface depth.

In order to extract the sample and experimental parameters such as feedback parameter, C, which is related to the sample reflectivity, R_{ext}, and other laser parameters, and the phase which gives the sample depth, a three-mirror model[105] was applied to describe the laser under feedback. In this model the laser frequency under feedback, ν, is related to the unperturbed frequency, ν_0 through the phase-matching equation

$$\frac{2(L_0 + \Delta L)(\nu_0 - \nu)}{c} = C \sin\left(\frac{2(L_0 + \Delta L)\nu}{c} + \arctan(\alpha)\right), \tag{4.1}$$

where L_0 is the nominal external cavity length formed by the sample, and ΔL is the change caused to the external cavity by the sample surface geometry, α is the linewidth enhancement factor and c is the speed of light in a vacuum.

Equation (2.24) can be modified to incorporate the change in cavity length caused by

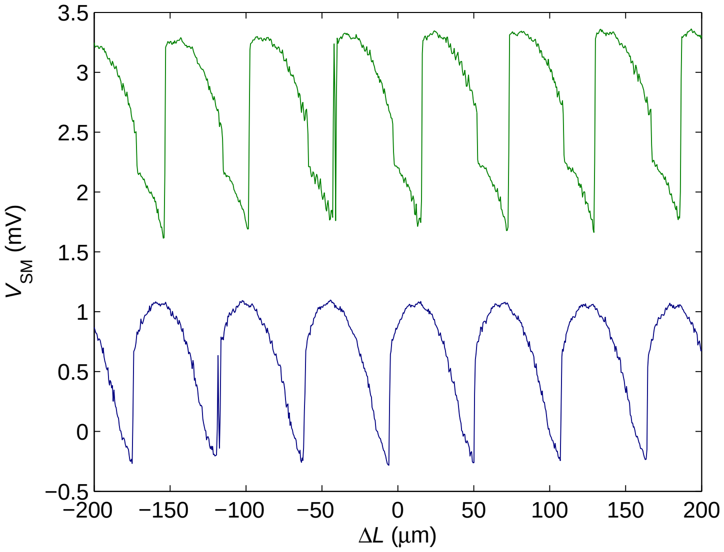

Figure 4.3: Exemplar interferometric waveforms for two individual pixels from an image, acquired using 3D imaging based on SM. V_{SM} is proportional to the sample surface reflectivity and the phase is proportional to the sample depth at that location on the surface for each waveform, and differences between these show changes in those parameters. Waveforms have been offset vertically for clarity.

the sample depth, ΔL, to give

$$\Delta V_{\mathrm{SM}} \propto \epsilon \sqrt{R_{2\mathrm{sExt}}} \cos \left(\frac{2(L_0 + \Delta L)\nu}{c} \right). \tag{4.2}$$

As ν is dependant on the cavity length as shown in Eq. (4.1), Eq. (4.2) will not result in a purely sinusoidal waveform. The level of feedback, C, and linewidth enhancement factor, α, also dictate the shape and symmetry of the measured waveform.

When fitting Eq. (4.2) to the acquired waveforms an initial fit was performed using the emission wavelength as the only free parameter as the fit was very sensitive to this value. Once an accurate value for the emission wavelength was extracted, a more complex fit was performed where C, $\epsilon\sqrt{R_{2\mathrm{sExt}}}$, α and ΔL were used as free parameters. This resulted in a much more robust and accurate fit to the waveforms. The result of such fitting can be seen in Fig. 4.4.

The values of ΔL extracted from the waveforms contained discontinuities as the fit can't differentiate between a positive or negative shift of 2π. As such, these had to be

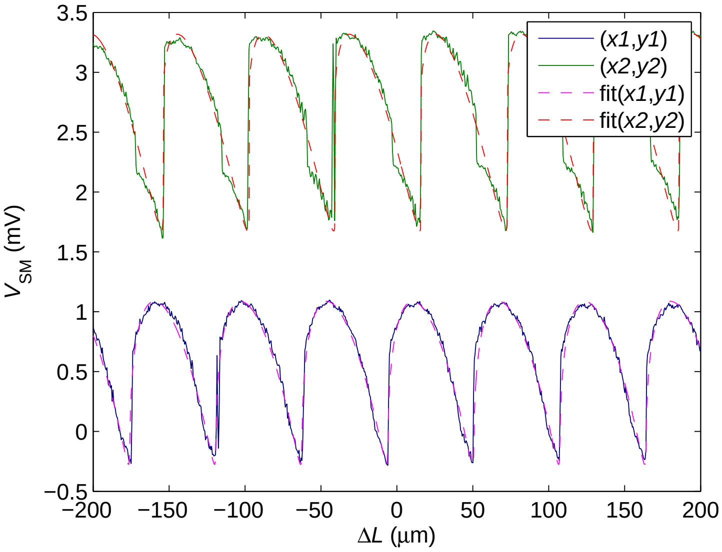

Figure 4.4: Equation (4.2) was fitted (red and purple) to the exemplar waveforms (green and blue) obtained from two individual (X, Y) locations on the sample surface to allow extraction of required parameters.

converted to round trip phase values to allow unwrapping to create an accurate surface profile of the sample. In order to achieve this a relationship with the laser emission frequency was used

$$\phi = \frac{\Delta L 4\pi}{\lambda}. \tag{4.3}$$

By removing any discontinuities greater than 2π, each column of data was unwrapped, as seen in Fig. 4.5(c) and (d). An unwrap was then performed in along the rows of data, representing the Y-dimension of the scan, the results of which are shown in Fig. 4.5(e). The unwrapped phase values were then converted back into depth values using the same relationship as shown in Eq. (4.3) and the unwrapped surface profile from a 3D SM image of the sample can be seen in Fig. 4.6.

As this technique utilises a similar system to the 2D imaging system, lock-in amplification was still required, meaning a modulation scheme was needed. Both mechanical and electrical modulation schemes were employed to perform 3D SM images of the sample surface, and the results of these experiments are shown below.

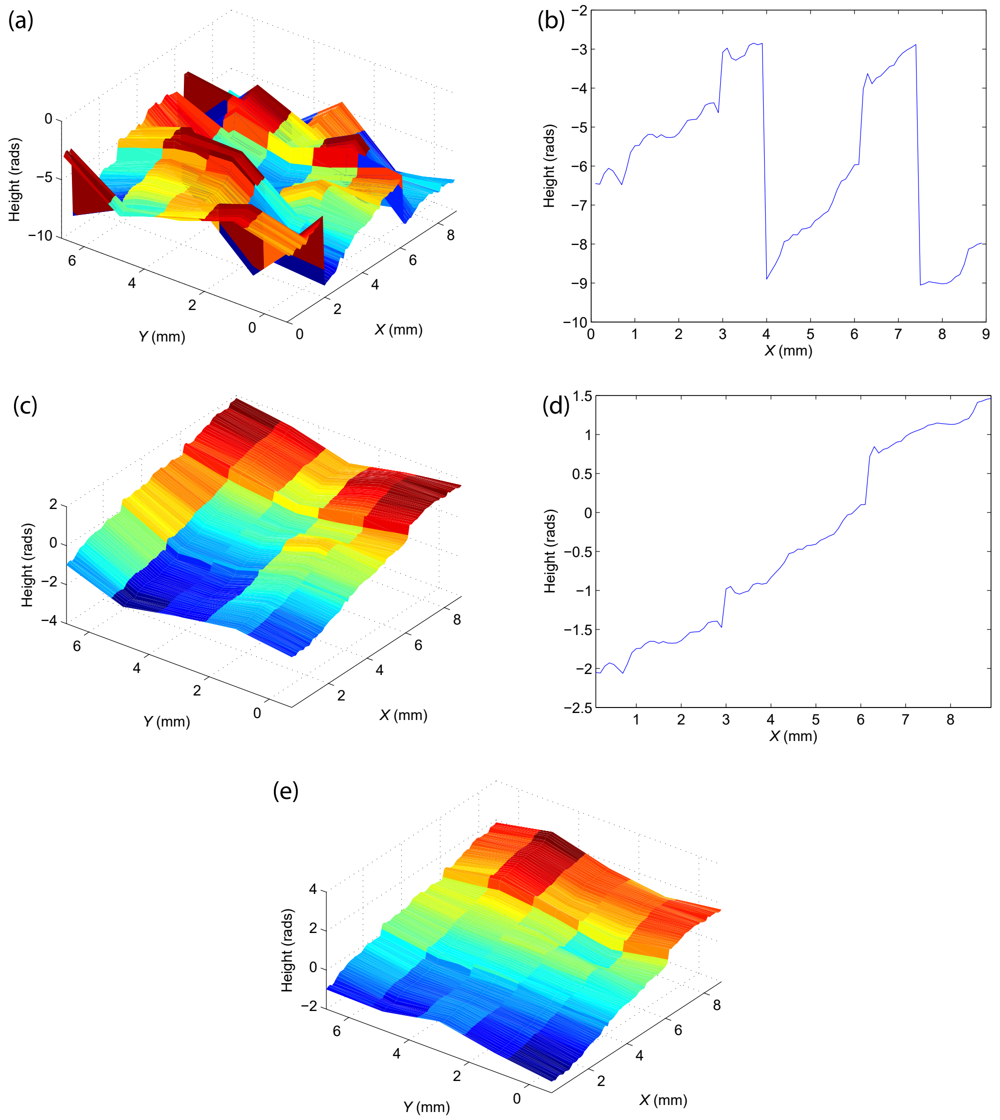

Figure 4.5: Phase maps for 3D SM image (a) before unwrapping, (c) after unwrapping in the X direction and (e) after unwrapping in both directions. (b) and (d) show individual columns before and after unwrapping respectively.

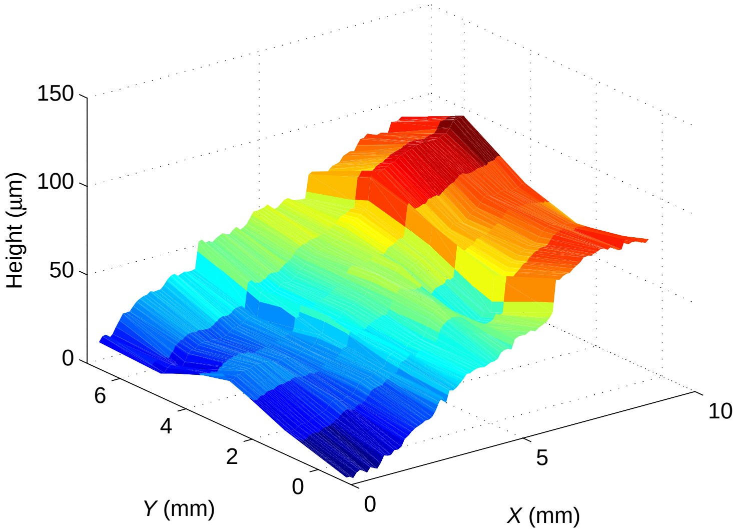

Figure 4.6: 3D surface profile of the sample created using 3D SM imaging with mechanical modulation. Colour scale represents sample height.

4.2 Mechanical modulation

Mechanical modulation for 3D imaging has the same benefits and limitations as when performing 2D image acquisition; namely high experimental sensitivity and large contrast between SM signal and background measurements, but low modulation speed.

The experimental set-up used for 3D imaging with mechanical modulation is shown in Fig. 4.7, in which a mechanical chopper is used to physically block and unblock the THz beam at a known frequency (∼200 Hz). This frequency was then used to allow lock-in amplification of the self-mixing signal measured as a perturbation to the terminal voltage of the QCL. Mechanical modulation allowed the use of a 100× differential pre-amplifier to be used before the LIA to amplify the small V_{SM} signal. A current source was used to drive the laser at a constant current of 1050 mA.

The profiles extracted from individual rows of pixels in the X-direction demonstrate an accurate measurement of the 10 µm steps in the sample surface, as shown in Fig. 4.8. The sample was also profiled using a non-contact optical profilometer (Bruker NPFLEX 3D), and the profile obtained from that measurement is shown in Fig. 4.8 also. A tilt equal

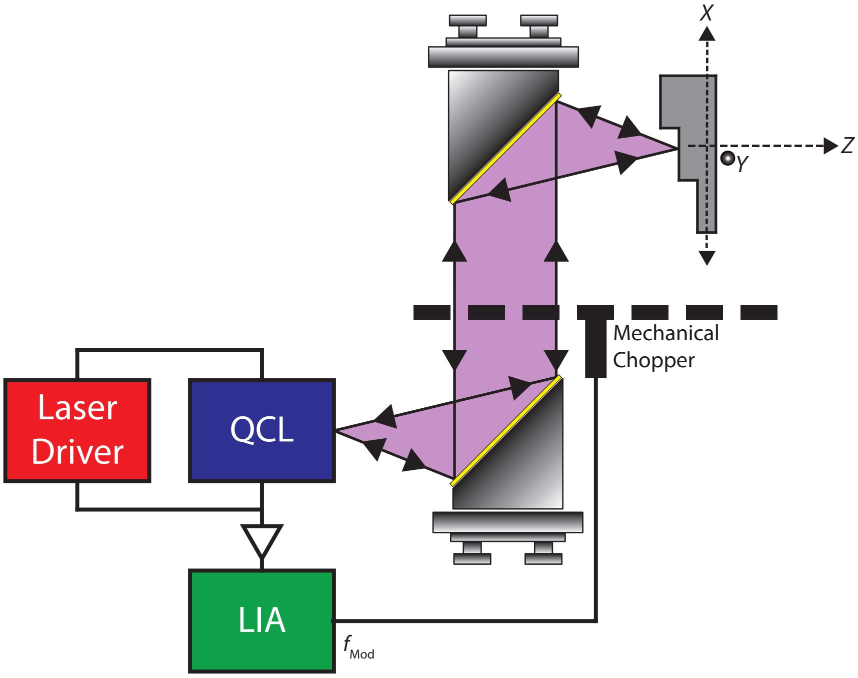

Figure 4.7: Schematic diagram of the experimental apparatus used for 3D SM imaging measurements with mechanical modulation.

to that on the sample surface during the measurements has been applied to that profile for comparison sake. As can be seen from the exemplar and average profiles, very good agreement is obtained between the measured profiles and those obtained from the optical profilometer. Imperfections observed at the steps of the exemplar profile are attributed to the simultaneous reflections of the QCL beam from multiple steps as its spot travels over the edges of the steps.

The three steps etched into the sample are clearly seen in the 3D profile displayed in Fig. 4.6. When mounting the sample, effort was made to reduce any tilt along the sample surface, but there was $\sim 0.4\,$deg of tilt measurable on the acquired image, shown as a change in height along the sample surface, in the X-direction.

To quantify the depth resolution of this technique two factors have to be considered; the sampling accuracy of the SM waveforms and the frequency instability of the QCL over the scan period. The first of these can be reduced at the expense of image acquisition speed by employing longer LIA time constants, by scanning the sample over a longer

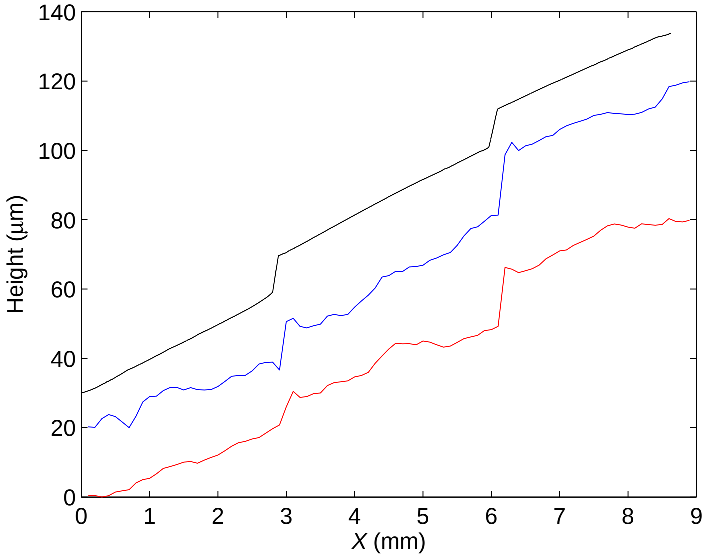

Figure 4.8: Experimental data showing side profiles of the sample surface obtained using mechanical modulation. An optical profile from a Bruker Optical Profilometer (black), an exemplar profile (blue) and the average profile along the entire sample surface (red) are displayed. Plots offset for clarity. A tilt has been applied to the optical profile to match the measured profiles.

distance with a smaller separation between samples (0.5 mm with a step of 0.5 µm was used here) or by greater averaging. An upper limit of the resolution limit (noise-equivalent displacement[206]), imposed by laser frequency instability, can be obtained by assuming typical frequency drift[85,86] $\Delta\nu/2\pi \approx$ 10-15 MHz. For small perturbations, change in emission frequency can be equated to a change in the external cavity given by

$$\frac{\Delta\nu}{\nu_0} = -\frac{\Delta L}{L_0}, \tag{4.4}$$

where ν is the emission frequency of the QCL and L_0 is the nominal external cavity length. Through this a resolution of ∼2 µm is obtained by our system, allowing the 10 µm features of the sample to be resolved. Due to the long acquisition time of this system, this resolution may potentially be degraded through thermal fluctuations in the QCL. Thermal fluctuations would explain the variations shown in Fig. 4.6 along the Y-direction.

Sample reflectivity was extracted as a value proportional to the amplitude of the SM fringes, $V_{\mathrm{SM}} \propto \epsilon\sqrt{R_{2\mathrm{sExt}}}$. By plotting the values of V_{SM} across the sample surface, Fig. 4.9

is generated showing the regions of the sample coated in gold as areas of high reflectivity; the gold-coated region is 3.75-6.75 mm in the Y-direction. Some of the GaAs regions of the sample (such as (6,-0.75) to (9,3.75) in Fig. 4.9) didn't generate as large variance from the gold-coated regions as expected, and this is most likely due to the etching process causing imperfections in the surface morphology of the sample, resulting in variation of the reflection angle of the beam, thereby causing variations in the coupling factor ϵ back into the facet. This could result in the GaAs region having a better coupling angle than the gold-coated region, reducing the contrast. The ratio of the parameters $\epsilon\sqrt{R_{\mathrm{2sExt}}}$ responding to the gold-coated and uncoated regions is 1.28. For comparison, a value of 1.77 is expected based on the Fresnel coefficient, assuming complete reflection from the gold layer and a refractive index of 3.6 for GaAs.

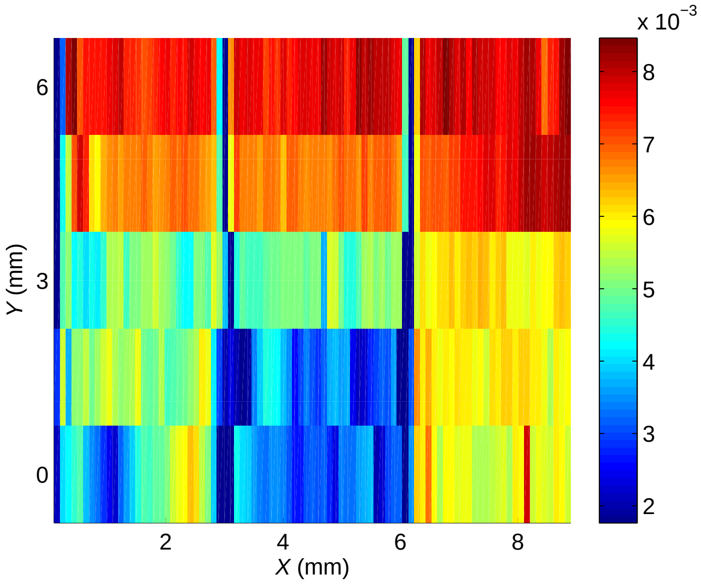

Figure 4.9: Experimental data showing reflectivity, $\epsilon\sqrt{R_{\mathrm{2sExt}}}$, across the surface of the sample. Gold coated regions are depicted as areas of high reflectivity, denoted by the color scale.

Figures 4.6 and 4.9 can be combined to show both the reflectivity and depth profiles of the sample together, and is shown in Fig. 4.10.

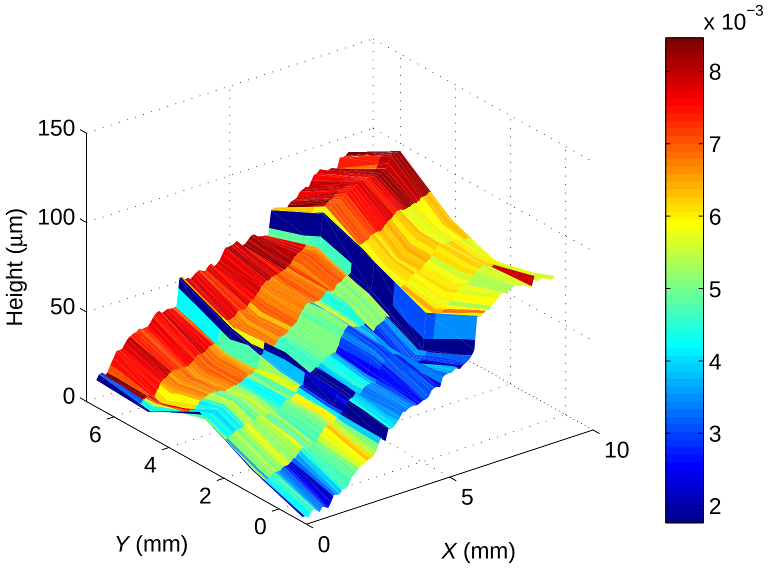

Figure 4.10: Experimental data showing depth profile of the sample surface. Sample reflectivity is shown by the colour of the plot. Gold coated regions are depicted as areas of high reflectivity, denoted by the color scale.

4.3 Electrical modulation

As with the 2D imaging presented in Chapter 3, electrical modulation allows an improvement in imaging speed over mechanical modulation by increasing the modulation speed greatly (>100 kHz compared with ∼200 Hz). By removing the mechanical chopper and instead biasing the QCL just below threshold and using a small (75 mA) square-wave modulation to drive the QCL into the lasing regime, much greater modulation frequencies can be reached. The general trade-off with this system is that as the modulation directly changes the terminal voltage of the QCL at the modulation frequency, lock-in detection measures not only V_{SM} but also the voltage change caused by the modulation, V_{Mod}, which is orders of magnitude greater. Also, due to the nature of the modulation scheme where the laser driving current is periodically changed, current and thermal fluctuations introduced into the laser will translate to frequency fluctuations in the device. This frequency change will further translate to voltage fluctuations on the terminal of the QCL. These limitations combine to result in a reduced experimental voltage sensitivity.

The experimental set-up for electrically modulated 3D self-mixing imaging is shown in Fig. 4.11. The experimental procedure is similar to that explained in the previous mechanical modulation section. Due to the fact that the modulation scheme employs a change in voltage, the 100× amplifier used in the mechanical modulation scheme was replaced with a 6× differential amplifier for this scheme in order to avoid saturating the LIA input. A modulation frequency of 10 kHz was employed by this system to avoid encroaching on the upper modulation limit of the laser driver.

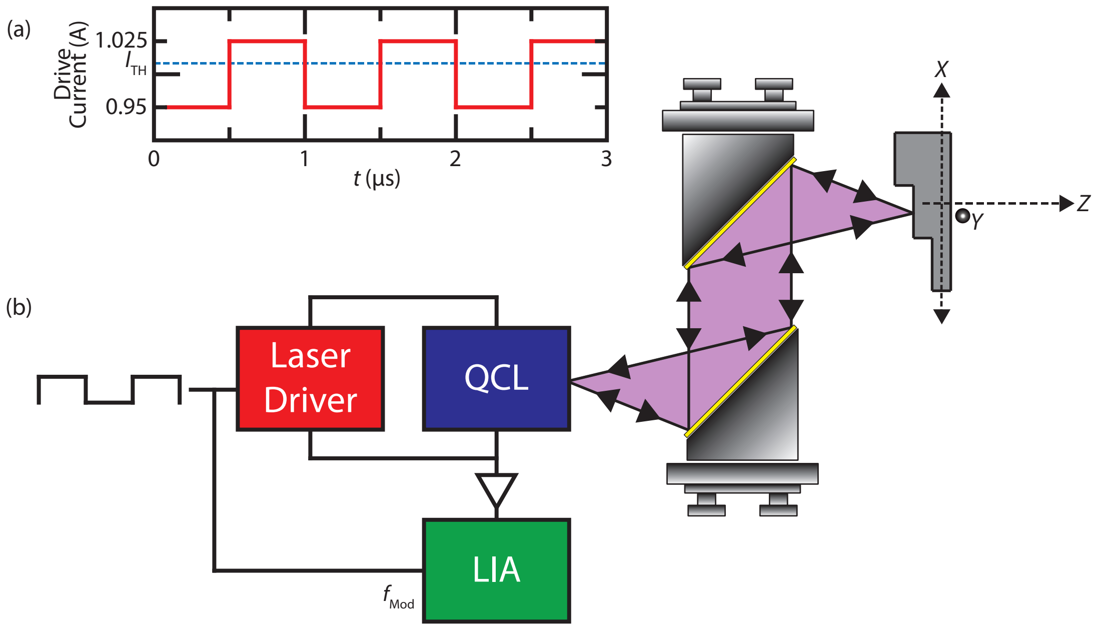

Figure 4.11: Schematic diagram of the experimental apparatus used for 3D SM imaging measurements with electrical modulation.

Using the same technique described for mechanical modulation, the sample was raster-scanned at the beam focus, with a pullback performed at each pixel to produce interferometric fringes, as shown in Fig. 4.12.

The resultant image extracted from these waveforms is shown in Fig. 4.13.

Due to the lower LIA sensitivity native to the electrical modulation technique, the surface profile of the sample is less accurate than that obtained using mechanical modulation. The electrical modulation frequency used in these measurements was 10 kHz, with the same 10 ms TC used as the mechanical modulation measurements, resulting in the

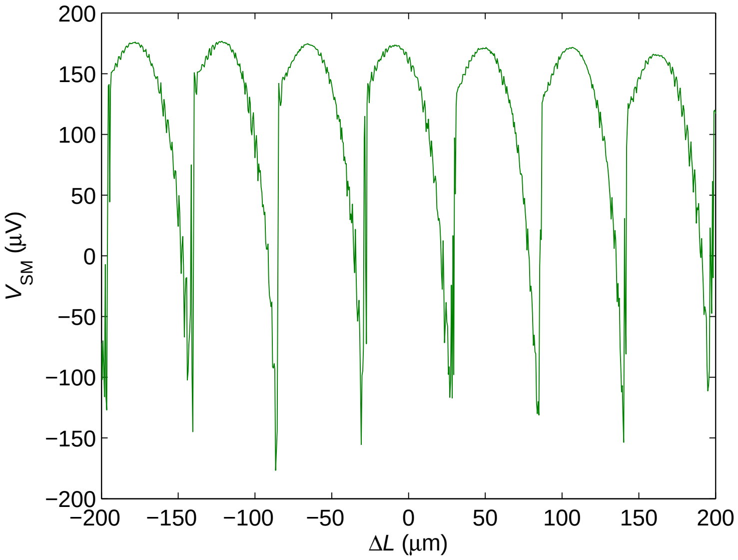

Figure 4.12: Exemplar interferometric fringes obtained using electrical modulation.

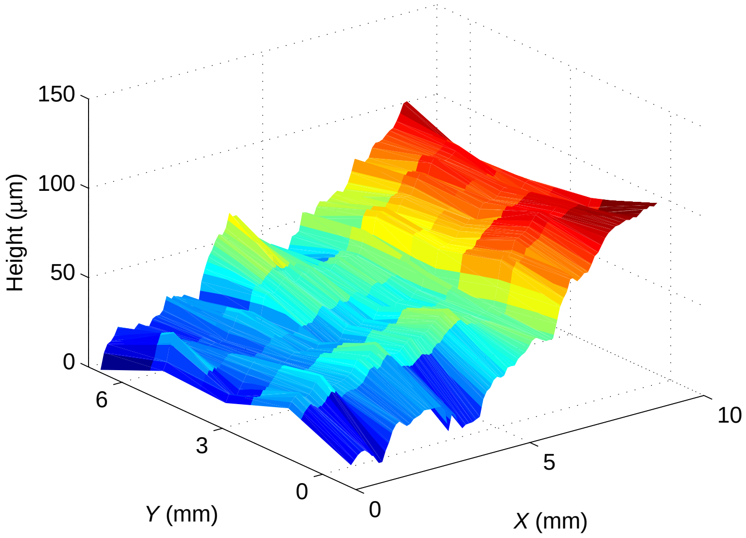

Figure 4.13: Experimental data showing the surface profile of the sample measured using electrical modulation. Colour scale depicts sample height.

same imaging rate of 20 secs/pixel. It is expected that image quality and speed could be further improved by increasing the modulation frequency. Averaging through the use of multiple pull backs per pixel could also be utilised, and the TC of the LIA could also be increased, but both of these would cause longer acquisition times per pixel. A higher imaging speed would also reduce any possible thermal drift that may have been detrimental to the image acquired. Figure 4.14 shows large variations (up to 20 µm) from the image profile expected from the sample. This could potentially be due to the reduced sensitivity or thermal drift in the QCL if there was a temporary problem with the device cooling regulation.

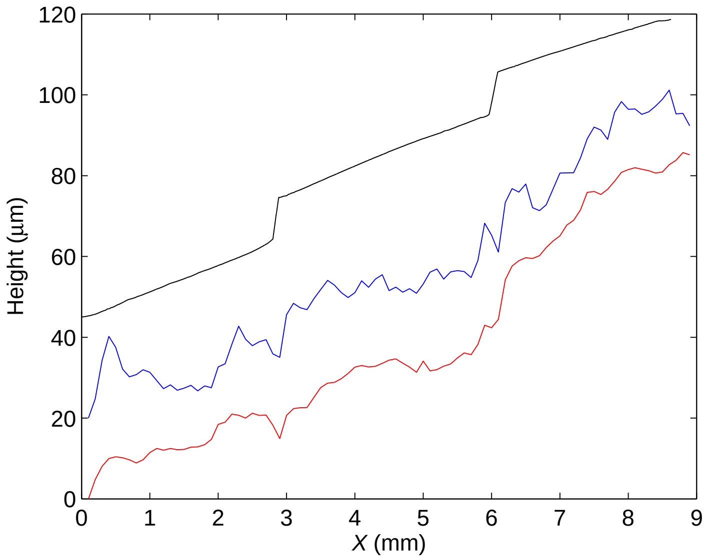

Figure 4.14: Experimental data showing side profiles of the sample surface obtained using electrical modulation. An optical profile from a Bruker Optical Profilometer (black), an exemplar profile (blue) and the average profile along the entire sample surface (red) are displayed. Plots offset for clarity. A tilt has been applied to the optical profile to match the measured profiles.

The amplitude of V_{SM} was also extracted across the surface of the sample as a measure of surface reflectivity, and shows a high area of reflectivity along the gold-coated area of the sample. A similar reflectivity profile as observed with the mechanical modulation is observed, where some of the non-gold-coated areas (such as (6,-0.75) to (8,3.75) in Fig. 4.15) show a higher than expected reflectivity. Again this could be attributed to a better coupling factor, ϵ, on this area due to variations in the surface morphology due to the etching process.

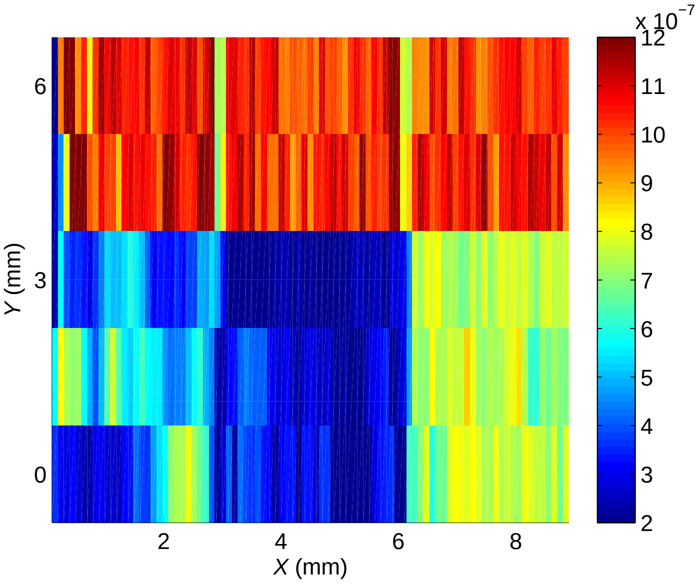

Figure 4.15: Experimental data showing reflectivity across the surface of the sample. Gold coated regions are depicted as areas of high reflectivity, denoted by the color scale.

Due to the operational nature of electrical modulation, where the driving signal of the QCL is not constant, a range of noise sources are imposed into the system. These include noise sources that are present in any THz QCL imaging system such as voltage noise from the current driver and thermal fluctuations in the laser and electrical noise in the LIA. However, current and thermal fluctuations due to the modulation scheme will also cause frequency drift within the device, which will translate to voltage fluctuations on the terminal of the QCL. The higher modulation frequency helps to reduce 1/f noise in an effort to counteract this, but all of these noise sources combined mean that the measurements of surface reflectivity here demonstrates a higher level of noise than that measured by the mechanically modulated approach. The use of an even higher modulation frequency could help to reduce 1/f noise further to improve this. By superimposing Fig. 4.15 onto Fig. 4.13 the depth profile and reflectivity map of the sample can both be shown together, and this is shown in Fig. 4.16.

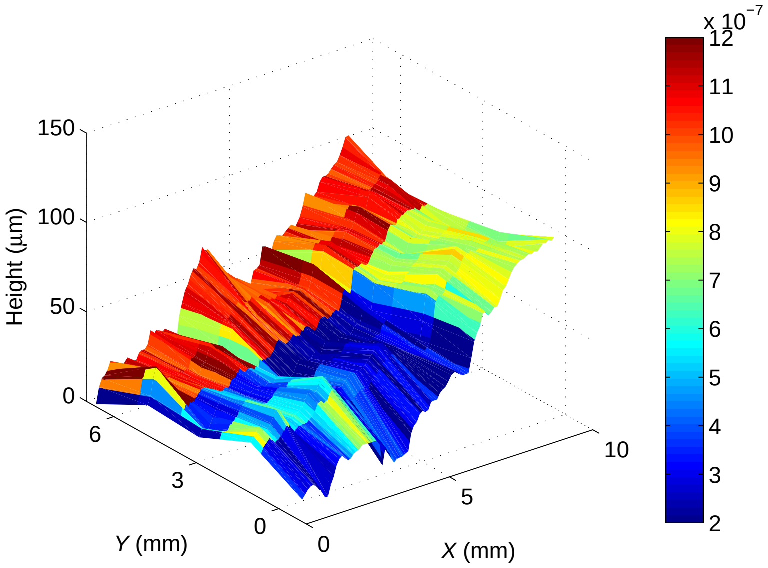

Figure 4.16: Experimental data showing depth profile of the sample surface. Sample reflectivity is shown as the colour of the plot. Gold coated regions are depicted as areas of high reflectivity, denoted by the color scale.

4.4 Discussion & limitations of 3D imaging with mechanical pullback

While this method to produce a 3D profile from the phase of the measured interferometric fringes works well, the main limitation is the image acquisition speed. The main reason the images in the above sections consist of only 89×5 pixels is that it took 20 seconds to acquire the fringes for an individual pixel. This means that a whole 3D scan over roughly $6\,\text{mm} \times 9\,\text{mm}$ took approximately 2 hours. When utilising an SM system over a scan period of that duration, good control of the QCL temperature is a concern as even a frequency drift of ~60 MHz would equate to a resolution change of ~10 µm meaning the step changes of the sample would be unmeasurable.

Another limitation is the method of fitting the 3-mirror-model as a form of analysis. This method takes an extremely long time to fit the fringes for an entire sample; due to the complex nature of the fit, even running across 8 parallel threads on 4 CPU cores at 3.2 GHz with 4 free parameters, the fitting takes ~24 hours. By reducing the number of free parameters, this computation time can be reduced but this also negatively affects the accuracy of the fit. Another problem is that the interferometric fringes extracted from the measurement sometimes aren't clean sinusoidal-like responses (an example is shown in Fig. 4.17), for example in pixels where the incident beam overlaps multiple steps on the sample. This can lead to a poor fit and incorrect extraction of parameters from the data.

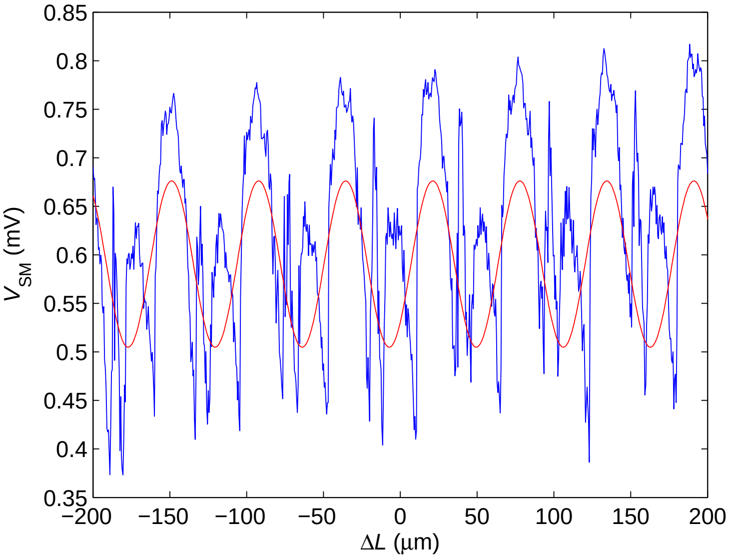

Figure 4.17: Interferometric fringes from certain pixels have non-sinusoidal shapes resulting in poor fitting and incorrect extraction of laser and feedback parameters.

Chapter 5 introduces a different analysis technique that is based on a Fast Fourier Transform (FFT) of the interferometric data to extract the phase and amplitude of the fringes. This technique proved to be orders of magnitude faster (<1 minute compared to ~24 hours) whilst producing comparable results. This technique was used to analyse the same data from the mechanical and electrical modulation experiments and the 3D surface images for the two analysis methods are shown below in Fig. 4.18 for comparison.

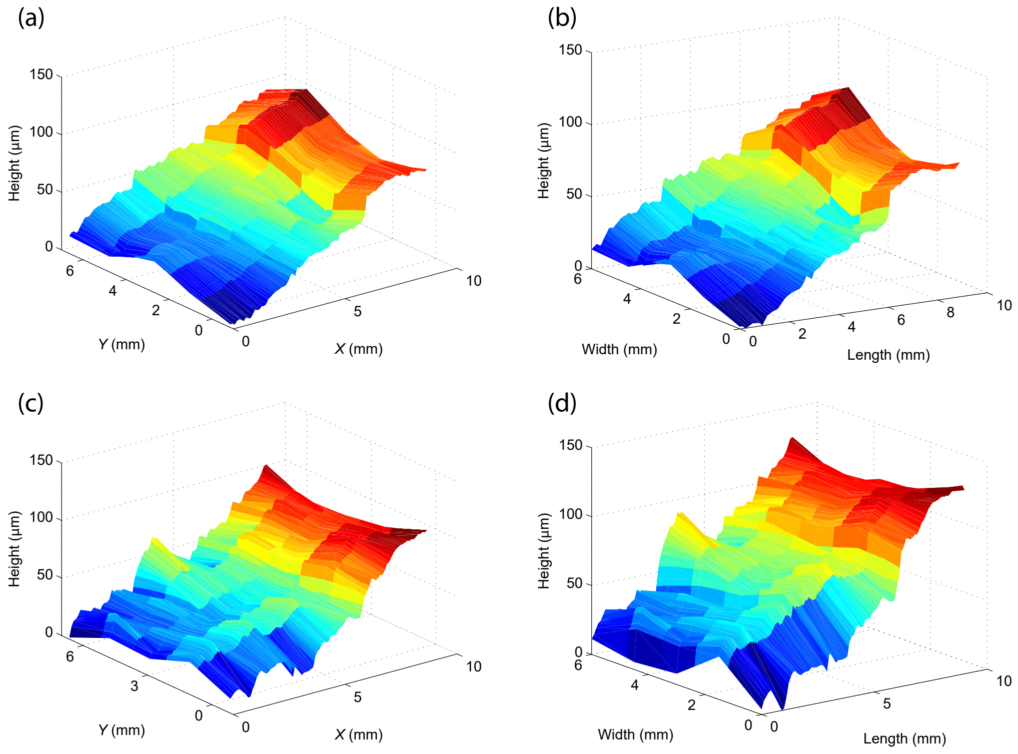

Figure 4.18: 3D coherent images measured using the mechanical (top) and electrical (bottom) modulation schemes. The images were constructed by (a) and (c) fitting a 3-mirror-model to the interferometric data and (b) and (d) performing an FFT on each set of interferometric fringes to extract the phase of each pixel.

5 SM techniques based on frequency modulation

The previous chapter demonstrated 3D THz image acquisition employing the self-mixing effect, based on longitudinal extension of the external cavity at each pixel. However, this mechanical cavity extension resulted in long acquisition times. In order to improve the acquisition rate of the system, a different approach is required. To this end, techniques based on swept-frequency modulation have been developed, with the additional advantage of removing further mechanical components from the system. In this chapter, these techniques are used for 3D image acquisition,[207] with substantially improved imaging rates. The swept-frequency approach is also applied to the analysis of inhomogeneous materials (plastic explosives), leading to extraction of their optical constants. Furthermore, frequency control of a QCL under feedback is used to demonstrate both real-time measurement of the frequency tuning coefficient of the QCL, k, and vibration sensing of moving targets.

5.1 Swept-frequency modulation of the QCL

In the previous mechanically modulated 3D imaging system, the QCL was driven at a constant current and the external cavity length was changed. This allowed the acquisition of interferometric fringes via the QCL terminal voltage as the round trip phase of the external cavity changed. The new modulation scheme presented here takes advantage of the relationship between the laser emission frequency and driving current. By applying a sawtooth modulation to the driving current the laser frequency is chirped, similarly leading to interferometric oscillations of the QCL voltage as the round-trip phase of the external cavity changes. In this way, the previous technique is flipped on its head, with the external cavity length being held constant, and the laser frequency being controlled.

5.2 Three-dimensional swept-frequency imaging

The initial application for this new technique was to improve the imaging rate and quality of the 3D images previously acquired using the mechanical pullback technique. Due to the mechanical longitudinal scan of the sample along the beam axis the previous technique required several hours to produce a 3D image with low transverse resolution (89×5 pixels). As with the mechanical pullback technique both sample height and reflectivity can be obtained with this swept-frequency technique, through the phase and amplitude components of the SM voltage signal.

5.2.1 Experimental set-up & measurement technique

The system used in this work is based on that described in Fig. 3.11[160] and is shown in Fig. 5.1. The THz QCL consisted of a 10-μm-thick BTC active region[183] emitting at ~2.65 THz ($\lambda \approx$113 μm), which was processed into a SISP ridge waveguide with dimensions of 3 mm × 140 μm. The device was cooled using a continuous flow helium cryostat and maintained at a heat-sink temperature of 25±0.1 K. The threshold current at 25 K was 1000 mA. Radiation from the laser was focused onto the sample using a pair of 2-inch-diameter $f/2$ off-axis parabolic reflectors, with the mean distance between the laser facet and the target being 0.41 m through an unpurged atmosphere. The beam spot size on the sample is estimated to be ~250 μm.[65] The laser radiation reflected from the sample was coupled back to the QCL facet along the same optical path as the emitted beam. A current source was used to drive the laser at a constant current of 1050 mA, with a sawtooth current modulation of frequency $f_{\mathrm{mod}}\approx$1 kHz (90% duty cycle) and an amplitude of 100 mA superimposed on the DC current; the corresponding modulation of the QCL emission frequency was measured to be 850 MHz (see Ch. 5.4), maintaining single mode emission throughout this range. Schematic diagrams of these signals are demonstrated in Fig. 5.2. The SM signal was monitored via the QCL terminal voltage, amplified using a 20 dB AC-coupled amplifier. In contrast to the previous modulation techniques, a LIA was not used to record the terminal voltage in these measurements. In order to allow a higher degree of averaging at a higher speed than was possible with the LIA (limited by a minimum LIA TC of 5 ms due to a buffer trigger rate of 200 Hz), a National Instruments data acquisition (DAQ) board (NI-DAQmx USB-6251 BNC) was used to acquire the QCL voltage directly. This allowed the SM waveform to be acquired at 500×10^3 samples/s with

16-bit resolution. The high speed of this acquisition allowed a high modulation frequency (1 kHz) to be used to modulate the QCL. The TTL signal from the signal generator that created the sawtooth (90% duty) modulation was used as a trigger to the DAQ board. In order to recover the SM interferometric fringes from the recorded QCL terminal voltage it was necessary to subtract the baseline modulation as discussed below.

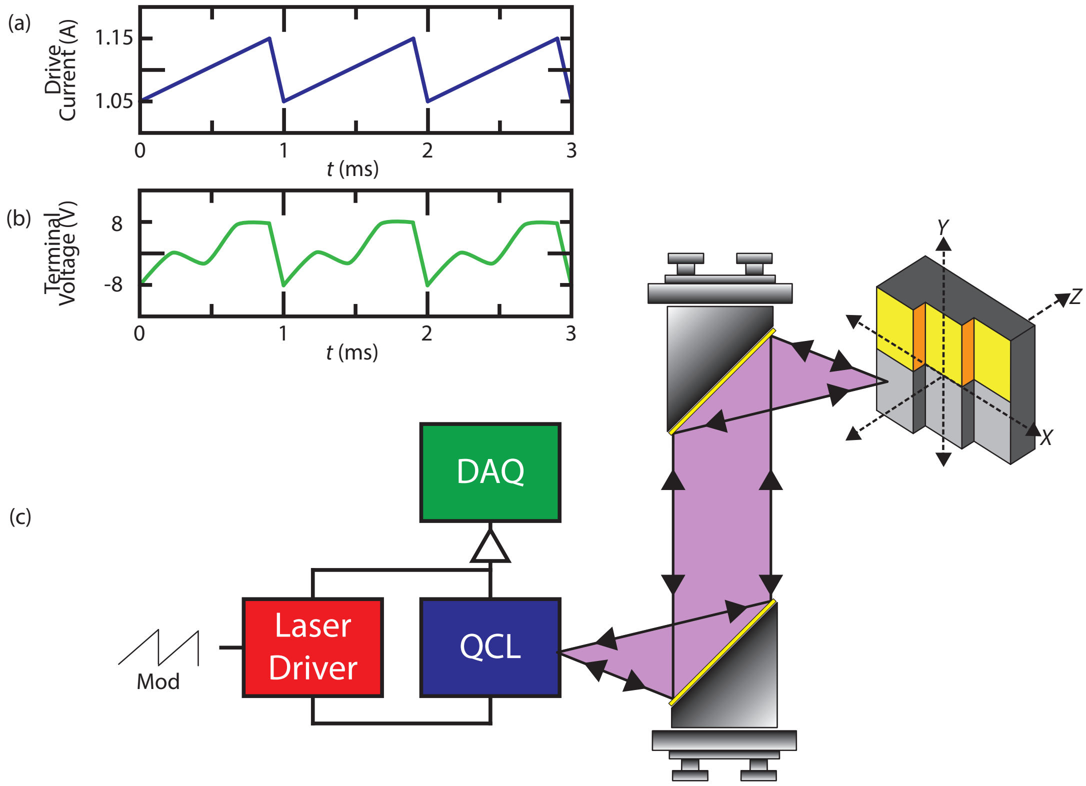

Figure 5.1: Schematic diagram of the experimental apparatus used for swept-frequency measurements. (a) The laser driver current was modulated to chirp the single mode QCL emission frequency where the QCL was most sensitive to optical feedback. Typical modulation currents for this experiment are shown. (b) Measured AC coupled terminal voltage measurements. The voltage signal shown is typical for this set-up after applying amplification. (c) The QCL is driven using a DC laser driver with a sawtooth modulation while a data acquisition (DAQ) board is used to record the QCL terminal voltage. A pair of parabolic mirrors focus the QCL beam to a point, at which the sample is raster scanned in the X- and Y-directions using computer controlled mechanical translation stages. 20 dB differential amplification was applied prior to measurement on the DAC board.

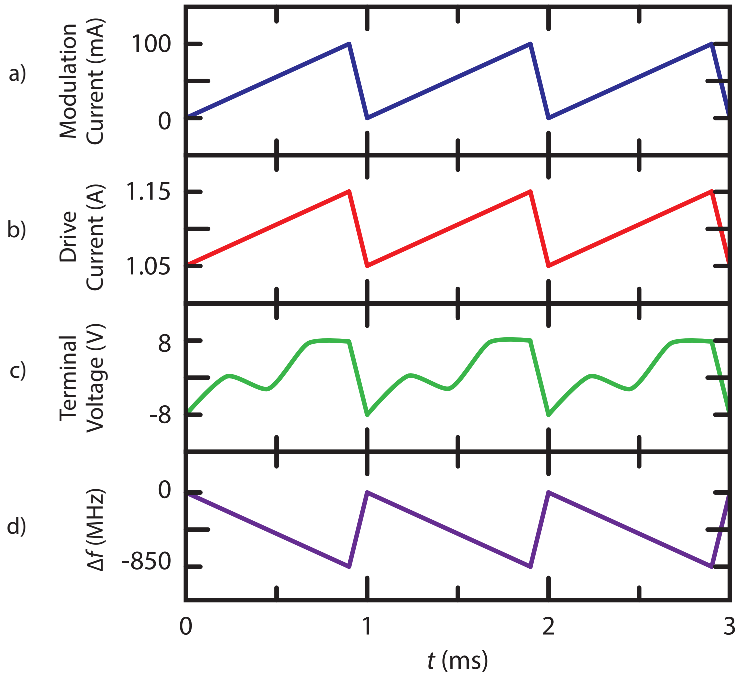

Figure 5.2: Schematic diagram of the waveforms involved in swept-frequency imaging. (a) The modulation current supplied by the signal generator as a modulation to the laser driver. (b) The QCL drive current delivered by the laser driver from 1050 mA with 100 mA modulation. (c) The amplified (20 dB) terminal voltage into the DAQ board showing interferometric fringes due to the changing QCL emission frequency. (d) Change in QCL emission frequency over the modulation period.

5.2.2 Baseline removal of the background modulation

The QCL terminal voltage without feedback is a combination of the DC voltage used to drive the laser above threshold and the sawtooth modulation voltage. Under feedback, the SM fringes (∼1 mV) are superimposed onto this voltage (∼5 V). To extract the interferometric fringes created by the sawtooth modulation of the QCL current, the background modulation must first be removed. To obtain the background modulation, the laser terminal voltage was measured with the THz beam blocked, and this waveform was subtracted from the terminal voltage measured under feedback. Exemplar waveforms of the laser voltage, with and without feedback, and the resolved interferometric fringes are shown in Fig. 5.3.

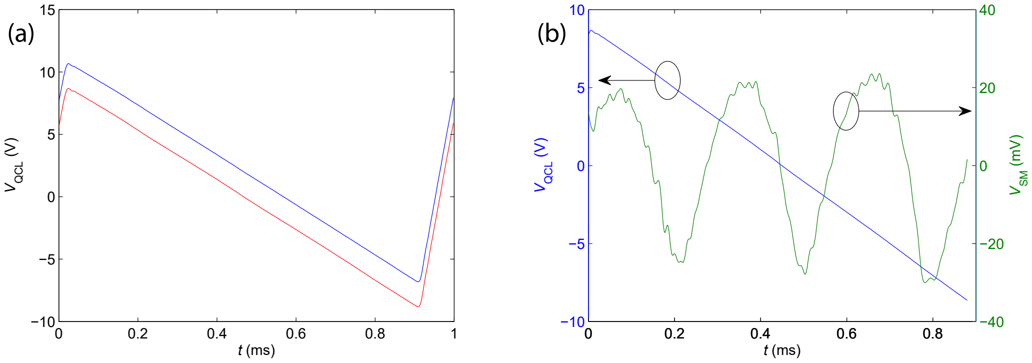

Figure 5.3: Recovering interferometric fringes from frequency chirping of the QCL. (a) Terminal voltage of the QCL with (red) and without (blue) feedback. Waveforms offset for clarity.(b) Interferometric fringes resolved from measured QCL terminal voltage. Voltage, V_{QCL_0} (no feedback) has been removed from voltage, V_{QCL} (with feedback), to leave V_{SM}. The voltage signals here are amplified by 20 dB.

In order to obtain the required number of interferometric fringes using this technique, the QCL must be tuned sufficiently to cause multiple fringes to occur over the applied sawtooth waveform. If the QCL was tuned too much, the resolution of the interferometric fringes would suffer due to the sampling rate and voltage resolution limits of the DAQ. By utilising the tuning coefficient of the QCL, a sensible starting value of modulation current can be applied. THz QCL's typically exhibit a tuning coefficient on the order of $k \approx -10\,\mathrm{MHz/mA}$.[59] In order to obtain the frequency tuning required for 3 interferometric fringes over a cavity length of 0.41 m, Eq. (4.4) can be used. The required number of fringes can be equated to the change in external cavity length in a double path system,

$$\Delta L = \frac{3\lambda}{2} = \frac{3c}{2\nu}, \tag{5.1}$$

which allows Eq. (4.4) to be simplified to

$$\Delta\nu = \frac{3c}{2L}. \tag{5.2}$$

For the cavity length of the described system, 0.41 m, a tuning value of $\Delta\nu = 1098\,\mathrm{MHz}$ is required, meaning a starting modulation of 110 mA was employed. The laser driver had a transconductance $G = 200\,\mathrm{mA/V}$ at it's modulation input, so to cause a current modulation of 110 mA, a 550 mV sawtooth waveform was required.

Once a modulation amplitude was chosen, the initial starting current was optimised in order to obtain the cleanest interferometric fringes. When the QCL was driven at I_{TH}, 1000 mA, the fringes had a large amplitude, but displayed a non-consistent amplitude over the tuning range. This could be a consequence of the fact that, in QCLs and other lasers, the magnitude of SM voltage signal is itself dependent on the driving current, as previously shown in Fig. 3.31.[65] By driving the QCL at a slightly higher "starting current, 1050 mA, the fringe amplitude decreased slightly, but the amplitude remained constant over the tuning range. These results are shown in Fig. 5.4.

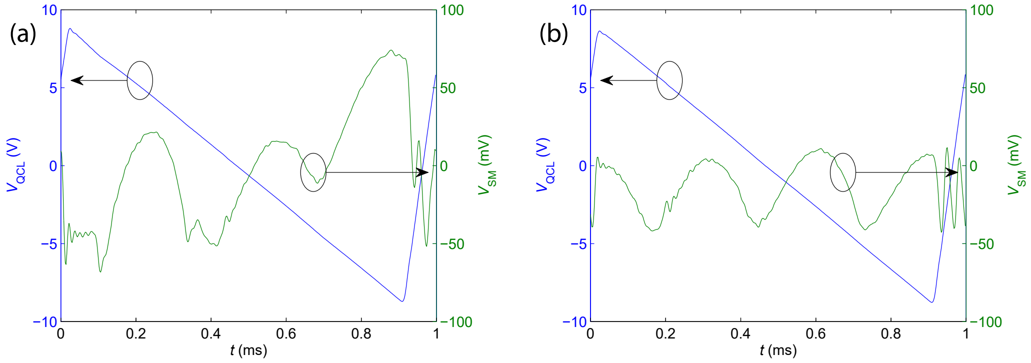

Figure 5.4: Choosing the optimal initial driving current for the QCL using sawtooth modulation. (a) Driving the QCL at 1000 mA resulted in fringes that changed amplitude over the tuning range. (b) Driving at 1050 mA resulted in more sinusoidal fringes with a more consistent amplitude. The voltage signals here are amplified by 20 dB.

5.2.3 Fast Fourier transform (FFT) analysis

At the end of Chapter 4, a new analysis method was briefly discussed. In the previous 3D imaging technique described in Chapter 4 the SM parameters were extracted from each interferometric waveform though a fitting procedure. This method was computationally very time consuming, taking upwards of 24 hours to extract the necessary parameters from the 445 pixels acquired using the mechanical pullback technique. A faster and less computationally demanding method was implemented for the swept-frequency imaging work, which could be used for any 3D imaging with interferometric waveforms.

Once the interferometric fringes have been recovered from the swept-frequency modulated terminal voltage of the QCL by removing the baseline modulation, a complex Fast Fourier Transform (FFT) is performed. A FFT transforms discrete time signals into measurements in the frequency space. The magnitude of the results depict the component of power at each frequency and the phase denotes the phase of the waveform at each frequency. In order to recover a 3D image of the sample we require the phase of the waveform at each pixel; the required information for this can be resolved from the phase of the FFT. Also, the sample surface reflectivity can be recovered from the amplitude of the interferometric fringes, which is given by the complex magnitude of the FFT. The interferometric phase of the SM signal under frequency modulation of the laser is given by[151,176]

$$\Phi(t) = \frac{4\pi L}{c}\gamma t + \frac{4\pi L}{c}\nu_0 = 2\pi f_\mathrm{c} t + \phi, \tag{5.3}$$

where $\phi = \arctan(\mathrm{Im}[\hat{I}(f)]/\mathrm{Re}[\hat{I}(f)])$ is the initial phase of the SM fringe, which can be calculated from the real and imaginary components of the FFT $\hat{I}(f_\mathrm{c})$, ν_0 is the laser frequency without feedback at t = 0, c is the speed of light, L is the external cavity length, γ = -945 GHz/s is the modulation rate of the system, calculated based on the tuning coefficient of the laser ($k \approx -8.5\,\mathrm{MHz/mA}$) and the applied modulation (100 mA over 0.9 ms), and f_c is the carrier frequency of the fringes given by $f_\mathrm{c} = 2\gamma L/c$.

As can be seen from Fig. 5.5(b) the resolution of the FFT is quite low. The frequency resolution of the FFT is dependant on the length of the dataset that the FFT acts upon, so the longer the waveform that can be acquired, the higher the resolution that can be recovered in the frequency space. In order to obtain more fringes a higher degree of tuning could be used, but that would cause mode-hopping to occur in this laser. An alternative approach would be to increase the external cavity length. Nevertheless, the resolution in Fig. 5.5(b) is sufficient to recover the power and phase at the frequency of the interferometric fringes since no other component of power occurs at a similar frequency. Zero-padding can be used to increase FFT resolution if necessary, but in reality this only serves to smooth out the FFT. This technique is demonstrated in Fig. 5.6.

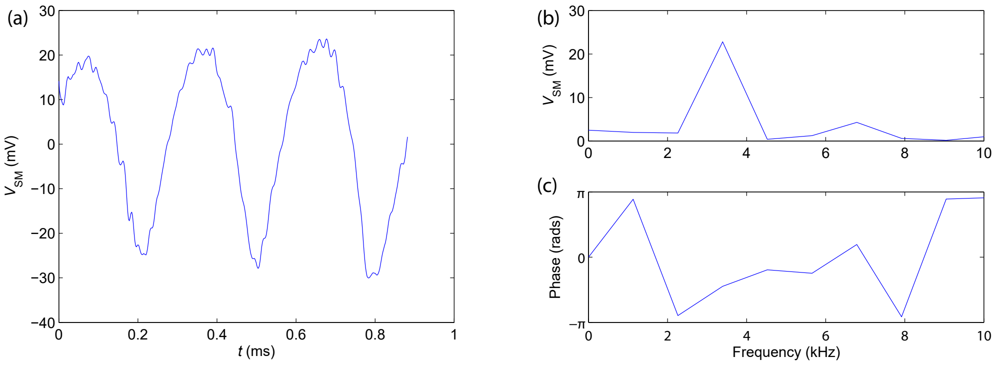

Figure 5.5: FFT analysis for extracting SM parameters from frequency-chirped terminal voltage measurements. (a) Exemplar interferometric waveform extracted by removing the baseline modulation from the recorded terminal voltage. The frequency of the interferometric fringes is 3.8 kHz. (b) Magnitude and (c) phase components of V_{SM} extracted by performing a complex FFT on the aforementioned fringes. Due to the resolution of the FFT, the values corresponding to the interferometric fringes are taken at 3.4 kHz.

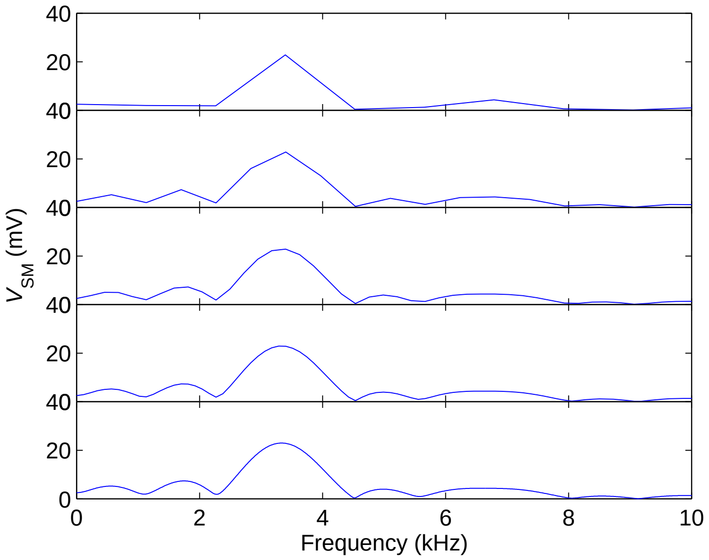

Figure 5.6: Magnitude values extracted from the same interferometric waveform shown in Fig. 5.5(a) with varying levels of zero-padding. From top down, (a) no padding. (b) Zero-padded by N, where N is the length of the original dataset, thereby creating a dataset of length $2N$. (c) Zero-padded to create a dataset of length $5N$. (d) Zero-padded to create a dataset of length $10N$. (e) Zero-padded to create a dataset of length $100N$.

Other techniques such as stitching repetitions of the recovered waveform together in post-analysis can be used to improve resolution, but any discontinuities at the joining point can result in components of power appearing at a high frequency that relates to the sharp discontinuity. By measuring (or truncating) the time-domain data to an integer number of periods (fringes), discontinuities can be minimised. This technique is demonstrated in Fig. 5.7. As there are no other components of power that occur at a frequency close to that of the interferometric fringes, neither of these two techniques are required here to extract an accurate measure of power or phase from the resolved fringes.

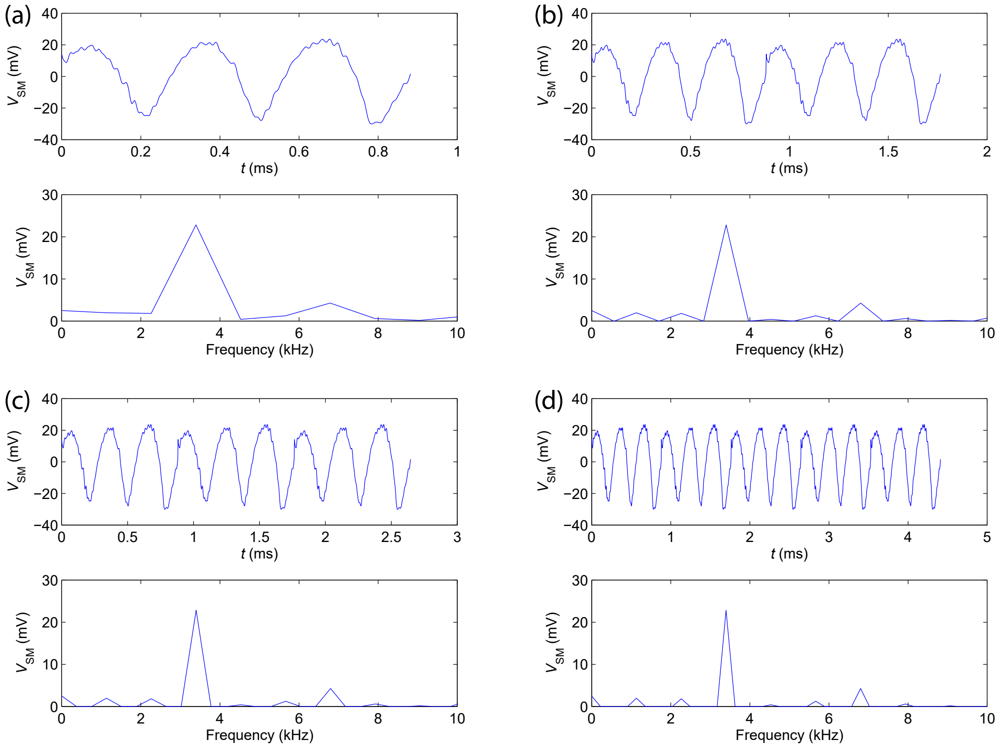

Figure 5.7: FFT resolution can be improved by concatenating numerous iterations of the resolved waveform. Shown are FFT results for (a) 1, (b) 2, (c) 3 and (d) 5 repetitions of the waveform. The FFT becomes zero at frequencies with no power, but frequencies with a power component remain at the correct amplitude.

One disadvantage of this technique when compared to the SM fitting technique is that individual laser parameters aren't extracted. This means that values such as the feedback coefficient cannot be calculated. But for the purpose of creating a 3D representation of a sample and performing a measure of sample surface reflectivity, these parameters aren't necessary and the improvement in computation time of the FFT approach is a significant advantage.

5.2.4 Software development

LabVIEW software was developed in order to obtain the required interferometric fringes at each pixel. The operation of the code is described in Fig. 5.8. The XPS is first initialised and a folder is created to save all of the averaged waveforms. Once the stages and folder are ready, X and Y stages move to their first position and imaging can begin.

The DAQ control (blue) section of the code functions as a state machine. The first state is a trigger creation stage, where a trigger is established on the DAQ, whereby a BNC input to the DAQ board waits for a rising edge of the TTL signal from the signal generator that is used to create the modulation signal. The next state is a trigger monitoring state; this state loops continuously if the trigger isn't activated, but if a rising edge is measured the state machine progresses onto the data acquisition state.

On the front panel of the LabVIEW code, the user specifies a window length in milliseconds and a sampling rate in kilo-samples per second. From these values, a number of samples is calculated, N. Once the measurement state of the LabVIEW code is entered N samples are acquired from the chosen BNC ports (which monitor the QCL terminal voltage), again chosen by the user on the front panel. Once these samples are acquired, they are displayed on the front panel as a graph. To improve imaging quality the user can specify the number of iterations of this measurement to be performed. If the current measurement is not the final iteration, the state machine loops back to the trigger state and awaits the next TTL trigger. If it is the final iteration, the waveforms are averaged and the data is saved with a file name denoting the X and Y imaging locations to allow the 3D image to be created in analysis. If the saved data isn't from the final pixel to be measured, the stages are moved to the next required location and the DAQ stage (blue) occurs again for the new position. The code loops until the final pixel is imaged and then the code ends.

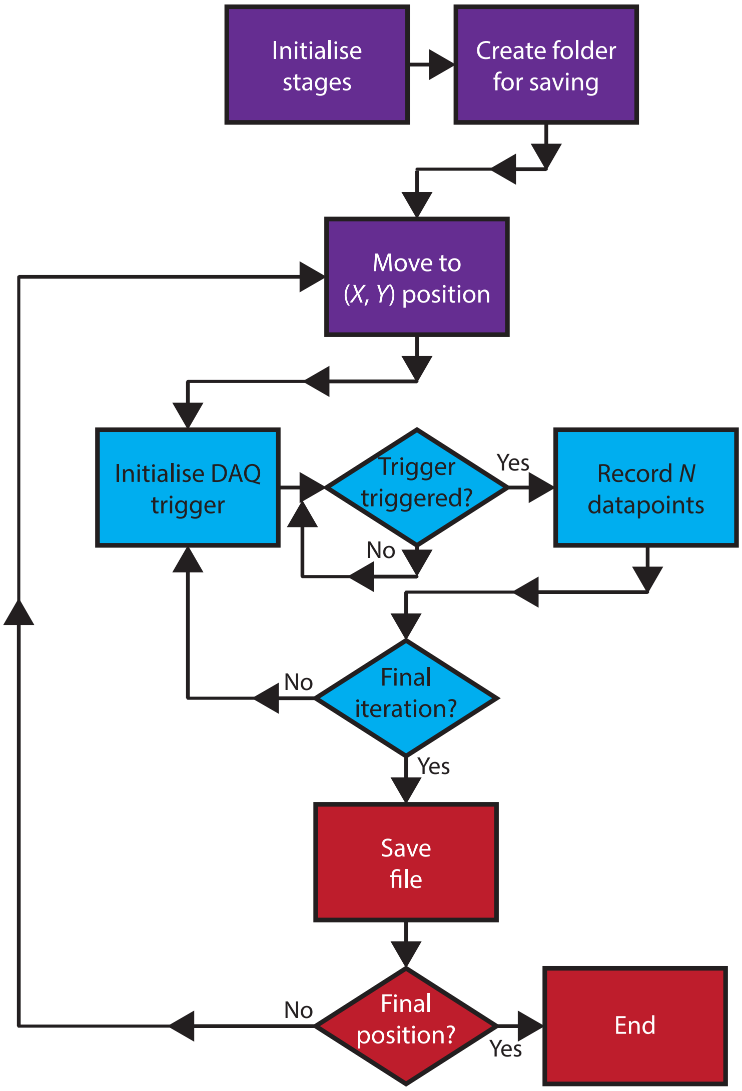

Figure 5.8: Operation of LabVIEW code for performing 3D imaging using frequency chirping of the THz QCL. The main functions can be broken down into XPS control and initialisation (purple), DAQ board control (blue) and saving and completion (red).

5.2.5 Three-dimensional imaging using swept-frequency modulation of the QCL

With the data acquisition and analysis methods understood, the method of creating the 3D image will now be discussed. By removing the mechanical pullback previously used for 3D imaging, the image acquisition rate of the swept-frequency system is significantly improved; $\sim$200 ms/pixel with 200 averages of the SM waveform (limited by computational time as discussed below) compared to 20 secs/pixel previously achieved. This presents an improvement of $\sim \times 100$. Due to the improved imaging rate of the swept-frequency system, an image with much higher transverse resolution (101×10 pixels) could be acquired in a shorter time ($\sim$minutes) than the previous imaging systems ($\sim$hours).

The sample imaged consisted of bulk GaAs semiconductor wet-etched to 3 different steps (in the X-dimension) of height 10 µm. Half of this sample was then coated with 125-nm-thick layer of gold resulting in areas of differing height and reflectivity. 200 iterations of the acquired SM signal were averaged at each pixel.

After the interferometric fringes were recovered from the measured terminal voltage by removing the baseline modulation, the FFT analysis can be performed. Fig. 5.9 demonstrates fringes from two different areas of the sample; waveform (a) is from a gold area of the sample, depicted by its large amplitude, and (b) is from a GaAs area, shown by its lower amplitude. The two waveforms are also from two different steps of the sample surface as shown by their different phase values, meaning a difference in cavity length is present.

The magnitude of the FFT of waveform (a) is shown in the inset, showing an amplitude of $\sim$24 mV, which the waveform shows to be correct. This analysis is performed for each pixel in order to extract the phase of the FFT to resolve the phase profile of the sample. Due to the fact that the phase values from the FFT lie between $-\pi$ and π, unwrapping is required across the sample surface to remove discontinuities. The wrapped surface profile is shown in Fig. 5.10, but even at this early stage the 3 distinct steps are visible, but not necessarily with the correct height.

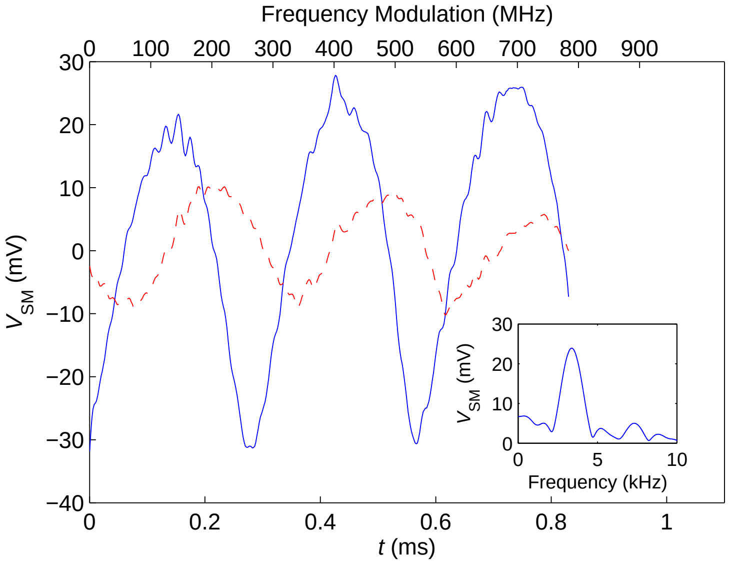

Figure 5.9: Interferometric fringes extracted from 2 different steps on the sample. The blue waveform (a) is from a gold covered region, as shown by its larger amplitude due to higher reflectivity, while the red waveform (b) is from a GaAs region, on another step, as shown by the phase delay between the waveforms. Inset: Fourier transform of waveform (a). Both waveforms are amplified by 20 dB.

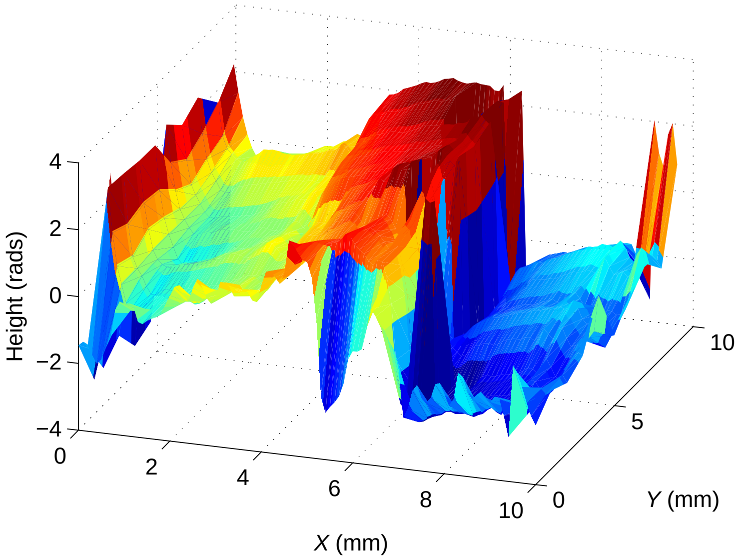

Figure 5.10: Wrapped phase profile of the sample obtained using the swept-frequency technique.

By performing unwrapping a phase map of the sample surface was obtained. The image was also slightly cropped, to remove the edges of the sample, to avoid them effecting the unwrapping procedure. The unwrapped phase map is shown in Fig. 5.11.

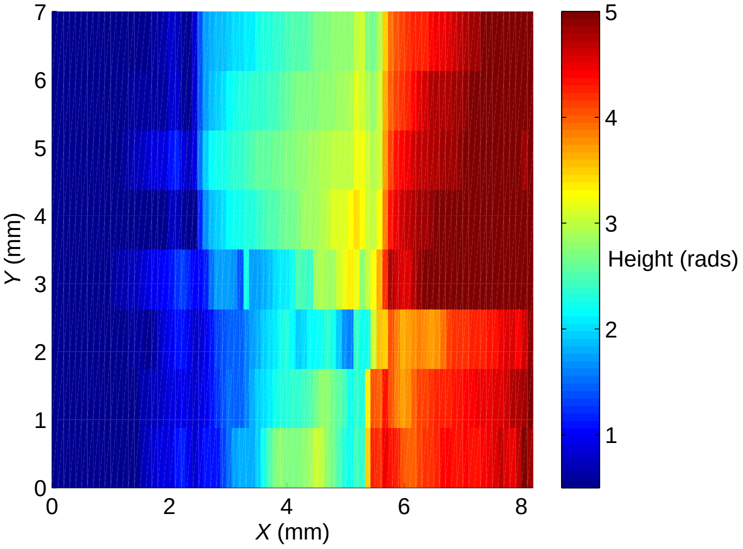

Figure 5.11: 2D height map of the sample showing 3 distinct steps.

In order to create a true 3D profile of the sample the phase map must be converted into a height map using the laser emission frequency and accounting for the double pass of the SM system[151]

$$dL = \frac{\phi\lambda}{4\pi}, \tag{5.4}$$

assuming no phase change on reflection due to the permittivity of the sample. The result of this is shown in Fig. 5.12.

Comparing the measured profile of the sample to the profile obtained from an optical profilometer (Bruker NPFLEX 3D) demonstrates the accuracy of the swept-frequency method for 3D imaging. Figure 5.13(a) compares the optical profile (black) to the average profile obtained from all rows of the sample in the Y-direction (red) and an exemplar row (blue). As the surface of the sample wasn't exactly perpendicular to the THz beam, a 0.356° tilt has been applied to the optical profile in this figure. The average profiles of the gold and GaAs areas of the sample are shown in Fig. 5.13(b). The imperfections observed

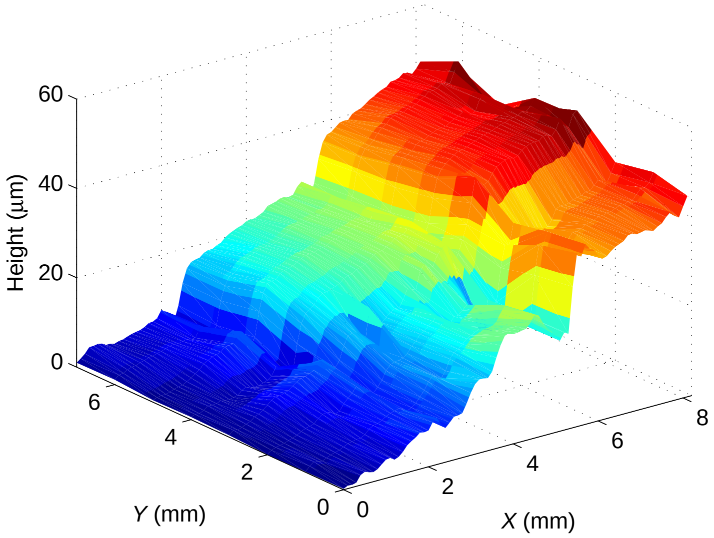

Figure 5.12: Three dimensional profile of the sample built using the phase extracted from an interferometric fringe at each pixel. Colour scale represents sample height.

at each step in the obtained profiles can be attributed to the spot of the beam overlapping the edge of the step, resulting in reflections from multiple lengths at the same time. This could potentially be improved by improving the size of the beam spot size at the focus.

As can be seen in Fig. 5.14, by superimposing the averaged profile onto the optical profile, the step height measured by the SM approach is reasonably accurate.

The reflectivity map of the surface was also extracted from the real component of the FFT at the carrier frequency, $|\hat{I}(f_c)|$, for each pixel; this is shown in Fig. 5.15. The reflectivity map shows a very high reflectivity on the gold-covered region of the sample (3.5-7 mm in the Y dimension) as expected. As with the previous 3D imaging technique, changes in the coupling efficiency of the reflected radiation to the laser facet between different steps result in differences in reflectivity across areas of identical material; this can be attributed to variations in surface morphology due to the wet-etching procedure.

The higher resolution allowed by the increased acquisition speed in this set-up results in a much better image than was previously available using THz SM imaging. Further to this the sample doesn't move longitudinally through the beam focus during acquisition of data, meaning better transverse resolution and a more consistent coupling efficiency

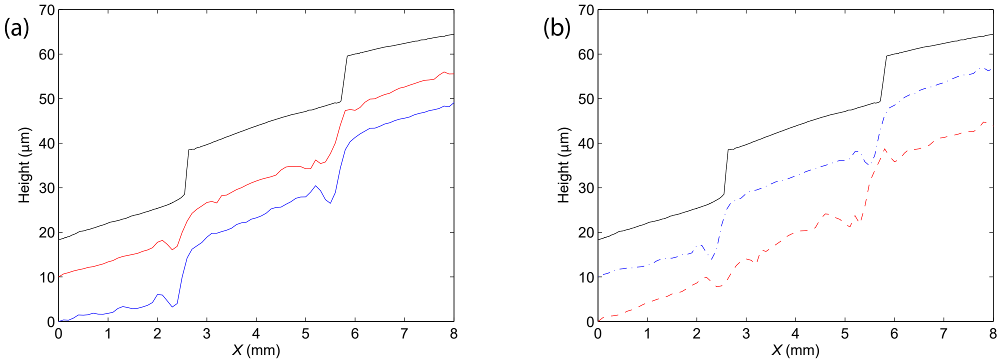

Figure 5.13: Surface profiles of the sample. (a) The red (center) profile shows the average of all the whole sample, while blue (bottom) displays an exemplar row. The black (top) profile is the average of the whole sample from an optical profilometer for comparison. Waveforms offset vertically for clarity. (b) Optical profile is compared to the average of the gold region of the sample (blue, center, dashed), and the GaAs region of the sample (red, bottom, dashed).

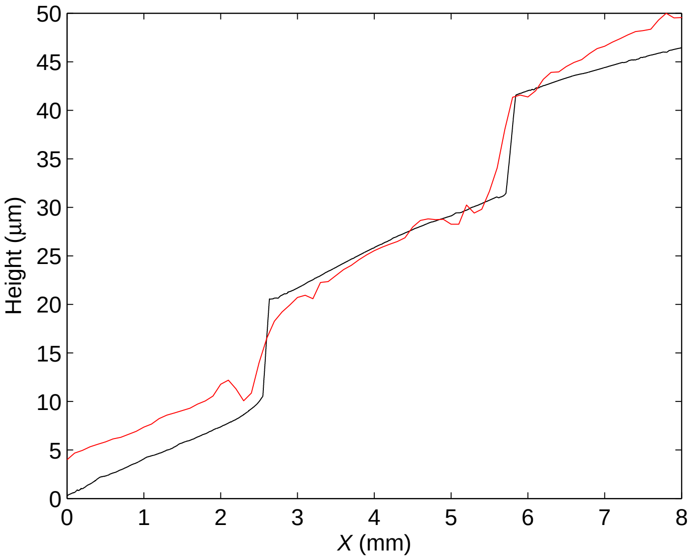

Figure 5.14: Optical profile (black) and the average side profile (red) obtained through 3D swept-frequency imaging shows the accuracy of the measured sample height of the new technique.

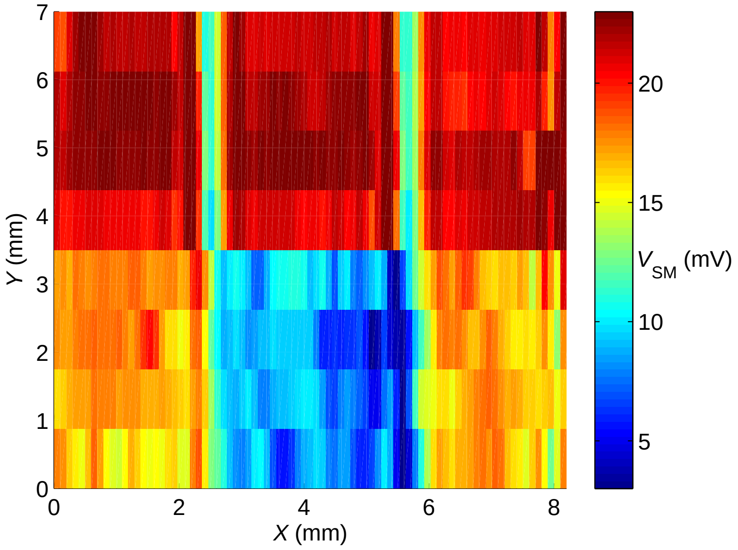

Figure 5.15: 2D reflectivity map showing the region of high reflectivity gold on top and low reflectivity GaAs below. Differences in reflectivity between steps are due to changes in coupling efficiency of radiation to the laser facet.

throughout the scan. This further improves the accuracy of the images. By superimposing the reflectivity map from Fig. 5.15 onto the 3D profile, a full representation of the sample can be created; shown in Fig. 5.16.

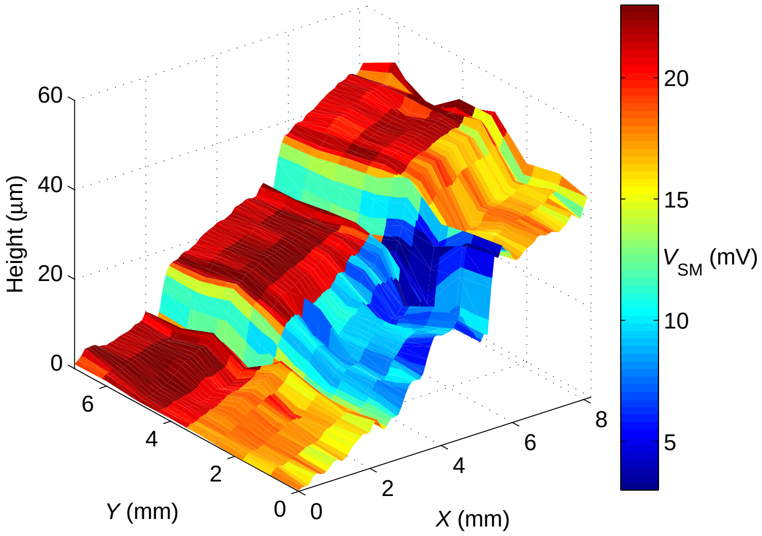

Figure 5.16: Three dimensional profile of sample built using the phase extracted from an interferometric fringe at each pixel. Colour scale represents sample surface reflectivity.

5.2.6 SNR & depth resolution quantification of the technique

The depth resolution of the swept-frequency technique can be influenced by voltage noise present in the SM waveforms. This noise can be reduced through the use of waveform averaging at the expense of imaging speed. A secondary source of depth resolution degradation in this system is the frequency instability of the laser, caused by temperature and current fluctuations. Thermal drift in particular can cause frequency drifts on the order of several MHz over the time-scale of seconds.[84,85] In the presented system, temperature instabilities of ±100 mK corresponds to a maximum frequency drift of ∼10 MHz.[85] As such, long averaging can in fact be detrimental to the depth resolution by allowing more frequency drift to occur.

With this system, variations in the permittivity of the sample can also result in a measurable phase change, which could be misconstrued as a change in the depth of the sample. Also, changes in coupling between the sample and the laser can result in variations in the measured amplitude of V_{SM}. These coupling variations can be caused by changes in the angle of the sample surface relative to the laser, or through depth changes resulting in the sample being no longer in the focus of the field. This change in V_{SM} can be incorrectly attributed to changes in reflectivity.

In order to quantify the depth resolution, and also determine the optimal amount of averaging required to obtain the best depth resolution, a statistical measurement of the depth was performed. In this measurement a mirror was used to create an external cavity with the laser facet. The length of this cavity was held at a known, stationary length L to remove any systematic effects of the system, and 50 SM waveforms were acquired consecutively, using the driving conditions described above for 3D imaging. From each of these waveforms the phase was extracted by FFT and converted to a change in cavity length using Eq. (5.4). The statistical variation of these measurements was then established by taking the standard deviation. This was repeated for various degrees of waveform averaging. If too much averaging was performed, the depth resolution would degrade as the acquisition time would increase, allowing more frequency drift to occur.

If too little averaging was performed, voltage noise wouldn't be averaged out to a high enough degree, leading to poor depth resolution. The results of these measurements are shown in Fig. 5.17.

For levels of averaging below 10 iterations, the variation in measured external cavity length decreases with increased averaging, due to the reduction of voltage noise. Beyond this, low frequency drift of the laser frequency results in an increase of variation in consecutive measurements of the cavity length, with variations of up to ±2µm at 2000-times averaging. This standard deviation, σ_{L}, can be plotted against the degrees of averaging in order to find the optimum. The results of this are shown in Fig. 5.18.

As shown, 10 iterations is the optimum degree of averaging to perform, giving a depth resolution of <0.1 µm (corresponding to a phase change of $\Delta\phi \approx 0.6\,\mathrm{deg}$).

In addition to these statistical errors, systematic errors may also affect the measurement of depth using this system. In order to investigate possible systematic errors a measurement was performed in which the cavity length was stepped in 1 µm steps and a swept-frequency measurement performed at each step. This measurement was repeated for various degrees of averaging. The results of these measurements are shown in Fig. 5.19.

As can be seen, the resolved cavity length is not heavily dependent on the level of averaging, and does not improve much through further averaging. Furthermore, the resolved position of the mirror consistently shows an error for certain mirror positions (~4 µm at $\Delta L = 12\,\mu\mathrm{m}$ for example) across all levels of averaging. This could be due to the mirror rotating laterally as it moves between scans, slightly perturbing the cavity length and altering the coupling back into the laser facet. Another reason could be systematic error in the positioning of the mirror by the motion controller. Neither of these possibilities imply an error in the measurement technique itself.

By taking the standard deviation of the measured cavity length compared to the expected cavity length, the accuracy of the measured cavity length can be determined. This is shown in Fig. 5.20, and reveals a systematic error of ~1.9 µm, which improves slightly through averaging. As the mechanical components of the experiment have an effect on this

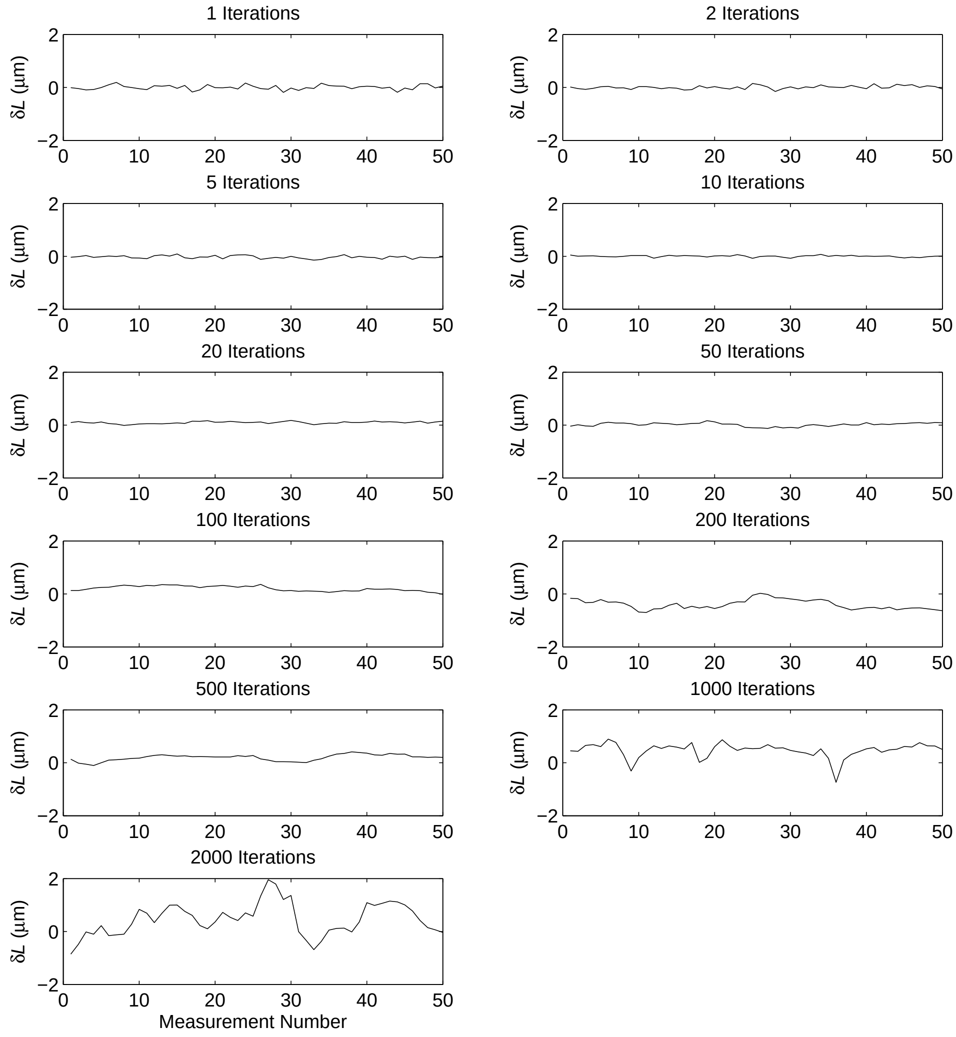

Figure 5.17: Resolved cavity lengths of 50 consecutive swept-frequency measurements were extracted for various degrees of waveform averaging. Plotted are the variation of these individual measurements from their mean.

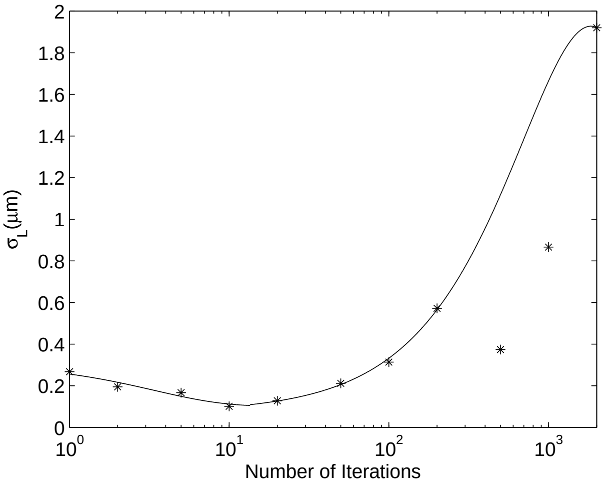

Figure 5.18: Standard deviation of the measured external cavity length as a function of waveform averaging for a held cavity length. This plot shows a measure of the statistical error of the system. Fitted line added to guide the eye.

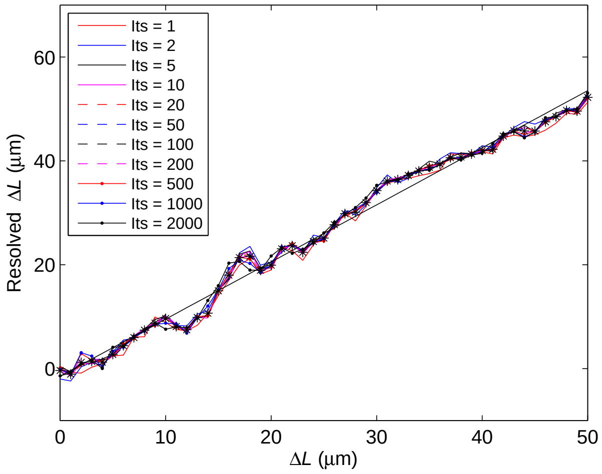

Figure 5.19: Resolved cavity length from swept-frequency modulation compared to actual cavity length for various degrees of waveform averaging.

measurement, this graph represents a systematic measure of the accuracy of the system.

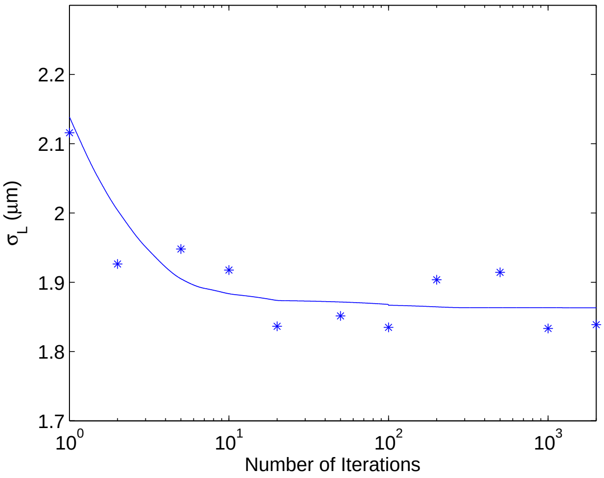

Figure 5.20: Standard deviation of the measured external cavity length compared to the actual external cavity length as a function of waveform averaging. A slight improvement is shown up to ∼200 iterations. Fitted line added to guide the eye.

The magnitude of both the systematic and statistical errors are compared in Fig. 5.21. For the system described above, in an ideal scenario with no systematic error, a depth resolution of <0.1 µm (corresponding to a phase change of $\Delta\varphi \approx 0.6\,\text{deg}$)could be obtained using 10 iterations of waveform averaging. Even allowing for systematic errors, which could arise from the mechanical components in the system rather than the measurement itself, a depth resolution of <2 µm is possible. This is much below the step height of 10 µm of the sample imaged, meaning an accurate representation of the sample was possible. For averaging above 2000 iterations, statistical error becomes the major source of error in the resolved depth.

Due to the computation time to control the movement of the stages and to average the waveforms, performing an acquisition takes longer than that implied by the sampling time per pixel, $t_{\text{samp}}N/f_{\text{mod}}$. In order to quantify the actual acquisition time per pixel for the various levels of averaging, 101 pixels were acquired in succession for various degrees of waveform averaging at a modulation rate of 1 kHz. The results of these measurements are shown in Fig. 5.22.

Figure 5.22 shows that the acquisition time per pixel rises with the number of iterations,

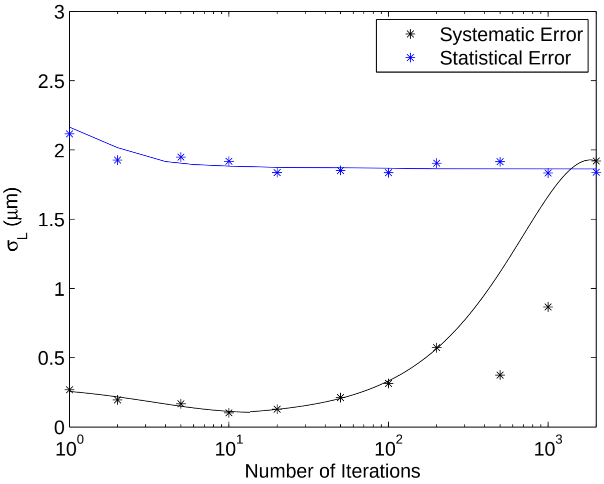

Figure 5.21: Systematic and statistic error of the system shown as a measure of depth resolution. Fitted lines added to guide the eye.

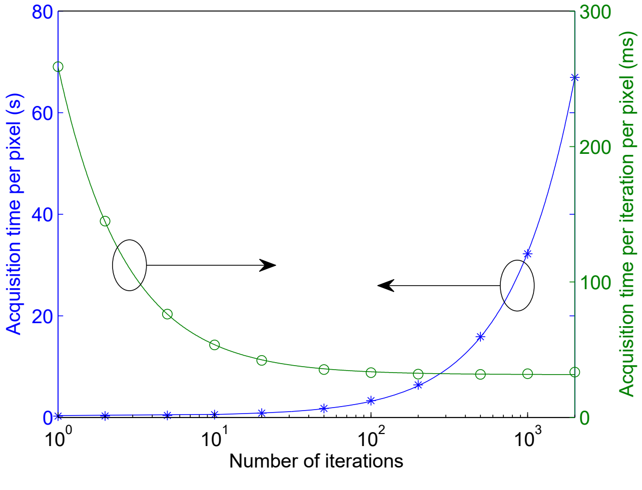

Figure 5.22: Acquisition time per pixel($\star$) and per iteration per pixel($\circ$) for various degrees of waveform averaging. Fitted lines added to guide the eye.

as expected. Furthermore, the acquisition time per iteration per pixel decreases due to the iteration-independent factors such as stage-movement and file saving being averaged out over the larger number of iterations. For $N = 1$, the lowest acquisition time per pixel for 1 kHz modulation is found to be 259 ms.

It would be expected that acquisition time could be improved through faster modulation. In order to quantify how these measurement-independent factors affect the acquisition time of any image (even 1×1 pixel) the acquisition time per pixel was measured over 101 pixels for a range of modulation frequencies using 200 iterations per pixel. 200 iterations allowed a higher degree of accuracy of measuring the acquisition time per pixel than 10 iterations would allow. Figure 5.23 shows how the acquisition time per pixel plateaus for increasing modulation frequencies.

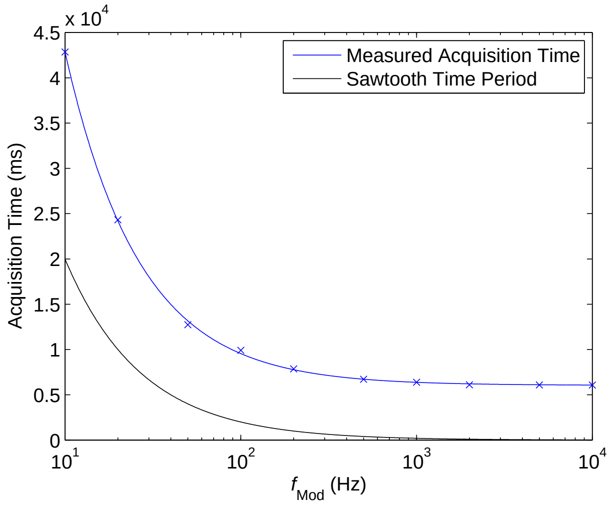

Figure 5.23: Acquisition time per pixel plateaus even as modulation frequency increases. The plateau value gives a measure of minimum computation time per pixel for 200 averages of ∼6 s. Fitted line added to guide the eye.

As shown by Fig. 5.23, even for a high modulation frequency f_{Mod}= 10 kHz, which results in modulation time of 20 µs, the acquisition time per pixel is actually ∼6 s. This acquisition time limit is systematic and depends on many factors ranging from the motion speed of the stages, the speed of the computer running the LabVIEW software, optimisation of the software and even the hard-drive read/write speed.

By combining the actual acquisition time per pixel measured for a modulation frequency of 1 kHz with the depth resolution measurement shown in Fig. 5.18 the number of iterations can be related to a real world measurement time. This is shown in Fig. 5.24.

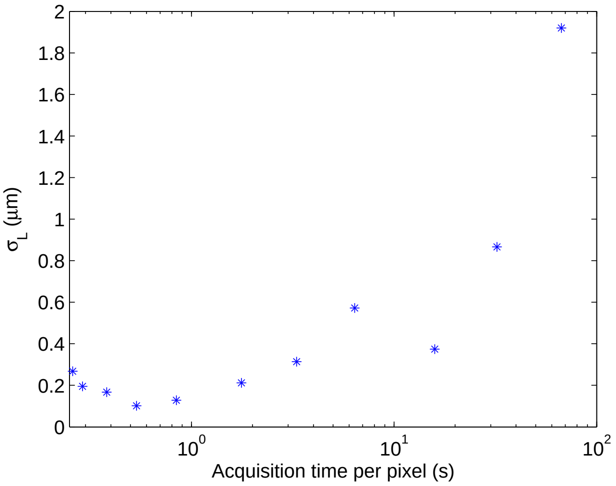

Figure 5.24: Depth resolution shown as a function of actual acquisition time per pixel.

The noise power spectral density (NPSD) associated with measurement of the SM voltage was also characterized for this system. Figure 5.25 shows how the NPSD changes relative to the modulation frequency. These values are determined from the magnitude of the FFT of the SM waveforms, relative to the noise floor, recorded at different modulation frequencies with $N = 10$ averages (blue). Also shown (green) is the NPSD measured for a resistor to simulate a device without feedback. The NPSD here can be attributed to the laser driver noise which is always present when it is operational. This translates to voltage noise on the terminals of the device when powering the laser. The additional noise present under feedback originates from the current and temperature fluctuations in the device causing frequency noise. This frequency noise translates into measured voltage noise.

As the modulation frequency increases up to 200 Hz the NPSD decreases approximately as $\sim 1/f^2$. At low modulation frequency, the longer acquisition time allows a higher degree of current- and temperature-induced frequency noise to affect the system. Even at $f_{\mathrm{Mod}} = 1\,\mathrm{kHz}$ (where $\sigma_{\mathrm{L}} < 0.1\,\mu\mathrm{m}$), the noise power is lower than -50 dB/Hz. For $f_{\mathrm{Mod}} > 10\,\mathrm{kHz}$, where the sampling time $t_{\mathrm{samp}} < 1\,\mathrm{ms/pixel}$, the NPSD decreases further to $<$ -60 dB/Hz. The upper modulation frequency limit of the laser driver used in these measurement prevents faster modulation, but this could be improved through use of a different driver. Faster modulation and shorter sampling times should allow even lower NPSDs.

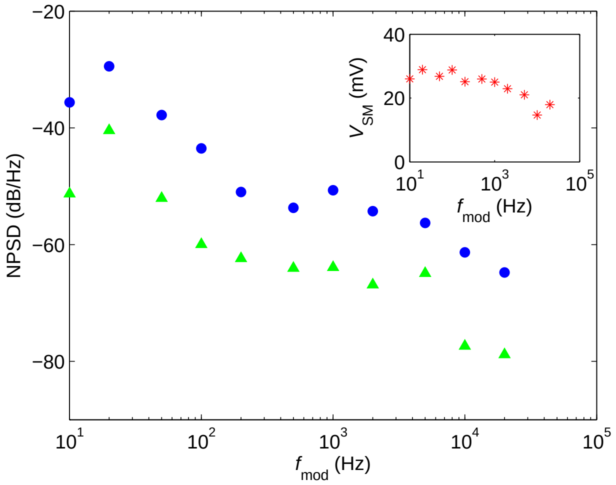

Figure 5.25: Noise power spectral density (NPSD) relative to the signal power, measured as a function of modulation frequency f_{mod} for N = 10 averages (blue). Also shown is the NPSD measured without feedback to the laser (green). Inset: corresponding SM signal amplitude.

5.2.7 Discussion

Swept-frequency SM 3D THz imaging has proven to present an improvement over previous SM 3D THz imaging techniques in a number of aspects. Similarly to the comparison of 2D imaging performed using mechanical modulation and electrical modulation of the QCL, described in Chapter 3, by further removing the mechanical components from the 3D imaging system (i.e. the longitudinal scan of the sample at each pixel), substantially faster acquisition rates could be achieved. Previously 3D imaging was limited to 0.05 pixels/sec, but by employing swept-frequency modulation an imaging rate of 40 pixels/sec was achieved, improving the image rate by a factor of $\sim \times 800$.

Through this improved imaging rate, waveform averaging could be implemented and studies found that N=10 iterations of waveform averaging resulted in a depth resolution of $< 0.1\,\mu\text{m}$.

Finally, utilising a modulation frequency of 1 kHz the system presented a NPSD of $\sim -50\,\mathrm{dB/Hz}$. Higher modulation frequencies have also been shown to improve system NPSD by a factor of $\sim 1/f^2$. As such, a higher modulation speed could be used to improve the system NPSD further. This has also been shown to improve image acquisition speed up to ~33 pixels/sec, which is currently limited by the hardware.

5.3 Measurement of optical constants of inhomogeneous explosive materials

Work in this section was completed in collaboration with Dr. Karl Bertling and She Han at University of Queensland. Experimental measurements were conducted by myself under supervision of Dr. Bertling and Dr. Dean, and the data analysis was conducted by She Han.

Coherent sensing in the THz frequency range has shown great potential as a means of rapid, non-contact detection of explosive materials due to it's non-ionising nature and the spectral features of many explosives covered by this frequency band.[7,15,50,208] Swept-frequency SM imaging provides a fast, sensitive method of coherent THz sensing that can be used to this end. Of particular use for identification of materials are the magnitude and phase of their reflection coefficients, measured across the sample surface, which can be related to the complex refractive index of the target. Previously published work[160,174] has demonstrated measurement of the optical constants of homogeneous organic materials by relying on their spatial homogeneity to reduce the variability of these optical constants over their surfaces. The ability to quickly identify these parameters makes swept-frequency SM imaging perfect for identification of homogeneous materials.

Many explosives on the other hand are far from homogeneous, consisting of mixtures of a number of materials where one ingredient is the active explosive to be identified. Plastic explosives are an example of this, but the same identification technique could be used for other inhomogeneous materials such as pharmaceuticals. Due to the inhomogeneous nature of such materials the optical properties would vary over the surface of the sample depending on the ingredients present at the various points across the surface. This makes measurement of optical constants difficult and identification of the material even more so. In order to implement fast identification of inhomogeneous materials with swept-frequency SM THz imaging various steps are required such as the removal of phase uncertainties and reliable location of centroids (representative of effective optical constants). In this section this approach is demonstrated using plastic explosives consisting of an explosive compound or mixture or explosives with various plasticizers, desensitizers, dyes, waterproof coatings and fabrics to aid storage and use.[209]

5.3.1 Experimental set-up and measurement technique

In the same way that swept-frequency modulation can be used to measure the sample depth and reflectance at a particular point on the sample surface, the complex refractive index (CRI) can also be measured, in cases where the sample is sufficiently flat, based on the amplitude and phase of the reflected field. The CRI, $\hat{n} = n - ik$ where n is the refractive index and k is the extinction coefficient, of an unknown material embedded in an optically flat target can be recovered using the known complex refractive indices of two other materials embedded in the same sample target. This approach has been demonstrated in previous work.[160,174] In order to demonstrate this, a custom target was prepared with three plastic explosive samples compressed gently against an optically flat reference plane (removed during measurements) in order to minimise tilt and position effects.[174] All of the plastic explosive samples were mildly inhomogeneous: SX2 (1,3,5-trinitroperhydro-1,3,5-triazine; RDX based), Metabel (1,3-dinitrato-2,2-bis(nitratomethyl)propane; PETN based), and Semtex-H (RDX and PETN based). The target also contains samples of high-density polyethylene (HDPE), polycarbonate (PC) and black HDPE (HDPE with black dye) to act as references. These plastics were injected before the sample holder surface was cut flat to ensure there is zero depth difference between them and the rest of the sample holder that could incorrectly be interpreted as a variation of the CRI of the plastic. The sample holder with mounted samples is shown in Fig. 5.26. Materials from the same batch of each explosive were compressed into pellets and measured using THz TDS (in transmission geometry) at nine points (in a 3×3, 0.5 mm grid) across each sample.

Reference values of n and k at 2.62 THz were extracted from the averages of each sample (results from these measurements are shown below in Table. 2).

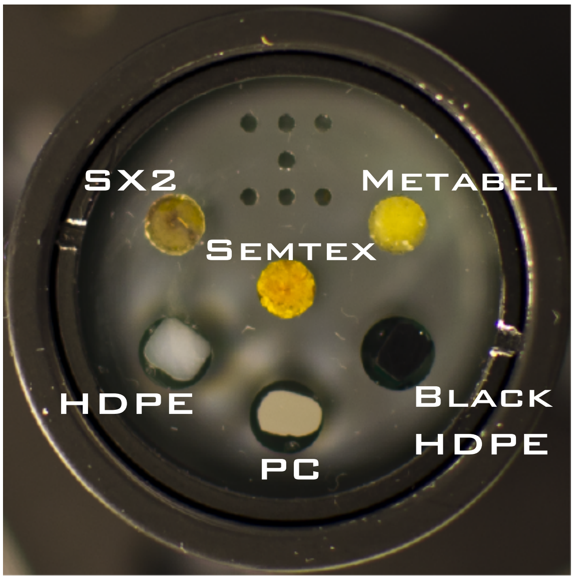

Figure 5.26: Photograph of sample holder and plastic explosive samples, labelled for clarity.

The THz QCL device used in our experiments was a 10 μm-thick BTC active region, processed into a SISP ridge waveguide with dimensions 3 mm × 140 μm, operating at ∼2.6 THz at a heat sink temperature of 25 K. The custom target was aligned perpendicular to the optical axis at a distance 0.41 m from the laser, and scanned in a raster fashion. A differential voltage amplifier was used to apply 20 dB of amplification to the measured voltage. The experimental set-up for this experiment is shown in Fig. 5.1.

The laser was driven at 930 mA with a 100 mA sawtooth (90% duty) modulation applied, resulting in an almost linear frequency change with time. The frequency of the sawtooth modulation waveform was 1 kHz, and the frequency modulation coefficient of the laser used was -15 MHz/mA. The laser driver had a transconductance of 200 mA/V at its modulation input. At each point in the raster scan the current sweep was repeated 64 times and an average waveform of the QCL terminal voltage was recorded. This measurement was performed before the number of iterations for this system was optimised. It is believed that with 10 iterations the performance of the systems could be further improved through a reduction in acquisition time and noise through a reduction in thermal fluctuations. 20 dB of amplification was applied to the recorded terminal voltage. The baseline modulation was then removed leaving the resultant SM interferometric fringes. Exemplar interferometric fringes acquired from swept-frequency imaging of the explosive samples and the calculated FFT magnitude are shown in Fig. 5.27.

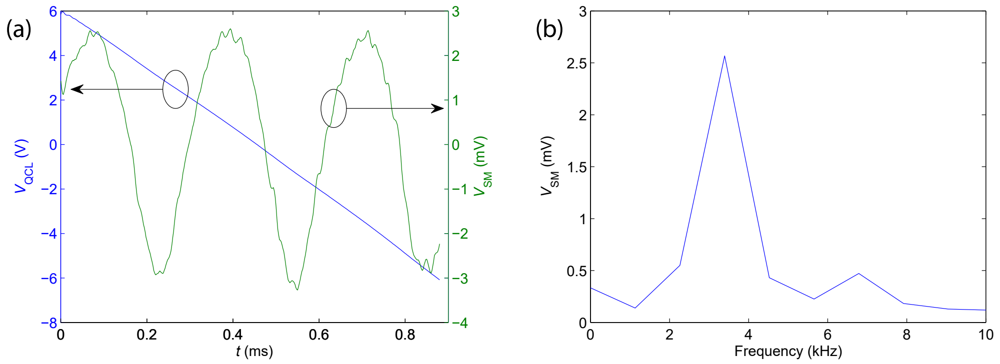

Figure 5.27: FFT analysis for extracting SM parameters from the swept-frequency terminal voltage measurements of explosive materials. (a) Exemplar interferometric waveform extracted by removing the baseline modulation from the recorded terminal voltage. The frequency of the interferometric fringes is 3.2 kHz. (b) Magnitude component of V_{SM} extracted by performing a complex FFT on the aforementioned fringes.

Through inspection of the SM signal array, all signals were acquired in the weak feedback regime (C < 1), which is a characteristic frequently associated with QCLs.[173]

5.3.2 Measurement of optical constants of inhomogeneous materials

Initial analysis was conducted to extract the magnitude and phase values of the reflected THz field from FFT analysis as described previously. These values are representative of the sample reflectivity and CRI of the sample respectively. The amplitude and phase maps of the sample are shown in Fig. 5.28 where the maps have been rotated to a vertical orientation according to the alignment holes in the sample holder.

Both the amplitude and phase of the signals measured across the homogeneous plastic reference samples are consistent across the entire surface of each sample. However, the explosives demonstrate a much wider range of amplitude and phase values. This can be attributed to the inhomogeneous nature of the samples with different ingredients having

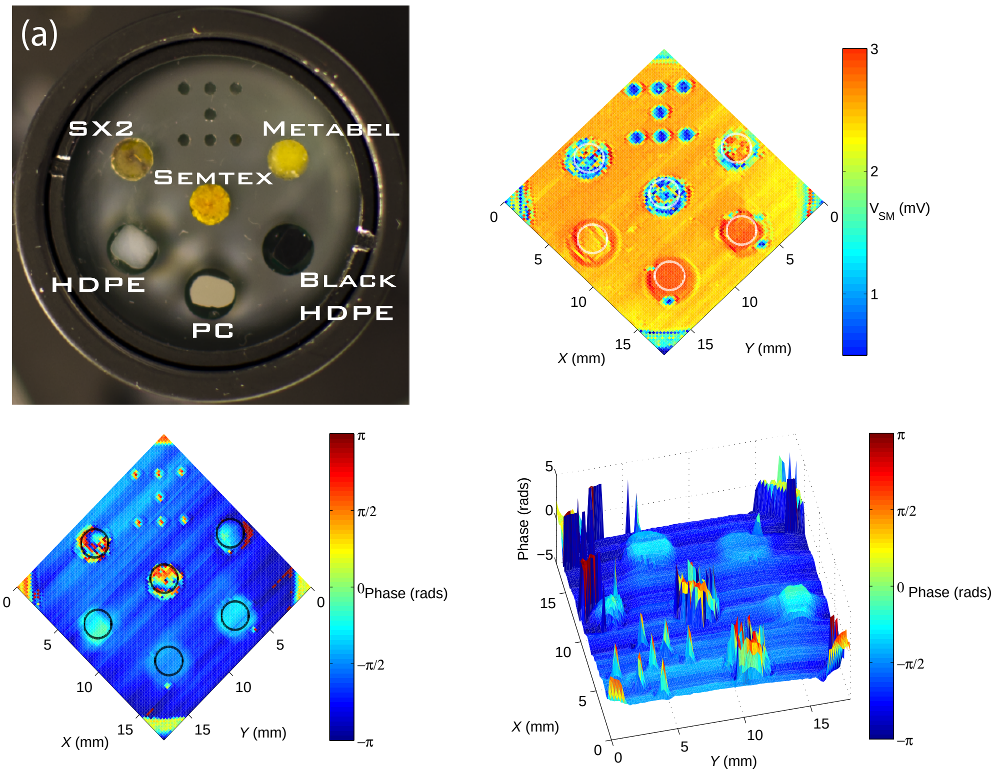

Figure 5.28: Imaging of explosive materials. (a) Photograph of explosives sample holder and samples. (b) The amplitude of V_{SM} across the sample surface demonstrating the reflectivity of the mounted samples. Colour scale represents SM interferometric fringe amplitude. (c) & (d) 2D and 3D phase profiles of samples showing the varying phases indicating varying CRIs. Colour scale represents measured phase of the sample surface.

different CRIs. By extracting representative phase and amplitude values from the pixels corresponding to each sample using a circular mask (shown on Figs 5.28(b) and 5.28(c) as white and black circles respectively) an amplitude/phase map can be created; this is shown in Fig. 5.29.

The pixels of the homogeneous plastic samples (+ data points) exhibit very narrow variation of both phase and amplitude values, which is representative of homogeneous materials. Conversely, the explosive samples (o data points) show phase values ranging between -π and π and amplitude values from 0.5 mV (very low reflectivity) to >3 mV (high reflectivity). This wide distribution proves the inhomogeneity of these samples.

Further analysis beyond this point was conducted by She Han at the University of Queensland,[210] but is presented here for completeness. By rewriting Eq. (2.32) in terms

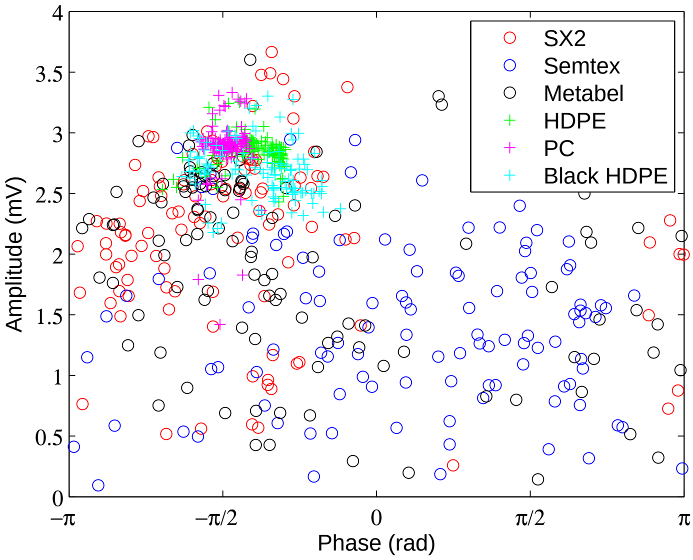

Figure 5.29: Amplitude/Phase map of the pixels obtained for each sample. Homogeneous plastic samples exhibit narrow ranges of both phase and amplitude values shown as tight clusters while inhomogeneous explosive samples demonstrate a much wider distribution.

of phase, the round trip phase of the external cavity at the frequency of the unperturbed laser, ϕ_0 can be related to the phase under feedback, ϕ_{FB} by

$$\phi_0 - \phi_{\mathrm{FB}} = C\sin(\phi_{\mathrm{FB}} + \arctan\alpha). \tag{5.5}$$

The laser terminal voltage under feedback can be written as

$$V_{\mathrm{QCL}} = V_0 + \beta\cos(\phi_{\mathrm{FB}}), \tag{5.6}$$

where V_0 is the voltage offset which may differ across the surface of the sample, β is the modulation coefficient of the SM signal, and ϕ_{FB} satisfies Eq. (5.5). The round trip phase ϕ_0 can be broken into three components

$$\phi_0(t) = \theta_0 + \frac{\Phi}{T}t - \theta_{\mathrm{R}}, \tag{5.7}$$

where θ_0 is the constant phase shift at the start of the frequency sweep, Φ is the phase modulation coefficient for the current sweep, T is the modulation time, and θ_{R} is the phase shift caused by reflection from the target. With this, Eq. (5.5) can be rewritten as

$$\theta_0 + \frac{\Phi}{T}t - \theta_{\mathrm{R}} - \phi_{\mathrm{FB}} = C\sin(\phi_{\mathrm{FB}} + \arctan\alpha), \tag{5.8}$$

which can be expanded as

$$\theta_0 + \frac{\Phi}{T}t - \theta_{\mathrm{R}} - \phi_{\mathrm{FB}} = \frac{C}{\sqrt{1+\alpha^2}}\sin(\phi_{\mathrm{FB}}) + \frac{C\alpha}{\sqrt{1+\alpha^2}}\cos(\phi_{\mathrm{FB}}). \tag{5.9}$$

Writing Eq. (5.9) in vector form gives

$$\frac{\Phi}{T}t - \phi_{\mathrm{FB}} = \left[\theta_{\mathrm{R}} - \theta_0, \frac{C}{\sqrt{1+\alpha^2}}, \frac{C\alpha}{\sqrt{1+\alpha^2}}\right] \begin{bmatrix} 1 \\ \sin(\phi_{\mathrm{FB}}) \\ \cos(\phi_{\mathrm{FB}}) \end{bmatrix}. \tag{5.10}$$

Values of C and α can be assumed to be constant throughout the frequency chirp and Φ/T and ϕ_{FB} can be recovered from the interferometric fringes as described below. With these values known Eq. (5.10) becomes a linear equation in $\left[\theta_{\mathrm{R}} - \theta_0, \frac{C}{\sqrt{1+\alpha^2}}, \frac{C\alpha}{\sqrt{1+\alpha^2}}\right]$ for each time point t. A least-squares method can then be applied to the time-dependent SM waveform recorded at each pixel to obtain the required coefficients.

To recover Φ/T from the SM voltage signal, we assume the period of the V_{SM} waveform to be T_1 as shown in Fig. 5.30. Eq. (5.6) shows that for each period T_1, ϕ_{FB} changes by 2π, for which Eq. (5.5) has a unique answer for $C \leq 1$.[176] As such, Eq. (5.5) dictates the same change in ϕ_0, which further implies $\Phi T_1/T = 2\pi$ from Eq. (5.7) from which Φ/T can be extracted. T_1 can be extracted from the average time between subsequent peaks of V_{SM}.

By selecting pixels wholly contained within the inhomogeneous sample surface area (within a radius of six pixels from the center of each material, shown in Fig. 5.28 by circles) SM signals who's components correspond to each material were recovered. From these, parameter extraction was completed and the fits corresponding to the largest 5% error were

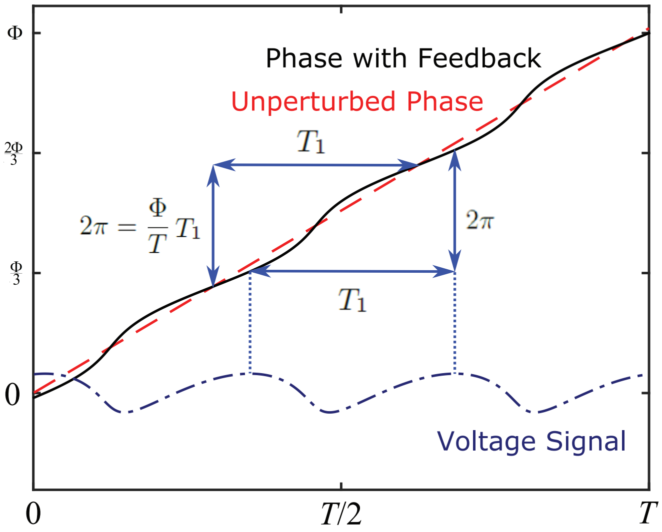

Figure 5.30: The period of V_{SM} (blue, dotted), T_1, demonstrates a phase change of the laser phase under feedback (black) of 2π.[210]

discarded to remove potential outliers. Finally fits with the largest 1% extracted feedback parameter were also discarded, where an unusually high reflectivity was suggested. After these steps were completed, the result was an array of fitted parameters for C, α and $\theta_{\mathrm{R}} - \theta_0$ for each material. The values of $\theta_{\mathrm{R}} - \theta_0$ can be unwrapped to lie between 0 and 2π resulting in point cloud values of $\left[\frac{C}{\sqrt{1+\alpha^2}}, \theta_{\mathrm{R}} - \theta_0\right]$, which are shown in Fig. 5.31. The centroid value for each material was chosen to be the centre of gravity of the point cloud.

Due to the homogeneity of the plastics, they demonstrate tight cloud points with little variability further corroborating the initial analysis shown in Fig. 5.29. The point clouds extracted from the analysis method show a much tighter clustering than the initial phase extraction shown in Fig. 5.29. The more complex analysis performed by University of Queensland also allows extraction of the $[n, k]$ values.[160,174,210] Briefly, the centroid values of the measured $\left[\frac{C}{\sqrt{1+\alpha^2}}, \theta_{\mathrm{R}} - \theta_0\right]$ coefficients can be related to actual values of reflectance $\sqrt{R}$ and phase change on reflection θ_{R} by calibration to the coefficients measured for the homogeneous plastics with known optical constants. These can then be related to n and

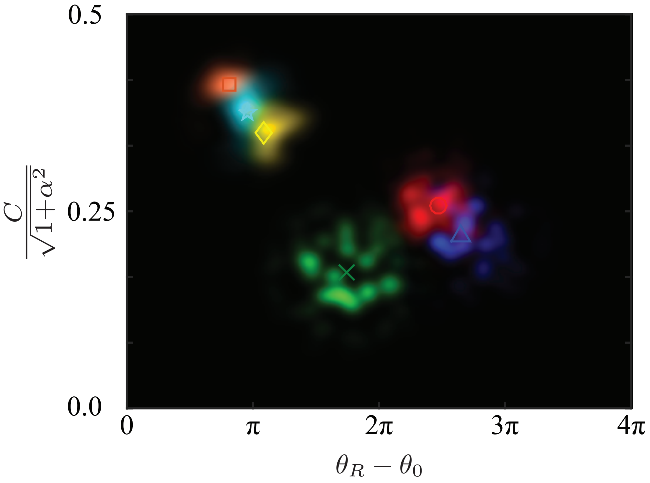

Figure 5.31: The distribution of the point cloud and the relative centroid for the three plastic explosives: METABEL, SEMTEX, SX2 (indicated by red, green, blue clouds and circle, cross and triangle markers respectively). Also shown for comparison are the point clouds of the three homogeneous plastics HDPE, PC and Black HDPE (indicated by orange, cyan, yellow clouds and square, star and diamond markers respectively).[210]

k values using the relations[160]

$$n = \frac{1-R}{1+R-2\sqrt{R}\cos(\theta_{\mathrm{R}})}, \tag{5.11}$$

and

$$k = \frac{2\sqrt{R}\sin(\theta_{\mathrm{R}})}{1+R-2\sqrt{R}\cos(\theta_{\mathrm{R}})}. \tag{5.12}$$

Identification of the $[n, k]$ values for each material are shown in Table 2.

Table 2: Reference and estimated n and k values for three homogeneous plastics and inhomogeneous composite plastic explosives. For reference values for plastics see[160]. Reference values for explosives were obtained using THz-TDS.[210]

	Ref. n	n^{160}	Est. n	Ref. k	k^{160}	Est. k
HDPE	1.54	1.54	1.54	0.002	0.002	0.006
PC	1.62	1.62	1.62	0.01	0.01	0.02
Black HDPE	1.58	1.58	1.58	0.02	0.02	0.02
SX2	1.75	-	1.76	0.09	-	0.09
SEMTEX	1.55	-	1.56	0.06	-	0.07
METABEL	1.66	-	1.66	0.07	-	0.06

5.3.3 Discussion

Values for the refractive index and extinction coefficient of inhomogeneous materials have been obtained using a THz swept-frequency SM approach. The optical constants obtained show good agreement with previously reported values (see Table 2). This has allowed non-contact measurement of explosive materials that could be further improved by replacing the single QCL with an array of QCLs emitting at different frequencies or through the use of a single QCL with a wide tuning range. In this way, the frequency dependant absorption coefficient of materials could be determined enabling unambiguous identification of materials.

5.4 Active phase-nulling of the self-mixing phase

Amongst the applications where THz sensing using the SM effect has previously shown great promise are displacement sensing[128] and velocimetry.[158] In all the previous SM studies using THz QCLs to date the QCL has been operated under free-running conditions without any feedback control. Previous near-infrared laser systems under optical feedback with feedback control have shown use for sub-wavelength displacement sensing of targets[211] and non-contact vibrometry of vehicles.[212]

By utilising feedback control, a system is demonstrated here where the QCL emission frequency is dynamically tuned to null the phase of the SM signal.[213] One application of this technique is the measurement of the frequency tuning of the laser as a function of drive current. Many applications of THz QCLs, such as gas spectroscopy and frequency-modulated approaches to imaging (such as the work presented on swept-frequency imaging in Chapter 5.2), require accurate characterisation of the laser tuning coefficient. In order to characterise the frequency tuning of a QCL previous methods have employed mixing of the QCL field with a local oscillator (either another QCL[85,214] or an optically pumped gas laser[84,215]) on a diode mixer in order to detect the high-frequency beat note. As such, these techniques are limited to the frequency range of the detector and employ multi-source systems which are inherently more complicated than a SM set-up. The scheme presented here allows real-time measurement of the tuning coefficient and a greatly reduced complexity compared to previously reported schemes. This new system also operates over the entire 1.2-5.2 THz spectral emission range of THz QCLs. This system also has another application of real-time displacement sensing of remote targets, achieving all previous advantages of SM-based systems while overcoming limitations such as resolution limits caused by the quantisation attributed to fringe counting methods[123,216] and avoiding the need to fit a feedback model in post-processing.[128]

5.4.1 Experimental set-up & measurement technique

The schematic system diagram is shown in Fig. 5.32. The THz QCL consisted of a 10 µm-thick BTC active region[183] emitting at ∼2.62 THz ($\lambda \approx$114 µm, measured using an FTIR with resolution 7.5 GHz), which was processed into a SISP ridge waveguide with dimensions of 3 mm × 140 µm. The device was cooled using a continuous-flow helium cryostat and maintained at a heat-sink temperature of 25 K. The threshold current at this temperature was 1000 mA. Radiation from the laser was focused onto a gold planar mirror using a pair of 2-inch-diameter $f/2$ off-axis parabolic reflectors, with the mean distance between the laser facet and the target $L_0 = 0.41$ m through an unpurged atmosphere. This method utilises a perturbed cavity length, through the use of a scanning mirror, in order to produce a perturbation to the QCL terminal voltage. A feedback control loop in turn controls the QCL emission frequency in order to correct this perturbation to the end of holding the SM signal constant.

The mirror position was recorded in real time at a sampling rate of 10 kS/s through the analogue output of the stage controller. A current source was used to drive the laser at a constant current of 1080 mA, with an electronically conditioned feedback current Δi superimposed on the DC current. The SM signal V_{SM} was monitored via the QCL terminal voltage, amplified using a 15 dB DC-coupled voltage amplifier. It was found that slow changes in V_{SM} were filtered out by AC-coupling, so DC-coupling was required on the amplifier. In order to avoid saturation of the amplifier, a DC voltage offset was applied to the terminal voltage.

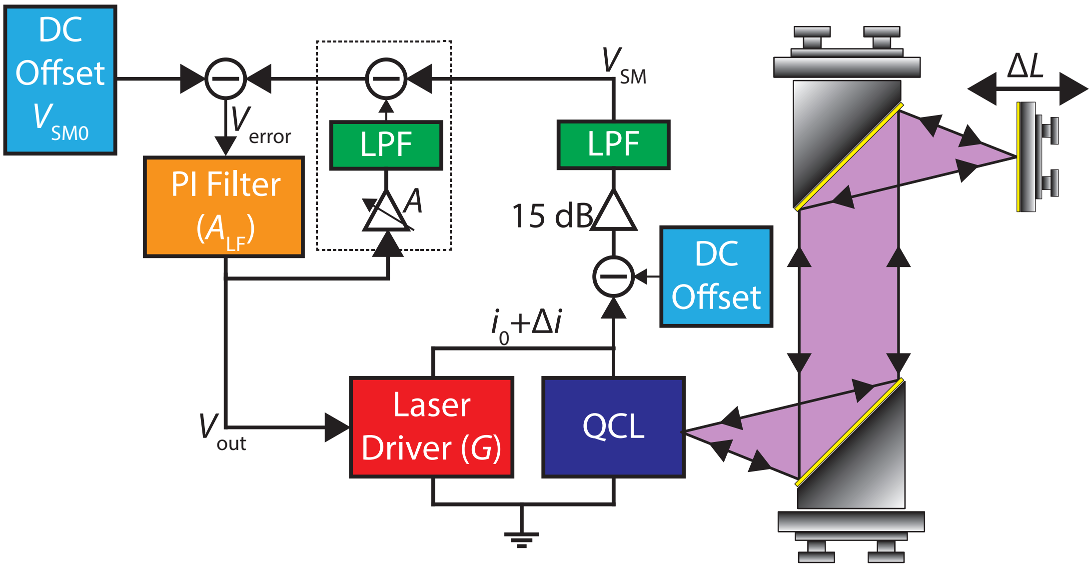

Figure 5.32: Schematic diagram of the experimental set-up. A modulation signal, V_{out} is generated by the PI loop filter (transfer function A_{LF}) acting on V_{SM}. The laser driver produces a corresponding perturbation to the QCL driving current Δi, actively phase-nulling V_{SM}. The compensation loop (dashed box) is used to cancel the laser voltage modulation. LPF-low pass filter.

With the feedback compensation switched off ($\Delta i = 0\,\text{mV}$), the laser experiences a voltage perturbation to the terminal voltage, producing SM fringes according to

$$V_{\text{SM}} = \beta \cos(\phi), \tag{5.13}$$

where β is the modulation index and ϕ is the external round-trip phase given by

$$\phi = \frac{4\pi L \nu}{c}, \tag{5.14}$$

in which ν is the laser emission frequency under feedback, L is the external cavity length and c is the speed of light in a vacuum.[166] From this it makes sense that through current modulation of the laser frequency ν, the change in phase $\Delta\phi$ due to a change in external cavity length ΔL can be counteracted through use of a feedback loop.[211] Under the feedback control loop, the condition $\Delta\phi = 0$ should always be true, such that the SM voltage stays constant. From differentiation of Eq. (5.14) an expression for the change in emission frequency $\Delta\nu$ can be obtained for small perturbations of the cavity length from Eq. (4.4).

As Fig. 5.32 shows, V_{SM} was input into an adjustable proportional-integral (PI) loop filter to create a feedback control signal to modulate the driving current and therefore the emission frequency of the QCL in response to the changing cavity length. To control the fringe locking position V_{SM0}, a DC offset stage was implemented such that the error signal $V_{\mathrm{error}} = V_{\mathrm{SM}} - V_{\mathrm{SM0}} \cong 0$ under feedback control. The gradient of the SM fringe at this position determines the optimum loop parameters for this technique to null the external phase. The shape of the SM fringes, and therefore this gradient is dependant on the feedback parameter that the laser is operating under, which was determined to be $C \approx 0.25$ here. However, it is expected that this method would also operate under moderate feedback $(C > 1)$[212] where the gradient is much steeper with respect to $\Delta\phi$ while avoiding instability. The transfer function of the PI filter A_{LF}, was tuned observationally to provide 0 dB of proportional gain for frequencies $f > 1$ kHz, with integral gain with a slope 10 dB/decade below this corner frequency, as depicted in Fig. 5.33.

The output of the PI filter, V_{out}, was used as a modulation source for the laser driver such that the resulting current perturbation was given by $\Delta i = GV_{\mathrm{out}} = GA_{\mathrm{LF}}V_{\mathrm{error}}$, where $G = 200\,\mathrm{mA/V}$ is the transconductance of the current driver. The subsequent frequency modulation to the QCL can be expressed as

$$\Delta\nu = k\Delta i = kGV_{\mathrm{out}}, \tag{5.15}$$

where k is the frequency tuning rate of the QCL. This current modulation also acts on the QCL as a modulation to the terminal voltage through the differential resistance of the device R, which for small perturbations around the laser driving point can be assumed to be constant and typically equals a few ohms. It was possible to remove this unwanted voltage modulation to the measured terminal voltage through the use of a compensation loop acting on V_{out}; shown by the dashed box in Fig. 5.32. To tune this compensation loop, a current modulation ramp of 30 mA was directly applied to the laser without feedback and

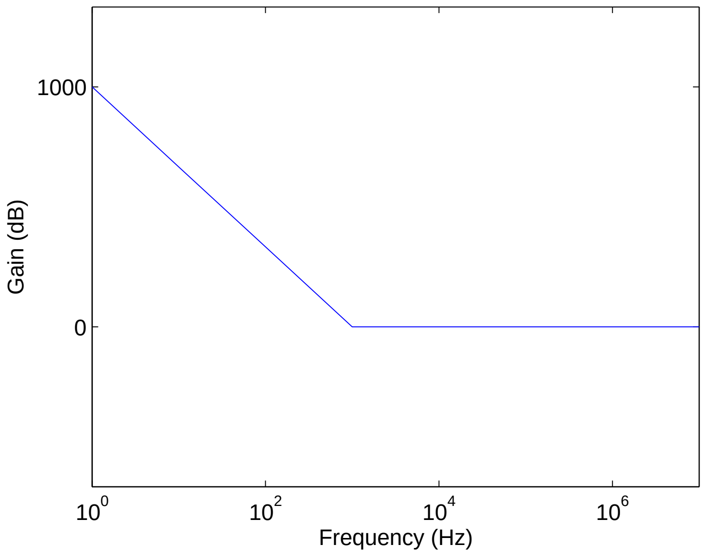

Figure 5.33: Gain response of the PI filter.

the compensation loop amplification A was tuned to match the resulting QCL voltage. The resultant amplification required was found to be $A = RG \cong 0.7$.

5.4.2 Hardware development

In order to facilitate this experiment certain custom components of the system had to be designed and built. A voltage signal from the compensation loop was needed in order to cancel the modulated component of the terminal voltage cause by the feedback loop to the QCL. This allowed a scaled and inverted version of V_{out} to be added to V_{SM} to achieve this cancellation. In order to achieve this an inverting amplifier was required. Further to this, a custom DC offset circuit and low-pass filters were required to reduce noise at the PI-filter input (see Fig. 5.32). Both the inverting amplifier and DC offset circuit required active components to function, so a single control box was created housing both of these components; this is shown in Fig. 5.34(a). Both components required positive and negative power so the compensation amplifier was powered with a DC power supply.

The inverting amplifier was designed around the classic inverting op-amp circuit where V_{in} is fed into the negative input of the op-amp with the positive input tied to ground (see Fig. 5.34(b)). The gain of the amplifier is controlled by the ratio between the feedback

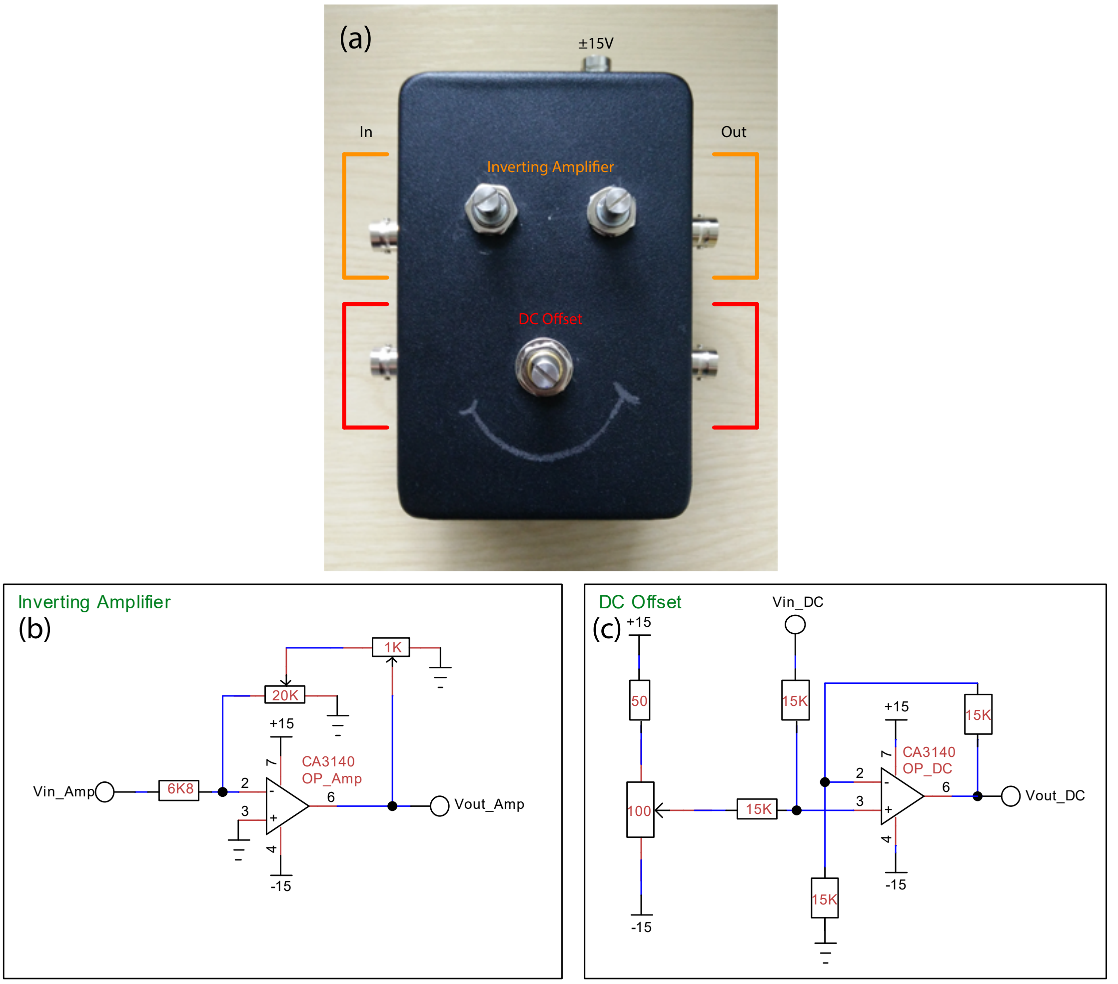

Figure 5.34: Signal correction circuits utilised in phase-nulling of the SM phase. (a) The left hand BNC connectors are inputs, while the right are outputs. The upper (orange) BNCs and potentiometers are used for the inverting amplifier circuit described in (b), with course and fine amplification tuning. The lower (red) BNCs and potentiometer are for controlling the level of DC offset applied. The circuit diagrams for the inverting amplifier and DC offset circuit are given in (b) and (c) respectively.

and input resistors such that

$$A = \frac{-R_{\text{feedback}}}{R_{\text{in}}}. \tag{5.16}$$

In order to allow adequate amplification while maintaining accurate control of the gain, a range of ×0 to ×-3 was chosen with course and fine control. To this end, resistor values of $R_{\text{in}} = 6.8\,\text{k}\Omega$ and $R_{\text{feedback}} = 21\,\text{k}\Omega$ were used, where R_{feedback} was divided into two potentiometers in series to allow the full amplification range to be covered; $R_{\text{course}} = 20\,\text{k}\Omega$ and $R_{\text{fine}} = 1\,\text{k}\Omega$. R_{fine} was chosen to be a high turn potentiometer to allow high precision control. Figure 5.35 shows oscilloscope traces of the inverting amplifiers operation for differing levels of amplification.

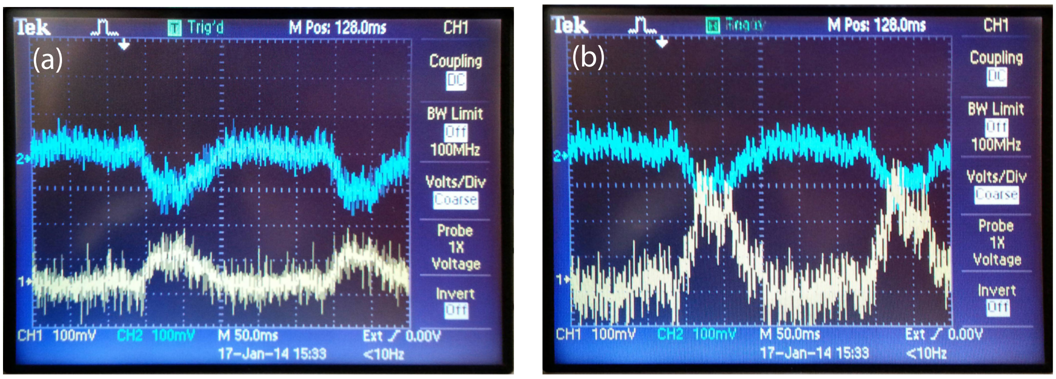

Figure 5.35: Oscilloscope screen traces showing the inverting amplifier circuit operation. Both traces show the inversion applied to the original (blue) trace, with various levels of gain. The level of gain shown is (a) ∼ ×-1 and (b) ∼ ×-2. Amplification between ×0 and ∼ ×-3 through course and fine (∼5% of full range over 20 turns) tuning was possible.

The other active circuit designed was a DC offset circuit. This circuit was required to remove the DC voltage component from V_{QCL} before it could be amplified by the DC-amplifier. The design of such a circuit was based on a resistive voltage adder, where the offset voltage input was a variable, negative value (see Fig. 5.34(b)). As the op-amp required input voltages of ±15 V, these were used as the input voltage range to the offset circuit. The normal operating voltage for a THz QCL such as the one utilised in this experiment is ∼5 V, so ±15 V is far more than would be required and would result in a low resolution on the potentiometer. In order to limit this, a potential divider circuit was added to the input to limit the input voltage to -15 V to +5 V. The resistive adding point where V_{in} and V_{DC} join was connected to the positive input of the op-amp to prevent any signal inversion. Figure 5.36 shows the operation of the DC offset circuit where a positive DC offset have been applied.

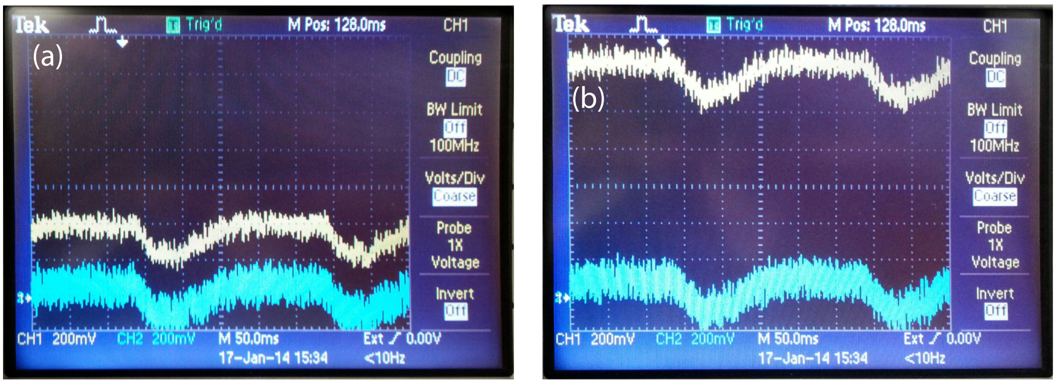

Figure 5.36: Oscilloscope screen traces showing the DC offset circuit operation. The level of DC offset applied to V_{QCL} (blue) is shown at (a) $\sim$ 350 mV and (b) $\sim$ 1.2 V. The full range of additional voltage of this circuit was -15 V to +5 V.

The final required component are the LPFs. Numerous designs were trailed including 1st- and 2nd-order LPF RC filters, but these designs suffered from low initial roll-off frequencies of ~17 Hz and full cut-off frequencies of ~1 kHz. In order to raise the initial roll-off frequency a 2nd-order RLC LPF was designed, as shown in Fig. 5.37.

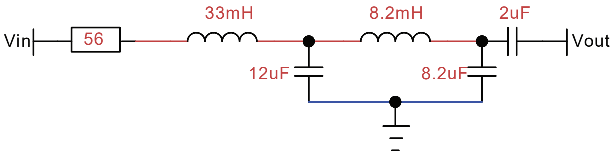

Figure 5.37: Design of custom LPF.

The response of the LPF is shown to remove the high-frequency noise component while retaining the slow SM fringes of the input voltage in Fig. 5.38.

5.4.3 Active phase-nulling of the SM phase

With all of the components designed and the system aligned, the PI loop generates feedback control of the QCL dependent on the round trip phase. The cavity control was

Figure 5.38: Oscilloscope screen trace showing the LPF circuit operation. High frequency noise on the input (blue) voltage is eliminated in the output (yellow) voltage.

accomplished using a sawtooth modulation supplied to the motion controller, with the position measured at a sampling rate of 10 kS/s though the analogue output of the stage controller. Figure 5.39(a) shows this measured change in external cavity length $\Delta L \approx 25\,\mu\text{m}$ (approximately half a fringe) at a rate of ~60 μm/s that was used to change the external phase. Figure 5.39(b) (red curve) shows the error signal V_{error} obtained in response to this modulation of the external cavity without any feedback control. Due to the lack of feedback control, V_{QCL} is perturbed due to the change in round trip phase ϕ; this perturbation cascades through the system to V_{error}. With feedback control active and the system running closed-loop, the modulation signal V_{out} is generated, as shown in Fig. 5.39(c), which in turn reduces V_{error} to near zero, demonstrated in Fig. 5.39(b) (blue). Running closed-loop, the modulation from the PI filter maintains V_{QCL} at a constant value counteracting the perturbation caused by the round-trip phase through control of the laser emission frequency.

From Eq. (4.4), the required change in emission frequency $\Delta\nu$ can be recovered from the known change in cavity length ΔL. The measured control signal in Fig. 5.39(c) can then be used to relate the frequency modulation to the current modulation of the QCL Δi using Eq. (5.15). The laser tuning rate k can therefore be calculated.

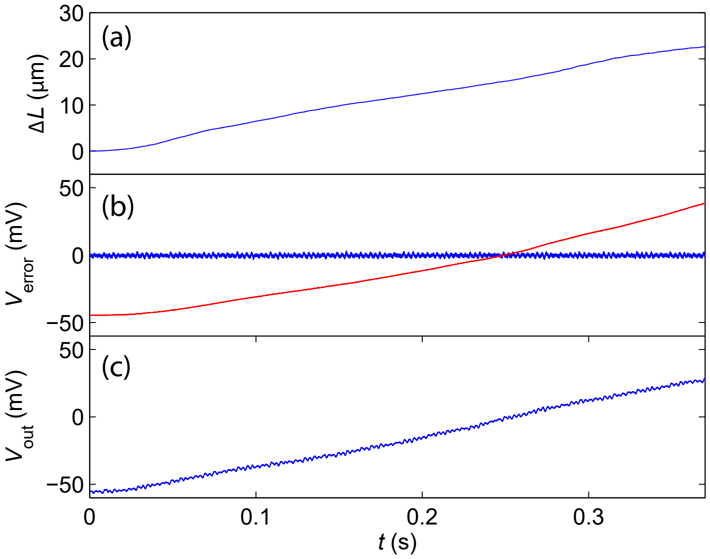

Figure 5.39: Feedback voltage signals of the QCL from the PI filter. (a) Change in cavity length ΔL. (b) Corresponding error signal V_{error} measured without (red) and with (blue) electronic feedback control of the QCL. (c) Corresponding control signal from the PI filter.

This relationship between $\Delta\nu$ and Δi is shown in Fig. 5.40. Through the use of a linear fit to the related data, a tuning rate of $k = -8.2 \pm 0.03\,\mathrm{MHz/mA}$ is recovered, which is consistent with previously reported values for THz QCLs.[59] In order to validate this further, an alternative, non-real time method of measurement of the tuning rate was employed.[160]

5.4.4 Measurement of laser tuning coefficient using swept-frequency modulation

In order to validate the results obtained using the phase-nulling technique, a different method of measuring the tuning coefficient of the QCL using swept-frequency modulation of the QCL, was applied. In this technique the external cavity length was discretely stepped in 2 μm steps and a sawtooth waveform applied to the QCL current at each external cavity position, generating a series of interferometric SM fringes. Peaks in the SM fringes occur when $\nu = c/2L$. Therefore, as the cavity length is changed the interferometric fringes will move with respect to the sawtooth waveform. By tracking one of these

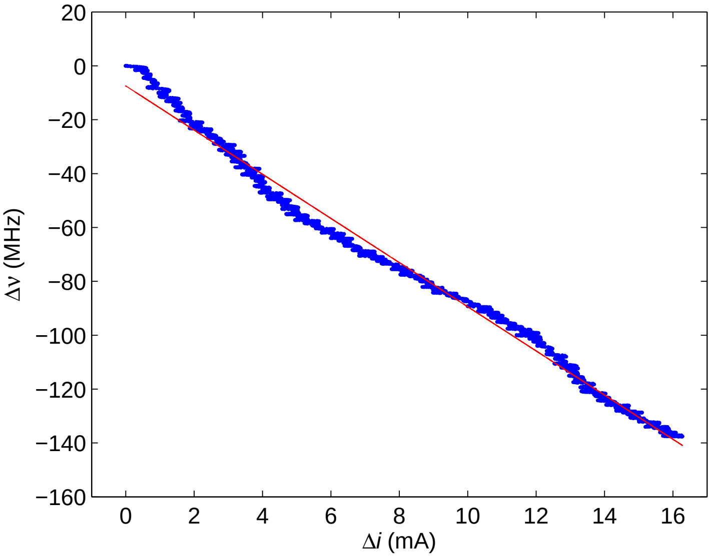

Figure 5.40: Extraction of the QCL tuning coefficient, k. Through compensation of the modulation of the external cavity length, the feedback control signal V_{out} causes a current perturbation to the QCL, resulting in frequency tuning $\Delta\nu$ of the device. A linear fit (red) to the measured data yields a tuning rate $k = -8.2 \pm 0.03\,\mathrm{MHz/mA}$.

fringes, the current modulation required to compensate for the changing cavity length can be determined. Using Eq. (4.4), the change in cavity length can be related to a change in frequency, thereby enabling a relationship between frequency and current to be determined.

In this experiment, the external cavity was stepped by 2 µm over a full range of 100 µm. Figure 5.41 shows a selection of SM fringes obtained for different external cavity lengths.

The resulting relationship between current and frequency is shown in Fig. 5.42.

By performing a linear fit to this data a tuning rate $k = -8.5 \pm 0.2\,\mathrm{MHz/mA}$ is recovered. This agrees well with previously reported values[59] and the value recovered through phase-nulling of the external phase of the QCL presented above.

A similar measurement was performed in which the temperature of the QCL was changed instead of the external cavity length in order to calculate the tuning caused by changes of the QCL temperature. The results of this experiment are shown in Fig. 5.43 where a temperature tuning coefficient of $k = -42.6 \pm 1.8\,\mathrm{MHz/K}$ was found.

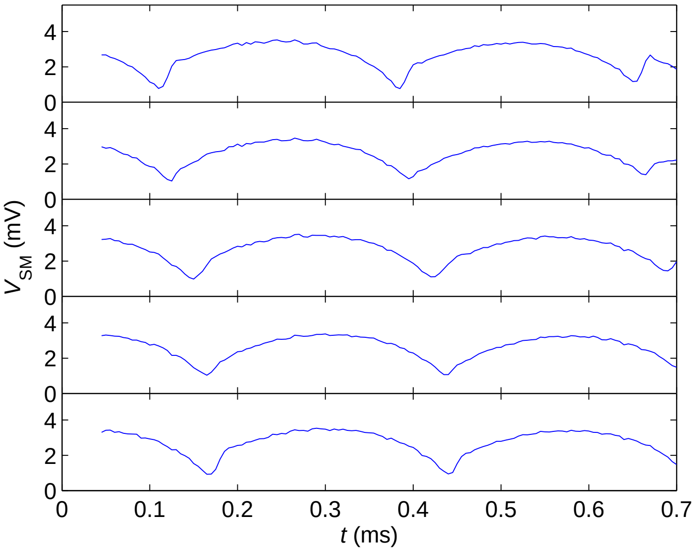

Figure 5.41: Exemplar SM fringes for various external cavity lengths. The external cavity length was stepped by 2 µm between plots. Individual fringes can be tracked to calculate the frequency tuning coefficient of the laser. The cause of the variation in fringe shape is unknown.

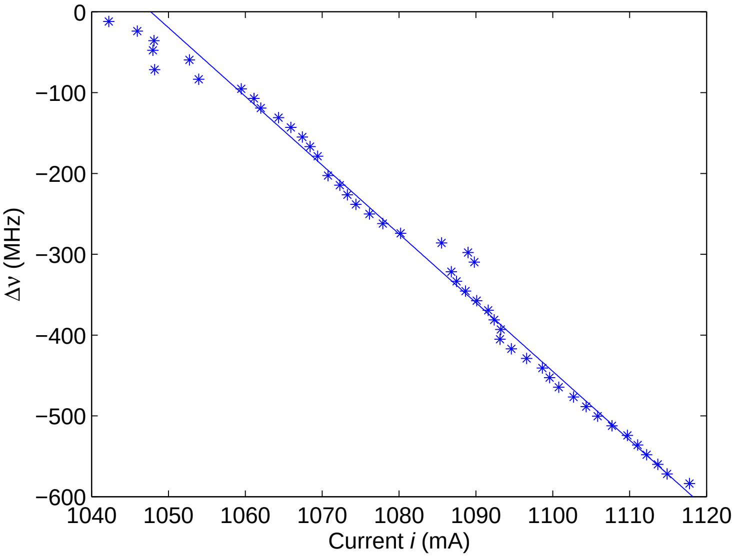

Figure 5.42: Relationship between driving current, i, and frequency tuning, $\Delta\nu$, determined using swept-frequency interferometric measurement (blue stars). A linear fit to this reveals a tuning rate $k = -8.5 \pm 0.2\,\mathrm{MHz/mA}$.

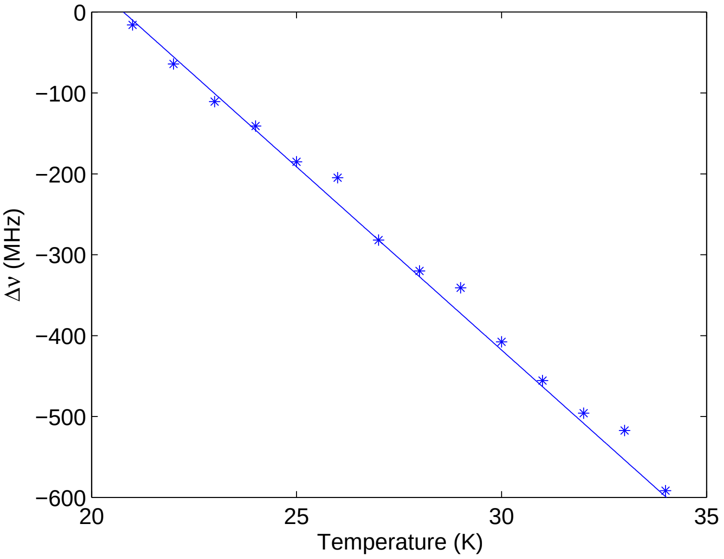

Figure 5.43: Relationship between device temperature and frequency tuning, $\Delta\nu$, determined using swept-frequency interferometric measurement (blue stars). A linear fit to this reveals a tuning rate $k = -42.6 \pm 1.8\,\mathrm{MHz/K}$.

5.4.5 Displacement sensing using an active phase-nulling technique

Another application of this phase-nulling technique is for the displacement sensing of remote targets, if the laser tuning coefficient is known. As V_{out} is generated in response to modulation of the external cavity it replicates the movement of the external target in real-time. This replication will be scaled due to the responsivity factor $R = -\nu/kGL_0 = 3.9\,\mathrm{V/mm}$ according to Eqs. (4.4) and (5.15) and using the recovered tuning rate $k = -8.2\,\mathrm{MHz/mA}$. Figure 5.44 shows the recovered displacement (blue) calculated, using this relation, from the voltage control signal V_{out} measured with the mirror target moving at 2 Hz with a peak-to-peak displacement, $D = 22.5\,\mu\mathrm{m}$. The recovered peak-to-peak displacement from V_{out} is $D = 23.1\,\mu\mathrm{m}$. This translates to an error of $\sim$2.5%.

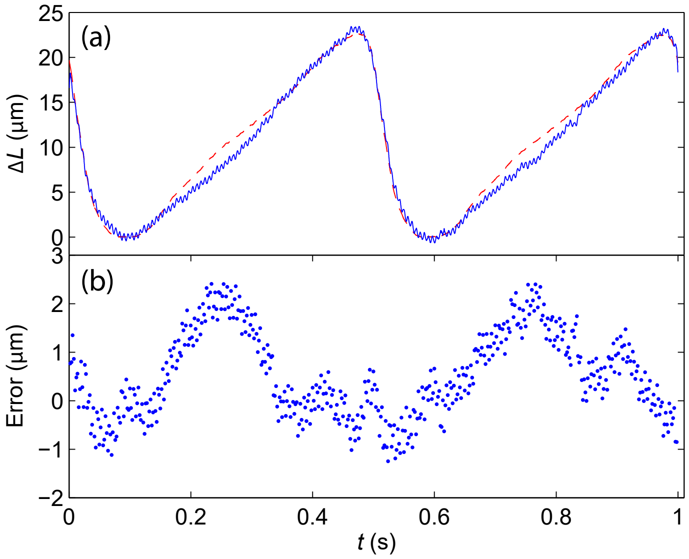

Figure 5.44: Recovered displacement measurement of a remote target. (a) Displacement (blue) determined from the feedback control signal V_{out}. The remote target consisted of a mirror vibrating at 2 Hz through a distance of $D = 22.5\,\mu\mathrm{m}$. The actual displacement is shown in red. (b) Displacement error between recovered and actual displacements.

Fourier analysis of V_{out} found that the noise equivalent displacement for this measurement was $\sim$0.2 μm for a 1-Hz measurement bandwidth centered around the mirror reciprocation frequency of 2 Hz. Through comparison of the measured and actual displacements, the maximum displacement error measured was ∼2.5 µm, as shown in Fig. 5.44(b). A likely source of this error is through the assumption that the differential resistance of the device is constant throughout the measurement, when in reality it is voltage-dependent. This would cause the compensation loop to subtract the voltage modulation incompletely. As can be seen from Fig. 5.44, the two recorded periods show similar error. The non-linear voltage-dependent differential resistance of the device also determines the limit of the practical current modulation of the system, which is empirically determined to be ∼30 mA. This translates to a measurable displacement of ∼40 µm based on Eq. (4.4). In order to improve this, the non-linear differential resistance would have to be properly compensated (using a digital synthesizer, for example). This would lead to an increase in the current modulation range, up to the mode-hop-free tuning range of the device under feedback (∼100 mA for this device), increasing the measurable displacement range in turn.

5.4.6 Simulation of feedback parameters

One assumption implicit to the techniques presented in Chapter 5.4.4 is that the tuning coefficient of the QCL is not dependent on the level of feedback it experiences. This was investigated by simulating the stepped-cavity, swept-frequency experiment (described in Chapter 5.4.4), for different feedback levels, using MATLAB. In order to simulate experimental results, the cavity length L was first chosen. The tuning effect of applying a sawtooth current modulation to the laser was then calculated, assuming a current tuning value $k = -8.2\,\mathrm{MHz/mA}$. Using this simulated frequency chirp, the external phase under feedback ϕ was then calculated from the excess phase equation Eq. (2.32) using code from Kliese.[176] This procedure was repeated for different cavity lengths.

The analysis discussed in Chapter 5.4.4 was then applied to this simulated data. Specifically, the time position of the fringe peak is calculated using the extracted phase. This allows the phase to be related to a modulation current at this time. The change in cavity length is related to a change in emission frequency using Eq. (4.4). Finally a linear fit was used to recover the tuning rate k, and to ensure that the same value entered as a simulation parameter was recovered by this analysis procedure. This was simulated for various feedback levels ($0 \leq C \leq 1$) to ensure the level of feedback had no effect on the recovered tuning rate. Results from these simulations are shown in Fig. 5.45. In each case, the correct tuning rate $k = -8.2\,\mathrm{MHz/mA}$ was recovered, proving the reliability of the analysis method.

5.4.7 Discussion

Phase-nulling by electrical feedback control of the QCL current has proven to be an accurate measurement technique for multiple purposes including characterisation of the tuning rate of a THz QCL, and displacement sensing of remote targets with a high degree of accuracy. This system has all of the benefits of previous SM systems including being compact while also delivering real-time measurement of the aforementioned parameters. Phase-nulling also demonstrates a significantly reduced experimental complexity when compared to previous methods of measuring the tuning rate of a QCL, which require external stable laser sources.

5.5 Discussion of SM techniques based on frequency modulation

Swept-frequency modulation of the THz QCL has been demonstrated for a number of purposes including 3D imaging, extraction of optical parameters of inhomogeneous materials and active phase-nulling of the self-mixing phase.

Compared to previous 3D SM imaging techniques (see Chapter 4) swept-frequency imaging poses a number of advantages. Through removal of mechanical components of the system, experimental complexity was reduced while also improving imaging rates by a factor of $\sim \times 800$. Also a depth resolution of <0.1 µm and a NPSD of ∼-50 dB/Hz was demonstrated with $N = 10$ averages and a modulation frequency $f_{\mathrm{Mod}} = 1\,\mathrm{kHz}$ respectively. It is suggested that higher modulation frequencies would allow further improvement to the NPSD.

Swept-frequency modulation also allowed measurement of the refractive index and extinction coefficient of numerous inhomogeneous materials in the form of plastic explosives. These values were in good agreement with values obtained using THz-TDS. Through the

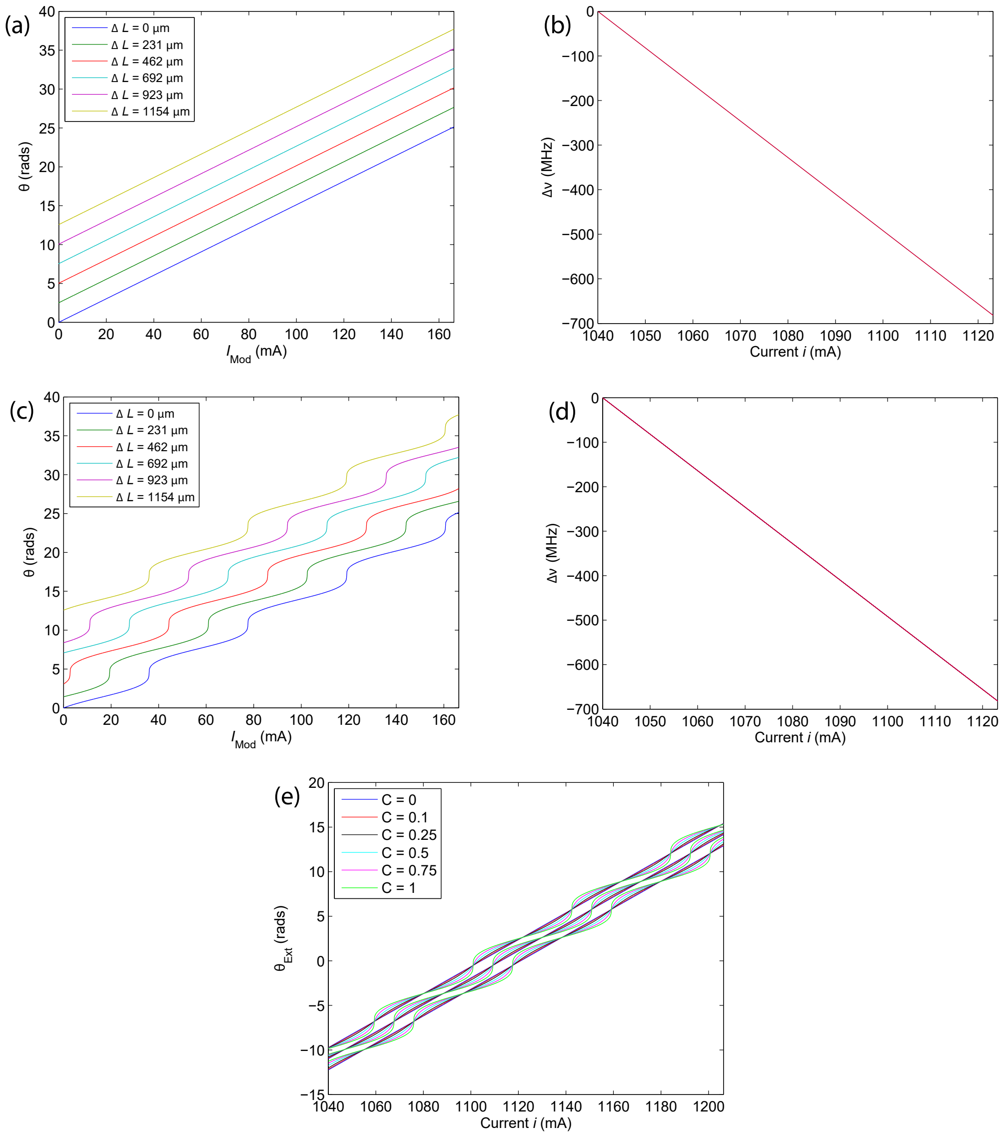

Figure 5.45: Simulations of the external phase for various feedback coefficients. (a) & (c) By simulating the phase of the signal for various cavity lengths and extracting the modulation current that a particular phase occurs at for each cavity length, the current needed to tune the QCL can be extracted. Feedback coefficients of $C = 0$ and $C = 1$ are shown. (b) & (d) For both feedback coefficients $C = 0$ and $C = 1$, respectively, the same, correct, tuning coefficient can be extracted. (e) Identical simulations were run for various feedback levels, with each resulting in the recovery of the same tuning rate.

use of a QCL with a wide tuning range, the frequency dependant absorption coefficient of materials could be determined using this method, allowing stand-off unambiguous identification of substances.

Finally, swept-frequency modulation was used for the purposes of phase-nulling of the SM phase through electrical feedback control. This was used to perform measurements of the tuning rate of a THz QCL and displacement sensing of remote targets. Both of these uses showed a high degree of accuracy, with multiple procedures and simulations providing similar values. This system also demonstrates a greatly reduced experimental complexity when compared to previous systems to measure the tuning rate of a QCL.

6 Measurement of the emission spectra of the THz QCL

As shown in Chapter 2, the voltage perturbation V_{SM} induced by feedback of radiation to the laser cavity contains a sinusoidal component involving both the external cavity length L_{Ext} and the emission frequency under feedback ν, given by Eq. (2.24). As such, and as shown in previous chapters, interferometric fringes can be acquired in a SM system by simply changing the cavity length, where the spacing of these fringes will have a relationship to the emission frequency of the QCL. The interaction that occurs between the emitted and reflected beams in a SM set-up is a very similar mixing effect to that used in Fourier transform infrared (FTIR) spectroscopy. For further information on the operation of an FTIR see Chapter 3.1.2.

While performing spectral measurements of a THz QCL using an FTIR, observations have previously noted that an FTIR is alignment sensitive.[217,218] By windowing the interferometric fringes obtained over the cavity extension and extracting the spectra of each window, a three-dimensional representation of the FTIR measurement can be obtained. Under conditions of poor alignment, the resolved QCL spectra can be seen to change to a completely different laser cavity mode for various path lengths of the variable arm in the interferometer, as shown in Fig. 6.1 (obtained using the laser described in Chapter 6.2). This can be attributed to the far-field pattern of the QCL where different modes are emitted at different angles from the device,[217,218] and these therefore couple through the FTIR at different angles. This phenomenon is particularly relevant to high-resolution FTIR systems in which a long interferometric path length is required.

As self-mixing is inherently self-aligning along the transverse mode of the laser cavity, this should be alleviated within a SM system and the main lasing Fabry-Pérot modes should always be observed. Other advantages include the removal of the need for a separate FTIR system to quantify the emission spectra of devices, and SM systems also remove the need for an external detector. The work in this chapter will present the use of a self-mixing interferometer to extract the emission frequency of a THz QCL and to explore the effects of feedback on the spectrum in the form of frequency pulling.

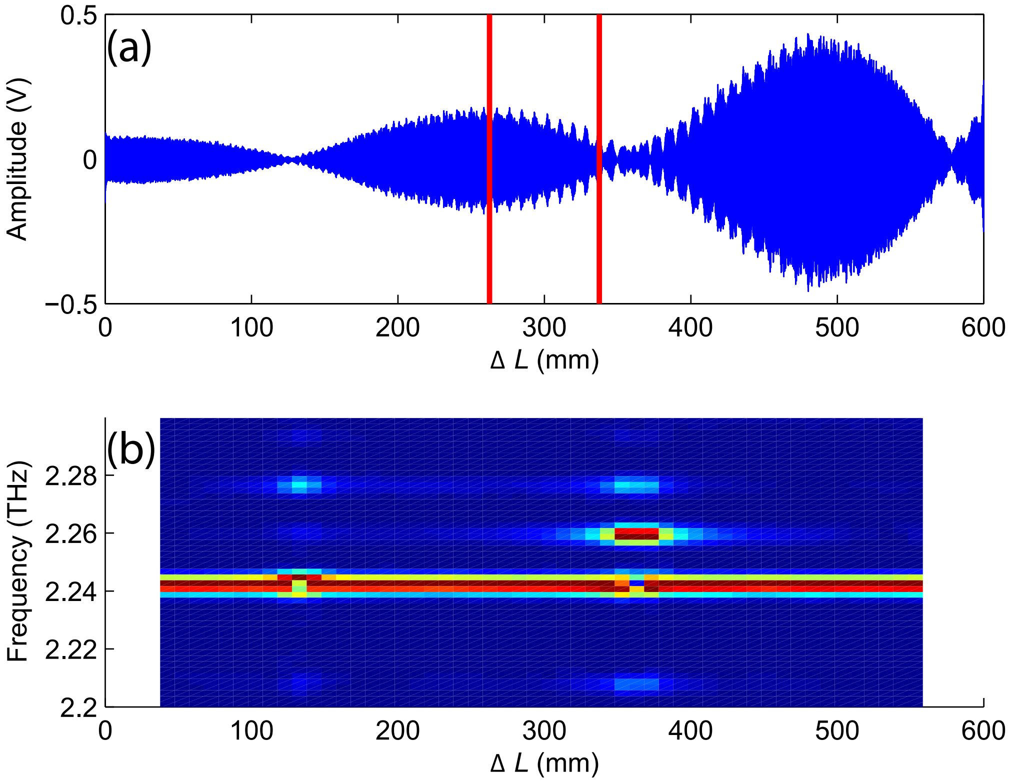

Figure 6.1: (a) Interferometric fringes acquired using a FTIR through a variable arm cavity extension of 600 mm under poor QCL alignment. Typical window size (75 mm) is shown in red. (b) The resolved spectra from windowed sections of the fringes in (a). The FTIR can show different modes than the main lasing mode due to the bad alignment, as shown here at 360 mm.

6.1 Self-mixing interferometry using a focused beam

Initial work in this area utilised a typical self-mixing system, where the beam is focused onto the target in order to extract the emission spectra from the QCL.

6.1.1 Experimental set-up & measurement technique

Initial, focused beam measurements utilised a THz QCL device with a 10 µm-thick BTC active region, processed into a SISP ridge waveguide with dimensions 3 mm × 140 µm, operating at ∼2.6 THz at a heat sink temperature of 25 K. The threshold current at this temperature was 925 mA. This system utilised a self-focusing SM set-up previously described in Chapter 3, where one $f/2$ focusing mirror is used to collimate the THz beam, and another is used to focus the light to the target/mirror for a total path length of 0.41 m through an unpurged environment. This system is shown in Fig. 6.2. With this set-up, a flat gold planar mirror was moved 20 mm through the beam focus resulting in a change in cavity length, and V_{SM} was recorded via the analog voltage input on the XPS motion controller, allowing accurate voltage-mirror position tracking and recording. V_{SM} was amplified by a 20 dB differential voltage amplifier prior to its measurement via the analog input of the XPS motion controller. A sawtooth voltage modulation was applied to modulate the mirror position where the voltage-distance ratio was 1 V = 1 mm.

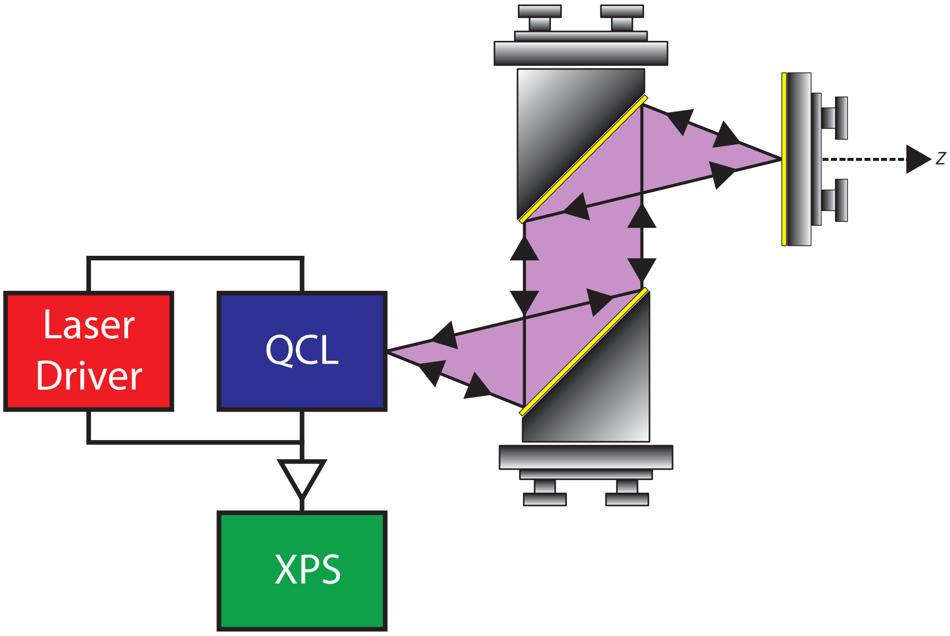

Figure 6.2: Schematic experimental SM set-up to extract laser emission parameters using a focused THz beam. A mirror is pulled-back through the beam focus to build up interferometric fringes. Differential voltage amplifier shown as circuit symbol.

The following chapter will demonstrate and discuss some of the problems inherent with such a focused system. Exemplar V_{SM} fringes for both an increasing and decreasing L_{Ext} are shown in Fig. 6.3.

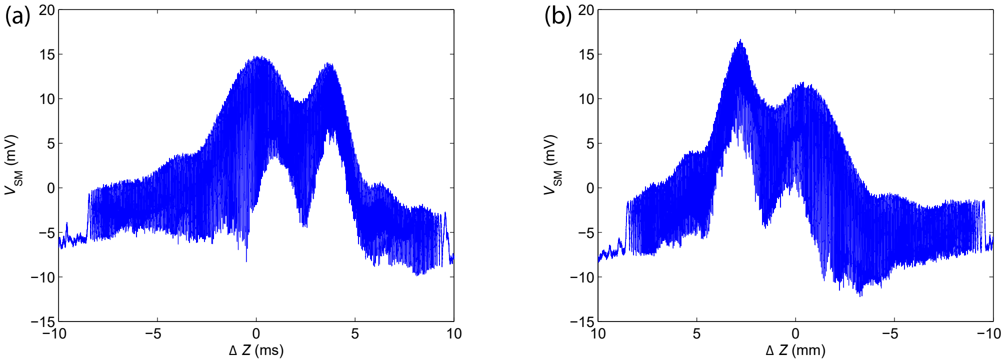

Figure 6.3: Exemplar measurements for V_{SM} for both (a) an increasing and (b) decreasing cavity length using a focused SM system.

When an FFT is performed on the measured fringes, the emission spectra of the laser can be recovered, as predicted, and this is shown in Fig. 6.4 with the red and blue spectra indicating an extending and shortening cavity respectively. Also shown is the spectrum measured using a commercial FTIR system under nominally the same driving conditions. Both the SM and FTIR systems utilised here have a resolution of 7.5 GHz.

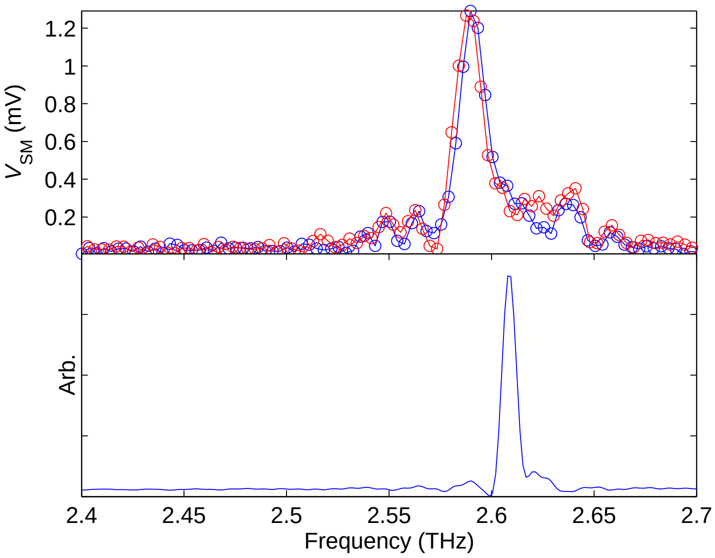

Figure 6.4: Top: Emission spectra extracted from SM fringes for both extending (blue) and shortening (red) cavity lengths. Bottom: Emission spectra from Bruker FTIR.

While in Fig. 6.4 the general shape and frequency of the spectra obtained from the SM system and the commercial FTIR are similar, there are a few discrepancies which are caused by the experimental set-up and measuring procedure. These will be discussed in the following sections.

6.1.2 General experimental considerations

The first and most obvious difference between the two spectra in Fig. 6.4 is the frequency offset apparent between them. There are a number of possible causes for the ∼19 GHz offset between the two spectral peaks, but the most likely here are differences in electrical grounding between the two measurements or the effects of feedback in the SM system.

The SM measurement and the FTIR measurement here were taken on different experimental set-ups on different optical benches. It has since been found that, due to the common-ground being electrically connected to the cryostat housing and hence the optical bench, slightly different QCL biases can occur for the same current supplied from the current driver. As such, the laser can emit slightly different frequencies on the two measurement set-ups, even for the same nominal driving current.

A second problem is the possibility of lasing on different cavity modes due to feedback. At the external cavity length L_{Ext} changes throughout the cavity extension, mode-hops of the emission frequency can occur. In the SM experiment, due to the long external cavity length (∼0.41 m), external cavity modes have a frequency separation of 365 MHz, given by

$$\Delta\nu = \frac{c}{2L_{Ext}}. \tag{6.1}$$

To observe this effect, the acquired SM fringes can be truncated before an FFT is applied to extract the lasing spectrum for the cavity length related to that truncated data. This has been demonstrated in Fig. 6.5 for a truncated dataset of 10 mm cavity perturbation, stepped by 5 mm between plots.

The emission frequency in the window 0-10 mm (50-100%) differs from that in the previous windows due to the effect of feedback forcing a mode-hop. This effect is explained in Chapter 2.2.3.

Another observation of note in relation to Fig. 6.4 related to mode-hopping is broad-

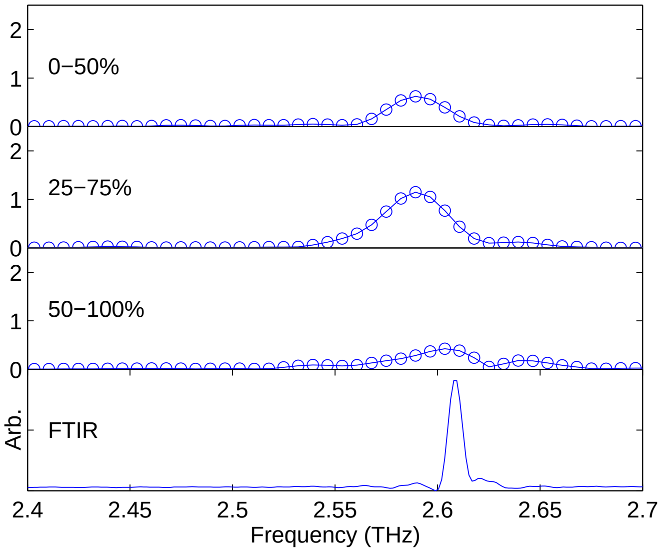

Figure 6.5: By truncating the interferometric fringes from an extending cavity length (Fig. 6.3(a)) the varying emission frequency can be observed. ΔZ ranges from (a) -10 to 0 mm, (b) -5 to 5 mm and (c) 0 to 10 mm are shown. Also demonstrated is the weighting impact of each section, with the centre fringes resulting in a much larger spectral amplitude. This is discussed in Chapter 6.1.3.

ening of the emission spectra obtained from the SM measurements. While the results from the SM and FTIR measurements broadly agree, the emission peak obtained from the SM measurements is notably broader. If the QCL emission frequency hops between the closely spaced external cavity modes along a single cavity extension, a frequency broadening of the peak would be observed in the FFT data, due to the superposition of these external modes. The observed broadening further suggests that the external cavity is affecting the emission frequency in the measurements. An example of these mode-hops is shown in Fig. 6.6.

Another feature of this technique is that the amplitude of V_{SM} varies over the scan range, as can be observed in Figs. 6.3 and 6.5. Particularly, Fig. 6.5 demonstrates that the amplitude of the recovered fringes increases in the center of the pullback, at the beam focus. This behaviour is a known property of confocal systems.

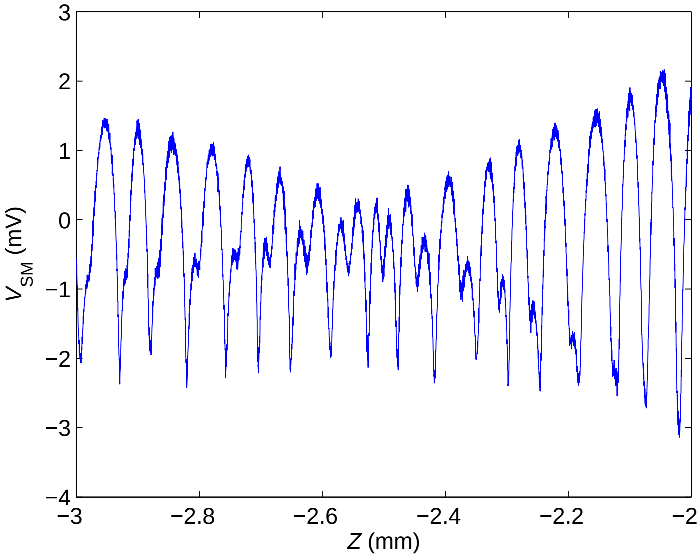

Figure 6.6: Change in the external cavity length can lead to mode hopping of the QCL.

6.1.3 Effect of a focused beam

One major difference between an FTIR system and the presented SM system is that the FTIR system uses collimated beams along its arms, whereas this SM system involves focused beams.

The numerical aperture of the focusing optics will effect the fringe spacing of the recovered interferometric fringes. The numerical aperture of a lens/mirror is defined as

$$NA = n_0 \sin(\theta) = n_0 \sin\left[\arctan\left(\frac{D}{2L_1}\right)\right], \tag{6.2}$$

where n_0 is the refractive index of the medium($n_0 = 1$ for air), θ is the half-angle from the center plane, D is the diameter of the mirror and L_1 is the focal length of the mirror. In the above SM system, all mirrors were 2 in. diameter with 4 in. focal lengths, resulting in a numerical aperture of 0.243.

The numerical aperture of a system can be related to the fringe spacing of the interferometric waveform[219,220] and will therefore have a direct impact on the frequency output of the FFT, resulting in a frequency-offset of the spectral peaks. This can be shown through the phase relationship of a confocal system[219]

$$\phi = \frac{2\pi}{\lambda} z(1 + \cos\alpha), \tag{6.3}$$

where λ is the laser emission wavelength, z is the mirror position, and $\alpha = \arctan\left(\frac{D}{2L_1}\right)$ from Eq. (6.2). This confocal phase relationship allows the offset between two systems to be calculated. As such, for a comparison to a confocal system such as an FTIR, the offset relationship can be simplified to

$$\frac{1 + cos(\alpha_{SM})}{1 + cos(\alpha_{FTIR})} = \frac{1 + cos(0.243)}{1 + cos(0)} = 0.985, \tag{6.4}$$

which relates to an offset frequency of 2.61 THz*0.985 = 2.57 THz, which agrees with the measurements in Fig. 6.4.

In Fig. 6.3 the amplitude of V_{SM} isn't equal along the scan range, such that the fringes in the center have a larger amplitude, and therefore will have more impact on the recovered spectra. In Fig. 6.5 where the data has been truncated to demonstrate the evolution of the emission spectra through the cavity extension, the fringes in the centre of the forward and backwards mirror scans result in an FFT with a much larger amplitude. The weighting observed here is due to the confocal nature of this set-up where the mirror passes through the focus of the THz beam. At the focus, the improved alignment of the system results in a better focusing of the light at the laser facet and an increase in amplitude inherent with this. This confocal response is given by[219,221]

$$I(u) = \left| \frac{\sin(u/2)}{u/2} \right|^2, \tag{6.5}$$

$$u = \frac{8\pi}{\lambda} z \sin^2(\alpha/2). \tag{6.6}$$

In general, a $sinc^2$ amplitude envelope would be expected.[220] However, the double peak observed in the fringes shown in Fig. 6.3 indicates astigmatism is present in the system. This causes two foci to occur at different positions along the beam axis Z. This is a problem that can occur with focusing systems, but with better alignment can be minimised. Even with perfect alignment, due to differing divergences parallel and perpendicular to the growth direction, this astigmatism could potentially still occur in QCLs. Indeed, when testing with another laser (as described in Chapter 6.2), no astigmatism was observed as shown in Fig. 6.7.

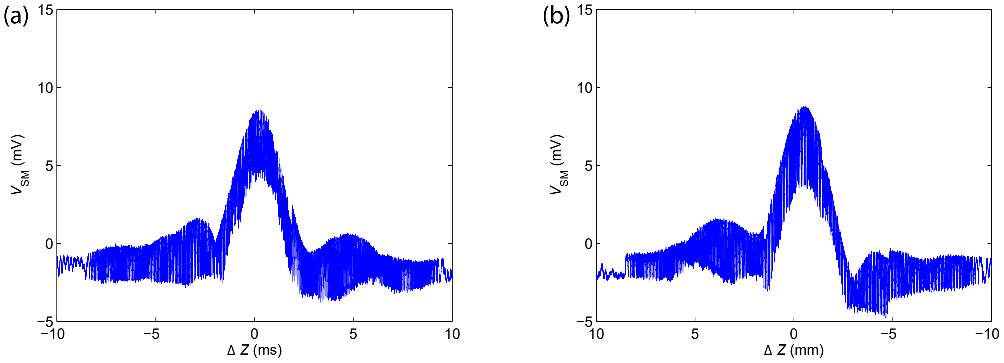

Figure 6.7: Interferometric fringes from the same measurement as shown in Fig. 6.3, but with a different laser (described in Chapter 6.2). Here with improved alignment, no astigmatism occurs.

By overlaying a simulated response of Eq. (6.5) onto these fringes, the confocal response can be shown to be the cause of the envelope of the fringes. Eq. (6.5) tells us that the amplitude of V_{SM} should be contained in a $sinc^2$ envelope. By simulating this envelope for a $NA = 0.24$, this system shows a broader than expected confocal response, as shown in Fig. 6.8.

This would suggest that the incident beam collimated onto the focusing mirror was not perfectly collimated. This would lead to a broader confocal response. Fig. 6.9(a) shows the same simulation for a NA = 0.2, which accounts for the imperfect collimation of the THz beam. Using this NA, the full-width half-maximum (FWHM) of both the simulated envelope and the measured SM fringes are very similar (2.6 mm and 2.8 mm respectively). Also worth noting, as the mirror moves through the beam focus, the laser enters the strong feedback regime due to the improved coupling, as shown in Fig. 6.9(b).

One further observation to note concerns the discrepancy between the spectra obtained in our SM measurements from the extending cavity and from the shortening cavity. Whilst

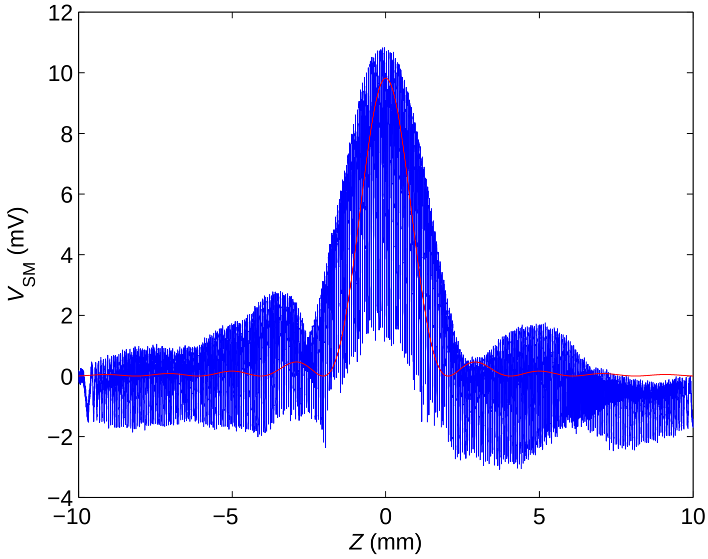

Figure 6.8: Simulation of the confocal envelope expected for NA = 0.24 shows a broader measured confocal response.

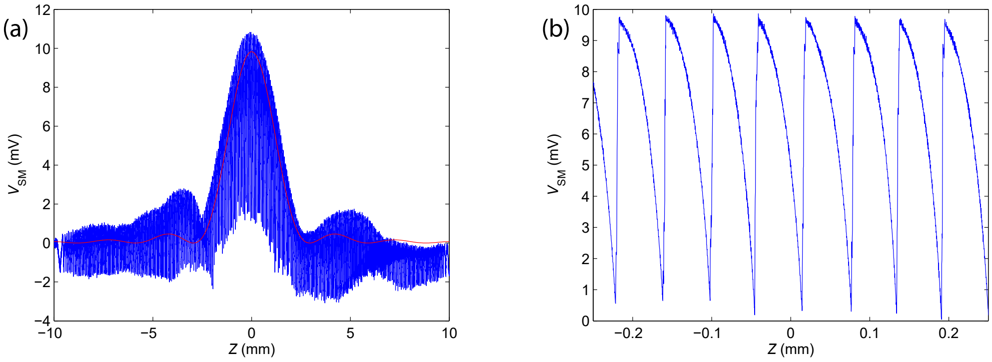

Figure 6.9: Simulating the confocal response. (a) V_{SM} has a voltage offset equal to the response predicted by Eq. (6.5). (b) At the focus the laser enters the intermediate feedback regime.

this problem isn't clearly apparent in Fig. 6.4, it can be more obviously observed in Fig. 6.10 where the same device was driven at 975 mA. The differences in these spectra can be attributed to a slight change in mirror alignment occurring at the turning point where $\Delta L_{Ext} = 10\,\mathrm{mm}$, causing a slight change in alignment of the system on forward and return sweeps. This was confirmed by projecting a visible laser beam onto a distant target after reflection from the moving mirror; the path traced by the reflected beam spot was observed to differ depending on the direction of motion of the mirror. The alignment change is not enough to misalign the system and stop the self-mixing effect, but it is enough to effect the level of feedback and therefore the fringe shape and amplitude. It is also feasible this effect could cause lasing on different compound cavity modes for forwards and backwards sweeps.

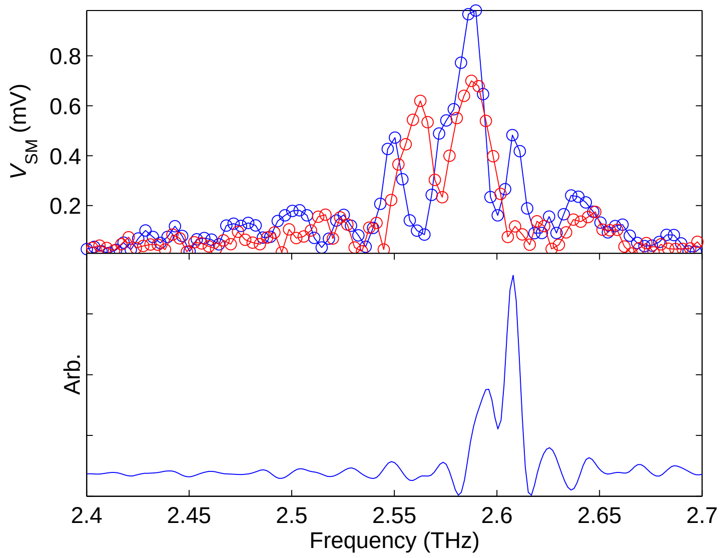

Figure 6.10: Top: Emission spectra extracted from SM fringes for both extending (blue) and shortening (red) cavity lengths. Differences in spectra can be attributed to changes in alignment due to the external mirror. Bottom: Emission spectra from Bruker FTIR.

Another consequence of moving the mirror through a beam focus is a very short ΔL_{Ext}, since far beyond the focus the light will not couple back to the laser facet sufficiently to cause SM. With the set-up shown in Fig. 6.2 the maximum useful extension of the external cavity was ∼20 mm. The resolution of the interferometer is dictated by the change in its variable arm length, which in the case of an SM system is the change in the external cavity length. The resolution can be obtained from

$$\Delta\nu = \frac{c}{2\Delta L_{Ext}}. \tag{6.7}$$

For a 20 mm change in cavity length a resolution of approximately 7.5 GHz is obtained.

The following section will describe how a slightly modified set-up was used to alleviate most of the problems discussed in this section.

6.2 Self-mixing interferometry using a collimated beam

A number of discrepancies and experimental problems have been identified in the focused SM system; mostly caused by the experimental set-up or measurement procedure. These problems can be summarized as follows:

- Frequency offsets of the spectral peaks caused by the finite numerical aperture of the system.
- Frequency offsets of the spectral peaks caused by common grounding differences between different systems.
- Astigmatism in the system due to the inherent sensitivity of the focused system to misalignment.
- Effects of the confocal response due to the focused set-up on the amplitude and shape of the recovered fringes.
- Short ΔL_{Ext} range causing poor frequency resolution in the resolved spectra.
- Broadening of recovered SM spectra due to mode-hops caused by the external cavity.

By removing the second, focusing, parabolic mirror the SM set-up not only becomes even more compact, but the majority of these problems are addressed.

6.2.1 Experimental set-up & measurement technique

In the new set-up, as shown in Fig. 6.11, the external mirror was placed in the collimated section of the emission path, removing the confocal nature of the previous experiment and the problems that this caused.

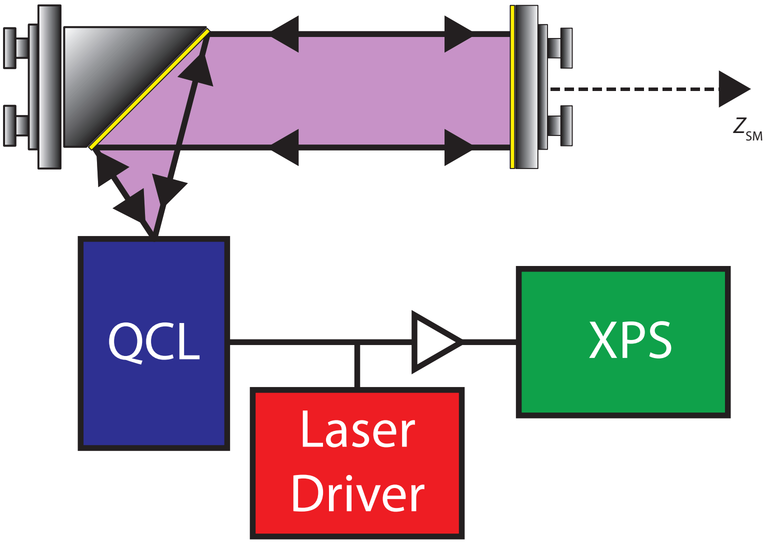

Figure 6.11: Schematic experimental set-up to extract laser emission parameters using a collimated THz beam. A mirror is pulled-back to extend the SM cavity length to build up interferometric fringes.

In order to allow comparison to an FTIR system, a THz QCL was required where emission could be collected from both facets, with one facet feeding each system. The THz QCL used in the collimated system and for comparison to the FTIR described in Chapter 6.3 consisted of a 14 µm-thick BTC active region[183] emitting at ∼2.24 THz ($\lambda \approx 134$ µm), which was processed into a SISP ridge waveguide with dimensions of 2.2 mm × 200 µm. The device was cooled using a continuous-flow helium cryostat and maintained at a heat-sink temperature of 25 K. The threshold current at this temperature was 750 mA.

6.2.2 Advantages of a collimated beam on the resolution of the emission spectra

Because the mirror now moves along a section of parallel beam, the cavity can be extended indefinitely without any changes in coupling as long as the initial collimating alignment is accurate. In the new system a 200 mm cavity extension was possible, increasing the spectral resolution 10 times to 750 MHz. Furthermore, in contrast to Fig. 6.3 the interferometric fringes now had a consistent amplitude over the entire change in the external cavity, as shown in Fig. 6.12.

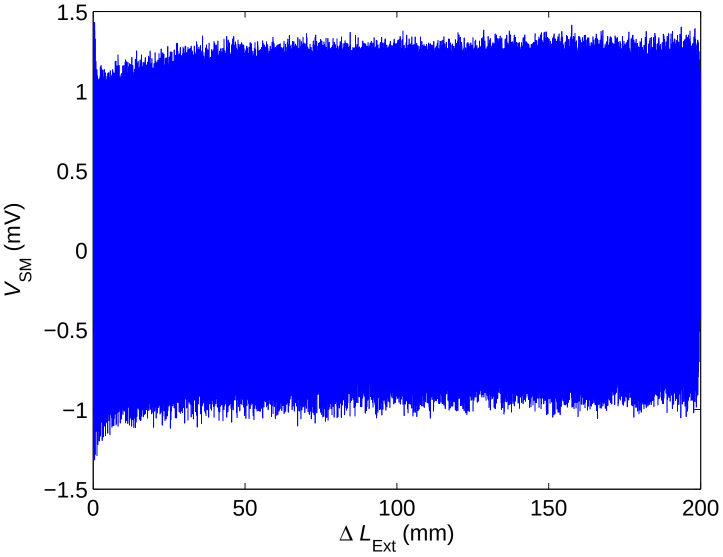

Figure 6.12: By positioning the external reflector in the collimated section of the THz beam, the SM fringes now have a consistent amplitude over the entire cavity change.

6.3 Simultaneous SM and FTIR measurement of the emission spectra

When constructing the SM set-up based on a collimated beam path, an attempt was made to remove one of the final problems from the initial experiments; differences in the common ground caused by different systems on different optical benches. In order to do this a custom FTIR was constructed on the same optical bench that took it's lasing input from the second QCL facet.

6.3.1 Experimental set-up & measurement technique

By constructing a custom FTIR the cavity length could also be increased from that of the commercial Bruker FTIR system (~20 mm) to match the increased SM cavity length (~200 mm) and it's improved spectral resolution. The SM system samples V_{SM} every 2 µm, while the FTIR system records the bolometer signal every 11 µm, dictated by the optimum response rate of the bolometer and the stage speed. Both systems use a scan length of 200 mm in order to obtain the same spectral resolution from the FFTs. 5 averages were performed on the SM system. The new system is shown in Fig. 6.13.

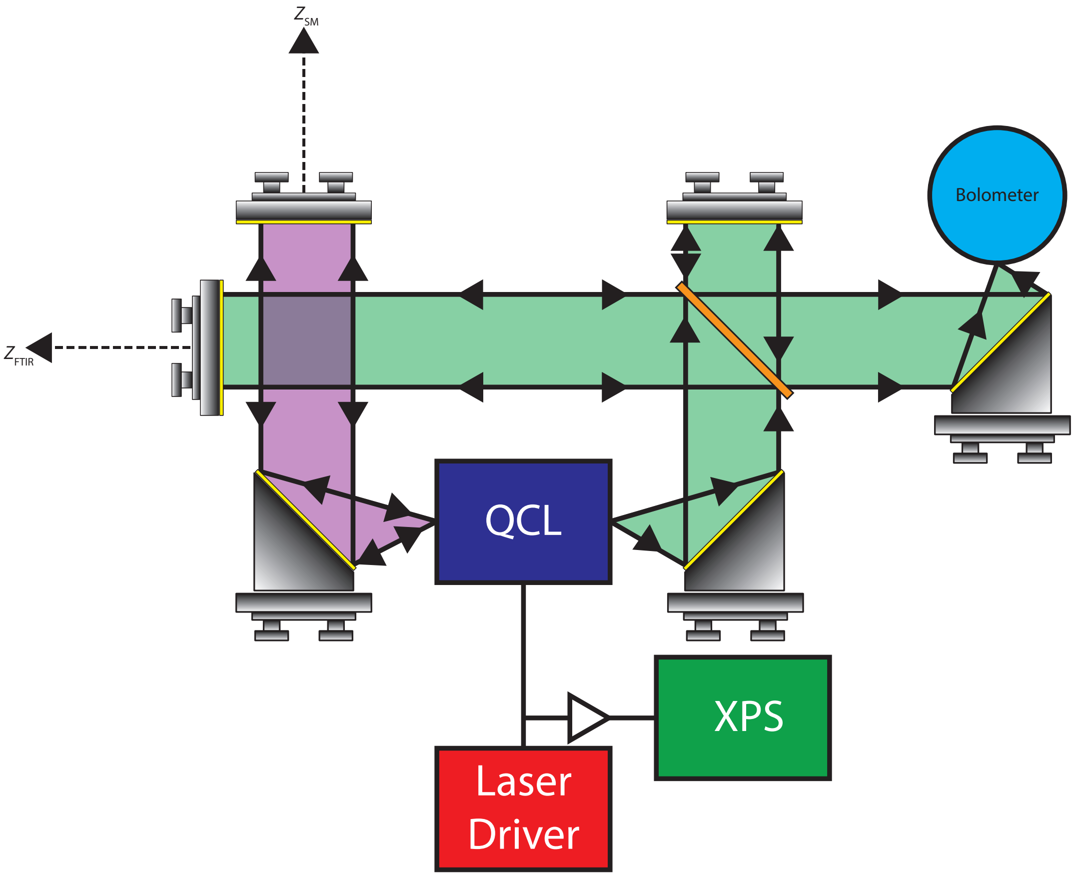

Figure 6.13: Schematic experimental set-up to directly compare the SM system to an FTIR. Emission from one facet (left) is coupled onto an external reflector used for SM interferometry, while emission from the other facet is directed into an FTIR system. This allows each system to be run directly one-after-another for direct comparison.

A major advantage of this set-up, on top of removing the initial problems, was that the SM and FTIR measurements could be executed consecutively or instantly one-after-another, leading to results obtained under the exact same conditions and negating problems such as thermal drift.

New controlling software had to be written to control the two experiments. Figure 6.14 shows a flowchart of the operation of the LabVIEW programme that was created to acquire measurements under a single bias condition on both systems, before the laser driving conditions were changed for the next measurement.

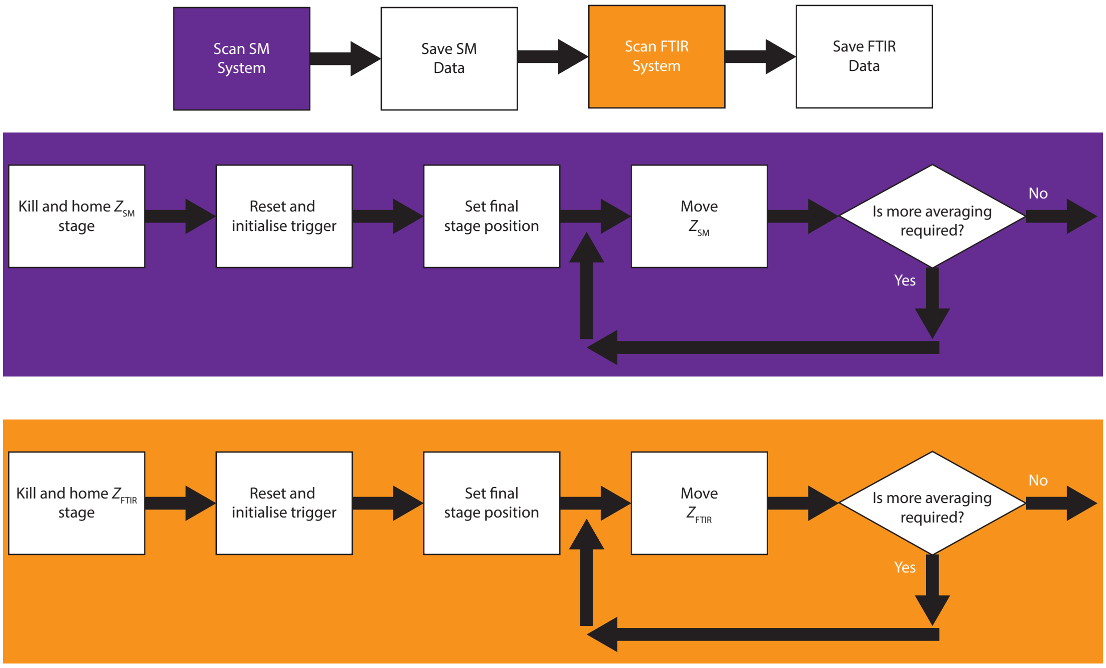

Figure 6.14: Structure of LabVIEW control system to run both experiments consecutively.

By designing the software in this way, repeated scans of the SM system were possible to allow averaging to reduce the noise in the data.

6.3.2 Comparison against FTIR spectroscopy

By utilising this set-up and the new software, SM and FTIR measurements were taken consecutively. The SM system was scanned repeatedly first, with the data from the scans being extracted from the XPS and averaged upon completion of the final iteration. Once the SM system had completed its scans, the FTIR system performed a cavity extension and the data recovered from the XPS was saved also. The same FFT analysis was performed on both sets of data, and exemplar data can be seen in Fig. 6.15.

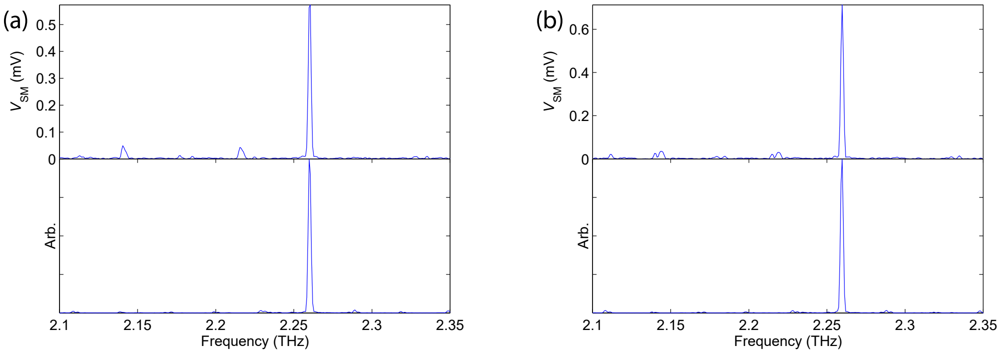

Figure 6.15: Under certain conditions (driven just after the lasing threshold) such as with driving currents of (a) 750 mA and (b) 800 mA, the SM (top) and FTIR (bottom) systems gave very similar results. High attenuation (~45 dB) was used in the SM external path to avoid strong feedback.

Under most conditions, as shown in Fig. 6.15, good agreement was found between the spectra obtained using each of the two systems. However, under some conditions such as those in Fig. 6.16 slightly different lasing modes were recovered from each system.

While the cause of this problem isn't fully understood, one potential explanation is, as previously demonstrated (Fig. 6.1), it is possible for certain modes to not couple into the FTIR system properly if there is poor alignment of the QCL to the FTIR system. In Fig. 6.16(b), the higher order mode at ~2.26 THz can be observed strongly in the SM system, but only weakly in the FTIR system for example. This can be observed more clearly in Fig. 6.17.

Lasing could also occur on compound cavity modes of the FTIR cavity. The QCL emission could be forced onto an external cavity mode depending on the position of the

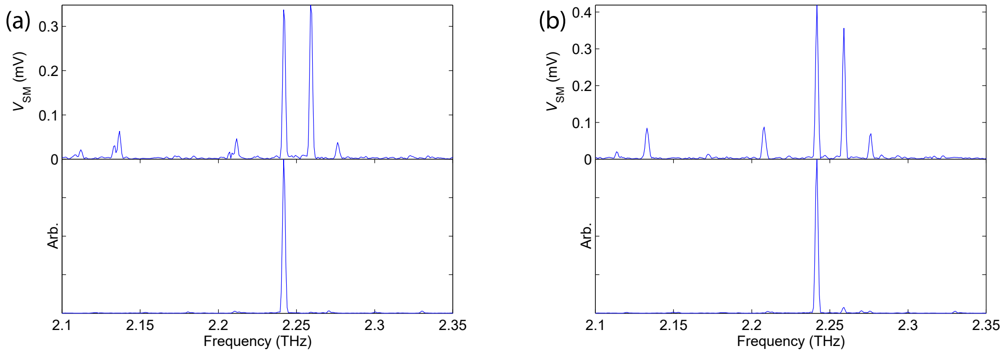

Figure 6.16: Under other conditions such as with driving currents of (a) 850 mA and (b) 900 mA, the SM (top) and FTIR (bottom) systems gave different emission spectra. High attenuation (∼45 dB) was used in the SM external path to avoid strong feedback.

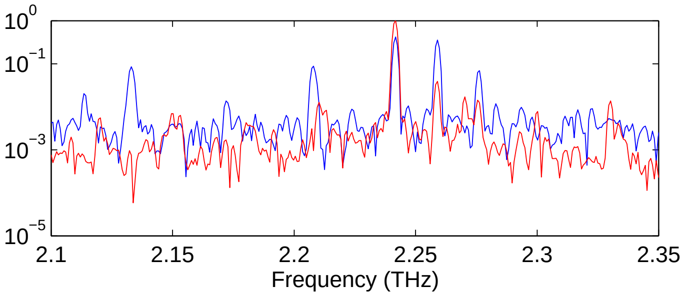

Figure 6.17: Modes have been observed to couple through the FTIR system at a different ratio than in the SM system, such as the emission at ∼2.26 THz.

FTIR mirror. As scans were taken alternately between the two systems, the SM system could measure external modes depending on where the FTIR mirror was when the SM scan was performed. To identify this, the FTIR mirror could be stepped and SM scans taken for each FTIR mirror position in order to see this effect. Alternately, isolators could be incorporated into the system to prevent feedback between the two systems. A final potential cause could be external cavity modes due to the SM external cavity. If the SM mirror was in a location where these modes did not occur when the FTIR scan was performed, the extra modes wouldn't be present in the FTIR data. Again, stepping the SM cavity and performing scans on the FTIR system could identify if this was a potential problem. High attenuation (∼45 dB) was added in the SM external cavity to attempt to limit the effect of feedback in the SM cavity and prevent this. Further work should be undertaken in this area to improve understanding.

6.4 Optical isolation of the SM and FTIR systems

One potential problem that was identified with the experimental arrangement of Fig. 6.13 is optical coupling between the two systems. As each system contains an external mirror that reflects emission back towards the laser facet, one system could couple light into the other. Observations were made that this could cause almost complete nulling of the measured signals under some conditions. Furthermore, as suggested above, feedback to the QCL from the FTIR mirrors was also possible, which could affect the lasing modes.

6.4.1 Experimental set-up & measurement technique

As such, grid polarisers were added to both sides of the system in opposite polarisations to block any coupling from one system to the next and any unwanted effects that could result from this. A quarter-wave plate was also added at 45° to the FTIR system to prevent any unwanted intra-system feedback here too. The quarter-wave plate and polariser in the FTIR system also act as an isolator to prevent feedback into the laser. A third grid polariser was added to the SM system to allow control of the feedback level and also ensure the system was operating in the weak feedback regime. The FTIR system was also realigned to help prevent potential problems due to poor alignment.

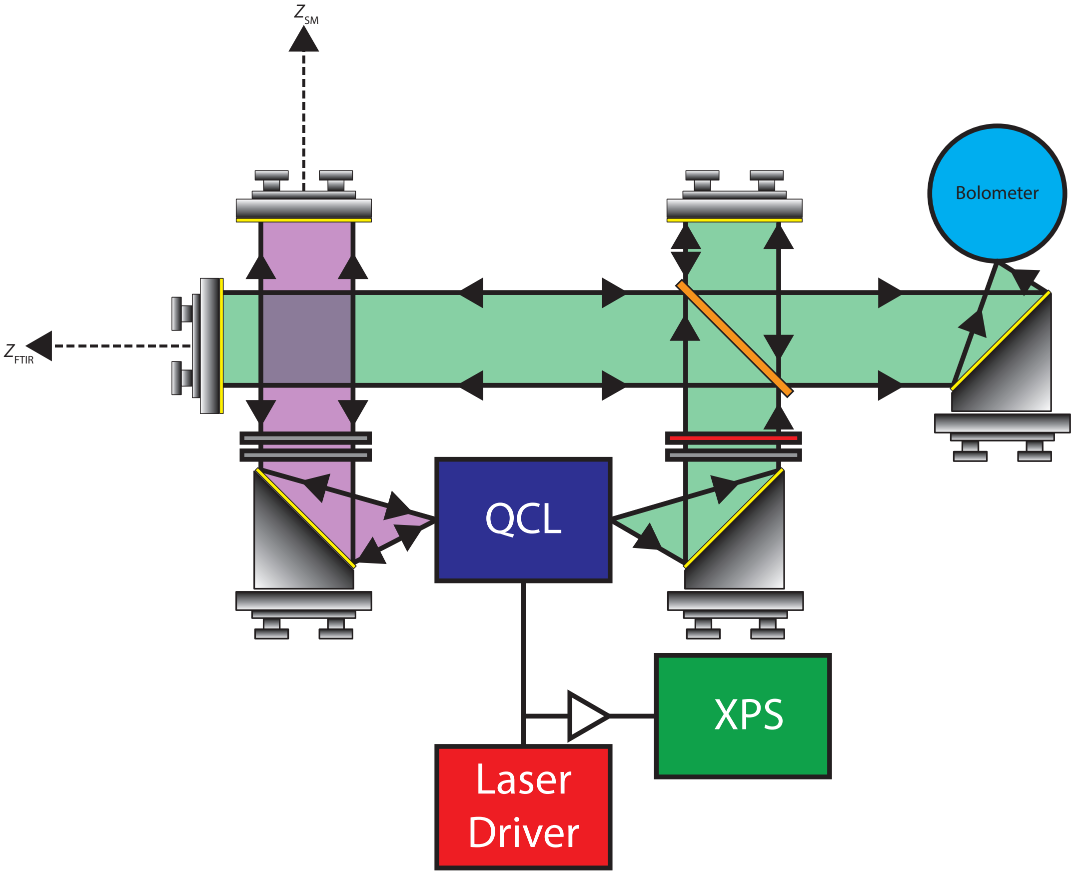

Figure 6.18: Further improvement made to the previously described FTIR and SM systems including a quarter-wave plate (red) and grid polarisers (grey) are used to ensure feedback from one system doesn't enter the other.

6.4.2 Comparison using optically isolated SM and FTIR systems

This final system design resulted in much more encouraging results. By suppressing inter-system mixing and feedback to the QCL from the FTIR mirrors, both systems were able to operate unaffected by one another and spectra recovered from each system gave very good agreement. Figure 6.19(a) shows that the new system shows extremely good agreement with the FTIR system. Both spectra have identical traits including single-mode, narrow-linewidth spectra occurring at 2.242 THz. It's also worth noting that the collimated SM system doesn't display any of the original problems such as frequency offset, spectral broadening or low frequency resolution of the FFT due to a short cavity length. By comparing the normalised logarithmic plots of the two systems it can also be noted that the systems display comparable noise levels, shown in Fig. 6.19(b).

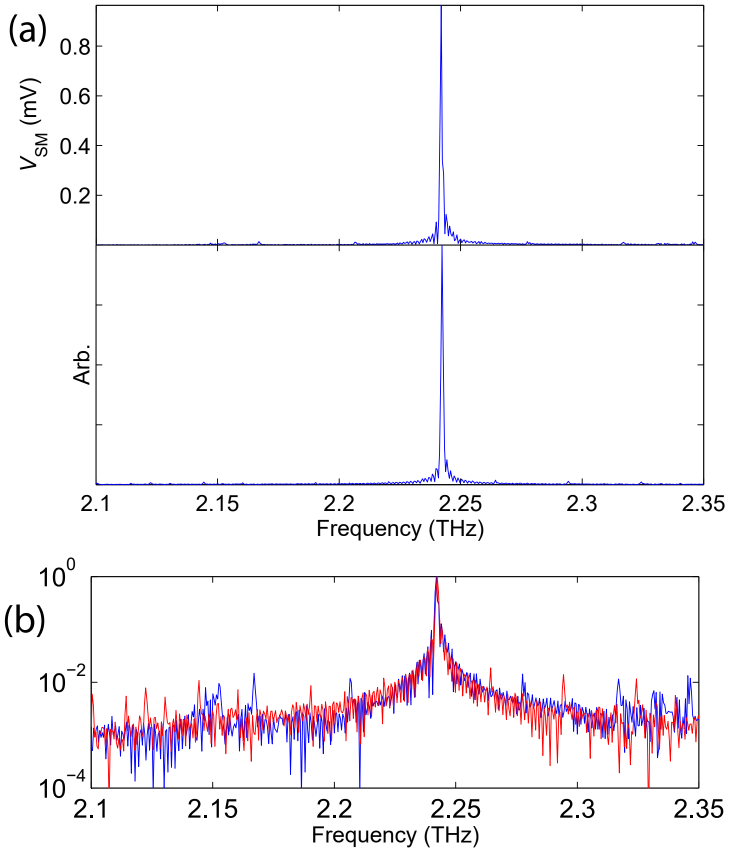

Figure 6.19: Exemplar spectra recovered from both SM ((a)top and (b) blue) and FTIR ((a) bottom and (b) red) systems showing comparable results driving the laser at 800 mA.

This system isn't limited to recovering single-mode spectra, and recovers multi-mode emission with equal accuracy, as displayed in Fig. 6.20 for the same laser at a different laser driving current (900 mA).

The same comparison was performed over the entire lasing range of the laser (725-1025 mA) and shows good agreement throughout in spectral frequency response, including good agreement of both multi-mode and single-mode regions and the bias-range that these occur over; as shown in Fig. 6.21.

Here agreement between the two systems is extremely good, with the same spectral

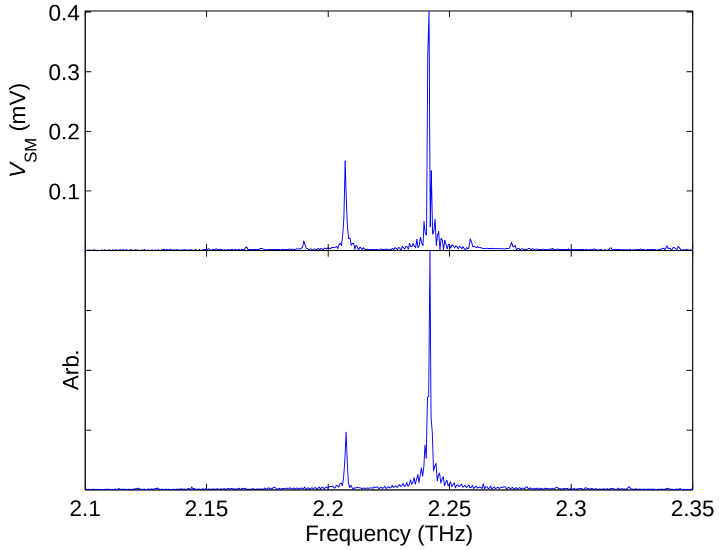

Figure 6.20: Exemplar multi-mode spectra recovered from both SM (top) and FTIR (bottom) systems performed under 900 mA bias.

features being recovered and for the most part relative mode intensities. There seems to be slight disagreement in the relative mode intensities for particular driving currents, such as 925 mA, where the FTIR spectra shows slightly higher amplitude of the secondary-mode at 2.207 THz in relation to the main-mode, but these differences are minimal and could be related to the alignment of the FTIR as mentioned in Fig. 6.1. Also, the SM system reveals lasing modes that are not resolved by the FTIR due to its alignment issues, such as those present from driving conditions beyond 850 mA at 2.26 and 2.275 THz.

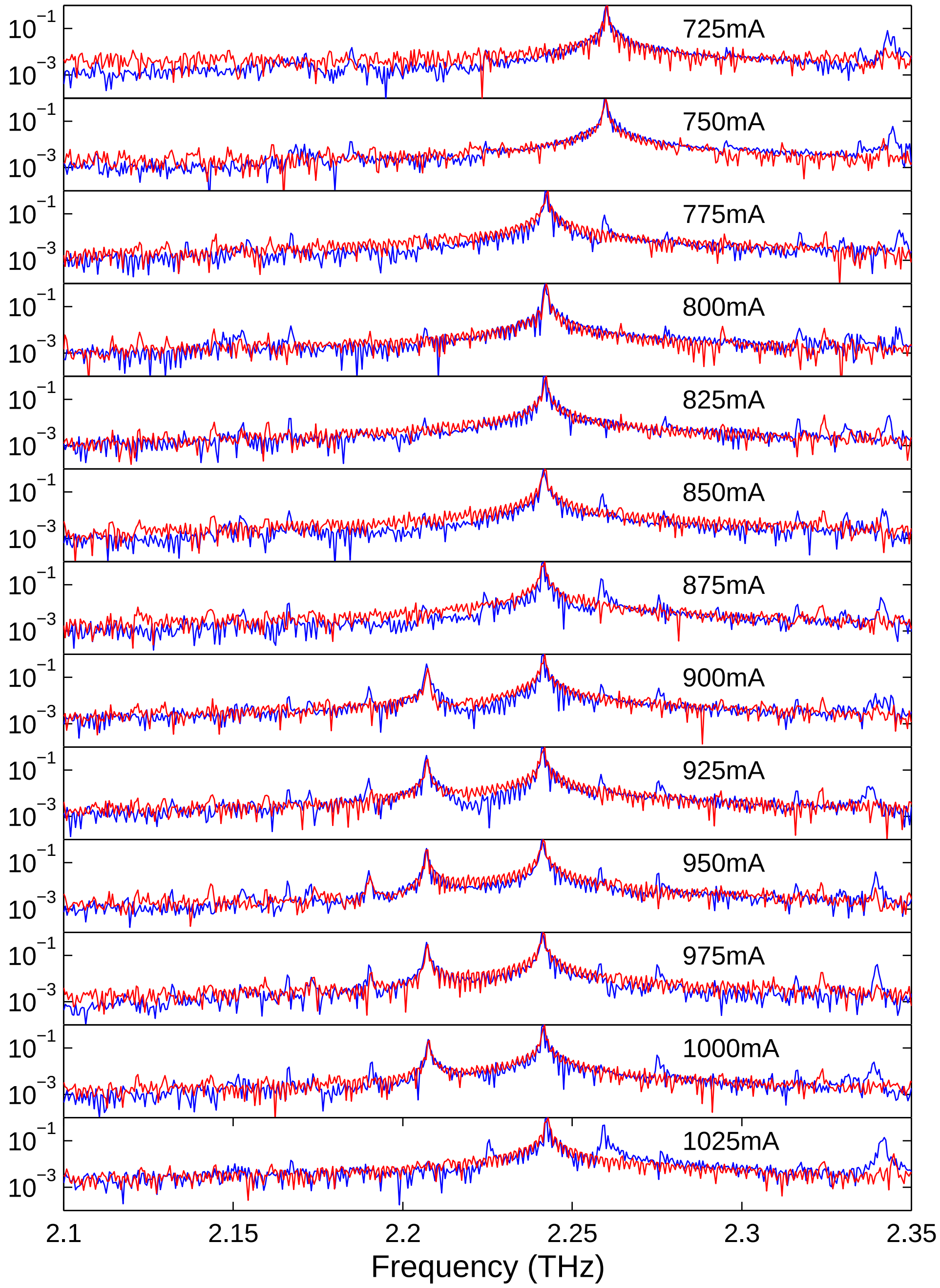

Figure 6.21: Normalised emission spectra recovered from both the SM (blue) and FTIR (red) systems over the entire lasing range of the QCL.

6.5 Measurement of frequency pulling under feedback

The previous Chapter has demonstrated that SM interferometry can be used to measure the emission spectra of a THz QCL. A further effect than can be measured using such a system is the frequency pulling effect predicted by the excess phase equation, Eq. (2.32). This effect suggests that the lasing frequency can be perturbed according to the external cavity length L_{Ext} and the level of feedback. The frequency perturbation should oscillate around the unperturbed lasing frequency ν_0 with a period $\Delta L_{Ext} = \lambda/2$. This effect was simulated using Kliese[176] code and the results are shown in Fig. 2.10 for various feedback levels.

Here the SM external cavity length is controlled and the emission frequency of the QCL perturbed according to the phase of the re-injected emission. Using the experimental set-up explained in Fig. 6.18 it was possible to both induce and measure this phenomenon.

To accomplish this, the SM cavity length was held at a nominal length $L_{Ext} = 100\,\mathrm{mm}$ and the spectra of the QCL was measured using the FTIR with a 1200 mm round trip change in path length, resulting in a high-resolution THz QCL spectrum (250 MHz resolution). The QCL was driven at 825 mA to give single mode emission to allow tracking of the exact emission frequency. The SM cavity length was then stepped by ΔL_{Ext} (2 µm in the below experiment) and the FTIR measurement was repeated. This was in turn repeated over a total cavity extension of 200 µm. As the frequency pulling effect also depends on the feedback level the grid polarisers on the SM arm of the system were used to control this.

An exemplar FTIR spectrum obtained is shown in Fig. 6.22. In order to obtain the exact peak of the emission frequency a Gaussian interpolation must be applied (shown in red). The typical center-frequency fitting error obtained using this technique is ∼1-2 MHz, as shown by the error bars in Fig. 6.24 and 6.25(b).

By stepping the external SM cavity length by 2 µm and repeating this measurement the emission frequency can be tracked. A range of exemplar peaks are shown in Fig. 6.23.

By plotting the peak emission frequency (as a change from the unperturbed emission

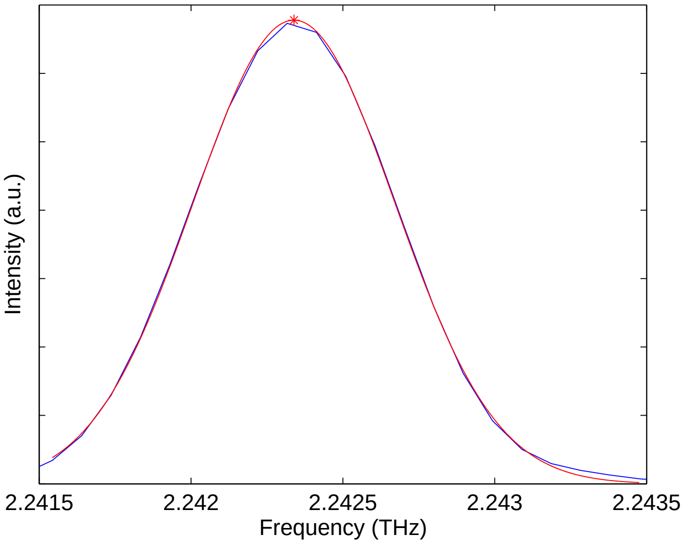

Figure 6.22: FTIR spectra of the QCL with $\Delta L_{\text{Ext}}= 0\,\mu\text{m}$ and zero SM cavity attenuation. Peak emission frequency (red star) is measured using a Gaussian interpolation (red fit).

frequency $\Delta\nu$) for each value of ΔL_{Ext} and fitting the excess phase equation to the experimental data, the feedback parameter can be extracted. This is shown in Fig. 6.24 where a feedback value of $C = 1.446$ was obtained. In Fig. 6.24 the sharp changes in emission peak demonstrate the intermediate feedback level and the sharp change that occurs when $\Delta L_{\text{Ext}} = \frac{m\lambda}{4}$ where m is an odd integer, as shown in the simulations in Fig. 2.10. As can be seen, the excess phase equation not only accurately reproduces the form of the experimental data, but also the magnitude of the frequency perturbation.

Further to this, as mentioned previously, grid polarisers were used in the SM system to allow control of the feedback level. By rotating one of the grid polarisers and keeping the other fixed (in cross-polarisation to the grid polariser on the FTIR system, to maintain a lack of inter-system coupling) the feedback into the laser is reduced by a factor of the double-pass attenuation between the two SM side polarisers (equivalent to the single-pass attenuation squared). This relationship is given by

$$R_{\text{eff}} = R_{\text{ext}}T^2 = R_{\text{ext}}\cos(\theta)^4, \tag{6.8}$$

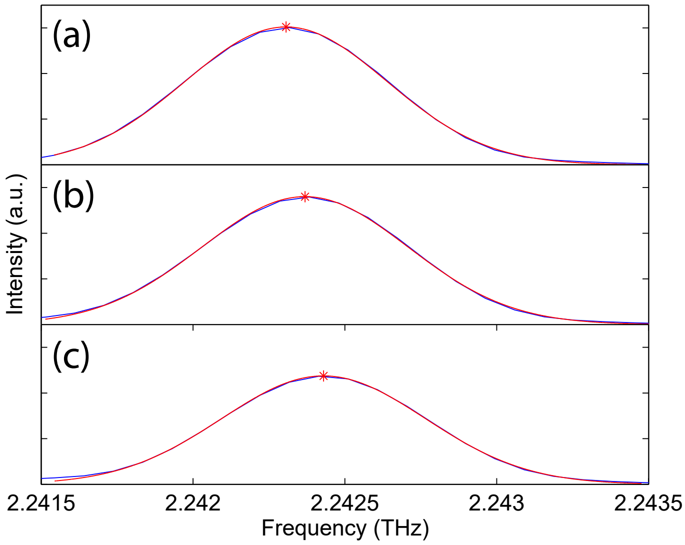

Figure 6.23: FTIR spectra of the QCL for a range of values of ΔL_{Ext}: (a) 44 µm (top) (b) 82 µm and (c) 108 µm (bottom). The peak emission frequency is shown for each spectra (red star).

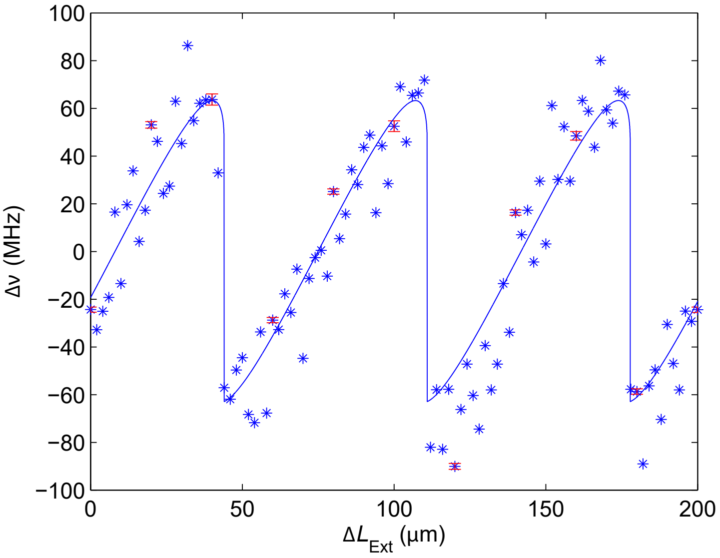

Figure 6.24: Change in frequency under feedback as a function of external SM cavity. A self-mixing model was fitted to extract the fitted value of $C = 1.446$. Exemplar fitting error is shown for exemplar cavity lengths (red).

where R_{ext} is the reflectivity of the target, T is the transmission through the polarisers and θ is the difference in polariser angles.

For a double-pass transmission level through the polarisers of $T^2 = 0.5$, the feedback level reduces to $C = 0.5977$, as shown in Fig. 6.25. Also worth noting is that the shape and amplitude of the waveform changes due to the level of feedback, as predicted by the simulations.

As the feedback level, and therefore the change in frequency under such feedback, reduces, frequency drift in the emission frequency causes the fit to become less reliable. As the overall frequency change decreases, the fit becomes more susceptible to frequency drift caused by thermal fluctuations in the QCL and the limited resolution of the FTIR. For values of transmission lower than $T^2 = 0.2$, these limitations were too great to recover the level of feedback reliably.

Through Eqs. (2.33) and (2.14) the feedback parameter can be shown to be proportional to the square root of the reflectance of the external target. By plotting the extracted feedback parameter against the square-root of the normalised reflectance of the external cavity (controlled though the polarisers), R_{eff}, Fig. 6.26 can be obtained, showing this relationship.

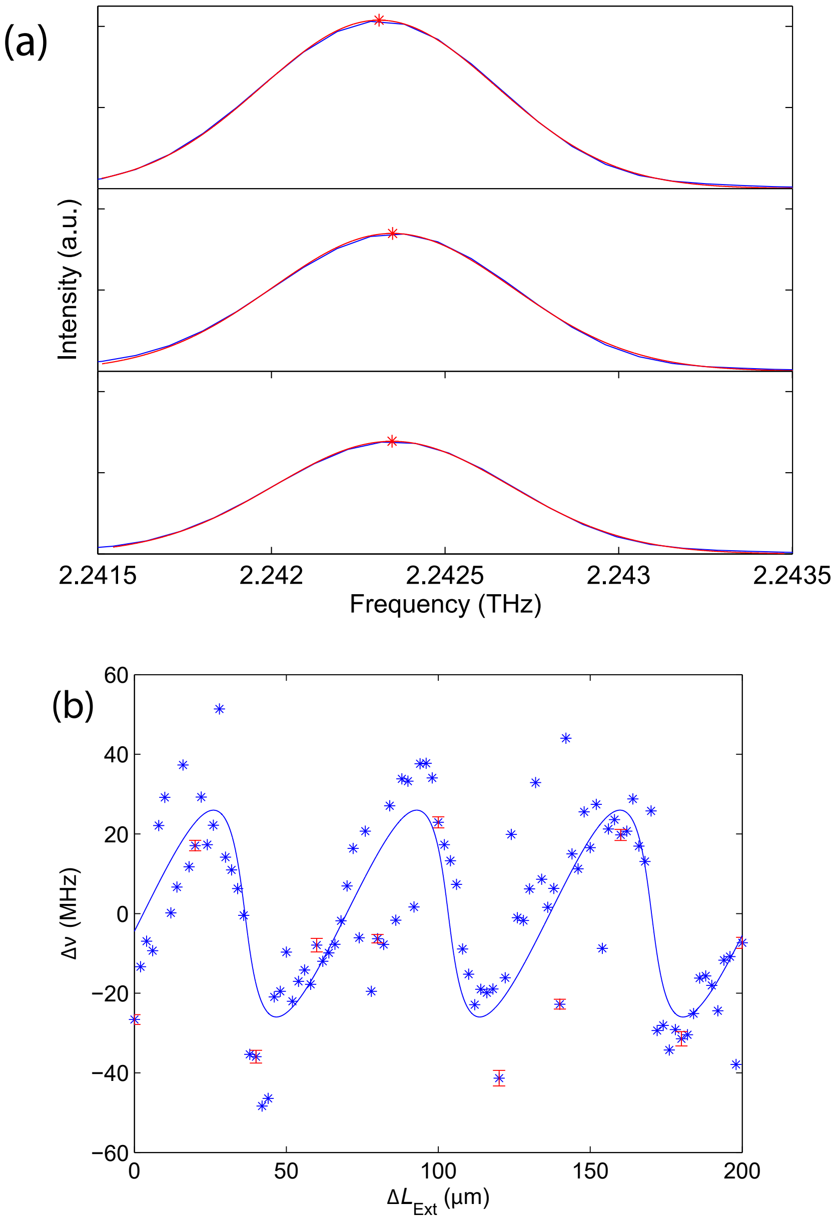

Figure 6.25: Frequency pulling results for an attenuated SM cavity where transmission $T^2 = 0.5$. (a) FTIR spectra of the QCL for a range of values of ΔL_{Ext}: 44 µm (top), 82 µm (middle) and 108 µm (bottom). The peak emission frequency is shown for each spectra (red star). (b) An SM model fitted to the change in emission frequency allowing extraction of the feedback coefficient ($C = 0.5977$). Exemplar fitting error is shown for exemplar cavity lengths (red).

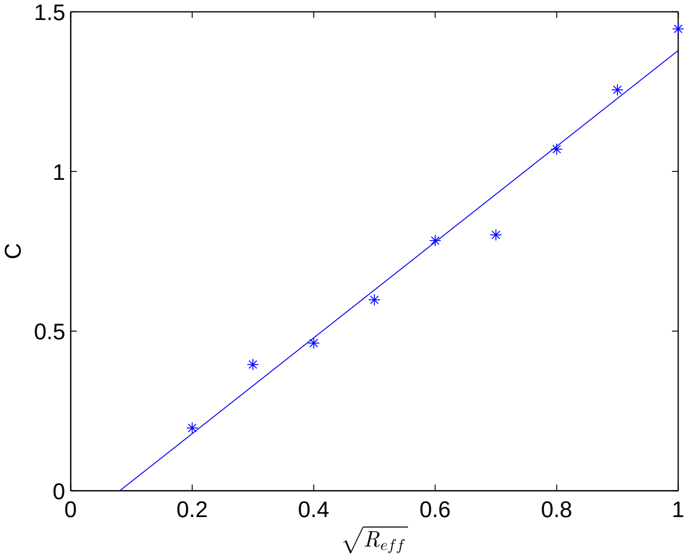

Figure 6.26: Extracted feedback parameter as a function of the normalised external cavity reflectivity.

7 Conclusion & future work

The motivation for the work presented in this thesis was the study of applications of the self-mixing (SM) phenomenon using terahertz (THz) quantum cascade lasers (QCL). A range of applications were developed and investigated with particular focus on THz imaging systems. Both two- (2D) and three-dimensional (3D) imaging performed using various modulation techniques and schemes in order to improve imaging quality and acquisition speed were demonstrated, as well as a swept-frequency scheme for the purposes of even faster and more accurate 3D imaging, extraction of the optical constants of explosive inhomogeneous materials and phase-nulling of the external phase. Finally a measurement of the laser emission spectra was performed using SM to the benefit of experimental complexity when compared to traditional techniques. The following sections will summarise the results obtained throughout the work and discuss potential areas of future work.

7.1 2D THz imaging

2D imaging was initially demonstrated using mechanical modulation to allow lock-in amplification of the small (∼mV) signal. SM imaging was achieved through raster-scanning a sample at the focus of the SM system, creating an external cavity between the sample and QCL. The QCLs terminal voltage was monitored in order to measure perturbations caused under feedback. A mechanical chopper was used to physically block the THz beam, allowing the LIA sensitivity to be set to the full dynamic range of the measured voltage perturbation. This resulted in a highly sensitive system with a strong contrast between the background and maxima of the measured SM voltage with a typical figure-of-merit of 477 extracted from an acquired image. The main limitation of this system was the upper modulation frequency of this scheme; ∼200 Hz, which made for an image acquisition time of ∼1 min for a 167×33 pixel image.

In order to bypass this limitation, an electrical modulation scheme was employed which removed the mechanical chopper and instead modulated the QCL driving current. In this method, the QCL was driven with a constant current source just below threshold with a square-wave modulation superimposed onto this in order to push the device into a lasing regime. This resulted in a system that could employ modulation frequencies $f_{\mathrm{Mod}} > 60\,\mathrm{kHz}$, only limited by the modulation bandwidth of the laser driver. One drawback of this system was that the LIA measured not only the change in voltage due to SM (∼1-2 mV) but also from the modulation scheme (∼ 75 mV), limiting the sensitivity of the LIA. This reduced the FOM of an image acquired under the same conditions as in the mechanical system (200 Hz modulation and 50 ms LIA time constant (TC)) to 36 (compared to 477), but through an increased modulation frequency of 60 kHz employing averaging through control of the LIA TC (kept at 50 ms), this could be raised to 111. Under this new system, the image acquisition time was reduced ten-fold by reducing the LIA TC to 5 ms and a FOM of 165 was recovered, comparable to the acquired image from mechanical modulation but with much improved acquisition time.

A near-field (NF) imaging system was also presented where scattering from a probe tip was detected using SM in order to improve the spatial imaging resolution. Most THz imaging systems spatial resolutions are limited by the spot size of the focused beam on the sample surface, typically ∼250 μm for THz QCL imaging systems. By employing a NF technique the spatial resolution is no longer limited by the spot size of the QCL but rather the radius of the probe tip, which resulted in a lateral imaging resolution perpendicular to the field of illumination of ∼ 1 μm. A surface approach technique also demonstrated the amplification supplied with the NF technique, and a coherent measurement component of this showed potential for mapping the phase of the incident THz field at a sample surface.

7.2 3D THz imaging with mechanical pullback

Due to the coherence afforded by SM systems, 3D depth measurements of sample surface morphology is possible. In order to achieve such a measurement, the external cavity length needs to be measured across the sample surface. To do this, the phase of the returning radiation can be obtained from an interferometric waveform at each location of the sample surface. To build up a single interferometric measurement of the SM voltage, the sample was pulled longitudinally away from the laser facet, perturbing the external cavity length.

By performing this pullback at each pixel, a measurement of the phase across the entire surface of the sample was built, and through fitting of an SM model to such waveforms, the phase of each was extracted. Through conversion using the known emission wavelength, this was converted to a measurement of the change in the external cavity due to the sample surface, resulting in a map of surface morphology.

The sample used was an exemplar GaAs structure with 3 wet-etched steps of 10 µm that was then coated in 125-nm-thick gold across the top half of each step resulting in areas of differing height and reflectivity. The surface reflectivity of the sample could be recovered through the amplitude of the measured interferometric waveform. 3D THz imaging was performed using both mechanical and electrical modulation schemes resulting in 3D images of the exemplar sample recovered with a high-degree of accuracy showing both sample height and reflectivity.

One major limitation of this system was the acquisition time of each measurement. Each longitudinal pullback took ∼20 seconds, resulting in a total imaging time of ∼2 hours for an image of 89×5 pixels. Good control of the QCL temperature is required over the entire measurement time in order to prevent frequency drift, as a change of ∼60 MHz would result in an imaging depth resolution less than 10 µm, making the morphology unrecoverable. Another limitation of the system is caused by the time taken for fitting of the SM model to the waveforms. For accurate fitting to the full 445 pixels of the acquired images, the analysis took ∼24 hours.

7.3 SM techniques based on frequency modulation

To the same end of building interferometric fringes as the pullback technique used in the 3D imaging chapter, the frequency of the laser can be chirped using an electrical sawtooth modulation. This technique was developed for a number of experimental purposes, the first of which was 3D imaging with increased accuracy and imaging speed. By employing frequency modulation, the longitudinal cavity extension was no longer required, removing this mechanical component from the system. This allowed the time to acquire one interferometric waveform to improve from ∼20 seconds to 1 µs by using a 1 kHz sawtooth modulation source. Some of this speed was traded to allow waveform averaging in order to improve the depth resolution of the system, which under optimal conditions of 10 iterations of averaging was found to be <0.1 µm. The noise power spectral density (NPSD) of the system reduced by a factor of $1/f^2$, and under these optimal conditions was measured at ~ -50 dB/Hz for 1 kHz modulation frequency. Further to these advantages, the faster imaging acquisition employed by this system allowed higher resolution images to be obtained faster, and as such a 101×10 pixel image could be acquired in minutes at an imaging rate of 40 pixels/sec, even with waveform averaging.

Another advantage of this system over previous work was an improvement of the analysis method. The previous fitting method used 5 different fitting parameters, of which only 2 were required for the final images, SM amplitude and phase. Performing an FFT on the interferometric waveforms would result in extraction of the same two parameters, but for a much reduced computational time. Using FFT analysis on the 1010 recovered waveforms took <1 minute compared for >48 hours for fitting an SM model to the same data.

It has previously been shown that the complex refractive index (CRI) of homogeneous samples can be measured as a phase change of the SM field. Building on this concept, work was performed to extract the CRI of inhomogeneous explosive materials for security purposes. By performing swept-frequency modulation on an optically flat sample holder, the CRI could be extracted from the acquired SM voltages. Analysis, performed through collaborative work with a group at the University of Queensland, allowed the extraction of the CRI for each of the 3 plastic explosives and 3 reference plastics in the holder to a high degree of agreement to time-domain spectroscopic measurements of the same samples.

A final use for swept-frequency modulation of the THz QCL is for active phase-nulling of the SM phase. Here, a perturbation in the SM voltage due to a change in the external cavity length could be counteracted through active feedback control of the laser emission frequency. This allows real-time measurement of the tuning coefficient of the QCL that previously required large, complex experimental set-ups. It also provided a technique of displacement and vibrometric measurement of the external cavity with a noise equivalent displacement of $\sim$0.2 μm.

7.4 Measurement of the emission spectra of the THz QCL

The final experimental work discussed in this thesis was the use of SM for the measurement of the emission spectra of the QCL. Recorded interferometric fringes from a cavity extension (with the QCL driven with a constant current supply) occur at a periodicity of $\lambda/2$. Work in Chapter 6 demonstrates recovery of the laser emission frequency from a high-resolution interferometric scan of the external cavity. Unlike most other SM system, a collimated external cavity was employed to remove confocal effects from the system. A fourier-transform interferometer (FTIR) was situated to allow simultaneous measurement of the laser frequency from the rear-facet of the device, and provided high agreement with the SM system. Certain modes were recovered in the SM system that couldn't be observed in the FTIR due to coupling problems through the FTIR system.

As the resolution of an FFT is related to the length of the data it is being performed on, using a long, collimated path in the FTIR resulted in a system that was so accurate (250 MHz) that the frequency-pulling effect of SM could be resolved. Under this effect, the frequency of the emission of a device will tune slightly dependant on the phase of the returning radiation. By stepping the SM cavity in 2 μm steps and performing an FTIR measurement at each SM cavity position, the position of the emission peak can be related to the external cavity length. A Gaussian fit to the single-mode peak provided an accurate frequency for each measurement, and by plotting the recovered frequencies against cavity position allowed not only the tuning effect of the frequency-pulling to be established, but also allowed the feedback parameter, C, of the SM system to be measured.

7.5 Future work

SM has only recently become an established method of THz QCL imaging, and as such there is a wide variety of areas that work could continue into. One area that was covered in this work was the combination of SM and near-field imaging. As with the 3D imaging techniques discussed in Chapters 4 and 5, by removing the longitudinal cavity extension and employing swept-frequency modulation of the QCL, faster imaging could be undertaken, or averaging could be used to improve the resolved SM voltage waveforms. This technique would also allow measurement of the CRI of samples for spectroscopic purposes.

Another area that shows promise for SM is for biomedical imaging. Due to the high sensitivity of SM, it is a prime candidate for measurements where a high degree of attenuation occurs on the radiated power, like imaging of samples with a high water content. Previous imaging systems have shown discrimination between cancerous and benign tissues[12] due to the difference in water content and SM could be used to improve such systems in terms of both sensitivity and experimental complexity.

SM could also be used for spectroscopy of compound gasses. Through use of a laser with a high tunability and an external cavity containing a gas cell, the absorption spectra of the gas could be recovered by sweeping the frequency of the THz QCL. This method could allow a compact detection method for identification of trace-gas species.[222]

Further work could also be performed with the system shown in Chapter. 6. In addition to the work performed to measure the frequency pulling of the SM effect, further work could allow observations of the mode broadening predicted by the L-K SM model.[105]

References

[1] S. A. Qaisar, *Fatigue and High Temperature Behaviour of the La-doped Bismuth-Ferrite Lead-Titanate System.* PhD thesis, University of Leeds, 2013.

[2] C. Sirtori, “Applied physics: Bridge for the terahertz gap,” *Nature*, vol. 417, pp. 132–133, may 2002.

[3] A. G. Davies and E. H. Linfield, “Bridging the terahertz gap,” *Phys. World*, vol. 17, no. 4, p. 37, 2004.

[4] B. S. Williams, *Terahertz quantum cascade lasers.* PhD thesis, 2003.

[5] B. B. Hu and M. C. Nuss, “Imaging with terahertz waves,” *Opt. Lett.*, vol. 20, p. 1716, aug 1995.

[6] P. H. Siegel, “Terahertz technology,” *IEEE Trans. Microw. Theory Tech.*, vol. 50, pp. 910–928, mar 2002.

[7] A. G. Davies, A. D. Burnett, W. Fan, E. H. Linfield, and J. E. Cunningham, “Terahertz spectroscopy of explosives and drugs,” *Mater. Today*, vol. 11, pp. 18–26, mar 2008.

[8] M. Tonouchi, “Cutting-edge terahertz technology,” *Nat. Photonics*, vol. 1, pp. 97–105, feb 2007.

[9] M. Shur, “Terahertz technology: devices and applications,” in *Proc. 35th Eur. Solid-State Device Res. Conf. 2005. ESSDERC 2005.*, vol. 2005, pp. 13–21, IEEE, 2005.

[10] J. F. Federici, B. Schulkin, F. Huang, D. Gary, R. Barat, F. Oliveira, and D. Zimdars, “THz imaging and sensing for security applications-explosives, weapons and drugs,” *Semicond. Sci. Technol.*, vol. 20, pp. S266–S280, jul 2005.

[11] P. Siegel, “Terahertz Technology in Biology and Medicine,” *IEEE Trans. Microw. Theory Tech.*, vol. 52, pp. 2438–2447, oct 2004.

[12] S. M. Kim, F. Hatami, J. S. Harris, A. W. Kurian, J. Ford, D. King, G. Scalari, M. Giovannini, N. Hoyler, J. Faist, and G. Harris, "Biomedical terahertz imaging with a quantum cascade laser," *Appl. Phys. Lett.*, vol. 88, no. 15, p. 153903, 2006.

[13] D. D. Arnone, C. M. Ciesla, A. Corchia, S. Egusa, M. Pepper, J. M. Chamberlain, C. Bezant, E. H. Linfield, R. Clothier, and N. Khammo, "Applications of terahertz (THz) technology to medical imaging," sep 1999.

[14] A. D. Burnett, W. Fan, P. Upadhya, J. E. Cunningham, H. Edwards, T. Munshi, M. Hargreaves, E. H. Linfield, and A. G. Davies, "Complementary spectroscopic studies of materials of security interest," sep 2006.

[15] J. Chen, Y. Chen, H. Zhao, G. J. Bastiaans, and X.-c. Zhang, "Absorption coefficients of selected explosives and related compounds in the range of 0.1-2.8 THz," *Opt. Express*, vol. 15, no. 19, p. 12060, 2007.

[16] W. S. Holland, J. S. Greaves, B. Zuckerman, R. A. Webb, C. McCarthy, I. M. Coulson, D. M. Walther, W. R. F. Dent, W. K. Gear, and I. Robson, "Submillimetre images of dusty debris around nearby stars," *Nature*, vol. 392, pp. 788–791, apr 1998.

[17] D. L. Woolard, R. Brown, M. Pepper, and M. C. Kemp, "Terahertz Frequency Sensing and Imaging: A Time of Reckoning Future Applications?," *Proc. IEEE*, vol. 93, pp. 1722–1743, oct 2005.

[18] A. G. Davies, E. H. Linfield, and M. B. Johnston, "The development of terahertz sources and their applications," *Phys. Med. Biol.*, vol. 47, pp. 3679–3689, nov 2002.

[19] G. Mourou, "Picosecond microwave pulses generated with a subpicosecond laser-driven semiconductor switch," *Appl. Phys. Lett.*, vol. 39, no. 4, p. 295, 1981.

[20] A. Bonvalet, M. Joffre, J. L. Martin, and A. Migus, "Generation of ultrabroadband femtosecond pulses in the mid-infrared by optical rectification of 15 fs light pulses at 100 MHz repetition rate," *Appl. Phys. Lett.*, vol. 67, no. 20, p. 2907, 1995.

[21] B. Ferguson and X.-c. Zhang, “Materials for terahertz science and technology,” *Nat. Mater.*, vol. 1, pp. 26–33, sep 2002.

[22] R. Kohler, A. Tredicucci, F. Beltram, H. E. Beere, E. H. Linfield, A. G. Davies, D. A. Ritchie, R. Iotti, and F. Rossi, “Terahertz semiconductor-heterostructure lasers,” in *Summ. Pap. Present. Lasers Electro-Optics. CLEO ’02. Tech. Diges*, vol. 417, pp. CPDC12–1–CPDC12–3, Opt. Soc. America, 2002.

[23] J. Faist, F. Capasso, D. L. Sivco, C. Sirtori, A. L. Hutchinson, and A. Y. Cho, “Quantum Cascade Laser,” *Science (80-.).*, vol. 264, pp. 553–556, apr 1994.

[24] B. S. Williams, S. Kumar, Q. Hu, and J. L. Reno, “High-power terahertz quantum-cascade lasers,” *Electron. Lett.*, vol. 42, no. 2, p. 89, 2006.

[25] L. H. Li, L. Chen, J. Zhu, J. R. Freeman, P. Dean, A. Valavanis, A. G. Davies, and E. H. Linfield, “Terahertz quantum cascade lasers with >1 W output powers,” *Electron. Lett.*, vol. 50, pp. 309–311, feb 2014.

[26] S. Fathololoumi, E. Dupont, C. W. I. Chan, Z. R. Wasilewski, S. R. Laframboise, D. Ban, A. Mátyás, C. Jirauschek, Q. Hu, and H. C. Liu, “Terahertz quantum cascade lasers operating up to ˜200 K with optimized oscillator strength and improved injection tunneling,” *Opt. Express*, vol. 20, p. 3866, feb 2012.

[27] P. Harrison and A. Valavanis, *Quantum Wells, Wires and Dots.* Chichester: J. Wiley & Sons Ltd, 4th ed., 2016.

[28] P. S. Zory, *Quantum Well Lasers.* OPTICS AND PHOTONICS SERIES, Academic Press, 1993.

[29] R. Paiella, *Intersubband Transitions In Quantum Structures.* McGraw-Hill nanoscience and technology series, McGraw-Hill Education, 2010.

[30] J. Faist, F. Capasso, C. Sirtori, D. L. Sivco, A. L. Hutchinson, and A. Y. Cho, “Vertical transition quantum cascade laser with Bragg confined excited state,” *Appl. Phys. Lett.*, vol. 66, no. 5, p. 538, 1995.

[31] J. Faist, F. Capasso, C. Sirtori, D. L. Sivco, J. N. Baillargeon, A. L. Hutchinson, S. N. G. Chu, and A. Y. Cho, "High power mid-infrared ($\lambda\tilde{}5$ μm) quantum cascade lasers operating above room temperature," *Appl. Phys. Lett.*, vol. 68, no. 26, p. 3680, 1996.

[32] B. S. Williams, H. Callebaut, S. Kumar, Q. Hu, and J. L. Reno, "3.4-THz quantum cascade laser based on longitudinal-optical-phonon scattering for depopulation," *Appl. Phys. Lett.*, vol. 82, no. 7, p. 1015, 2003.

[33] R. W. Adams, K. Vijayraghavan, Q. J. Wang, J. A. Fan, F. Capasso, S. P. Khanna, L. H. Li, A. G. Davies, E. H. Linfield, and M. A. Belkin, "GaAs/Al0.15Ga0.85As terahertz quantum cascade lasers with double-phonon resonant depopulation operating up to 172 K," in *2011 Int. Conf. Infrared, Millimeter, Terahertz Waves*, pp. 1–2, IEEE, oct 2011.

[34] M. I. Amanti, G. Scalari, R. Terazzi, M. Fischer, M. Beck, J. Faist, A. Rudra, P. Gallo, and E. Kapon, "Bound-to-continuum terahertz quantum cascade laser with a single-quantum-well phonon extraction/injection stage," *New J. Phys.*, vol. 11, p. 125022, dec 2009.

[35] B. S. Williams, "Terahertz quantum-cascade lasers," *Nat. Photonics*, vol. 1, pp. 517–525, sep 2007.

[36] Q. Hu, B. S. Williams, S. Kumar, H. Callebaut, S. Kohen, and J. L. Reno, "Resonant-phonon-assisted THz quantum-cascade lasers with metal-metal waveguides," *Semicond. Sci. Technol.*, vol. 20, pp. S228–S236, jul 2005.

[37] B. S. Williams, S. Kumar, Q. Hu, and J. L. Reno, "Distributed-feedback terahertz quantum-cascade lasers with laterally corrugated metal waveguides," *Opt. Lett.*, vol. 30, p. 2909, nov 2005.

[38] V. P. Wallace, E. MacPherson, J. A. Zeitler, and C. Reid, "Three-dimensional imag-

ing of optically opaque materials using nonionizing terahertz radiation," *J. Opt. Soc. Am. A*, vol. 25, p. 3120, dec 2008.

[39] D. R. Grischkowsky and D. M. Mittleman, *Sensing with Terahertz Radiation*, vol. 85 of *Springer Series in Optical Sciences.* Berlin, Heidelberg: Springer Berlin Heidelberg, 2003.

[40] B. Senitzky and A. A. Oliner, *Submillimeter waves-a transition region.* New York: Proc. Symp. on Submillimeter Waves, 1970.

[41] T. S. Hartwick, D. T. Hodges, D. H. Barker, and F. B. Foote, "Far infrared imagery," *Appl. Opt.*, vol. 15, p. 1919, aug 1976.

[42] P. K. Cheo, "Far-infrared laser system for detection of defects in polyethylene-insulated power cables," *Opt. Lett.*, vol. 2, p. 42, feb 1978.

[43] J. E. Bjarnason, T. L. J. Chan, A. W. M. Lee, M. A. Celis, and E. R. Brown, "Millimeter-wave, terahertz, and mid-infrared transmission through common clothing," *Appl. Phys. Lett.*, vol. 85, no. 4, p. 519, 2004.

[44] J. A. Zeitler, Y. C. Shen, C. Baker, P. F. Taday, M. Pepper, and T. Rades, "Analysis of Coating Structures and Interfaces in Solid Oral Dosage Forms by Three Dimensional Terahertz Pulsed Imaging," *J. Pharm. Sci.*, vol. 96, pp. 330–340, feb 2007.

[45] T. Yasui, T. Yasuda, K.-i. Sawanaka, and T. Araki, "Terahertz paintmeter for noncontact monitoring of thickness and drying progress in paint film," *Appl. Opt.*, vol. 44, p. 6849, nov 2005.

[46] J. A. Zeitler, P. F. Taday, D. A. Newnham, M. Pepper, K. C. Gordon, and T. Rades, "Terahertz pulsed spectroscopy and imaging in the pharmaceutical setting - a review," *J. Pharm. Pharmacol.*, vol. 59, pp. 209–223, feb 2007.

[47] Y. C. Shen, P. F. Taday, D. A. Newnham, and M. Pepper, "Chemical mapping using reflection terahertz pulsed imaging," *Semicond. Sci. Technol.*, vol. 20, pp. S254–S257, jul 2005.

[48] B. Fischer, M. Hoffmann, H. Helm, G. Modjesch, and P. Uhd Jepsen, “Chemical recognition in terahertz time-domain spectroscopy and imaging,” *Semicond. Sci. Technol.*, vol. 20, pp. S246–S253, jul 2005.

[49] M. Lu, J. Shen, N. Li, Y. Zhang, C. Zhang, L. Liang, and X. Xu, “Detection and identification of illicit drugs using terahertz imaging,” *J. Appl. Phys.*, vol. 100, no. 10, p. 103104, 2006.

[50] Y. C. Shen, T. Lo, P. F. Taday, B. E. Cole, W. R. Tribe, and M. C. Kemp, “Detection and identification of explosives using terahertz pulsed spectroscopic imaging,” *Appl. Phys. Lett.*, vol. 86, no. 24, p. 241116, 2005.

[51] A. J. Fitzgerald, V. P. Wallace, M. Jimenez-Linan, L. Bobrow, R. J. Pye, A. D. Purushotham, and D. D. Arnone, “Terahertz Pulsed Imaging of Human Breast Tumors 1,” *Radiology*, vol. 239, pp. 533–540, may 2006.

[52] V. P. Wallace, A. J. Fitzgerald, S. Shankar, N. Flanagan, R. J. Pye, J. A. Cluff, and D. D. Arnone, “Terahertz pulsed imaging of basal cell carcinoma ex vivo and in vivo,” *Br. J. Dermatol.*, vol. 151, pp. 424–432, aug 2004.

[53] H. Shimosato, M. Ashida, T. Itoh, S. Saito, and K. Sakai, “Ultrabroadband Detection of Terahertz Radiation from 0.1 to 100 THz with Photoconductive Antenna,” in *Ultrafast Opt. V SE - 41* (S. Watanabe and K. Midorikawa, eds.), vol. 132 of *Springer Series in Optical Sciences*, pp. 317–323, Springer New York, 2007.

[54] K. J. Siebert, T. Löffler, H. Quast, M. Thomson, T. Bauer, R. Leonhardt, S. Czasch, and H. G. Roskos, “All-optoelectronic continuous wave THz imaging for biomedical applications,” *Phys. Med. Biol.*, vol. 47, pp. 3743–3748, nov 2002.

[55] I. S. Gregory, W. R. Tribe, C. Baker, B. E. Cole, M. J. Evans, L. Spencer, M. Pepper, and M. Missous, “Continuous-wave terahertz system with a 60 dB dynamic range,” *Appl. Phys. Lett.*, vol. 86, no. 20, p. 204104, 2005.

[56] T. Löffler, T. May, A. Alcin, B. Hils, C. am Weg, and H. G. Roskos, "Continuous-wave terahertz imaging with a hybrid system," in *2007 Conf. Lasers Electro-Optics*, vol. 091111, pp. 1–2, IEEE, may 2007.

[57] E. BruÌĹndermann, M. Havenith, G. Scalari, M. Giovannini, J. Faist, J. Kunsch, L. Mechold, and M. Abraham, "Turn-key compact high temperature terahertz quantum cascade lasers: imaging and room temperature detection," *Opt. Express*, vol. 14, no. 5, p. 1829, 2006.

[58] H. Richter, M. Greiner-Bär, S. G. Pavlov, A. D. Semenov, M. Wienold, L. Schrottke, M. Giehler, R. Hey, H. T. Grahn, and H.-W. Hübers, "A compact, continuous-wave terahertz source based on a quantum-cascade laser and a miniature cryocooler," *Opt. Express*, vol. 18, p. 10177, may 2010.

[59] M. S. Vitiello and A. Tredicucci, "Tunable Emission in THz Quantum Cascade Lasers," *IEEE Trans. Terahertz Sci. Technol.*, vol. 1, pp. 76–84, sep 2011.

[60] M. Ravaro, V. Jagtap, G. Santarelli, C. Sirtori, L. H. Li, S. P. Khanna, E. H. Linfield, and S. Barbieri, "Continuous-wave coherent imaging with terahertz quantum cascade lasers using electro-optic harmonic sampling," *Appl. Phys. Lett.*, vol. 102, no. 9, p. 091107, 2013.

[61] P. Dean, A. Valavanis, J. T. Keeley, K. Bertling, Y. L. Lim, R. H. S. Alhathlool, S. Chowdhury, T. Taimre, L. H. Li, D. Indjin, S. J. Wilson, A. D. Rakić, E. H. Linfield, and A. Giles Davies, "Coherent three-dimensional terahertz imaging through self-mixing in a quantum cascade laser," *Appl. Phys. Lett.*, vol. 103, no. 18, p. 181112, 2013.

[62] P. Dean, N. K. Saat, S. P. Khanna, M. Salih, A. D. Burnett, J. E. Cunningham, E. H. Linfield, and A. G. Davies, "Dual-frequency imaging using an electrically tunable terahertz quantum cascade laser," *Opt. Express*, vol. 17, p. 20631, nov 2009.

[63] J. Darmo, V. Tamošinuas, G. Fasching, J. Kröll, K. Unterrainer, M. Beck, M. Gio-

vannini, J. Faist, C. Kremser, and P. Debbage, “Imaging with a Terahertz quantum cascade laser,” *Opt. Express*, vol. 12, no. 9, p. 1879, 2004.

[64] P. Dean, M. U. Shaukat, S. P. Khanna, S. Chakraborty, M. Lachab, A. D. Burnett, A. G. Davies, and E. H. Linfield, “Absorption-sensitive diffuse reflection imaging of concealed powders using a terahertz quantum cascade laser,” *Opt. Express*, vol. 16, p. 5997, apr 2008.

[65] P. Dean, Y. L. Lim, A. Valavanis, R. Kliese, M. Nikolić, S. P. Khanna, M. Lachab, D. Indjin, Z. Ikonić, P. Harrison, A. D. Rakić, E. H. Linfield, and A. G. Davies, “Terahertz imaging through self-mixing in a quantum cascade laser,” *Opt. Lett.*, vol. 36, p. 2587, jul 2011.

[66] U. Siciliani de Cumis, J. Xu, L. Masini, R. Degl’Innocenti, P. Pingue, F. Beltram, A. Tredicucci, M. S. Vitiello, P. A. Benedetti, H. E. Beere, and D. A. Ritchie, “Terahertz confocal microscopy with a quantum cascade laser source,” *Opt. Express*, vol. 20, p. 21924, sep 2012.

[67] M. Ravaro, M. Locatelli, L. Viti, D. Ercolani, L. Consolino, S. Bartalini, L. Sorba, M. S. Vitiello, and P. De Natale, “Detection of a 2.8 THz quantum cascade laser with a semiconductor nanowire field-effect transistor coupled to a bow-tie antenna,” *Appl. Phys. Lett.*, vol. 104, p. 083116, feb 2014.

[68] P. Dean, A. Valavanis, J. T. Keeley, K. Bertling, Y. L. Lim, R. H. S. Alhathlool, A. D. Burnett, L. H. Li, S. P. Khanna, D. Indjin, T. Taimre, A. D. Rakić, E. H. Linfield, and A. G. Davies, “Terahertz imaging using quantum cascade lasers-a review of systems and applications,” *J. Phys. D. Appl. Phys.*, vol. 47, p. 374008, sep 2014.

[69] A. A. Danylov, J. Waldman, T. M. Goyette, A. J. Gatesman, R. H. Giles, K. J. Linden, W. R. Neal, W. E. Nixon, M. C. Wanke, and J. L. Reno, “Transformation of the multimode terahertz quantum cascade laser beam into a Gaussian, using a hollow dielectric waveguide,” *Appl. Opt.*, vol. 46, p. 5051, aug 2007.

[70] A. A. Danylov, T. M. Goyette, J. Waldman, M. J. Coulombe, A. J. Gatesman, R. H. Giles, X. Qian, N. Chandrayan, S. Vangala, K. Termkoa, W. D. Goodhue, and W. E. Nixon, "Terahertz inverse synthetic aperture radar (ISAR) imaging with a quantum cascade laser transmitter," *Opt. Express*, vol. 18, p. 16264, jul 2010.

[71] N. Rothbart, H. Richter, M. Wienold, L. Schrottke, H. T. Grahn, and H.-W. Hubers, "Fast 2-D and 3-D Terahertz Imaging With a Quantum-Cascade Laser and a Scanning Mirror," *IEEE Trans. Terahertz Sci. Technol.*, vol. 3, pp. 617–624, sep 2013.

[72] K. L. Nguyen, M. L. Johns, L. F. Gladden, C. H. Worrall, P. Alexander, H. E. Beere, M. Pepper, D. A. Ritchie, J. Alton, S. Barbieri, and E. H. Linfield, "Three-dimensional imaging with a terahertz quantum cascade laser," *Opt. Express*, vol. 14, no. 6, p. 2123, 2006.

[73] X. Yin, B. W.-H. Ng, J. A. Zeitler, K. L. Nguyen, L. F. Gladden, and D. Abbott, "Local Computed Tomography Using a THz Quantum Cascade Laser," *IEEE Sens. J.*, vol. 10, pp. 1718–1731, nov 2010.

[74] A. W. M. Lee, Q. Qin, S. Kumar, B. S. Williams, Q. Hu, and J. L. Reno, "Real-time terahertz imaging over a standoff distance (>25 meters)," *Appl. Phys. Lett.*, vol. 89, no. 14, p. 141125, 2006.

[75] A. W. M. Lee, B. S. Williams, S. Kumar, Qing Hu, and J. L. Reno, "Real-time imaging using a 4.3-THz quantum cascade laser and a 320 x 240 microbolometer focal-plane array," *IEEE Photonics Technol. Lett.*, vol. 18, pp. 1415–1417, jul 2006.

[76] B. N. Behnken, G. Karunasiri, D. R. Chamberlin, P. R. Robrish, and J. Faist, "Real-time imaging using a 28 THz quantum cascade laser and uncooled infrared microbolometer camera," *Opt. Lett.*, vol. 33, p. 440, mar 2008.

[77] A. W. M. Lee, B. S. Williams, S. Kumar, Q. Hu, and J. L. Reno, "Tunable terahertz quantum cascade lasers with external gratings," *Opt. Lett.*, vol. 35, p. 910, apr 2010.

[78] J. Xu, J. M. Hensley, D. B. Fenner, R. P. Green, L. Mahler, A. Tredicucci, M. G. Allen, F. Beltram, H. E. Beere, and D. A. Ritchie, "Tunable terahertz quantum cascade lasers with an external cavity," *Appl. Phys. Lett.*, vol. 91, no. 12, p. 121104, 2007.

[79] L. Mahler, A. Tredicucci, F. Beltram, H. E. Beere, and D. A. Ritchie, "Tuning a distributed feedback laser with a coupled microcavity," *Opt. Express*, vol. 18, p. 19185, aug 2010.

[80] I. Kundu, P. Dean, A. Valavanis, L. Chen, L. H. Li, J. E. Cunningham, E. H. Linfield, and A. G. Davies, "Discrete Vernier tuning in terahertz quantum cascade lasers using coupled cavities," *Opt. Express*, vol. 22, p. 16595, jun 2014.

[81] L. Lever, N. M. Hinchcliffe, S. P. Khanna, P. Dean, Z. Ikonić, C. A. Evans, A. G. Davies, P. Harrison, E. H. Linfield, and R. W. Kelsall, "Terahertz ambipolar dual-wavelength quantum cascade laser," *Opt. Express*, vol. 17, p. 19926, oct 2009.

[82] J. R. Freeman, O. P. Marshall, H. E. Beere, and D. A. Ritchie, "Electrically switchable emission in terahertz quantum cascade lasers," *Opt. Express*, vol. 16, p. 19830, nov 2008.

[83] S. P. Khanna, M. Salih, P. Dean, a. G. Davies, and E. H. Linfield, "Electrically tunable terahertz quantum-cascade laser with a heterogeneous active region," *Appl. Phys. Lett.*, vol. 95, no. 18, p. 181101, 2009.

[84] A. Barkan, F. K. Tittel, D. M. Mittleman, R. Dengler, P. H. Siegel, G. Scalari, L. Ajili, J. Faist, H. E. Beere, E. H. Linfield, A. G. Davies, and D. A. Ritchie, "Linewidth and tuning characteristics of terahertz quantum cascade lasers," *Opt. Lett.*, vol. 29, p. 575, mar 2004.

[85] S. Barbieri, J. Alton, H. E. Beere, E. H. Linfield, D. A. Ritchie, S. Withington, G. Scalari, L. Ajili, and J. Faist, "Heterodyne mixing of two far-infrared quantum

cascade lasers by use of a point-contact Schottky diode," *Opt. Lett.*, vol. 29, p. 1632, jul 2004.

[86] D. Rabanus, U. U. Graf, M. C. Phillips, O. Ricken, J. Stutzki, B. Vowinkel, M. C. Wiedner, C. Walther, M. Fischer, and J. Faist, "Phase locking of a 15 Terahertz quantum cascade laser and use as a local oscillator in a heterodyne HEB receiver," *Opt. Express*, vol. 17, p. 1159, feb 2009.

[87] A. A. Danylov, T. M. Goyette, J. Waldman, M. J. Coulombe, A. J. Gatesman, R. H. Giles, W. D. Goodhue, X. Qian, and W. E. Nixon, "Frequency stabilization of a single mode terahertz quantum cascade laser to the kilohertz level.," *Opt. Express*, vol. 17, no. 9, pp. 7525–32, 2009.

[88] A. Benz, G. Fasching, A. M. Andrews, M. Martl, K. Unterrainer, T. Roch, W. Schrenk, S. Golka, and G. Strasser, "Influence of doping on the performance of terahertz quantum-cascade lasers," *Appl. Phys. Lett.*, vol. 90, no. 10, p. 101107, 2007.

[89] Q. Wu, T. D. Hewitt, and X.-c. Zhang, "Two-dimensional electro-optic imaging of THz beams," *Appl. Phys. Lett.*, vol. 69, no. 8, p. 1026, 1996.

[90] D. A. Kleinman and P. P. Kisliuk, "Discrimination Against Unwanted Orders in the Fabry-Perot Resonator," *Bell Syst. Tech. J.*, vol. 41, pp. 453–462, mar 1962.

[91] H. Kogelnick and C. K. N. Patel, "Mode Suppression and Single Frequency Operation in Gaseous Optical Masers," *IRE, Proc.*, vol. 50, pp. 2365–2366, 1962.

[92] P. G. R. King and G. J. Steward, "Metrology with an optical maser," *New Sci.*, vol. 17, pp. 180–182, 1963.

[93] D. M. Clunie and N. H. Rock, "The laser feedback interferometer," *J. Sci. Instrum.*, vol. 41, pp. 489–492, aug 1964.

[94] C. B. Wheeler and S. J. Fielding, "Interferometry using a laser as radiation source, amplifier and detector," *J. Phys. E.*, vol. 5, p. 032, jan 1972.

[95] T. M. Quist, R. H. Rediker, R. J. Keyes, W. E. Krag, B. Lax, A. L. McWhorter, and H. J. Zeigler, "SEMICONDUCTOR MASER OF GaAs," *Appl. Phys. Lett.*, vol. 1, no. 4, p. 91, 1962.

[96] R. N. Hall, G. E. Fenner, J. D. Kingsley, T. J. Soltys, and R. O. Carlson, "Coherent Light Emission From GaAs Junctions," *Phys. Rev. Lett.*, vol. 9, pp. 366–368, nov 1962.

[97] M. I. Nathan, W. P. Dumke, G. Burns, F. H. Dill, and G. Lasher, "STIMULATED EMISSION OF RADIATION FROM GaAs p-n JUNCTIONS," *Appl. Phys. Lett.*, vol. 1, no. 3, p. 62, 1962.

[98] N. Holonyak and S. F. Bevacqua, "COHERENT (VISIBLE) LIGHT EMISSION FROM Ga(As1-xPx) JUNCTIONS," *Appl. Phys. Lett.*, vol. 1, no. 4, p. 82, 1962.

[99] J. W. Crowe and R. M. Craig, "GaAs LASER LINEWIDTH MEASUREMENTS BY HETERODYNE DETECTION," *Appl. Phys. Lett.*, vol. 5, no. 4, p. 72, 1964.

[100] A. Bogatov, P. Eliseev, L. Ivanov, A. Logginov, M. Manko, and K. Senatorov, "Study of the single-mode injection laser," *IEEE J. Quantum Electron.*, vol. 9, pp. 392–394, feb 1973.

[101] H. Bachert and S. Raab, "The Influence of External Optical Coupling on the Threshold Current Density of GaAs Injection Lasers," *Phys. Status Solidi*, vol. 29, no. 2, pp. K175–K178, 1968.

[102] V. N. Morozov, V. V. Nikitin, A. A. Sheronov, and P. N. Lebedev, "Self-synchronization of modes in a GaAs semiconductor injection laser," *Sov. J. Exp. Theor. Phys. Lett.*, vol. 6, pp. 256–258, 1968.

[103] R. F. Broom, "Self modulation at gigahertz frequencies of a diode laser coupled to an external cavity," *Electron. Lett.*, vol. 5, no. 23, p. 571, 1969.

[104] R. F. Broom, E. Mohn, C. Risch, and R. Salathe, "Microwave self-modulation of

a diode laser coupled to an external cavity," *IEEE J. Quantum Electron.*, vol. 6, pp. 328–334, jun 1970.

[105] R. Lang and K. Kobayashi, "External optical feedback effects on semiconductor injection laser properties," *IEEE J. Quantum Electron.*, vol. 16, pp. 347–355, mar 1980.

[106] J. H. Churnside, "Signal-to-noise in a backscatter-modulated Doppler velocimeter," *Appl. Opt.*, vol. 23, p. 2097, jul 1984.

[107] J. H. Churnside, "Laser Doppler velocimetry by modulating a CO_2 laser with backscattered light," *Appl. Opt.*, vol. 23, p. 61, jan 1984.

[108] S. Shinohara, A. Mochizuki, H. Yoshida, and M. Sumi, "Laser Doppler velocimeter using the self-mixing effect of a semiconductor laser diode," *Appl. Opt.*, vol. 25, p. 1417, may 1986.

[109] L. Scalise, Y. Yu, G. Giuliani, G. Plantier, and T. Bosch, "Self-Mixing Laser Diode Velocimetry: Application to Vibration and Velocity Measurement," *IEEE Trans. Instrum. Meas.*, vol. 53, pp. 223–232, feb 2004.

[110] M. H. Koelink, F. F. M. de Mul, A. L. Weijers, J. Greve, R. Graaff, A. C. M. Dassel, and J. G. Aarnoudse, "Fiber-coupled self-mixing diode-laser Doppler velocimeter: technical aspects and flow velocity profile disturbances in water and blood flows," *Appl. Opt.*, vol. 33, p. 5628, aug 1994.

[111] M. J. Rudd, "A laser Doppler velocimeter employing the laser as a mixer-oscillator," *J. Phys. E.*, vol. 1, p. 305, jul 1968.

[112] S. Okamoto, H. Takeda, and F. Kannari, "Ultrahighly sensitive laser-Doppler velocity meter with a diode-pumped Nd:YVO4 microchip laser," *Rev. Sci. Instrum.*, vol. 66, no. 5, p. 3116, 1995.

[113] P. J. de Groot, G. M. Gallatin, and S. H. Macomber, "Ranging and velocimetry signal

generation in a backscatter-modulated laser diode," *Appl. Opt.*, vol. 27, p. 4475, nov 1988.

[114] R. Kliese, Y. L. Lim, K. Bertling, and A. D. Rakić, "Self-mixing laser velocimetry: A realistic model," in *COMMAD 2012*, pp. 83–84, IEEE, dec 2012.

[115] U. Zabit, R. Atashkhooei, T. Bosch, S. Royo, F. Bony, and A. D. Rakić, "Adaptive self-mixing vibrometer based on a liquid lens," *Opt. Lett.*, vol. 35, p. 1278, apr 2010.

[116] M. Norgia, A. Pesatori, and L. Rovati, "Low-Cost Optical Flowmeter With Analog Front-End Electronics for Blood Extracorporeal Circulators," *IEEE Trans. Instrum. Meas.*, vol. 59, pp. 1233–1239, may 2010.

[117] M. Norgia, A. Pesatori, and L. Rovati, "Self-Mixing Laser Doppler Spectra of Extracorporeal Blood Flow: A Theoretical and Experimental Study," *IEEE Sens. J.*, vol. 12, pp. 552–557, mar 2012.

[118] M. Norgia, A. Pesatori, and S. Donati, "A Lensless Self-Mixing Blood-Flow Sensor," in *2nd Int. Conf. Biophotonics*, pp. 65–67, 2011.

[119] F. F. M. de Mul, M. H. Koelink, A. L. Weijers, J. Greve, J. G. Aarnoudse, R. Graaff, and A. C. M. Dassel, "A semiconductor laser used for direct measurement of the blood perfusion of tissue," *IEEE Trans. Biomed. Eng.*, vol. 40, no. 2, pp. 208–210, 1993.

[120] C. Zakian, M. Dickinson, and T. King, "Particle sizing and flow measurement using self-mixing interferometry with a laser diode," *J. Opt. A Pure Appl. Opt.*, vol. 7, pp. S445–S452, jun 2005.

[121] F. J. Azcona, R. Atashkhooei, S. Royo, J. M. Astudillo, and A. Jha, "A Nanometric Displacement Measurement System Using Differential Optical Feedback Interferometry," *IEEE Photonics Technol. Lett.*, vol. 25, pp. 2074–2077, nov 2013.

[122] G. Berkovic and E. Shafir, "Optical methods for distance and displacement measurements," *Adv. Opt. Photonics*, vol. 4, p. 441, dec 2012.

[123] S. Donati, G. Giuliani, and S. Merlo, “Laser diode feedback interferometer for measurement of displacements without ambiguity,” *IEEE J. Quantum Electron.*, vol. 31, no. 1, pp. 113–119, 1995.

[124] Y. Fan, Y. Yu, J. Xi, and J. F. Chicharo, “Improving the measurement performance for a self-mixing interferometry-based displacement sensing system,” *Appl. Opt.*, vol. 50, p. 5064, sep 2011.

[125] D. Guo, “Quadrature demodulation technique for self-mixing interferometry displacement sensor,” *Opt. Commun.*, vol. 284, pp. 5766–5769, dec 2011.

[126] H. Hao, D. Guo, M. Wang, W. Xia, and X. Ni, “Micro-displace sensor based on self-mixing interference of the fiber laser with phase modulation,” *Photonic Sensors*, vol. 4, pp. 379–384, dec 2014.

[127] R. Kliese, Y. L. Lim, K. Bertling, A. A. A. Bakar, T. Bosch, and A. D. Rakić, “Self-mixing displacement sensing using the junction voltage variation in a GaN laser,” in *2008 Conf. Optoelectron. Microelectron. Mater. Devices*, no. c, pp. 23–25, IEEE, jul 2008.

[128] Y. L. Lim, P. Dean, M. Nikolić, R. Kliese, S. P. Khanna, M. Lachab, A. Valavanis, D. Indjin, Z. Ikonić, P. Harrison, E. H. Linfield, A. Giles Davies, S. J. Wilson, and A. D. Rakić, “Demonstration of a self-mixing displacement sensor based on terahertz quantum cascade lasers,” *Appl. Phys. Lett.*, vol. 99, no. 8, p. 081108, 2011.

[129] Q. Liu and M. Wang, “Implementation of the reflection phase-shift laser self-mixing interferometer for large-scale displacement measurement,” *Opt. - Int. J. Light Electron Opt.*, vol. 126, pp. 4484–4488, dec 2015.

[130] F. P. Mezzapesa, L. L. Columbo, G. De Risi, M. Brambilla, M. Dabbicco, V. Spagnolo, and G. Scamarcio, “Nanoscale Displacement Sensing Based on Nonlinear Frequency Mixing in Quantum Cascade Lasers,” *IEEE J. Sel. Top. Quantum Electron.*, vol. 21, pp. 107–114, nov 2015.

[131] M. Norgia and S. Donati, “A displacement-measuring instrument utilizing self-mixing interferometry,” *IEEE Trans. Instrum. Meas.*, vol. 52, pp. 1765–1770, dec 2003.

[132] N. Servagent, T. Bosch, and M. Lescure, “A laser displacement sensor using the self-mixing effect for modal analysis and defect detection,” *IEEE Trans. Instrum. Meas.*, vol. 46, no. 4, pp. 847–850, 1997.

[133] N. Servagent, F. Gouaux, and T. Bosch, “Measurements of displacement using the self-mixing interference in a laser diode,” *J. Opt.*, vol. 29, pp. 168–173, jun 1998.

[134] M. Wang and G. Lai, “Displacement measurement based on Fourier transform method with external laser cavity modulation,” *Rev. Sci. Instrum.*, vol. 72, no. 8, p. 3440, 2001.

[135] S. Donati, “Laser interferometry by induced modulation of cavity field,” *J. Appl. Phys.*, vol. 49, no. 2, p. 495, 1978.

[136] F. Gouaux, N. Servagent, and T. Bosch, “Absolute distance measurement with an optical feedback interferometer,” *Appl. Opt.*, vol. 37, p. 6684, oct 1998.

[137] T. Bosch, N. Servagent, R. Chellali, and M. Lescure, “Three-dimensional object construction using a self-mixing type scanning laser range finder,” *IEEE Trans. Instrum. Meas.*, vol. 47, no. 5, pp. 1326–1329, 1998.

[138] T. Bosch, N. Servagent, and M. Lescure, “A displacement sensor for spectrum analysis using the optical feedback in a single-mode laser diode,” in *IEEE Instrum. Meas. Technol. Conf. Sensing, Process. Networking. IMTC Proc.*, vol. 2, pp. 870–873, IEEE, 1997.

[139] T. Gensty, J. Von Staden, M. Peil, W. Elsäßer, G. Giuliani, and C. Mann, “Investigations of the Linewidth of Intersubband Quantum Cascade Lasers,” in *2006 IEEE 20th Int. Semicond. Laser Conf. 2006. Conf. Dig.*, pp. 65–66, IEEE, 2006.

[140] G. Giuliani, M. Norgia, and S. Donati, “Laser diode linewidth measurement by means of self-mixing interferometry,” in *1999 IEEE LEOS Annu. Meet. Conf. Proceedings. LEOS’99. 12th Annu. Meet. IEEE Lasers Electro-Optics Soc. 1999 Annu. Meet. (Cat. No.99CH37009)*, vol. 2, pp. 726–727, IEEE, 2000.

[141] Y. Yu, J. Xi, J. F. Chicharo, and T. Bosch, “Toward Automatic Measurement of the Linewidth-Enhancement Factor Using Optical Feedback Self-Mixing Interferometry With Weak Optical Feedback,” *IEEE J. Quantum Electron.*, vol. 43, pp. 527–534, jul 2007.

[142] L. Wei, J. Xi, Y. Yu, and J. F. Chicharo, “Linewidth enhancement factor measurement based on optical feedback self-mixing effect: a genetic algorithm approach,” *J. Opt. A Pure Appl. Opt.*, vol. 11, p. 045505, apr 2009.

[143] M. Ishihara, T. Morimoto, S. Furuta, K. Kasahara, N. Akikusa, K. Fujita, and T. Edamura, “Linewidth enhancement factor of quantum cascade lasers with single phonon resonance-continuum depopulation structure on Peltier cooler,” *Electron. Lett.*, vol. 45, no. 23, p. 1168, 2009.

[144] A. Villafranca, G. Giuliani, S. Donati, and I. Garcés, “Investigation on the linewidth enhancement factor of multiple longitudinal mode semiconductor lasers,” in *Proc. SPIE* (K. P. Panajotov, M. Sciamanna, A. A. Valle, and R. Michalzik, eds.), vol. 6997, pp. 699719–699719–8, apr 2008.

[145] R. P. Green, J. Xu, L. Mahler, A. Tredicucci, F. Beltram, G. Giuliani, H. E. Beere, and D. A. Ritchie, “Linewidth enhancement factor of terahertz quantum cascade lasers,” *Appl. Phys. Lett.*, vol. 92, no. 7, p. 071106, 2008.

[146] Y. Yu, G. Giuliani, and S. Donati, “Measurement of the Linewidth Enhancement Factor of Semiconductor Lasers Based on the Optical Feedback Self-Mixing Effect,” *IEEE Photonics Technol. Lett.*, vol. 16, pp. 990–992, apr 2004.

[147] N. Kumazaki, Y. Takagi, M. Ishihara, K. Kasahara, N. Akikusa, and T. Edamura,

"First Direct Observation of Small Linewidth Enhancement Factor of Fabry-Perot Quantum Cascade Laser," *Jpn. J. Appl. Phys.*, vol. 47, pp. 1606–1608, mar 2008.

[148] Y. Fan, Y. Yu, J. Xi, G. Rajan, Q. Guo, and J. Tong, "Simple method for measuring the linewidth enhancement factor of semiconductor lasers," *Appl. Opt.*, vol. 54, p. 10295, dec 2015.

[149] B. Ovryn and J. H. Andrews, "Phase-shifted laser feedback interferometry," *Opt. Lett.*, vol. 23, p. 1078, jul 1998.

[150] A. Bearden, M. P. O'Neill, L. C. Osborne, and T. L. Wong, "Imaging and vibrational analysis with laser-feedback interferometry," *Opt. Lett.*, vol. 18, p. 238, feb 1993.

[151] M. Wang and G. Lai, "Self-mixing microscopic interferometer for the measurement of microprofile," *Opt. Commun.*, vol. 238, pp. 237–244, aug 2004.

[152] É. Gagnon, *A 3-D Laser Range Scanner Based on the Self-Mixing Effect in a Laser Diode*. PhD thesis, University of Ottawa, 1998.

[153] S. Shinohara, T. Suzuki, H. Yoshida, H. Ikeda, and M. Sumi, "Acquisition of 3-D image of still or moving objects utilizing laser diode range-finding speedometer," in *Proc. IECON '93 - 19th Annu. Conf. IEEE Ind. Electron.*, vol. 3, pp. 1730–1735, IEEE, 1993.

[154] H. Uda, S. Shinohara, H. Yoshida, H. Ikeda, and M. Sumi, "Reduction of measuring time to acquire 3-D image of moving objects utilizing laser diode range-finding speedometer," in *Conf. Proceedings. 10th Anniv. IMTC/94. Adv. Technol. I M. 1994 IEEE Instrum. Meas. Technolgy Conf. (Cat. No.94CH3424-9)*, no. 3, pp. 1325–1328, IEEE, 1880.

[155] S. Shinohara, H. Uda, Y. Ichioka, H. Yasui, H. Yoshida, H. Ikeda, and M. Sumi, "Detection of mesa spots and indents on slowly moving object surface by laser-light beam scanning," in *SICE '95. Proc. 34th SICE Annu. Conf. Int. Sess. Pap.*, pp. 1167–1170, Soc. Instrum. & Control Eng, 1995.

[156] T. Bosch, N. Servagent, R. Chellali, and M. Lescure, “A scanning range finder using the self-mixing effect inside a laser diode for 3-D vision,” in *EEE Instrum. Meas. Technol. Conf.*, vol. 1, pp. 226–231, IEEE, 1996.

[157] É. Gagnon and J.-F. Rivest, “Laser range imaging using the self-mixing effect in a laser diode,” *IEEE Trans. Instrum. Meas.*, vol. 48, pp. 693–699, jun 1999.

[158] A. Valavanis, P. Dean, Y. L. Lim, R. H. S. Alhathlool, M. Nikolić, R. Kliese, S. P. Khanna, D. Indjin, S. J. Wilson, A. D. Rakić, E. H. Linfield, and A. G. Davies, “Self-Mixing Interferometry With Terahertz Quantum Cascade Lasers,” *IEEE Sens. J.*, vol. 13, pp. 37–43, jan 2013.

[159] T.-I. Jeon and D. R. Grischkowsky, “Characterization of optically dense, doped semiconductors by reflection THz time domain spectroscopy,” *Appl. Phys. Lett.*, vol. 72, no. 23, p. 3032, 1998.

[160] A. D. Rakić, T. Taimre, K. Bertling, Y. L. Lim, P. Dean, D. Indjin, Z. Ikonić, P. Harrison, A. Valavanis, S. P. Khanna, M. Lachab, S. J. Wilson, E. H. Linfield, and A. G. Davies, “Swept-frequency feedback interferometry using terahertz frequency QCLs: a method for imaging and materials analysis,” *Opt. Express*, vol. 21, p. 22194, sep 2013.

[161] H. S. Lui, T. Taimre, K. Bertling, Y. L. Lim, P. Dean, S. P. Khanna, M. Lachab, A. Valavanis, D. Indjin, E. H. Linfield, A. G. Davies, and A. D. Rakić, “Terahertz inverse synthetic aperture radar imaging using self-mixing interferometry with a quantum cascade laser,” *Opt. Lett.*, vol. 39, p. 2629, may 2014.

[162] F. P. Mezzapesa, L. L. Columbo, M. Dabbicco, M. Brambilla, and G. Scamarcio, “QCL-based nonlinear sensing of independent targets dynamics,” *Opt. Express*, vol. 22, p. 5867, mar 2014.

[163] S. Donati, *Electro-Optical Instrumentation Sensing and Measuring with Lasers.* New Jersey: Prentice Hall Professional Technical Reference, 1 ed., 2004.

[164] J. R. Tucker, *A Self-Mixing Imaging System Based on an Array of Vertical-Cavity Surface-Emitting Lasers (VCSELs).* PhD thesis, University of Queensland, mar 2007.

[165] J. T. Verdeyen, *Laser Electronics.* Englewood Cliffs, NJ: Prentice Hall, 3rd. ed., 1995.

[166] K. Petermann, *Laser Diode Modulation and Noise.* Dordrecht: Springer Netherlands, 1988.

[167] M. H. Koelink, M. Slot, F. F. M. de Mul, J. Greve, R. Graaff, A. C. M. Dassel, and J. G. Aarnoudse, "Laser Doppler velocimeter based on the self-mixing effect in a fiber-coupled semiconductor laser: theory," *Appl. Opt.*, vol. 31, p. 3401, jun 1992.

[168] J. Y. Law and G. P. Agrawal, "Effects of optical feedback on static and dynamic characteristics of vertical-cavity surface-emitting lasers," *IEEE J. Sel. Top. Quantum Electron.*, vol. 3, pp. 353–358, apr 1997.

[169] Y. Yu, H. Ye, and J. Yao, "Analysis for the self-mixing interference effects in a laser diode at high optical feedback levels," *J. Opt. A Pure Appl. Opt.*, vol. 5, pp. 117–122, mar 2003.

[170] K. I. Kallimani and M. J. O'Mahony, "Relative intensity noise for laser diodes with arbitrary amounts of optical feedback," *IEEE J. Quantum Electron.*, vol. 34, no. 8, pp. 1438–1446, 1998.

[171] F. W. Kellaway and E. Kreyszig, "Advanced Engineering Mathematics," *Math. Gaz.*, vol. 53, p. 444, dec 1969.

[172] S. Donati, "Responsivity and Noise of Self-Mixing Photodetection Schemes," *IEEE J. Quantum Electron.*, vol. 47, pp. 1428–1433, nov 2011.

[173] F. P. Mezzapesa, L. L. Columbo, M. Brambilla, M. Dabbicco, S. Borri, M. S. Vitiello, H. E. Beere, D. A. Ritchie, and G. Scamarcio, "Intrinsic stability of quantum cascade lasers against optical feedback," *Opt. Express*, vol. 21, p. 13748, jun 2013.

[174] T. Taimre, K. Bertling, Y. L. Lim, P. Dean, D. Indjin, and A. D. Rakić, "Methodology for materials analysis using swept-frequency feedback interferometry with terahertz frequency quantum cascade lasers," *Opt. Express*, vol. 22, p. 18633, jul 2014.

[175] G. Giuliani, M. Norgia, S. Donati, and T. Bosch, "Laser diode self-mixing technique for sensing applications," *J. Opt. A Pure Appl. Opt.*, vol. 4, pp. S283–S294, nov 2002.

[176] R. Kliese, T. Taimre, A. A. A. Bakar, Y. L. Lim, K. Bertling, M. Nikolić, J. Perchoux, T. Bosch, and A. D. Rakić, "Solving self-mixing equations for arbitrary feedback levels: a concise algorithm," *Appl. Opt.*, vol. 53, p. 3723, jun 2014.

[177] A. Grier, *Modelling the optical and electronic transport properties of AlGaAs and AlGaN intersubband devices and optimisation of quantum cascade laser active regions.* PhD thesis, University of Leeds, 2016.

[178] K. Kawase, Y. Ogawa, Y. Watanabe, and H. Inoue, "Non-destructive terahertz imaging of illicit drugs using spectral fingerprints," *Opt. Express*, vol. 11, p. 2549, oct 2003.

[179] A. D. Rakić, K. Bertling, Y. L. Lim, S. J. Wilson, M. Nikolić, T. Taimre, D. Indjin, A. Valavanis, E. H. Linfield, A. G. Davies, G. Walker, B. Ferguson, T. W. Prow, H. Schaider, and H. P. Soyer, "Biomedical applications of terahertz self-mixing interferometry," *SPIE Newsroom*, pp. 4–6, oct 2014.

[180] H. Hoshina, Y. Sasaki, A. Hayashi, C. Otani, and K. Kawase, "Noninvasive Mail Inspection System with Terahertz Radiation," *Appl. Spectrosc.*, vol. 63, pp. 81–86, jan 2009.

[181] S. Donati, "Developing self-mixing interferometry for instrumentation and measurements," *Laser Photon. Rev.*, vol. 6, pp. 393–417, may 2012.

[182] A. A. Michelson and E. W. Morley, "On the relative motion of the Earth and the luminiferous ether," *Am. J. Sci.*, vol. s3-34, pp. 333–345, nov 1887.

[183] S. Barbieri, J. Alton, H. E. Beere, J. Fowler, E. H. Linfield, and D. A. Ritchie, “2.9 THz quantum cascade lasers operating up to 70 K in continuous wave,” *Appl. Phys. Lett.*, vol. 85, no. 10, p. 1674, 2004.

[184] A. J. L. Adam, “Review of Near-Field Terahertz Measurement Methods and Their Applications,” *J. Infrared, Millimeter, Terahertz Waves*, vol. 32, pp. 976–1019, sep 2011.

[185] F. F. Buersgens, R. Kersting, and H.-T. Chen, “Terahertz microscopy of charge carriers in semiconductors,” *Appl. Phys. Lett.*, vol. 88, no. 11, p. 112115, 2006.

[186] A. J. Huber, F. Keilmann, J. Wittborn, J. Aizpurua, and R. Hillenbrand, “Terahertz Near-Field Nanoscopy of Mobile Carriers in Single Semiconductor Nanodevices,” *Nano Lett.*, vol. 8, pp. 3766–3770, nov 2008.

[187] O. Mitrofanov, T. Tan, P. R. Mark, B. Bowden, and J. A. Harrington, “Waveguide mode imaging and dispersion analysis with terahertz near-field microscopy,” *Appl. Phys. Lett.*, vol. 94, no. 17, p. 171104, 2009.

[188] K. Nielsen, H. K. Rasmussen, A. J. L. Adam, P. C. Planken, O. Bang, and P. U. Jepsen, “Bendable, low-loss Topas fibers for the terahertz frequency range,” *Opt. Express*, vol. 17, p. 8592, may 2009.

[189] C.-M. Chiu, H.-W. Chen, Y.-R. Huang, Y.-J. Hwang, W.-J. Lee, H.-Y. Huang, and C.-K. Sun, “All-terahertz fiber-scanning near-field microscopy,” *Opt. Lett.*, vol. 34, p. 1084, apr 2009.

[190] O. Mitrofanov, I. Brener, M. C. Wanke, R. R. Ruel, J. D. Wynn, A. J. Bruce, and J. F. Federici, “Near-field microscope probe for far infrared time domain measurements,” *Appl. Phys. Lett.*, vol. 77, no. 4, p. 591, 2000.

[191] O. Mitrofanov, I. Brener, R. Harel, J. D. Wynn, L. N. Pfeiffer, K. W. West, and J. F. Federici, “Terahertz near-field microscopy based on a collection mode detector,” *Appl. Phys. Lett.*, vol. 77, no. 22, p. 3496, 2000.

[192] Y. Kawano and K. Ishibashi, “An on-chip near-field terahertz probe and detector,” *Nat. Photonics*, vol. 2, pp. 618–621, oct 2008.

[193] R. Lecaque, S. Grésillon, and C. Boccara, “THz emission Microscopy with subwavelength broadband source,” *Opt. Express*, vol. 16, p. 4731, mar 2008.

[194] M. A. Seo, A. J. L. Adam, J. H. Kang, J. W. Lee, S. C. Jeoung, Q. H. Park, P. C. M. Planken, and D. S. Kim, “Fourier-transform terahertz near-field imaging of one-dimensional slit arrays: mapping of electric-field-, magnetic-field-, and Poynting vectors,” *Opt. Express*, vol. 15, p. 11781, sep 2007.

[195] A. Bitzer and M. Walther, “Terahertz near-field imaging of metallic subwavelength holes and hole arrays,” *Appl. Phys. Lett.*, vol. 92, no. 23, p. 231101, 2008.

[196] B. Knoll and F. Keilmann, “Near-field probing of vibrational absorption for chemical microscopy,” *Nature*, vol. 399, pp. 134–137, may 1999.

[197] H.-T. Chen, R. Kersting, and G. C. Cho, “Terahertz imaging with nanometer resolution,” *Appl. Phys. Lett.*, vol. 83, no. 15, p. 3009, 2003.

[198] H.-G. von Ribbeck, M. Brehm, D. W. van der Weide, S. Winnerl, O. Drachenko, M. Helm, and F. Keilmann, “Spectroscopic THz near-field microscope,” *Opt. Express*, vol. 16, no. 5, p. 3430, 2008.

[199] R. Degl’Innocenti, M. Montinaro, J. Xu, V. Piazza, P. Pingue, A. Tredicucci, F. Beltram, H. E. Beere, and D. A. Ritchie, “Differential Near-Field Scanning Optical Microscopy with THz quantum cascade laser sources,” *Opt. Express*, vol. 17, p. 23785, dec 2009.

[200] A. J. Baragwanath, J. R. Freeman, A. J. Gallant, J. A. Zeitler, H. E. Beere, D. A. Ritchie, and J. M. Chamberlain, “Terahertz near-field imaging using subwavelength plasmonic apertures and a quantum cascade laser source,” *Opt. Lett.*, vol. 36, p. 2393, jul 2011.

[201] P. Dean, O. Mitrofanov, J. T. Keeley, I. Kundu, L. H. Li, E. H. Linfield, and A. Giles Davies, “Apertureless near-field terahertz imaging using the self-mixing effect in a quantum cascade laser,” *Appl. Phys. Lett.*, vol. 108, p. 091113, feb 2016.

[202] V. Astley, H. Zhan, R. Mendis, and D. M. Mittleman, “A study of background signals in terahertz apertureless near-field microscopy and their use for scattering-probe imaging,” *J. Appl. Phys.*, vol. 105, no. 11, p. 113117, 2009.

[203] B. Knoll and F. Keilmann, “Enhanced dielectric contrast in scattering-type scanning near-field optical microscopy,” *Opt. Commun.*, vol. 182, pp. 321–328, aug 2000.

[204] M. B. Raschke and C. Lienau, “Apertureless near-field optical microscopy: Tip-sample coupling in elastic light scattering,” *Appl. Phys. Lett.*, vol. 83, no. 24, p. 5089, 2003.

[205] R. Hillenbrand and F. Keilmann, “Complex Optical Constants on a Subwavelength Scale,” *Phys. Rev. Lett.*, vol. 85, pp. 3029–3032, oct 2000.

[206] S. Donati, G. Martini, and T. Tambosso, “Speckle Pattern Errors in Self-Mixing Interferometry,” *IEEE J. Quantum Electron.*, vol. 49, pp. 798–806, sep 2013.

[207] J. T. Keeley, P. Dean, A. Valavanis, K. Bertling, Y. L. Lim, R. H. S. Alhathlool, T. Taimre, L. H. Li, D. Indjin, A. D. Rakić, E. H. Linfield, and A. G. Davies, “Three-dimensional terahertz imaging using swept-frequency feedback interferometry with a quantum cascade laser,” *Opt. Lett.*, vol. 40, p. 994, mar 2015.

[208] M. C. Kemp, P. F. Taday, B. E. Cole, J. A. Cluff, A. J. Fitzgerald, and W. R. Tribe, “Security applications of terahertz technology,” in *Proc. SPIE* (R. J. Hwu and D. L. Woolard, eds.), vol. 5070, pp. 44–52, aug 2003.

[209] J. R. Hobbs, “Analysis of Semtex Explosives,” in *Adv. Anal. Detect. Explos.*, pp. 409–427, Dordrecht: Springer Netherlands, 1993.

[210] S. Han, K. Bertling, P. Dean, J. T. Keeley, A. D. Burnett, Y. L. Lim, S. P. Khanna, A. Valavanis, E. H. Linfield, A. G. Davies, D. Indjin, T. Taimre, and A. D. Rakić,

"Laser Feedback Interferometry as a Tool for Analysis of Granular Materials at Terahertz Frequencies: Towards Imaging and Identification of Plastic Explosives," *Sensors*, vol. 16, p. 352, mar 2016.

[211] S. Donati, M. Norgia, and G. Giuliani, "Self-mixing differential vibrometer based on electronic channel subtraction," *Appl. Opt.*, vol. 45, p. 7264, oct 2006.

[212] G. Giuliani, S. Bozzi-Pietra, and S. Donati, "Self-mixing laser diode vibrometer," *Meas. Sci. Technol.*, vol. 14, pp. 24–32, jan 2003.

[213] P. Dean, J. T. Keeley, A. Valavanis, K. Bertling, Y. L. Lim, T. Taimre, R. H. S. Alhathlool, L. H. Li, D. Indjin, A. D. Rakić, E. H. Linfield, and A. G. Davies, "Active phase-nulling of the self-mixing phase in a terahertz frequency quantum cascade laser," *Opt. Lett.*, vol. 40, p. 950, mar 2015.

[214] J. M. Hensley, J. Montoya, M. G. Allen, J. Xu, L. Mahler, A. Tredicucci, H. E. Beere, and D. A. Ritchie, "Spectral behavior of a terahertz quantum-cascade laser," *Opt. Express*, vol. 17, p. 20476, oct 2009.

[215] N. Beverini, G. Carelli, A. De Michele, A. Moretti, L. Mahler, A. Tredicucci, H. E. Beere, and D. A. Ritchie, "Frequency Characterization of a Terahertz Quantum-Cascade Laser," *IEEE Trans. Instrum. Meas.*, vol. 56, pp. 262–265, apr 2007.

[216] S. Donati and S. Merlo, "Applications of diode laser feedback interferometry," *J. Opt.*, vol. 29, pp. 156–161, jun 1998.

[217] E. E. Orlova, J. N. Hovenier, T. O. Klaassen, I. Kašalynas, A. J. L. Adam, J. R. Gao, T. M. Klapwijk, B. S. Williams, S. Kumar, Q. Hu, and J. L. Reno, "Antenna Model for Wire Lasers," *Phys. Rev. Lett.*, vol. 96, p. 173904, may 2006.

[218] A. J. L. Adam, I. KasÌŇalynas, J. N. Hovenier, T. O. Klaassen, J. R. Gao, E. E. Orlova, B. S. Williams, S. Kumar, Q. Hu, and J. L. Reno, "Beam patterns of terahertz quantum cascade lasers with subwavelength cavity dimensions," *Appl. Phys. Lett.*, vol. 88, no. 15, p. 151105, 2006.

[219] Y. Tan, W. Wang, C. Xu, and S. Zhang, “Laser confocal feedback tomography and nano-step height measurement,” *Sci. Rep.*, vol. 3, p. 2971, oct 2013.

[220] R. Juškaitis, T. Wilson, and F. Reinholz, “Spatial filtering by laser detection in confocal microscopy,” *Opt. Lett.*, vol. 18, p. 1135, jul 1993.

[221] K. S. Youngworth and T. G. Brown, “Focusing of high numerical aperture cylindrical-vector beams,” *Opt. Express*, vol. 7, p. 77, jul 2000.

[222] P. H. Siegel, “THz Instruments for Space,” *IEEE Trans. Antennas Propag.*, vol. 55, pp. 2957–2965, nov 2007.